Search for The Higgs Boson decaying to a b-quark pair produced in association with a W Boson using Missing Transverse Energy Triggered events at ATLAS

Benedict Marc Miller Allbrooke

Thesis submitted for the degree of
Doctor of Philosophy

Particle Physics Group,
School of Physics and Astronomy,
University of Birmingham.

February 6, 2015

Abstract

The $WH \rightarrow \ell\nu b\bar{b}$ production and decay mode of the standard model Higgs Boson is searched for using the 2012 LHC proton-proton data recorded by the ATLAS detector at a centre-of-mass energy $\sqrt{s} = 8$ TeV. Events containing $W \rightarrow \mu\nu$ that fail muon triggers are recovered using a novel technique of recording these events with $E_{\mathrm{T}}^{\mathrm{miss}}$ based triggers.

Two analyses are employed, one based on simple selection criteria to enhance the signal-to-background ratio and one that uses more complex multivariate techniques to separate signal from background. Both analyses exploit the different signal-to-background ratios in regions of the reconstructed W transverse momentum and b-jet tagging categorisation. The events recorded using the $E_{\mathrm{T}}^{\mathrm{miss}}$ triggers are analysed exclusively as well as merged with the events recorded using lepton triggers to improve the sensitivity of the final analyses.

The multivariate merged analysis is found to be the more sensitive of the two analyses, gaining 18.5% compared to the equivalent cut-based analysis. The observed (expected) 95% CL limit for the $WH \rightarrow \ell\nu b\bar{b}$ mode is found to be 2.507 (1.369) and the observed (expected) significance is 1.905 (1.534). The final value of the signal strength for $WH \rightarrow \ell\nu b\bar{b}$ is $\hat{\mu} = 1.231^{+0.733}_{-0.665}$ which is consistent with the Standard Model expectation.

Author's Contribution

The work presented in this thesis would not have been possible without the huge number of people who have contributed to the construction and running of the ATLAS detector. I have contributed to the running of ATLAS through work on the Level 1 Calorimeter trigger and numerous control room shifts.

Chapters 2, 3, 4 & 5 are reviews of the theoretical background, Large Hadron Collider, ATLAS Detector and Level 1 Calorimeter Trigger respectively. I have not been involved in the development of these areas and so these chapters contain no original research.

Chapter 6 contains studies which are entirely my own work.

The analyses described in Chapter 7 are my own work but are implemented using a set of packages developed with others.

The fit model summarised in Chapter 8 is the work of a large number of people within the ATLAS VH search group, the development of which I have been part of. The plots made with this fit are my own work.

I developed and performed the entirety of the correlation analysis presented in Chapter 9. The input files used for this analysis were provided by others within the ATLAS VH search group.

The results presented in Chapter 10 are my own work, using a mixture of input analyses produced by myself and others. The exact analysis contributions by others are noted in the text.

Dedicated to my Grandmother, the first Allbrooke Physicist

Acknowledgements

I am very grateful to a large number of people who have helped me academically and/or personally in the completion of this thesis.

I owe huge thanks to my supervisors Alan Watson and Paul Thompson without whom this thesis, and the work contained within it, would not have been possible. Both have shown enormous patience over the past 4 years. I would also like to thank the rest of the Particle Physics Group for giving me the opportunity to study in Birmingham and who have provided a very friendly and welcoming atmosphere. I have been taught and helped greatly by many members of the group during my time here. My fellow Physics West 316 and CERN B104-1-B04 office mates Andy, Neil, Dave, Tim, Jody, Tom, Hardeep, Richard, Andrew, Javier, Mark, Matt and Rhys have made both work time and free time immeasurably more enjoyable and entertaining.

My parents have always given me a huge amount of support, both before and during my studies. Without them I could not have got to where I am today and I am constantly thankful for their help.

Finally, I am immensely thankful to Sarah for supporting me, looking after me and putting up with my unsociable working hours during the completion of this thesis.

What's hard, in hacking as in prose, is not writing, it's deciding what to write

Neal Stephenson - *In the Beginning... Was the Command Line*

Contents

List of Tables

List of Figures

Definitions Of Acronyms

ALICE A Large Ion Collider Experiment

ATLAS A Toroidal LHC Apparatus

BCID Bunch Crossing Identification

BDT Boosted Decision Tree

CMS Compact Muon Solenoid

CPM Cluster Processor Module

CSC Cathode Strip Chambers

CTP Central Trigger Proccessor

EF Event Filter

FCal Forward Calorimeter

FPGA Field Programmable Gate Array

HI Heavy Ion

HLT High Level Trigger

IBL Insertable B-Layer

JEM Jet/Energy Sum Module

JES Jet Energy Scale

JVF Jet Vertex Fraction

L1Calo Level 1 Calorimeter Trigger

L1Mu Level 1 Muon Trigger

LAr Liquid Argon

LHC Large Hadron Collider

LHCb LHC beauty

LUT Look Up Table

MBTS Minimum Bias Trigger Scintillator

MC Monte Carlo

MDT Monitored Drift Tubes

PDF Parton Distribution Function

PPM Pre-Processor Module

QCD Quantum Chromodynamics

RoI Regions of Interest

RPC Resistive Plate Chambers

SCT Semi-Conductor Tracker

SPS Super Proton Synchrotron

TGC Thin Gap Chambers

TRT Transition Radiation Tracker

VBF Vector Boson Fusion

CHAPTER 1

Introduction

The search for the standard model Higgs Boson is a cornerstone of the Large Hadron Collider physics programme, particularly for the ATLAS and CMS experiments, which have been optimised for identifying and measuring Higgs final states. The Higgs mechanism is a fundamental part of the standard model and provides an elegant way of adding masses to fundamental particles. This thesis presents a search for the standard model Higgs Boson with the ATLAS experiment at the LHC using the $WH \rightarrow \ell\nu b\bar{b}$ production and decay mode. A novel technique, the use of transverse missing energy triggers, is employed to recover events lost by the standard lepton triggers. An important requirement for physics analyses at the LHC is to efficiently record physics processes and to reduce backgrounds. This thesis also contains a study of the identification efficiency of ATLAS calorimeter signal pulses.

Chapter 2 covers background information on the Higgs mechanism. This includes a description of the theoretical basis, production and decay of the Higgs Boson and a survey of the experimental status, current as of January 2015, for the different decay modes.

A brief overview of the Large Hadron Collider is provided in Chapter 3 and a more complete breakdown of the ATLAS detector and its component subdetectors can be found in Chapter 4. Studies performed of the efficiency for the ATLAS Level 1 Calorimeter Trigger, described in Chapter 5, to match ATLAS Calorimeter pulses to LHC bunch crossings are presented in Chapter 6.

Chapter 7 details two analyses used to search for a Higgs Boson decaying to a b-quark pair, produced in association with a W Boson that decays to a charged lepton, in this case a muon, and a neutrino. A significant portion of the events containing this process are not recorded by single muon triggers so both of these analyses use triggers based on the missing transverse energy of the event to recover events. One of the analyses uses a conventional cut-based selection to attempt to extract a signal while the other uses more sophisticated multivariate techniques to separate signal and background processes.

Chapter 8 describes the statistical fitting procedure applied to the $WH \rightarrow \ell\nu b\bar{b}$ analyses. The missing transverse energy triggered cut-based and multivariate analyses are fitted both exclusively and merged into the ATLAS single lepton analyses to search for this process. The results are presented in Chapter 10 for both the missing transverse energy triggered analyses and the merged analyses.

An additional study is presented in Chapter 9 that seeks to measure the correlation between the cut-based and multivariate analyses used in the ATLAS searches for a Higgs Boson decaying to a b-quark pair, produced in association with a W or Z Boson. This is also used to estimate the consistency of the results measured in data.

A brief summary of the results of the analyses and studies contained in this document is included in Chapter 11.

CHAPTER 2

The Higgs Boson

2.1 The Standard Model

The Standard Model of particle physics is a theoretical framework that describes fundamental particles and their interactions [1]. A single Lagrangian equation is the common representation of the Standard Model. The fundamental particles are divided into fermions, the matter forming particles that have half integer spin, and bosons, the force mediators that have integer spins. Fermions are further divided into quarks, which experience the strong force, and leptons that do not. Both quarks and leptons contain three generations with two particles in each generation. The family of quarks consists of the up (u), down (d), charm (c), strange (s), top (t) and bottom (b). The properties of these six quarks are summarised in Table 2.1. The family of leptons consists of the electron (e), muon (μ), tau (τ) and a corresponding neutrino (ν) for each. The properties of these six leptons are summarised in Table

2.2. Neutrino masses are given as upper bounds based on current experimental limits. Each of the fermions has an anti-particle partner with the same properties apart from having equal and opposite charge and internal quantum numbers. The first generation of quarks and leptons are the matter that makes up the majority of our universe.

Quark	Generation	Mass	EM Charge
Up	1	$2.3^{+0.7}_{-0.5}$ MeV	+2/3
Down	1	$4.8^{+0.5}_{-0.3}$ MeV	-1/3
Charm	2	1.275 ± 0.025 GeV	+2/3
Strange	2	95 ± 5 MeV	-1/3
Top	3	173.1 ± 1.3 GeV	+2/3
Bottom	3	4.18 ± 0.03 GeV	-1/3

Table 2.1: Properties of the six quarks in the Standard Model. Charge is expressed as a fraction of the electron charge e [1].

Lepton	Generation	Mass	EM Charge
e	1	0.511 MeV	-1
ν_e	1	< 2 eV	0
μ	2	105.66 MeV	-1
ν_μ	2	< 2 eV	0
τ	3	1.78 GeV	-1
ν_τ	3	< 2 eV	0

Table 2.2: Properties of the six leptons in the Standard Model. Charge is expressed as a fraction of the electron charge e [1].

The bosons act as mediators for the fundamental forces of nature, allowing the interactions between quarks, leptons and other bosons to occur. The photon carries the electromagnetic force, the 8-fold family of gluons carry the strong force and the $W^{\pm}$ and Z carry the weak force. All charged particles can experience electromagnetic interactions, fermions experience the weak force and particles carrying colour charge (quarks and gluons) experience the strong force. The properties of the bosons are summarised in Table 2.3.

Bosons and leptons do not form (or rather are not known to form) composite particles apart from positronium, an electron and positron bound state, but quarks can be bound together by the strong force to form hadrons. Hadrons are split into mesons that are made up of a quark and an anti-quark and baryons that consist of three quarks or three anti-quarks. One prominent example of a baryon is the proton which is composed, at valence level in the quark model, of two up quarks and a down quark. The strength of the strong force bonding the valence quarks together causes a huge flux of gluons to be produced, many of which create virtual pairs of quarks and anti-quarks. It is the combination of the valence quarks, sea quarks and gluons which forms the full proton and its mass. The total longitudinal momentum of the proton is shared out between its composite particles according to its Parton Distribution Function (PDF). The PDF shows the probability for finding a particular parton type at a given x value, the fraction of the proton's momentum. PDFs are calculated specifically for the energy scale, Q^2, at which the interaction occurs due to the mediator. Different versions of the PDF for a proton at LHC energy are produced, by groups using different calculation and experimental data, which are referred to as PDF sets. An example of a PDF set produced for the LHC is shown in Figure 2.1 for two different values of Q^2.

Gravity has not been discussed here as it currently does not fit into the Standard Model. No boson has been observed to mediate gravity though many theories postulate the existence of the graviton. Gravity has a strength approximately 10^{25} times weaker than the weak force (dependant on the particles involed), for reasons currently unknown, and so is generally neglected in particle physics.

Force	Boson	Mass	EM Charge
Electromagnetic	γ	0	0
Weak	Z	91.2 GeV	0
Weak	W	80.4 GeV	±1
Strong	g	0	0

Table 2.3: Properties of the Bosons in the Standard Model. Charge is expressed as a fraction of the electron charge e [1].

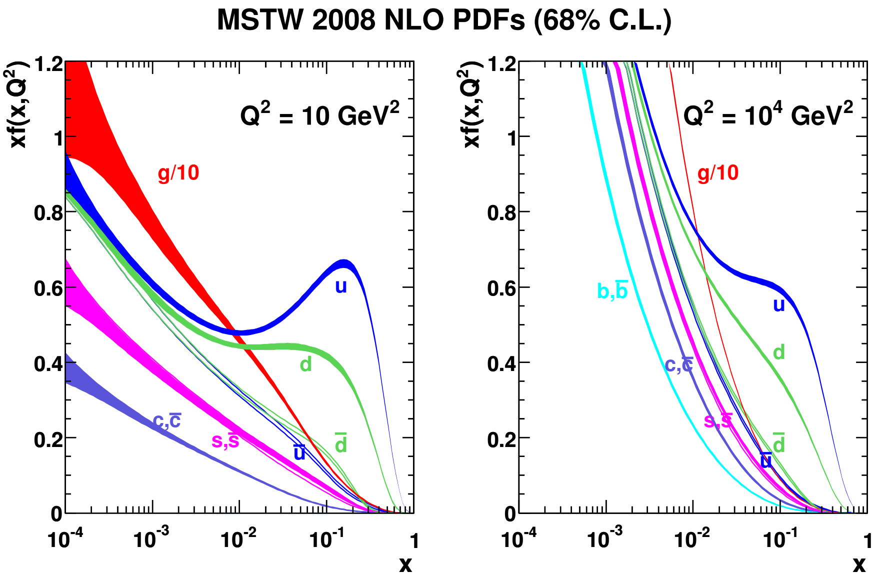

Figure 2.1: Example of a PDF which is part of the MSTW 2008 set [2]. The PDF shows all parton flavours for two different values of Q^2. The bands of each line represent the $\pm 1\sigma$ errors on the calculations.

2.2 The Higgs Mechanism

The Standard Model describes strong and electroweak interactions well but on its own has no way of giving masses to fermions and bosons without an additional mechanism. The weak and electromagnetic sectors were theoretically unified by Glashow, Salam and Weinberg [3, 4, 5]. The Standard Model electroweak sector is described in group theory as $SU(2)_L \times U(1)_Y$ where L denotes the left-handed fermions and Y denotes the weak hypercharge.

The $SU(2)$ group gives rise to 3 weak isospin bosons which are the $W^{\pm}$ and W^0 while the $U(1)$ group gives a single weak hypercharge boson which is the B^0. These are, however, not the same set of bosons which are observed in the electroweak sector (i.e. the $W^{\pm}$, Z and γ). Based on the electroweak theory all four bosons should be massless but it is known that three of the four electroweak bosons have mass, the Z and $W^{\pm}$, and only one is massless, the photon. Therefore something additional must be added to the theory to account for this and give mass to these three bosons.

To bridge the gap between the bosons produced from the gauge group and the observable bosons, the electroweak symmetry must be spontaneously broken by an additional mechanism. This causes the rotation of the B^0 and W^0 to form the Z and γ as shown in Equation 2.1 in terms of the weak mixing angle, θ_W. The relationship of the electromagnetic and weak force bosons means that for the high energy limit, where the masses become negligible, the electromagnetic and weak forces behaviour identically. The combining of the two forces, theoretically, is known as electroweak unification. The weak mixing angle brings with it a discrepancy between the W and Z masses which can be expressed as shown in Equation 2.2.

$$\begin{pmatrix} \gamma \\ Z \end{pmatrix} = \begin{pmatrix} \cos\theta_W & \sin\theta_W \\ -\sin\theta_W & \cos\theta_W \end{pmatrix} \begin{pmatrix} B^0 \\ W^0 \end{pmatrix}. \tag{2.1}$$

$$M_Z = \frac{M_W}{\cos\theta_W}. \tag{2.2}$$

The method Glashow used to spontaneously break the electroweak symmetry was to explicity add masses to the bosons without any additional field or mechanism. It is a beneficial property of a theory, such as the Standard Model, that it be gauge invariant. Gauge invariance means that the outcome of the theory is not dependent on the gauge, or phase of the measurement relative of the wave function. The Lagrangian should be unchanged by a change of gauge such as $\psi \rightarrow e^{i\alpha(x)}\psi$, i.e. invariance with a phase choosen at each point in spacetime. This is known as local gauge invariance. Explicity adding a mass term to account for boson masses would break the gauge invariance of the Standard Model Lagrangian.

This problem was overcome independently by Higgs [6], Brout & Englert [7] and Guralnik, Hagen & Kibble [8]. The solution is to introduce a field into the Standard

Model characterised by an $SU(2)$ doublet [4] that takes the form:

$$\psi = \begin{pmatrix} \psi^+ \\ \psi^0 \end{pmatrix}, \tag{2.3}$$

where ψ^+ and ψ^0 are both fields defined in terms of four real components, ψ_{1-4}, such that:

$$\psi^+ = \frac{\psi_1 + i\psi_2}{\sqrt{2}}, \tag{2.4}$$

$$\psi^0 = \frac{\psi_3 + i\psi_4}{\sqrt{2}}. \tag{2.5}$$

The Lagrangian of this field can be written as:

$$\mathcal{L} = (D_\mu \psi)^\dagger (D^\mu \psi) - V(\psi), \tag{2.6}$$

where D_μ is the covariant derivative that refers to left handed fermions and with the field's potential energy, $V(\psi)$ defined as:

$$V(\psi) = \mu^2 \psi^\dagger \psi + \lambda(\psi^\dagger \psi)^2, \tag{2.7}$$

λ is a coupling constant so it would be expected that $\lambda > 0$, which also guarantees that minima exist for the potential. The choice for μ then becomes $\mu^2 > 0$ or $\mu^2 < 0$. In the case of $\mu^2 > 0$ there is only a single minimum at $\psi = 0$ with no possibility of a broken symmetry. Taking $\mu^2 < 0$ gives the potential shown in Figure 2.2, often described as the "Mexican Hat" potential. This potential has a degenerate, rotationally symmetric minimum in terms of the vacuum expectation value, v, of:

$$\psi^\dagger \psi = \frac{\mu^2}{\lambda} \equiv \frac{v}{2}. \tag{2.8}$$

The degeneracy of this ground state must be removed so one particular point on the circle of possible values, at a radius of $v/2$ must be chosen. By convention in the

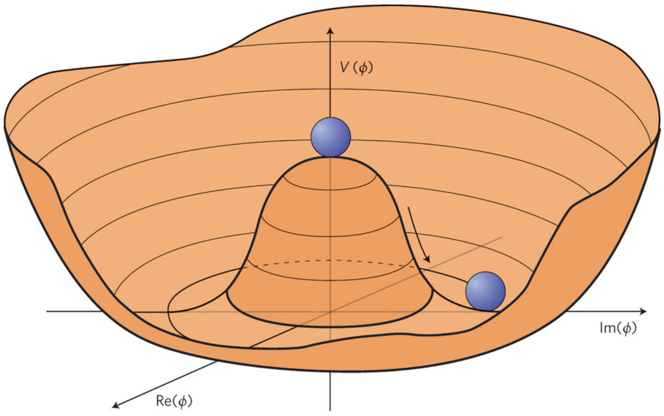

Figure 2.2: Diagram showing the Higgs "Mexican Hat" potential [9].

standard model the gauge is chosen such that $\psi_1 = \psi_2 = \psi_4 = 0$ and $\psi_3 = v$. This gives a chosen ground state of

$$\psi_0 = \sqrt{\frac{1}{2}}\begin{pmatrix} 0 \\ v \end{pmatrix} \tag{2.9}$$

and equation 2.4 then becomes:

$$\psi = \sqrt{\frac{1}{2}}\begin{pmatrix} 0 \\ v + H \end{pmatrix} \tag{2.10}$$

in terms of the Higgs Boson field H, which is a radial excitation of the ground state.

This choice of direction for ψ is the crucial element of electroweak symmetry breaking and causes the Z and $W^{\pm}$ to experience an interaction with the Higgs field that is not experienced by the photon. The potential of the Higgs field causes spontaneous symmetry breaking of 3 of the 4 generators of the electroweak $SU(2) \times U(1)$ gauge group, usually referred to as the unphysical Goldstone bosons. The Z and $W^{\pm}$ absorb the Goldstone bosons which gives the Z and $W^{\pm}$ mass and is then only observable as their integer spin. The fourth, leftover, generator can be interpreted as the Higgs boson itself.

This provides an explanation for how the Z and $W^{\pm}$ acquire mass but does not explain the masses of the fermions. An important property of the Higgs field is its non-zero vacuum expectation value. Particles will therefore interact with the Higgs field anywhere in space, obtaining mass through this interaction as if the Higgs field were impeding their progress through a medium [10]. The strength of the interaction between a fermion and the Higgs field is defined by each fermion's Yukawa coupling.

The Higgs mechanism is not the only possible method of breaking electroweak symmetry and giving mass to particles. Many other models such as Technicolour [11] or a Top quark condensate [12] allow electroweak symmetry breaking but this happens in a less elegant way, requiring many additional parameters. The Higgs mechanism is an attractive theory because its solution yields only one additional free parameter, the mass of the Higgs Boson. The Higgs Boson brings with it a convenient way to provide a negative contribution to certain processes such as WW scattering which would otherwise have divergent cross sections at the TeV scale [13].

Under many extensions to the standard model such as Sypersymmetry there are multiple Higgs Bosons predicted. Under these models there may be heavy Higgs, charged Higgs doublets that would interact in a similar way to the $W^{\pm}$ and a light Higgs within the mass range of current searches [14].

2.3 Production and Decay at the LHC

The Higgs Boson is very difficult to search for experimentally due to its very small production cross section. This is exacerbated by the numerous ways that the Higgs boson can decay giving a very small cross section times branching ratio for each of the different final states. The total Higgs production cross section in comparison to other processes is shown in Figure 2.3. This necessitates high energy colliders with very large luminosities to produce enough Higgs Bosons to permit observation.

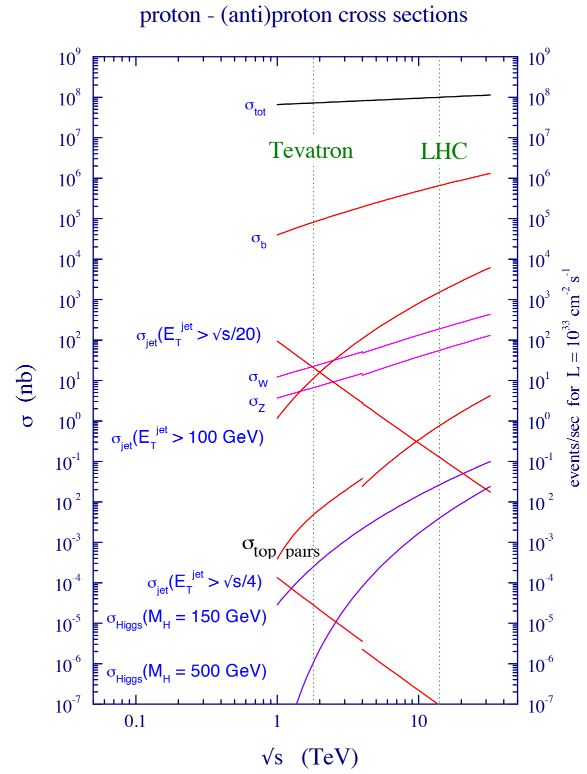

Figure 2.3: Cross-sections of various processes as function of energy. The discontinuity observed in several channels are due to changing from the $p\bar{p}$ of the TeVatron to the pp of the LHC [15].

.

A variety of processes can produce a Higgs Boson in proton-proton collisions, for which Feynman diagrams are shown in Figure 2.4. The production modes are gluon-gluon fusion, vector boson fusion, top quark pair fusion and radiation by a vector boson.

Production by gluon-gluon fusion via a top quark loop is dominant at the LHC due to the huge density of low x (fraction of the proton's momentum) gluons that are high enough energy to produce a Higgs at LHC beam energies. This production mode is dominant for all Higgs masses considered at the LHC up to 1 TeV. Production by gluon-gluon fusion yields only the Higgs decay products in the final state and no additional QCD radiation.

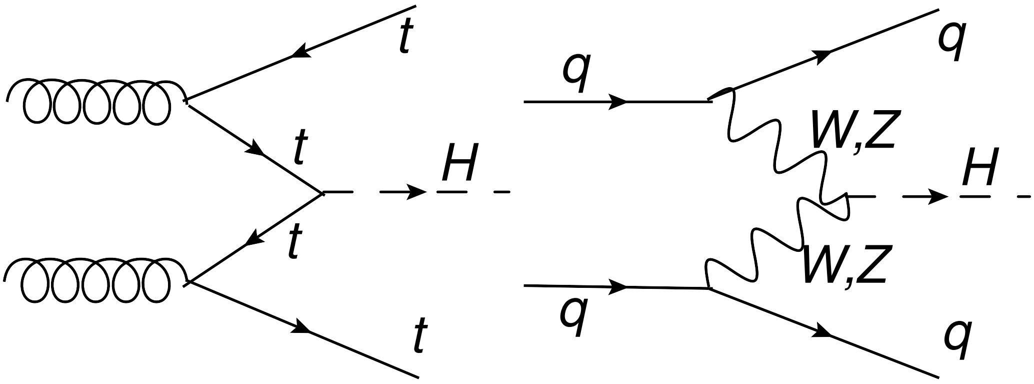

(a) $t\bar{t}$ Fusion (b) Vector Boson Fusion

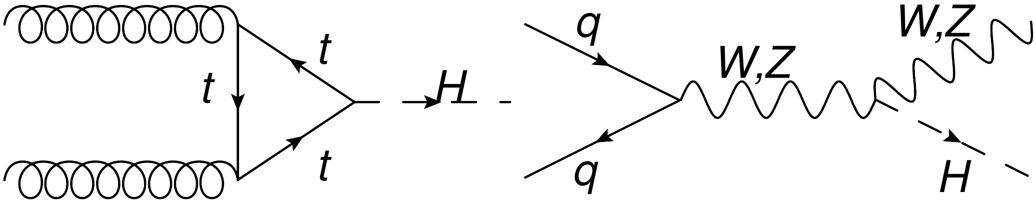

(c) Gluon-Gluon Fusion (d) Associated Production

Figure 2.4: Feynman diagrams of the different possible production modes of the Standard Model Higgs Boson.

A Higgs could also be produced by Top quark pair fusion or Vector Boson Fusion (VBF) whereby two massive objects join to produce a Higgs Boson. The Higgs couples to mass so massive objects are required for this process. In top quark pair fusion, two pairs of top quarks are produced followed by one from each fusing to form a Higgs Boson. The final state will contain the Higgs boson decay products and the decay products from a top quark pair decay. In VBF, a quark from each incoming proton radiates a vector boson (a W or Z) which then fuse to form a Higgs boson. The final state contains the Higgs decay products and two quark initiated jets, likely to be travelling at a small angle with respect to the beam line and in opposite directions. VBF has the next largest cross-section after gluon-gluon fusion but a large fraction of the events will contain jets that travel too close to the beam line to be detected.

The final possible production mode is the radiation of a Higgs by a vector boson (a W or Z), often described as Associated Production, VH or “Higgsstrahlung” by analogy to bremsstrahlung. The final state of VH events contain the Higgs decay products as well as the W or Z decay products. By looking for events that also contain a vector boson it is possible to make use of Higgs decay modes that are otherwise too background-dominated. These production modes all have cross-sections which decrease with increasing Higgs mass because it becomes increasingly difficult to produce a more massive object. The cross-sections for the different processes as a function of the Higgs mass are shown in Figure 2.5 for centre-of-mass energies $\sqrt{s} = 7$ TeV and $\sqrt{s} = 8$ TeV. The blue line in Figure 2.5 represents gluon-gluon fusion, as shown in Figure 2.4c, the red line represents VBF, as shown in Figure 2.4b, the green and brown lines represent associated production, as shown in Figure 2.4d and the pink line represents $t\bar{t}$ fusion, as shown in Figure 2.4a.

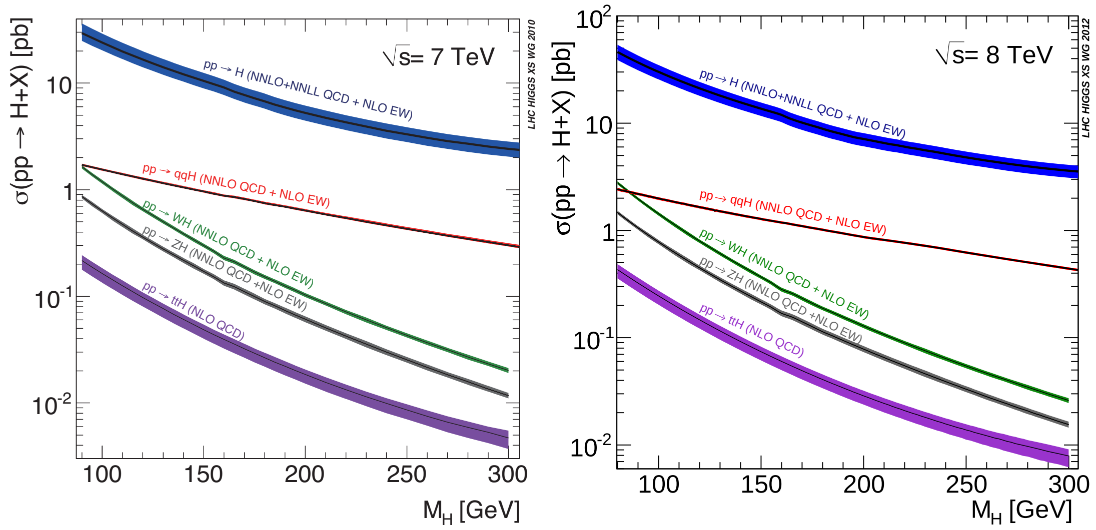

Figure 2.5: Cross-sections as a function of Higgs mass for the different production modes for a centre-of-mass energy, $\sqrt{s}$, of 7 TeV (Top) and 8 TeV (Bottom) [16].

The Higgs Boson can decay in a variety of ways, the relative fractions for which change with the Higgs mass and are shown in Figure 2.6 for the low mass case. Some of the decay modes that form a part of the LHC search strategies are described in Section 2.4. The total width as a function of Higgs mass is shown in Figure 2.7

The quark decay modes, such as the $H \to b\bar{b}$ which is used in this thesis, are harder

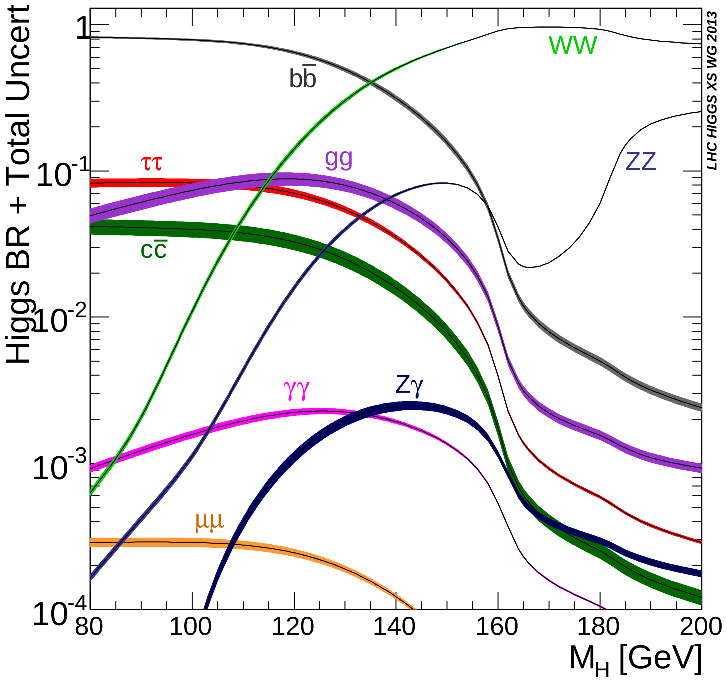

Figure 2.6: Branching ratio of different decay modes as function of Higgs mass. Left: for low Higgs masses, Right: for a wider mass range [16].

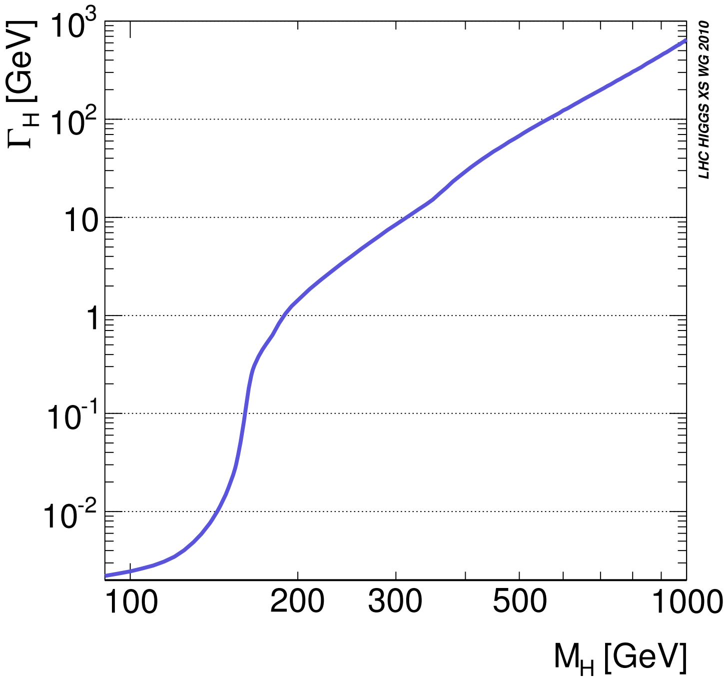

Figure 2.7: Total width of the Standard Model Higgs Boson as a function of the Higgs mass [16].

to observe because “naked” quarks can not be observed as they have colour charge, a property known as colour confinement. Colour confinement is largelly a result of the strength of the strong interaction increasing with separation. The initially produced quarks will, as their separation increases when exiting the interaction, first radiate gluons that produce quark and anti-quark pairs. These quarks and anti-quarks can then further radiate gluons and so the initial quarks can produce a large number of particles, the process of which is called parton showering [17].

As the quark and anti-quark pairs separate from each other a very strong gluon field forms between the two. As the two particles continue to separate, there becomes a distance at which it is more energetically favourable to bring a new quark and anti-quark pair out of the vacuum than to continue to extend the field. This happens continually such that a huge number of particles are produced together and form colourless hadrons. This process is known as hadronisation [18].

Parton showering and hadronisation are processes which are modelled by Monte Carlo generators, some of which are designed specifically for these and some of which are more general. The use of Monte Carlo generators for this in an analysis is described in Section 7.2. The combination of the two processes converts the initial quark into a large cone of hadrons travelling close to collinear. The collection of hadrons, initiated by the quark, is known as a jet [19].

2.4 Experimental Status

The experiments at CERN’s previous accelerator, the Large Electron-Positron Collider (LEP) were able to place a lower bound on the Standard Model Higgs mass of 114.4 GeV using electron positron collisions at a centre-of-mass energy, $\sqrt{s}$, of up to 209 GeV [20]. Direct searches able to place this limit used the associated production mode with a Z boson (as described in Section 2.3). The decay channels used were the Higgs decaying to a b-quark pair with the Z decaying to two quarks, two neutrinos or two leptons (including taus) and the Higgs decaying to two taus and the Z decaying to two quarks [21]. The LEP experiments also fitted simultaneously many measurements in the electroweak sector that have a dependence on the Higgs mass. This provides a constraint for the consistency of different Higgs masses with LEP electroweak observations. This consistency, as well as the direct exclusion, are shown in Figure 2.8.

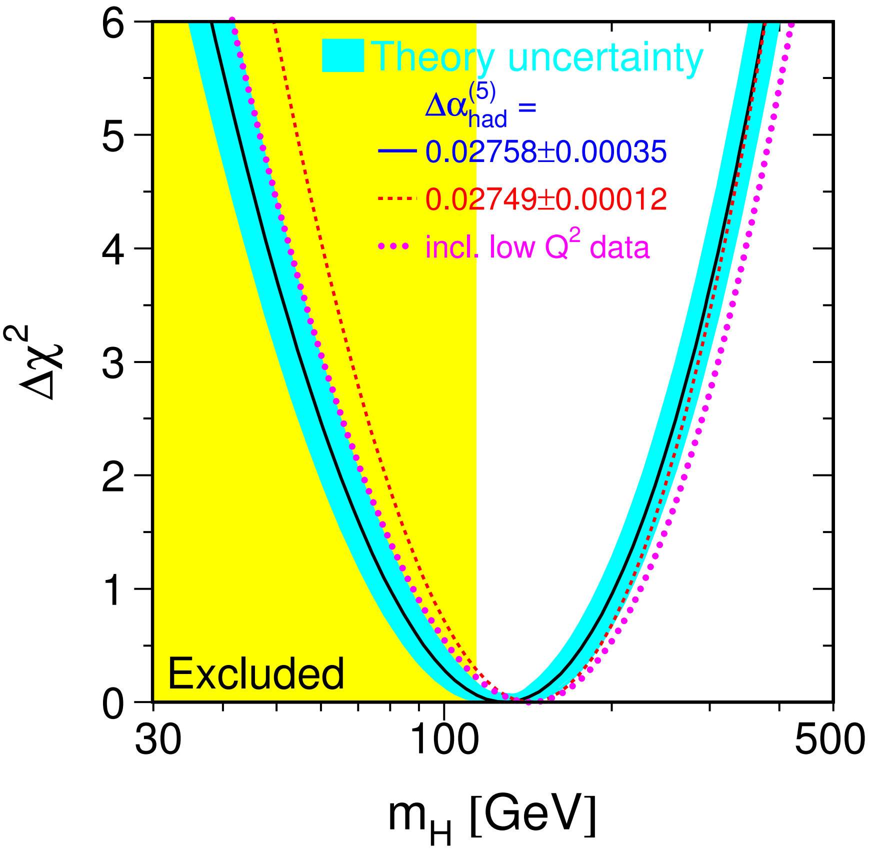

Figure 2.8: Final results of the LEP Higgs Search. The direct exclusion below 114.4 GeV is shaded in yellow and the consistency with EW measurements is shown as a function of Higgs mass [22].

Searches by the two experiments at the TeVatron, Fermilab's most recent collider, were able to exclude the region $149 < m_H < 182$ GeV at 95% confidence limit using proton anti-proton collisions at $\sqrt{s} = 1.96$ TeV [23]. Exclusion limits at 95% for the full TeVatron dataset are shown in Figure 2.9. Some significant deviations from the background expectation were found, the largest being a local significance of 3.1σ at a candidiate Higgs mass of 120 GeV. The significant excesses were found in the $H \to WW$ channel and using associated production VH channels where the Higgs decays to a b-quark pair. The associated production modes contribute the majority of the significance because direct gluon-gluon fusion production is unlikely to proceed at Tevatron energies. There are few gluons with a high enough fraction of the proton/anti-proton's momentum to create a massive object such as the Higgs Boson.

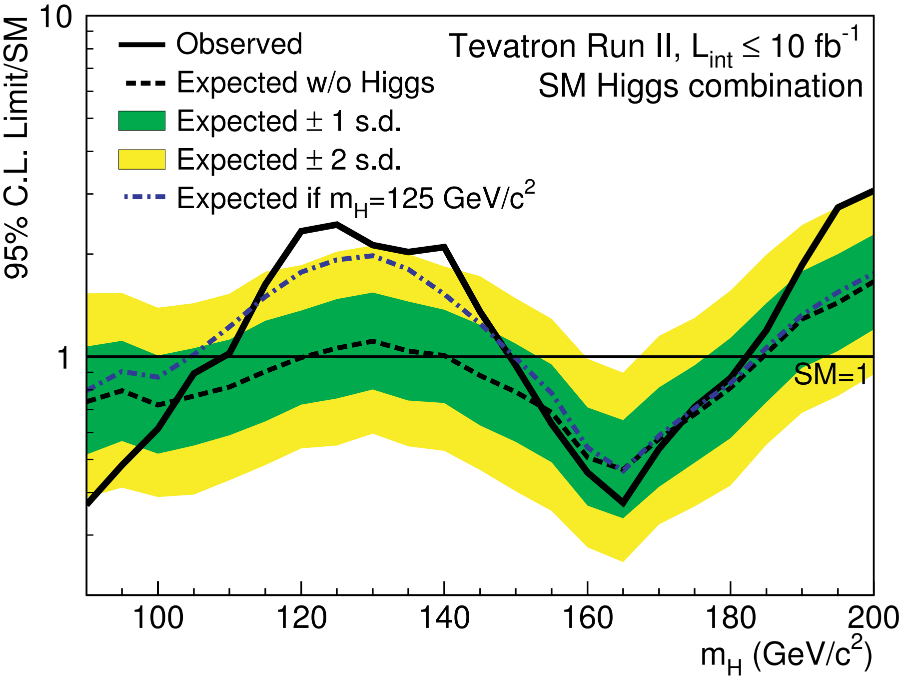

Figure 2.9: Final results of the Tevatron Higgs Search. The direct exclusion of the $149 < m_H < 182$ GeV mass range is shown by the region in which the observed limit drops below 1 times the Standard Model cross-section [23].

The search for the Higgs Boson is one of the cornerstones of the LHC program and for this reason both the ATLAS and CMS detectors are optimised for the reconstruction and measurement of potential Higgs decay products. On July 4th 2012 both the ATLAS and CMS Collaborations announced the observation of a "Higgs-like" Boson at a mass of approximately 125 GeV with a significance of 5.0σ [24] and 4.9σ [25] respectively. This result was announced using the full 2011 dataset of up to 5.1 fb^{-1} and the then current 2012 dataset of up to 5.9 fb^{-1}.

Since the discovery by ATLAS and CMS, both collaborations have updated all Higgs analyses as well as performing statistical fits on the combination of the analyses. Both experiments use many of the decay modes shown in Figure 2.6. A brief description of the more commonly used decay modes in Higgs searches is given below as well as selected latest public results from these searches, as of January 2015. Analysis of the decay modes is generally split up further, based on the particles in the final state, into channels. There are many additional rare decay modes not described here, which have not been part of the main search strategies during LHC Run 1, such as decays to $J/\psi\gamma$ [26]. Results are generally described in terms of the observed signal strength, $\hat{\mu}$, or the limit on the signal strength. The signal strength is the measured multiple of the theoretical expected Standard Model cross section times branching ratio for the process. The limit on the signal strength is expressed as a 95% confidence level upper bound.

- $\gamma\gamma$: Despite a very small branching ratio, the decay to $\gamma\gamma$ is one of the most sensitive channels. This channel offers good resolution and a smooth continuum background of non Higgs $\gamma\gamma$ and events faking photons that can be modelled. This channel can be fully reconstructed which, coupled with good resolution, allows this channel to be used for mass measurements. ATLAS has measured a signal strength of 1.17 ± 0.27 [27]. The Higgs mass is measured in this channel, by ATLAS, to be $m_H = 124.51 \pm 0.52$ GeV [28]. The distribution of reconstructed Higgs mass that this value is extracted from is shown in Figure 2.10. CMS has measured a signal strength in this channel of $1.14^{+0.26}_{-0.23}$ at a mass of $m_H = 124.70 \pm 0.34$ GeV [29].
- ZZ: The branching ratio to ZZ increases with increasing Higgs mass. The Zs produced from this decay can be real or virtual. The ZZ decay modes are cleaner and less background dominated than WW but have lower branching ratios. This decay can be searched for in several channels based on the decays

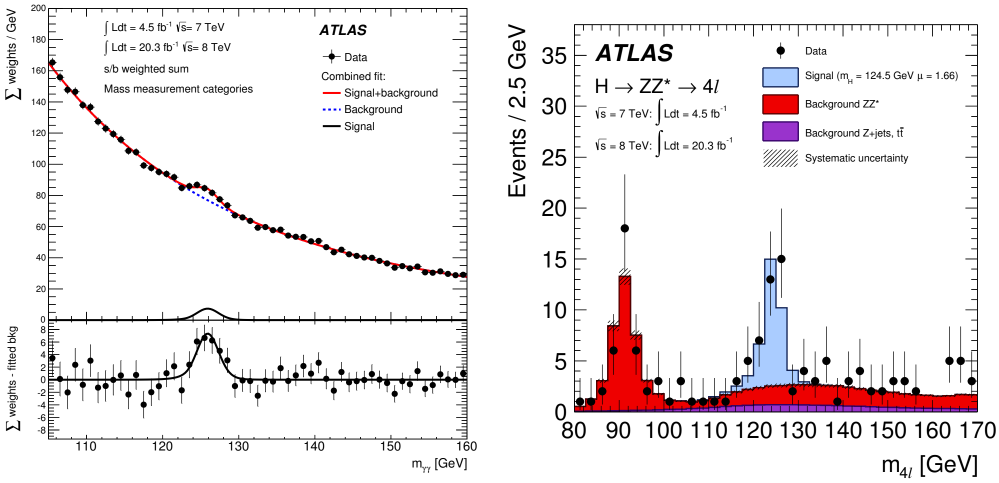

(a) $H \to \gamma\gamma$ (b) $H \to ZZ \to 4\ell$

Figure 2.10: Distributions of reconstructed Higgs mass in the ATLAS $\gamma\gamma$ and 4ℓ final states using the full 2011 7 TeV and 2012 8 TeV datasets [28].

of the two Zs. In all the decay channels used, one of the Zs decays to charged leptons as this allows for better triggering, reconstruction and sensitivity. The channels used are $ZZ \to \ell\ell\ell\ell$, $\ell\ell\nu\nu$, $\ell\ell qq$. The 4 lepton channel is often considered to be the "Golden Channel" for LHC Higgs physics as it allows for full reconstruction of the final state, good resolution and very low backgrounds, making it suitable for measurements such as mass and spin/charge-parity. ATLAS has measured a signal strength of $1.44^{+0.40}_{-0.33}$ in the 4 lepton channel, the most sensitive of the ZZ decay modes, and exploiting multiple production modes [30]. The Higgs mass is measured in this channel, by ATLAS, to be $m_H = 125.98 \pm 0.50$ GeV [28]. The distribution of reconstructed Higgs mass that this value is extracted from is shown in Figure 2.10. CMS has measured a signal strength of $0.93^{+0.31}_{-0.27}$ at a mass of $m_H = 125.63 \pm 0.44$ GeV [31].

- WW: At masses above $m_H \sim 130$ GeV, Higgs decays to WW become dominant. The Ws produced from this decay can be real or virtual. This decay can be searched for in different channels based on the decays of the two Ws. The main channels used are $WW \to \ell\nu\ell\nu$ and $\ell\nu qq$ as other decays are too difficult to reconstruct and extract a signal from. The case where both Ws decay leptonically gives the best sensitivity but the presence of two neutrinos in the final state prevents the system from being fully reconstructed and prevents the channel being used for a mass measurement. At around twice the W mass the decay to WW is almost 100%, a resonance effect, which has allowed the TeVatron to achieve its best limits around this mass. CMS measures a signal strength of $0.72^{+0.20}_{-0.18}$ in the $\ell\nu\ell\nu$ channel [32] and ATLAS measures a signal strength of $1.09^{+0.16}_{-0.15}(\text{stat.})^{+0.17}_{-0.14}(\text{syst.})$ [33].

- $Z\gamma$: In a narrow mass range around $m_H = 120 - 140$ GeV, the $Z\gamma$ decay mode has a comparable branching ratio to $\gamma\gamma$. Only the leptonic Z decays are used so this significantly reduces the effective branching ratio to a level that makes extracting a signal very challenging. This channel benefits from being able to trigger and reconstruct the final state due to high transverse momentum leptons and photon. ATLAS has placed a limit of 11.0 times the Standard Model prediction for the cross section times branching ratio of the process at $m_H = 125$ GeV [34] and CMS has placed a better limit of 10.0 [35].

- $\tau\tau$: At very low masses the $\tau\tau$ decay hass one of the largest branching ratios. This channel is difficult to exploit due to the problems of triggering and reconstructing τ leptons. Tau leptons can decay in several different ways, to lighter leptons and to different multiplicities of pions and kaons, such that several signatures must be searched for simultaneously. The wide resolution of the di-τ mass reconstruction and the nearby $Z \to \tau\tau$ peak make extracting a signal very challenging. The combination of the different channels with the $\tau\tau$ search provides a powerful way to observe that the Higgs decays to fermions. CMS measured a signal strength of 0.78 ± 0.27 [36] whereas ATLAS measured a signal strength of $1.42^{+0.44}_{-0.38}$ [37].

- $b\bar{b}$: At low masses, up to $m_H \sim 130$ GeV, the dominant decay mode is to a b-quark pair. This final state is made difficult to search for at hadron colliders because it is a common signature of QCD multijet production processes. At the LHC, QCD multijet $b\bar{b}$ production has a cross-section approximately 9 orders of magnitude higher than that for Higgs production. This mode is only possible to exploit when considering one of the production modes that contains other final state particles and not through direct gluon-gluon fusion, e.g. $t\bar{t}H$ or VH. VBF is also possible but very hard due to the resulting all hadronic final state. An important aspect of this channel is distinguishing between b-quark induced jets and light quark jets. CMS measured a signal strength of $0.67^{+1.35}_{-1.33}$ using the $t\bar{t}H, H \rightarrow b\bar{b}$ channel [38] whereas ATLAS measured a signal strength of 1.69 ± 1.37 [39]. In the $VH, H \rightarrow b\bar{b}$ mode, ATLAS measured a signal strength of $0.51^{+0.41}_{-0.37}$ [40] and CMS measured 1.0 ± 0.5 [41].

- $\mu\mu$: Though offering a clean signature, this channel suffers from very large backgrounds and has a very low branching ratio such that associated production modes have too low an event yield to be useable. This decay mode is mostly used in SuperSymmetric Higgs searches [42] that have modified branching ratios and properties. In the Standard Model scenario the branching ratio is low enough to be difficult to distinguish from other standard model processes such as Drell-Yan production. ATLAS has placed a limit of 7.0 times the Standard Model prediction in this channel at $m_H = 125$ GeV [43] whereas CMS has placed a slightly weaker limit of 7.4 [44].
- $c\bar{c}$ and gg: These modes have branching ratios at least an order of magnitude lower than $b\bar{b}$ but suffer from the same problems. The QCD background to these processes is even larger than for $b\bar{b}$ and it is harder to distinguish c or g initiated jets from other jets than in the b-jet case. The branching ratio to gg is higher than $c\bar{c}$ due to additional contributions from virtual top quark loops and bottom quark loops.

A summary of the observed signal strengths measured by each experiment as a multiple of the standard model expectation is shown in Figure 2.11. ATLAS measures a combined signal strength of $\hat{\mu} = 1.30^{+0.18}_{-0.17}$ while CMS measures $\hat{\mu} = 1.00 \pm 0.13$ [45, 46].

After the discovery of what appears to be the standard model Higgs Boson, both

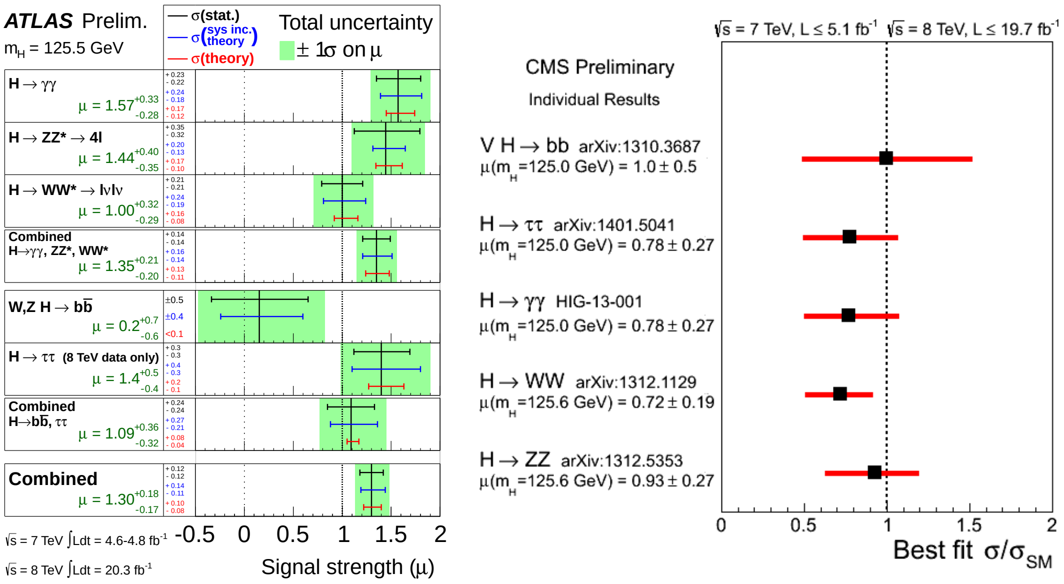

Figure 2.11: Signal strengths observed for the different Higgs decay modes, expressed as multiples of the Standard Model expectation. Left: Results from the ATLAS Collaboration. Right: Results from the CMS Collaboration. Results use the full 2011 7 TeV and 2012 8 TeV datasets [45, 46].

the ATLAS and CMS collaborations made measurements of a variety of properties including mass and couplings. These measurements mostly use the more sensitive decay modes such as $\gamma\gamma$, ZZ and WW. ATLAS uses the $\gamma\gamma$ and $ZZ \to 4\ell$ channels to measure a Higgs mass of 125.36±0.37(stat.)±0.18(syst.) GeV [28] while CMS uses a wider selection of channels to measure a mass of $125.03^{+0.26}_{-0.27}$(stat.)$^{+0.08}_{-0.07}$(syst.) GeV [47]. Several analyses have been performed to study the spin-parity of the observed Higgs boson including the CMS distributions in the WW leptonic final state that strongly favour $J^P = 0^+$ against a narrow resonance from $J^P = 2^+$ or $J^P = 0^-$ [32]. Indirect constraints from the CMS 4 lepton and 2 lepton 2 neutrino analyses have placed an upper limit on the Higgs width of $\Gamma_H < 22$ MeV [48], which is much stricter than any direct measurement and only 5.4 times larger than the expected standard model value. This limit is extracted by comparing the rates of on-shell and off-shell Higgs production, both of which depend on the Higgs couplings but only the on-shell production depends on the Higgs width. The ratio of these two production rates gives access to the ratio of the Higgs width to the Standard Model expected value.

CHAPTER 3

The Large Hadron Collider

The Large Hadron Collider (LHC) [49] is a particle accelerator based at CERN with a full circumference of 27 km which runs beneath the French and Swiss countryside at a depth of between 45 m and 175 m underground, in tunnels originally built for the previous CERN accelerator, LEP. Much of the accelerator infrastructure used by the LHC was part of CERN's existing accelerator complex including the Super Proton Synchrotron (SPS), which is the final stage before injection into the LHC. The full CERN accelerator complex chain used for the LHC is shown in Figure 3.1. The LHC was designed to accelerate two beams of protons to 7 TeV per proton and then collide them at a centre-of-mass energy, $\sqrt{s}$, of 14 TeV. At this energy protons will be travelling at 99.999999% the speed of light and make 11,000 full circuits of the LHC ring per second. The beams of protons are not in a continuous stream but instead organised in bunches containing up to 10^{11} protons. The LHC design parameters are for 2808 bunches of protons with a spacing between bunches of 25 ns. The LHC can also be used to collide Lead ions at energies of up to 5.5 TeV per nucleon pair [50].

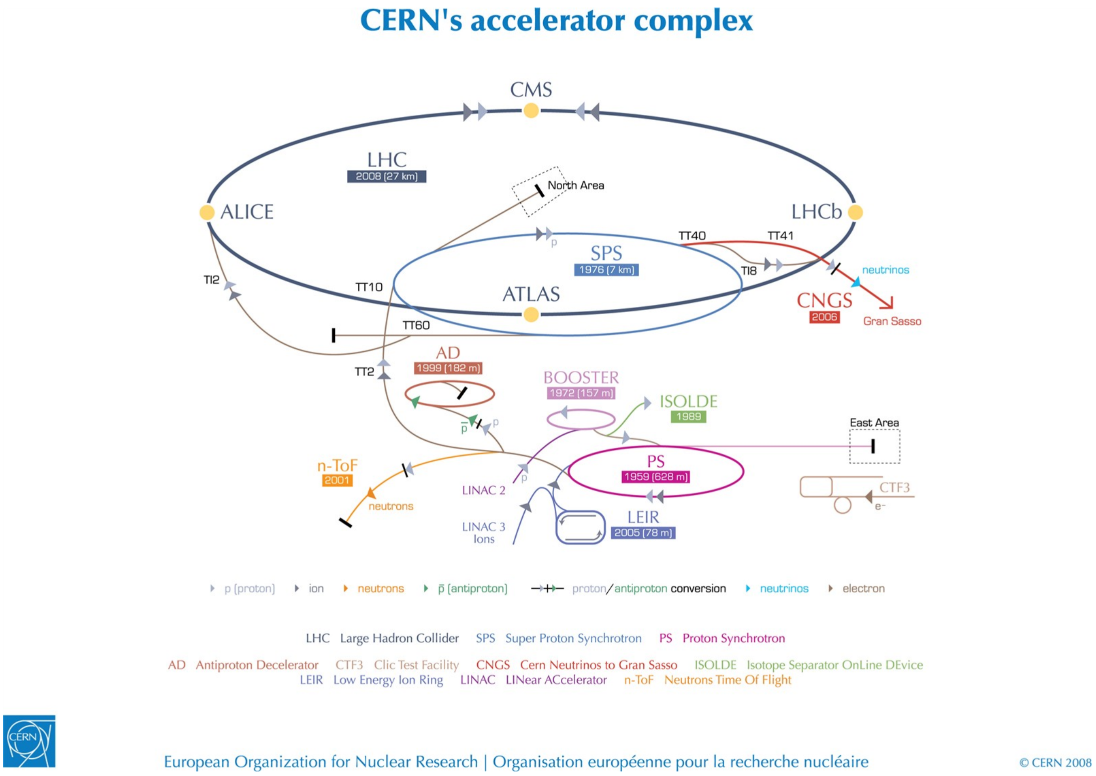

Figure 3.1: Schematic of the full CERN accelerator complex. © 2014 CERN.

The instantaneous luminosity of a colliding beam experiment, L, can be written in terms of the machine parameters as:

$$L = \frac{fnN^2}{A} \tag{3.1}$$

where f is the frequency of beam circulation, n is the number of bunches circulated, N is number of particles per bunch (assuming equal bunches in each direction) and A is the transverse area of each bunch crossing. It is convenient to describe an accelerator by its luminosity, as the rate, W, of a certain type of event can then be determined as $W = L \times \sigma$ where σ is the cross section of a particular process. The LHC is designed to have a peak instantaneous luminosity of 10^{34} cm^{-2}s^{-1}, at which processes with cross sections of 100 pb will have a production rate of 1 Hz, giving the LHC experiments great experimental reach [51].

The LHC has 4 main detectors placed at different interaction points: LHC beauty (LHCb) [52], A Large Ion Collider Experiment (ALICE) [53], Compact Muon Solenoid (CMS) [54] and A Toroidal LHC Apparatus (ATLAS) [55]. LHCb was designed to make precise measurements to probe CP violation, asymmetries between matter and antimatter, in the b-quark sector. ALICE was primarily designed to search for the Quark Gluon Plasma in Heavy Ion (HI) collisions. CMS and ATLAS are both designed to study a wide range of physics but particularly for searches for the Higgs Boson and physics beyond the Standard Model. The positions of the 4 detectors on the LHC ring are shown in Figure 3.2.

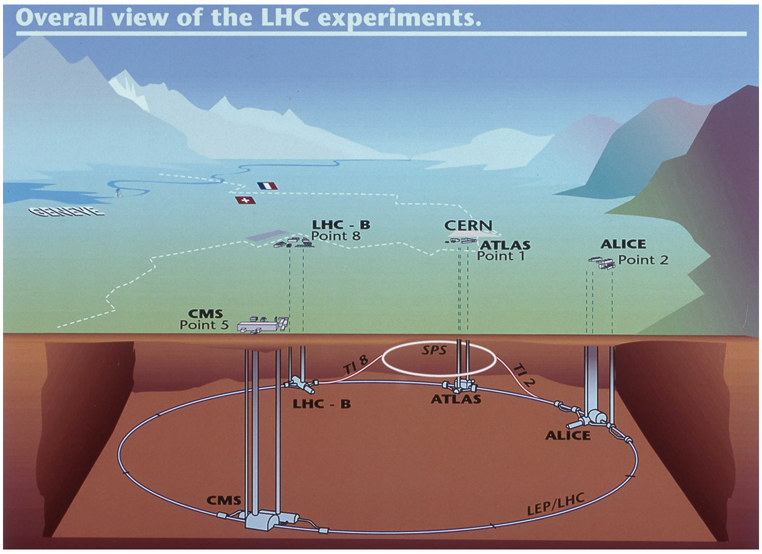

Figure 3.2: Underground view of the LHC [56].

After an unsuccessful attempted start in September 2008, the LHC started colliding beams of protons in November 2009. The early collisions occurred with proton beams at their injection energy, giving a centre-of-mass energy of 900 GeV with an increase to 2.36 TeV, a record for a collider, by the end of 2009. It was decided that it was not safe to run the LHC machine at 14 TeV, as originally planned, until upgrades and additional quench protection systems had been installed.

In early 2010 the LHC was recommissioned to accelerate protons to 3.5 TeV, providing collisions at $\sqrt{s} = 7$ TeV. The LHC ran at this energy for the duration of 2010 and 2011, providing 48.1 pb^{-1}(2010) and 5.46 fb^{-1}(2011) of data to both ATLAS and CMS. For 2012 running the beam energy was increased to 4 TeV per proton, giving a total centre-of-mass energy of 8 TeV. During 2012 operation 22.8 fb^{-1} of data were provided to ATLAS and CMS. The luminosities delivered to ATLAS by the LHC during each year of running are shown in Figure 3.3. ALICE and LHCb received a smaller amount of data due to the process of luminosity levelling, which deliberately reduces the instantaneous luminosity received by each experiment. The LHC ceased operation in early 2013 to perform upgrades to allow operation at a centre-of-mass energy of up to 14 TeV.

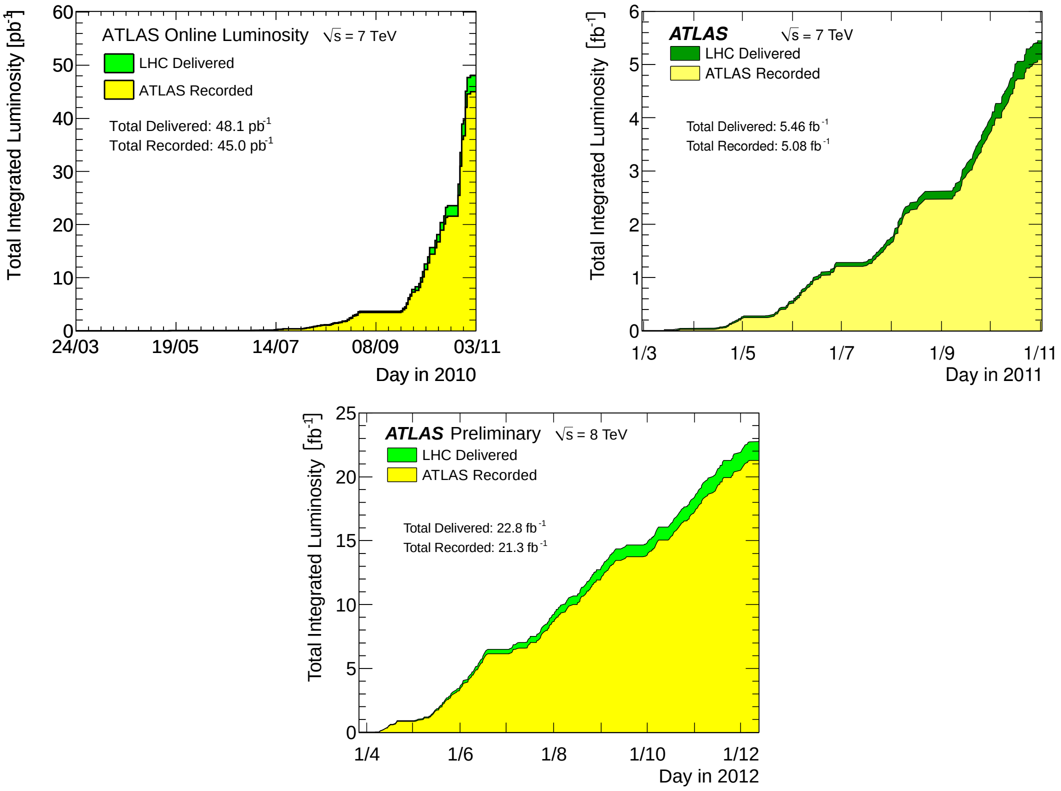

Figure 3.3: Integrated Luminosity delivered to ATLAS by the LHC as a function of time for 2010 (Top Left), 2011(Top Right) & 2012(Bottom). ATLAS Experiment © 2014 CERN.

CHAPTER 4

The ATLAS Experiment

The ATLAS detector [55], shown in Figure 4.1, is located at point 1 on the LHC ring and is the largest detector ever built at a collider, being 44 m long, 25 m in diameter and weighing over 7000 tons. Design and construction of the detector has taken thousands of people almost 20 years to complete. The main strengths of ATLAS are excellent particle identification, large muon acceptance, highly performant calorimeters and good vertex reconstruction. The ability to accurately reconstruct muons is an especially important property for ATLAS as the cleanest channels for many new physics are those containing high energy muons.

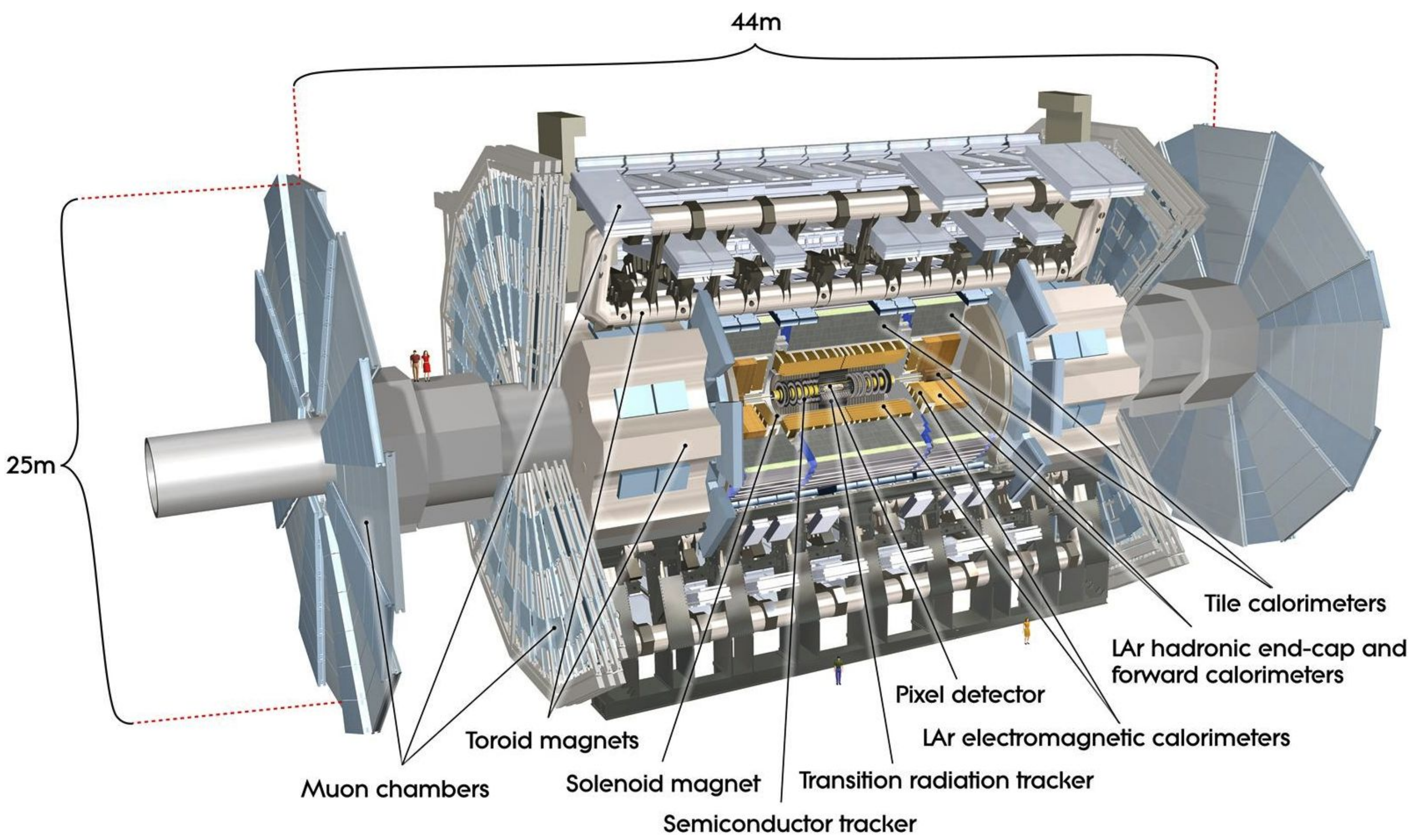

Figure 4.1: The full ATLAS detector showing all sub-detectors [56].

ATLAS follows the typical design for colliding beam detectors, often described as an "onion", whereby the detector is segmented into layers of different types of sub-detectors, each layer fully surrounding those which are closer to the interaction point. By combining all the separate detector components, it is possible to directly detect and measure all stable particles except for neutrinos. The penetration and visibility of different types of particles is shown in Figure 4.2.

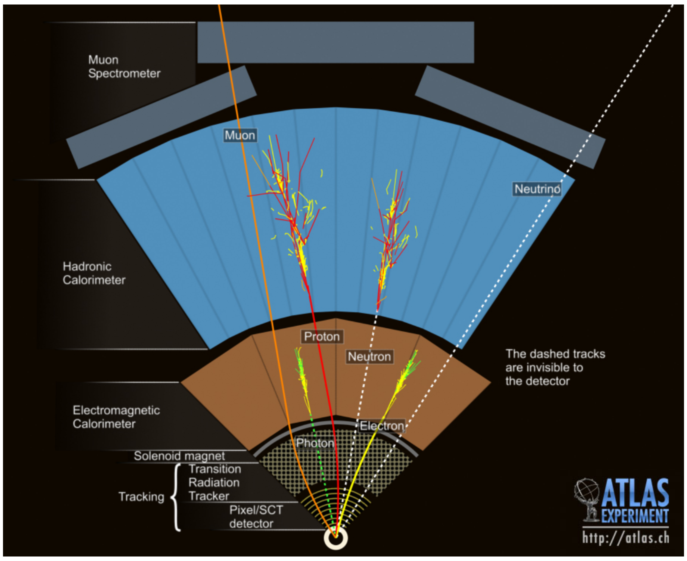

Figure 4.2: Visibility of particles in sub-detectors [56].

ATLAS sub-detectors and events within ATLAS are described using a right-handed cylindrical co-ordinate system consisting of azimuthal angle around the beam axis, ϕ, radial distance from the beam axis, r, and pseudorapidity, η, which is defined as:

$$\eta = -\ln\left[\tan\left(\frac{\theta}{2}\right)\right], \tag{4.1}$$

where θ is defined as the elevation from the beam line axis. The angle ϕ is oriented such that $\phi = 0$ points towards the centre of the LHC ring. Pseudorapidity increases from 0 when perpendicular to the beam axis up to infinity when on the beam axis. The pseudorapidity difference between two particles, $\Delta\eta$, is a Lorentz invariant quantity. Pseudorapidity is a convenient unit to use because particle fluxes are approximately constant per unit pseudorapidity at hadron colliders.

Pseudorapidity is the high energy limit of the relativistic quantity rapidity, which is defined as:

$$y = \frac{1}{2}\ln\frac{E + p_z}{E - p_z}, \tag{4.2}$$

where E is the total energy of a given object and p_z is the corresponding momentum along the z axis, the beam pipe. The orientation of z is such that $z > 0$ covers the A-side of the detector (facing towards Geneva) and $z < 0$ covers the C-side (facing towards the Jura department of France).

The distance between two particles in ATLAS or the size of a cone around a particle is defined in terms of ΔR:

$$\Delta R = \sqrt{(\Delta\phi)^2 + (\Delta\eta)^2}. \tag{4.3}$$

where $\Delta\phi$ and $\Delta\eta$ are the angles in ϕ and η respectively.

4.1 Inner detector

The Inner Detector of ATLAS is made up of three sub-detectors, which are shown in Figure 4.3, inside one another and slotted inside a solenoidal magnet. The different sub-detectors are used in combination with each other to track the paths of charged particles as they are bent within the magnetic field. Using precise determination of the positions of hits in the different sub-detectors along with offline minimisation algorithms allows full reconstruction of tracks. The curvature of these tracks caused by the magnetic field allows the momentum of the particle responsible for a given track to be calculated and the direction of curvature gives the charge of the particle. Particles must have momentum of at least 0.5 GeV for a measurement to be made due to the strength of the magnetic field. When the LHC reaches design parameters, approximately 1000 charged particles will be radiated from the interaction point during every bunch crossing, due to multiple collisions, which necessitates very fine granularity tracking in the Inner Detector. The fractional tracking resolution is required by design to be ${}^{\sigma_{p_{\mathrm{T}}}}/_{p_{\mathrm{T}}} = 0.05\% p_{\mathrm{T}} \bigoplus 1\%$ [55].

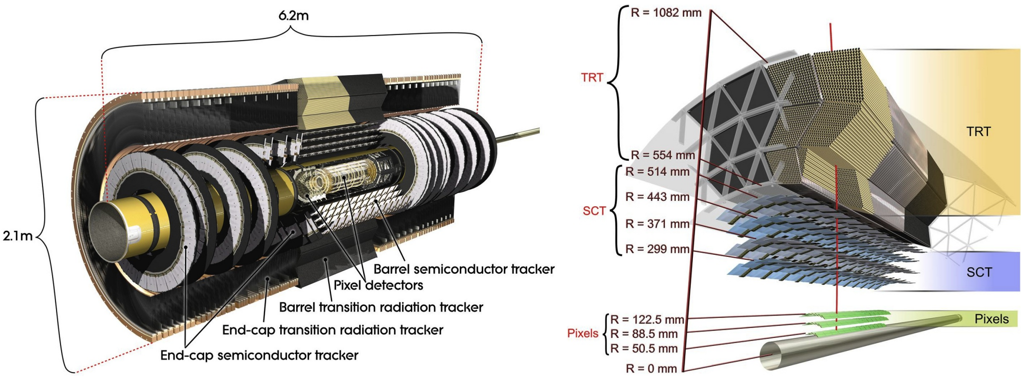

Figure 4.3: Cross-sectional views of the Inner Detector [56].

The Pixel detector is the first sub-detector moving out from the beam axis and covers the area from a radius of about 5 cm to a radius of about 12 cm within $|\eta| < 2.5$. The Pixel detector is composed of three layers of semi-conducting silicon pixels which are each of size 50 μm by 400 μm. There are in total over 80.4 million pixels spread across the three layers. The small pixel size gives extremely precise spatial information that is required at this distance from the beam axis to reconstruct both the primary vertex where a collision occurred and any secondary vertices caused by unstable particles which travel a distance before decaying, such as τ leptons or b-hadrons. Identification of b-hadrons is very important for a wide range of ATLAS physics topics such as Top quark measurements and searches for $H \to b\bar{b}$. The fine granularity of the Pixel detector means that it has the best resolution of the Inner detector sub-detectors. The radiation flux hitting the pixel detectors will cause significant damage, creating additional noise and reducing the number of points on each track, which reduces the precision of measurements. The Pixel detector is the part of ATLAS most likely to require replacement due to radiation damage. During the long shutdown after Run I ATLAS installed the Insertable B-Layer (IBL) [57]. The IBL is an extra layer of silicon pixels at a radius of 2.5 cm from the beam pipe, closer than the Pixel detector, designed to improve the precision of tracking measurements.

Around the Pixel detector is the Semi-Conductor Tracker (SCT), which covers the area from a radius of about 25 cm out to about 55 cm within $|\eta| < 2.5$. The SCT is constructed from approximately 6.3 million silicon strips of width 80 μm and length about 12 cm lying parallel to each other on modules. It is impossible to know how far along its length an individual strip has been hit so a single layer of strips gives information only in one dimension. To obtain a two dimensional measurement layers are arranged in pairs, overlapping at an angle of approximately 40 mrad so that the intersection of two strips receiving a hit marks the position of a track. With eight layers of the SCT, arranged in pairs, each particle should give four full spatial points to form a track. SCT modules are mounted both on a cylindrical construction, surrounding the interaction point in ϕ, and on endcap wheels to cover the forward regions. The arrangement of pairs of SCT layers greatly improves the resolution of the strips but still does not give as a resolution as narrow as for the Pixel detector.

The Transition Radiation Tracker (TRT) is the outer layer of the inner detector and extends from a radius of approximately 55 cm out to approximately 1.1 m in the region $|\eta| < 2.0$. The TRT is made up of roughly 350,000 straw tubes, of length 144 cm and diameter 4 mm, filled with gaseous Oxygen, Xenon and Carbon Dioxide. The straws are densely packed in layers such that each track should leave deposits in an average of 36 straw tubes. The TRT increases the precision of the momentum resolution of tracks by providing a very large number of measurements and extending the length over which a track is measured. Very thin sheets of aluminium (approximately 0.2 μm) are placed between the tubes, which cause charged particles to emit photons, known as “transition radiation” at a wavelength dependent on the particle’s relativistic boost. The large size of the tubes gives the TRT the poorest individual resolution of the sub-detectors within the Inner detector. As the luminosity of the LHC increases, the usefulness of the TRT will decrease due to the mean occupancy per tube rising above 1 at a luminosity of 10^{34} cm^{-2}s^{-1} [55].

4.2 Calorimetry

ATLAS makes use of two calorimeters, shown in Figure 4.4: an Electromagnetic Calorimeter to identify and measure the energies of electrons and photons and a Hadronic Calorimeter to identify and measure the energies of hadrons. Both ATLAS calorimeters are sampling calorimeters, which means that they use one dense material, the absorber, to initiate showers of particles from a high energy incoming particle and another material, the sampler, to collect the energy deposited and the characterise the shape of the shower. The two different materials are placed alternately in layers to build up the calorimeter. Both calorimeters require high granularity to be able to separate the showers from two particles entering the calorimeters close together.

The dominant processes of shower production in the electromagnetic calorimeter are bremsstrahlung, emission of photons by the acceleration of charged particles, and pair production from the conversion of a photon. These two processes combine to develop an electromagnetic shower with a characteristic shape that is different in width- for incoming electrons and photons. Absorbers are characterised by their radiation length, X_0, the mean thickness of material in which an electron will lose all but a fraction $^1/_e$ of its energy by bremsstrahlung.

Hadronic shower production is far more complex than electromagnetic shower production due to the complexity of processes involved and that some processes will also produce an electromagnetic core within the shower. The nuclear interactions involved in hadronic showers are less well understood than electromagnetic interactions and can fluctuate greatly in terms of the energy lost and the number of non-hadronic particles produced. This complexity and poorer understanding leads to a poorer energy resolution than for an electromagnetic calorimeter [58]. The nuclear interaction length, λ, is the mean distance in which a hadron will lose all but a fraction $^1/_e$ of its energy by strong interaction processes and is typically, though not always, much larger than a material's radiation length.

For both calorimeters, offline algorithms are used to convert the pattern of activated calorimeter cells into a shower shape. From the shape and magnitude of signals observed, the energy of the particle which initiated the shower can be calculated. In the case of multiple particles travelling close together, more complex algorithms are required to resolve the different shower shapes. The shape of a shower can also provide some particle identification, for example, by complementing other detector information to distinguish between photons and electrons.

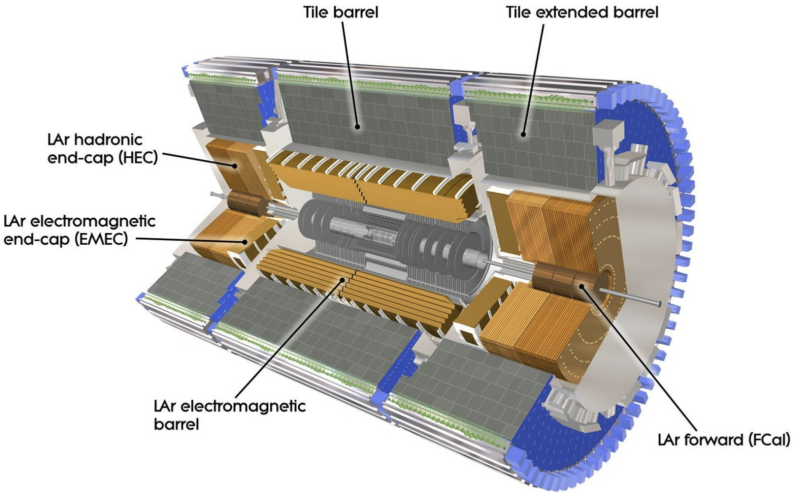

Figure 4.4: The ATLAS Calorimeters: An electromagnetic calorimeter, shown in orange, and a hadronic calorimeter, shown in grey and blue [56].

The ATLAS electromagnetic calorimeter is constructed from layers of lead to act as an absorber and cooled Liquid Argon (LAr) as a sampling material. Lead has a radiation length of 0.5612 cm [1]. To reduce dead material in front of the barrel section of the calorimeter it is placed within the solenoid's cryostat. The barrel section of the calorimeter is made from two sections joined at $|\eta| = 0$ and covers the region $|\eta| < 1.475$ while two coaxial wheels make up the endcaps which cover $1.375 < |\eta| < 3.2$. The electromagnetic calorimeter has a depth in the barrel of more than 22 radiation lengths and more than 24 in the endcaps [59]. The overlapping region requires careful calibration as showers will not go the full depth of the calorimeter in either section of the calorimeter, so information from both must be combined using offline algorithms. To improve the coverage and symmetry in ϕ the calorimeter layers are constructed as accordions as opposed to just being flat sheets [60]. The ATLAS design requirement is for the fractional electromagnetic shower resolution to be ${}^{\sigma_E}/_{E} = {}^{10\%}/_{\sqrt{E}} \bigoplus 0.7\%$ [55].

The hadronic calorimeter is constructed from layers of steel absorber and scintillating plastic tiles for sampling in the region $|\eta| < 1.7$, but uses copper as the absorber and LAr for sampling in the endcaps, which cover the region $1.5 < |\eta| < 3.2$. Copper has a nuclear interaction length of 15.32 cm [1], lower than the 17.59 cm of lead [1], which allows the hadronic endcap calorimeter to be constructed more compactly. The Tile section of the calorimeter is partitioned into a barrel section covering $|\eta| < 1.0$ and an extended barrel on each side which covers $0.8 < |\eta| < 1.7$. The hadronic calorimeter is designed such that the electromagnetic and hadronic calorimeters combined have a depth of at least 10 interaction lengths throughout. The ATLAS design requirement is for the fractional hadronic shower resolution to be ${}^{\sigma_E}/_{E} = {}^{50\%}/_{\sqrt{E}} \bigoplus 3\%$ [55].

Between $3.2 < |\eta| < 4.9$ both the electromagnetic and hadronic calorimeters are replaced by the Forward Calorimeter (FCal), which is positioned within the cryostat of the Hadronic Calorimeter endcaps. The FCal uses LAr, the same material used in the electromagnetic calorimeter, as a sampling material but uses two different metals as absorbers. The first module of the FCal uses Copper and is primarily optimised for measuring the electromagnetic component of a shower while the second and third modules use Tungsten and are designed for hadronic measurements. The FCal is a total of 10 interaction lengths throughout. The ATLAS design requirement is for the fractional resolution in the FCal to be ${}^{\sigma_E}/_{E} = {}^{100\%}/_{\sqrt{E}} \bigoplus 10\%$ [55].

4.3 Muon Spectrometer

The outside of ATLAS is entirely surrounded by the Muon Spectrometer, covering the full length of 44 m and diameter of 25 m, which is separated into three cylindrical layers in the barrel region plus three wheels at either end to cover the forward/backward regions, as shown in Figure 4.5. The muon spectrometer is constructed from four different types of instrument: Cathode Strip Chambers (CSC) and Monitored Drift Tubes (MDT) are used for accurate spatial measurements to reconstruct a full muon trajectory, but their slow read out necessitates the use of Resistive Plate Chambers (RPC) and Thin Gap Chambers (TGC) for triggering and matching of a particular muon to an LHC bunch crossing. The fast response instruments, the RPC and TGC, are sandwiched around the more spatially accurate instruments, the CSC and MDT. Coincidences in the RPCs and TGCs are used to quickly postulate the presence of a muon. The design of the muon spectrometer ensures nearly full coverage of ATLAS and provides three spatial and temporal measurements per muon passing through. This allows a track to be precisely reconstructed and a radius of curvature to be calculated. The ATLAS design requirement is for the fractional tracking resolution in the muon spectrometer to be $\sigma_{p_\mathrm{T}}/p_\mathrm{T} = 10\%$ at p_T=1 TeV[55].

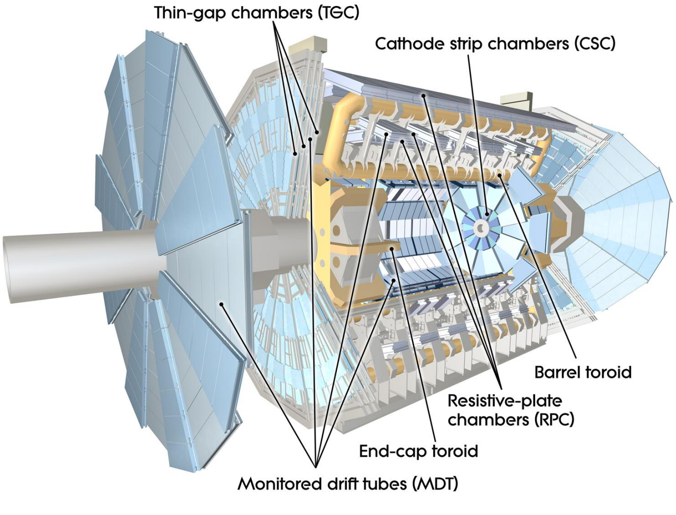

Figure 4.5: The ATLAS Muon Spectrometer consisting of 4 different types of muon chambers [56].

4.4 Magnet System

ATLAS uses a combination of two magnetic systems to bend the paths of charged particles so that their momenta may be measured. The Inner Detector is completely surrounded by a 5.3 m long solenoidal magnet found at a radius of 1.25 m from the beam axis. The magnetic field produced by the solenoid has a strength of 2 Tesla and runs parallel to the beam axis to curve the paths of tracks in the Inner Detector. The paths of muons travelling through the Muon Spectrometer are bent by the toroidal magnet system.

The use of toroids is fairly uncommon in High Energy Physics experiments where the more conventional approach is to place everything within the return flux of the solenoid. The size of the ATLAS Calorimeters and Muon Spectrometer make this option unattractive as the bending power would neither be strong enough at the required distances from the interaction point nor extend far enough forward in η. A second solenoid around the entire detector would be prohibitively expensive so a toroidal system was determined to be the most performant option within budget [61]. The ATLAS Toroid system is made up of a large barrel, in the region $|\eta| < 1.0$, consisting of coils housed in 8 air core cryostats (as shown in Figure 4.6) and 2 end-caps in the region $1.4 < |\eta| < 2.7$, which are slotted into the barrel. In the region $1.0 < |\eta| < 1.4$ the magnetic field is provided by a combination of both systems. The magnetic field produced by the toroidal system has an average strength of 0.5 Tesla although there is a significant variation of the field strength. The strength of the magnetic field in the direction of the beam axis, in Tesla, formed by the combination of the Solenoid and Toroid is shown in Figure 4.7.

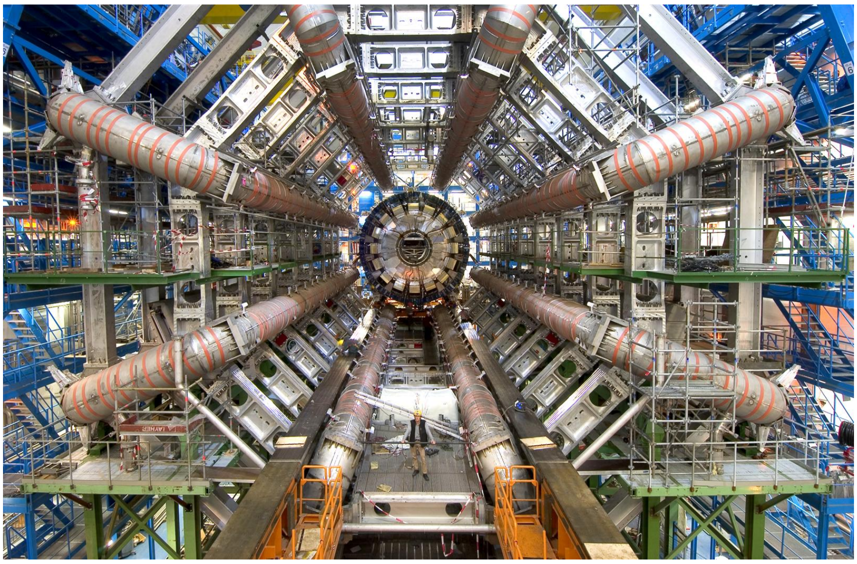

Figure 4.6: ATLAS Barrel Toroid before insertion of Calorimeters and Inner Detector [56].

4.5 Trigger

At design energy and luminosity there will be a bunch crossing interval of only 25 ns and an expected average collision rate of 23 events per bunch crossing. The full zero-suppressed binary data for each event totals approximately 1.6 Megabytes which equates to a raw data rate of approximately 1 Petabyte per second. This is unfeasible, both because too much storage space would be required and because the speed of read-out would be beyond the capabilities of current technologies. Handling this rate necessitates a highly selective trigger that reduces the event rate to a manageable level while still preserving events that are expected to contain interesting physics processes. During the 2010 - 2012 running period (LHC Run I) the bunch crossing interval was 50 ns with a collision rate of up to 40 events per bunch crossing but taking a wide range of values.

The full trigger must reduce the LHC bunch crossing rate of 40 MHz down to an event rate of only 200-400 Hz [55], the limit that can be processed and reconstructed properly for storage to disk. The ATLAS Trigger is split into Level 1, Level 2 and

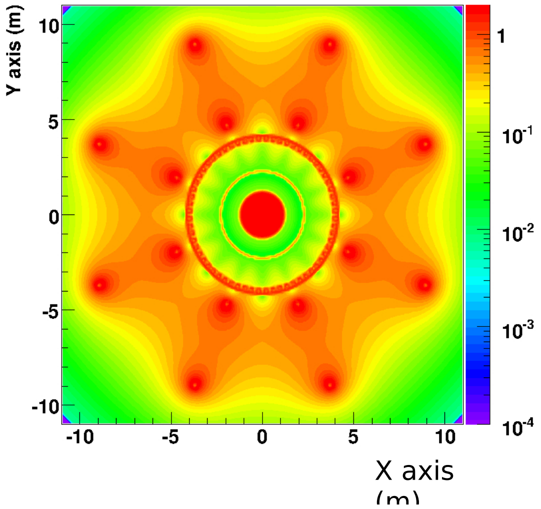

Figure 4.7: Field map showing strength of the ATLAS magnetic field in the z direction, along the beam axis [62]. The x and y directions represent the horizontal and vertical dimensions of the ATLAS detector. The units for the z axis is Tesla.

the Event Filter. A schematic diagram of the trigger layout is shown in Figure 4.8. All trigger levels can have a pre-scale set for each threshold where a pre-scale of x will mean that only a randomly sampled proportion $\frac{1}{x}$ passing that threshold will be selected. This allows very high rate processes to be recorded without swamping the trigger and allows the trigger settings to be adjusted to changing beam conditions.

The Level 1 trigger consists of three sections: The Level 1 Calorimeter Trigger (L1Calo), the Level 1 Muon Trigger (L1Mu) and the Central Trigger Proccessor (CTP). All of the Level 1 systems are built from custom electronics and use reduced granularity from the detector, seeking only to recognise individual physics objects and not to reconstruct event topologies. The time between events is very small so a technique called pipelining is used whereby multiple events are stored within on-board electronics allowing more than the time between events for the trigger to act. Events must be processed by Level 1 within 2.5 μs, of which about 1μs is taken by cable length, otherwise an event will fall off the end of the pipeline and be lost. Level 1 is designed to reduce the rate down to a maximum of 75 kHz.

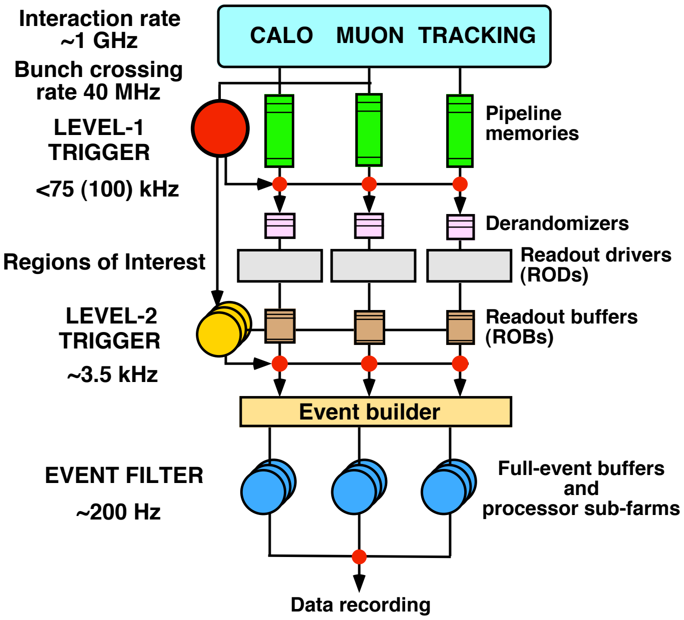

Figure 4.8: Schematic diagram of the ATLAS Trigger systems [63].

L1Mu uses data from the Muon Spectrometer to identify muons and pass information on their positions and momenta to the CTP. L1Calo, which will be described in more detail in Chapter 5, uses information from all the calorimeters to identify electrons, photons, taus and jets as well as to measure large missing transverse energy ($E_{\mathrm{T}}^{\mathrm{miss}}$) and large total transverse energy and passes their information to the CTP. The CTP compares information received from L1Mu and L1Calo to the preloaded trigger menu, which specifies the features and thresholds that are likely to be of interest for physics analyses. If an object is found that passes the required thresholds of a trigger item then the CTP will send a Level 1 Accept signal to read the event data out into Level 2. The CTP can also check for combinations of items such as an electron and $E_{\mathrm{T}}^{\mathrm{miss}}$ to select W decays. L1Mu and L1Calo transmit Regions of Interest (RoI), which specify the coordinates of the Level 1 objects and a list of thresholds passed.

Level 2 and the Event Filter (EF) are collectively known as the High Level Trigger (HLT) and run on standard large processor farms. Level 2 takes RoI from Level 1 and uses information from the RoIs and the surrounding areas to further reduced the event rate. This is done both by refining the identification of individual physics objects and looking for combinations/correlations of different RoI. Level 2 reduces the event rate down to approximately 4 kHz with a mean processing time of around 40ms per event, though the number of RoI significantly increases the processing time.

The Event Filter is designed to reconstruct the full event topology and then determine through the use of complex algorithms whether events pass one of the menu items. These menu items can contain requirements about individual objects or more complex multiple object requirements. EF menus are constructed to try to ensure that there is enough data available for all physics analyses, generally by allocating bandwidth to each physics group. The EF must reduce the bandwidth to around 200-400 Hz with a mean processing time of 4 seconds [64].

Data events are recorded to different streams depending on the types of trigger items found. For instance events triggered by muons are recorded to the `Muon` stream while events triggered by jets, taus or high $E_{\mathrm{T}}^{\mathrm{miss}}$ are recorded to the `JetTauEtmiss` stream. There is a degree of overlap in the data recorded in different streams, because the streams are inclusive and each event may pass triggers belonging to more than one stream.

4.6 Luminosity

It is important, for ATLAS physics analyses, that the total luminosity of a dataset, $\int Ldt$, is known. To determine this, ATLAS was designed to be able to measure the instantaneous luminosity, as defined in Equation 3.1. The instantaneous luminosity can be defined experimentally as:

$$L = \frac{R_{inel}}{\sigma_{inel}}, \tag{4.4}$$

Where R_{inel} is the rate of inelastic collisions and σ_{inel} is the proton-proton inelastic cross section. This can be rewritten in terms of the machine parameters as:

$$L = \frac{\mu n_b f_r}{\sigma_{inel}}, \tag{4.5}$$

Where f_r is the revolution frequency of the collider, n_b are the number of bunches crossing and μ is the average number of inelastic interactions per bunch crossing. The machine parameters, n_b and f_r, are both known so techniques which can measure the ratio ${}^{\mu}/_{\sigma_{incl}}$ can be used to calculate the luminosity. Several sub-detectors, such as the Minimum Bias Trigger Scintillator (MBTS) and parts of the inner detector, are able to detect the products of inelastic interactions and so can be used for luminosity calculations. ATLAS uses event counting methods [65] in which selection criteria, based on specific detector responses, are used to determine wether each LHC bunch crossing contains at least one inelastic collision. The selection efficiency for such events, ϵ, can be used to rewrite Equation 4.5 in terms of the average number of visible inelastic interactions per bunch crossing, $\mu^{vis} = \epsilon\mu$, and the visible inelastic cross section, $\sigma_{vis} = \epsilon\sigma_{inel}$ as follows:

$$L = \frac{\mu n_b f_r}{\sigma_{inel}} = \frac{\mu^{vis} n_b f_r}{\epsilon\sigma_{inel}} = \frac{\mu^{vis} n_b f_r}{\sigma_{vis}}. \tag{4.6}$$

The visible event rate, μ^{vis}, is an experimentally measured quantity while the value of σ_{vis} is determined by the calibration of the method and sub-detector used. This calibration has a dependence on the pseudorapidity and particle type of the collision products. The absolute scale of σ_{vis} is determined by scanning for collision activity as the beam separation is adjusted which a technique known as a Van der Meer scan.

CHAPTER 5

Level 1 Calorimeter Trigger

As outlined in Section 4.5, the ATLAS trigger must greatly reduce the event rate, with the largest reduction comeing from Level 1. The Level 1 Calorimeter Trigger (L1Calo) is responsible for using the information from all the calorimeter subsystems, but at reduced granularity (by merging cell information), to identify electrons, photons, taus and jets as well as measure missing transverse energy ($E_{\mathrm{T}}^{\mathrm{miss}}$) and total transverse energy.

The L1Calo system divides the calorimeter cells into 7168 towers, half in each of the electromagnetic and hadronic calorimeters, which are of average size $\Delta\eta \times \Delta\phi = 0.1 \times 0.1$ but increase in size with increasing η. The L1Calo system is constructed from custom-built electronics with processing performed by FPGAs, a type of microchip with speed comparable to an application-specific chip, but with the ability to modify its internal logic into different digital circuits. The L1Calo electronics are located in the USA15 cavern, next door to the main cavern, protected from the high radiation environment in the main cavern by the thick cavern walls. Signals are carried from the ATLAS sub-detectors to L1Calo along cables which are up to 70 m in length. The main processes performed by L1Calo are split into three different sets of modules, a diagram of which is shown in Figure 5.1. The Pre-Processor Module (PPM) transforms the incoming data from the calorimeters into a form which can be used by the Cluster Processor Module (CPM) and Jet/Energy Sum Module (JEM) to identify physics objects of interest [66].

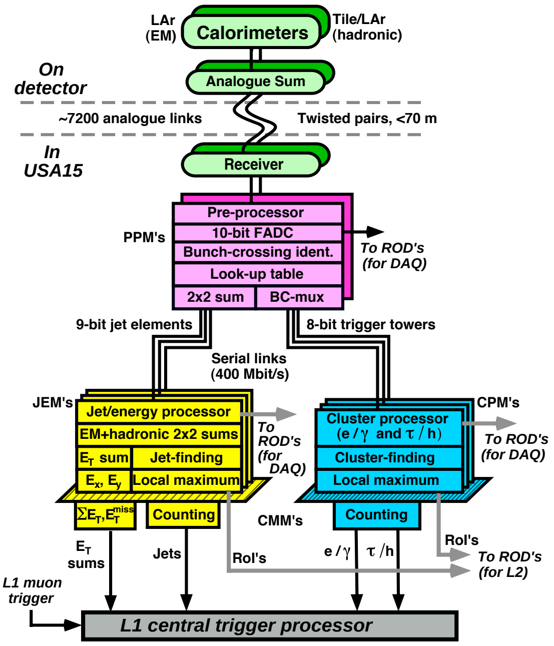

Figure 5.1: Schematic design of the Level 1 Calorimeter Trigger [63].

5.1 Pre-Processor Module

The signals entering the PPM are analogue voltage pulses from individual trigger towers which have been summed in depth (the different layers of a particular calorimeter) across all cells making up a tower. The analogue pulses are then calibrated using gains to transform total energy to a common E_T, the energy associated with momentum in the transverse plane. The calibration depends on the position of towers within the calorimeter.

The PPM must first turn the analogue signals coming from the calorimeter into digital logic pulses, which are required for the rest of the PPM and CPM/JEM which all run on digital electronics. This is performed by 10 bit Flash Analogue to Digital Converters (FADCs) which sample the analogue pulses at 25 ns intervals (the bunch crossing interval). A fine timing adjustment of between 1 and 25 ns is applied to each signal to correct for any differences in cable length or other electronic delays. Five 25 ns time slices are read out at a time from the PPM.

The PPM then performs an operation called Bunch Crossing Identification, which is described more fully in Section 5.2, to associate the signal with a particular LHC bunch crossing and then passes the signal to the Look Up Table (LUT). The LUT uses the central ADC slice (the digital version of the calorimeter signal) to make an E_T estimation. The pedestal associated with each tower is subtracted and then a noise threshold is applied to prevent swamping L1Calo with noise signals. The pulse height is then calibrated to an 8-bit E_T value. The LUT can also be used to mask towers by setting their output to zero to cancel the effect of bad towers.

5.2 Bunch Crossing Identification

Bunch Crossing Identification (BCID) is a technique which uses a pulse shape (the five time slices from the FADC) to associate a pulse from a single trigger tower to a particular LHC bunch crossing. This is not a trivial process because pulse shapes are several bunch crossings wide. The simplest approach of selecting the peak value is not the most effective as real physics pulses have varying shapes as well as a noise component that can be better discriminated by a filter. The method of BCID is different for saturated and non-saturated signals where saturated signals are above

250 GeVand exhaust the 8 bits allocated for their storage. The BCID system is shown in Figure 5.2.

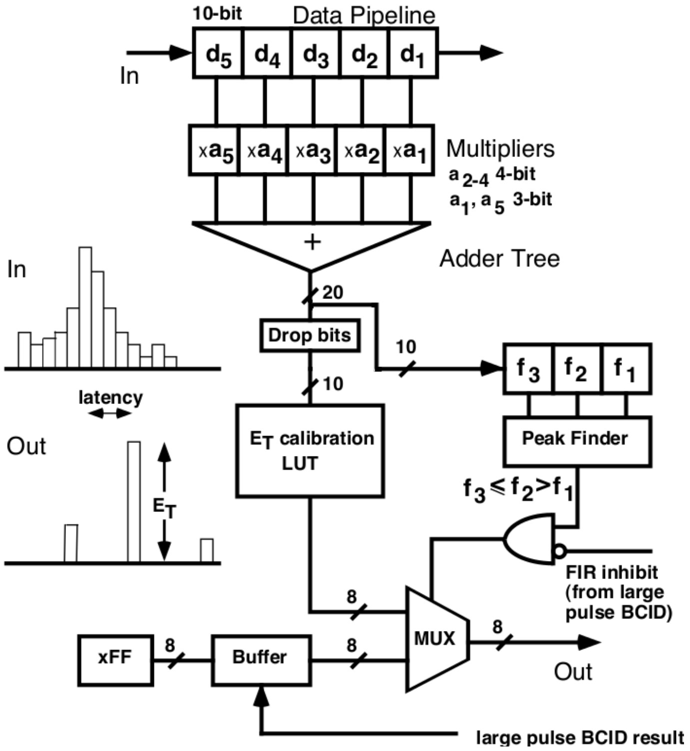

Figure 5.2: Schematic diagram of the FIR filter and peak finder implemented within the PPM [67].

For saturated pulses there may be several time slices which saturate the ADC value so there is not even a single peak to use. In this case time slices from the rising edge are compared to a low and a high threshold to determine the expected shape of the pulse and thus determine the true peak. The slices from the rising edge of the pulse are used instead of the falling edge as these are less distorted. For the saturated case it is not possible for the LUT to assign correct E_T values so all saturated pulses are given a value of 255 GeV, the maximum that can be stored in 8 bits when the smallest stored bit is equivalent to 1 GeV.

For non-saturated pulses a combination of a Finite Impulse Response (FIR) filter and a peak finder is used for BCID. The five time slices of ADC data are passed through the FIR filter which multiplies each time slice by its corresponding FIR coefficient to give the output, $\mathrm{f_{output}}$ as:

$$\mathrm{f_{output}} = \sum_{\mathrm{i}=1}^{5} \mathrm{a_i d_i} \tag{5.1}$$

where $\mathrm{d_i}$ are the ADC values of each time slice and $\mathrm{a_i}$ are the FIR coefficients as shown in Figure 5.2. The output value for each bunch crossing is then compared to the output in neighbouring bunch crossings. The FIR output must be greater than the output from the previous bunch crossing and at least as great as the next bunch crossing to pass BCID. If the BCID flag is not set then a pulse is automatically zeroed. The values of the FIR filter coefficients are optimised to enhance true signals while suppressing noise. Filter coefficients currently take the same values for each tower within particular regions, e.g. hadronic FCal, which is known as a “Common” filter. The alternative is to set coefficients individually for each tower, which is a small improvement over the “Common” case but requires a lot of calibration and increases the complexity of the system [68].

5.3 Cluster Processor and Jet/Energy Processor Modules

The Cluster Processor Module (CPM) and Jet/Energy Processor Module (JEM) both receive $\mathrm{E_T}$ values, aligned to the correct bunch crossing, from the PPM and perform algorithms on the information from multiple towers to identify physics objects. The two systems have many similar features.

The CPM is designed to identify electrons, photons and hadronically decaying taus. These objects are also expected to form fairly narrow clusters with little activity nearby, so they can be distinguished from jets by looking for large $\mathrm{E_T}$ deposits in single towers or small groups rather than spread across many. For electrons and photons the CPM uses a sliding window algorithm, shown in Figure 5.3, to identify candidates. The algorithm selects a 2 × 2 core of electromagnetic trigger towers summed with the hadronic core behind, an RoI, which are a local $\mathrm{E_T}$ maximum (higher than windows of the same size in the surrounding area) and in which one of the four possible horizontal or vertical electromagnetic tower sums is above a threshold. The cluster can then be required to pass certain isolation requirements such that the electromagnetic isolation ring, hadronic isolation ring and hadronic core (marked as yellow, pink and red in Figure 5.3) are below preset thresholds. For taus the RoI is defined in the same way but the sums to identify taus use the combination of both the electromagnetic cluster and the hadronic core but the algorithm is otherwise the same. As a result of this, the hadronic core isolation requirement is removed. The triggers handled by the CPM cover the region $|\eta| < 2.5$, which is as far as the electromagnetic calorimeter and inner detector can make precision measurements.

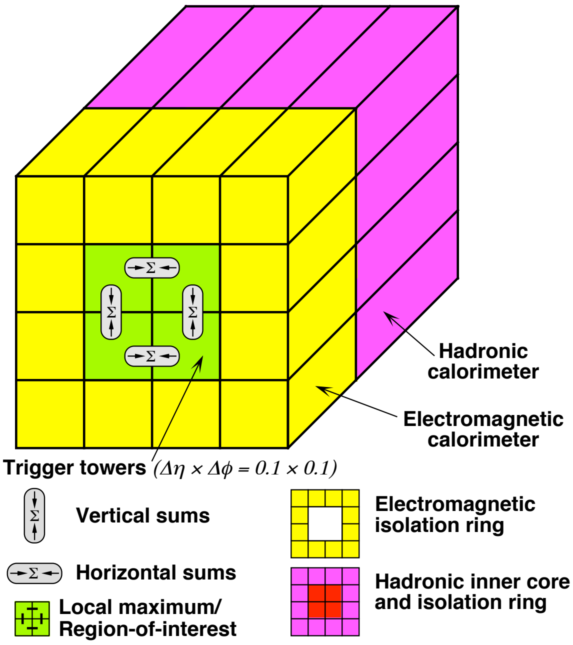

Figure 5.3: Diagram of the L1Calo sliding window algorithm used within the CPMs [63].

The JEM is designed to identify jets as well as calculate $E_{\mathrm{T}}^{\mathrm{miss}}$, total $\mathrm{E_T}$ and $E_{\mathrm{T}}^{\mathrm{miss}}$

significance ($E_{\mathrm{T}}^{\mathrm{miss}}$ compared to total $\mathrm{E_T}$, a vector versus scalar sum). The algorithm used to identify jets is similar to the sliding window algorithm used by the CPM. Jet elements are constructed as sums of 2×2 trigger towers, summed across both electromagnetic and hadronic calorimeters. The algorithm then calculates $\mathrm{E_T}$ sums within windows made from 2×2, 3×3 or 4×4 jet elements. The $\mathrm{E_T}$ sums are required to pass thresholds that are different for the different candidate jet cluster sizes. The window used must surround the 2×2 set of jet elements that represents a local maximum, to avoid double counting, and this defines the jet RoI. The jet triggers cover the region $|\eta| < 3.2$. The algorithm also uses the region $3.2 < |\eta| < 4.9$ to trigger on forward jets, though these are generally less reliable due to the large fluxes of particles in the forward region and large total energy deposition. The total $\mathrm{E_T}$ sum and vectorial $E_{\mathrm{T}}^{\mathrm{miss}}$ sum include all towers out to $|\eta| = 4.9$.

CHAPTER 6

Bunch Crossing Identification

As shown in Section 5.2, the BCID system is very important within L1Calo. If calorimeter deposits are not accurately associated with LHC bunch crossings then the L1Calo algorithms in the later modules will not have the full information with which to identify features. It is expected that the efficiency of BCID will be approximately 100% for highly energetic towers, around the thresholds of triggers used for narrow single objects such as electrons. Objects such as jets or calculated quantities such as $E_{\mathrm{T}}^{\mathrm{miss}}$ are built from many lower $\mathrm{E_T}$ towers where the efficiency may be lower. The ability to resolve $E_{\mathrm{T}}^{\mathrm{miss}}$ and jet $\mathrm{E_T}$ accurately is highly reliant on the ability to match many small calorimeter deposits to a single bunch crossing. To understand these trigger quantities, as well as the general system performance, it is important to quantify the efficiency of BCID in data. The aim of the study presented here is to characterise the performance of the BCID implementation in L1Calo and identify any unexpected effects. The efficiency can be described in terms of a turn-on curve showing the increasing efficiency with increasing $\mathrm{E_T}$ but can also be split up into on-off curves based on a categorisation by L1Calo pulse height as will be shown in Section 6.3.

6.1 Methodology

This study has been performed using L1Calo ntuples, a data format derived from one of the core ATLAS data formats, AOD [69]. The L1Calo ntuples contain information from both the electromagnetic and hadronic layers of trigger towers where at least one layer records either an $\mathrm{E_T}$ greater than 0.5 GeV or an ADC value greater than 36 counts, 4 counts above the mean pedestal value. The ADC value is the height of the digital pulse as described in Section 5.1. The selection criteria cause a significant bias in the region $\mathrm{E_T} < 0.5$ GeV. The ntuples are analysed within the L1Calo Ntuple Analysis framework [70].

The dataset used for this study was recorded during the 2010 LHC HI collisions. A comparison between different runs is performed for consistency but the majority of the results are obtained using a single run, 169884, as this run contains better statistics than the majority of other runs and was recorded with stable, calibrated beam and trigger settings. The other runs used for consistency checks were 168759, 168865, 168875 and 169045.

Data recorded during HI collisions is more useful for this study than proton-proton collisions because the collisions are better separated in time and the statistics are much larger in the $\mathrm{E_T}$ region in which the efficiency turns on and approaches 100%. As this study relies only on the offline $\mathrm{E_T}$ values and Bunch Crossing Identification (BCID) decisions based on ADC values, it should not matter whether Heavy Ions or protons are in the beam pipe, only what charge is deposited in the trigger tower. There are, however, differences in angular multiplicities and $\mathrm{E_T}$ spectra between HI and proton collisions. The E_T spectrum in particular is softer in HI, which causes efficiencies summed over a range of E_T to be reduced by the large flux of low E_T deposits.

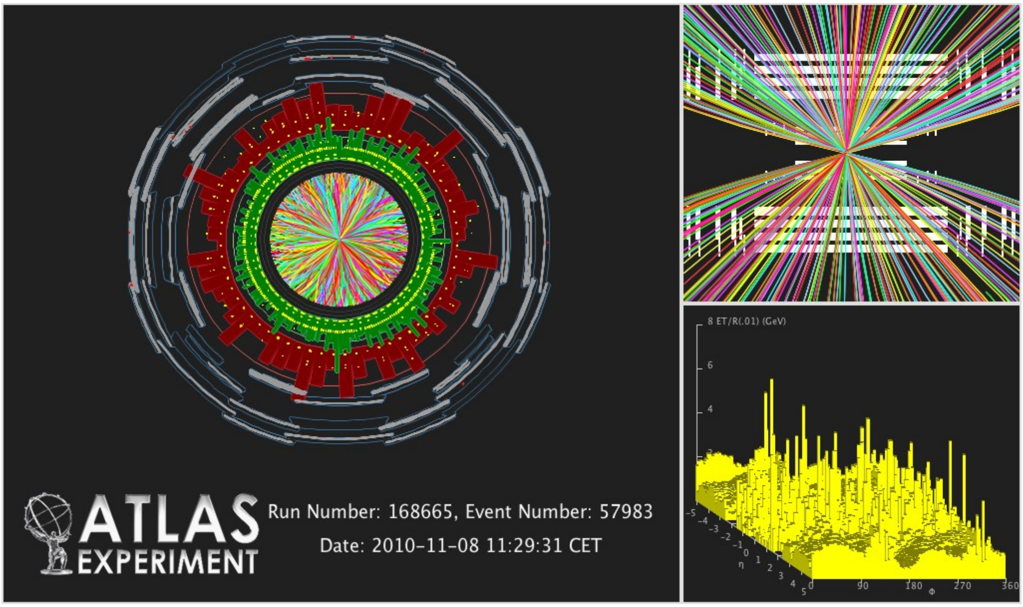

Figure 6.1: Atlantis event display of a Heavy Ion event showing the huge flux of low E_T particles and leaving deposits in almost all trigger towers. The bottom right portion of the display shows the calorimeter deposits on an un-rolled layout of the calorimeters. ATLAS Experiment ©2014 CERN.

The events used are those which are found in the `MinBias` stream, used for recording a random selection of bunch crossings containing collisions but minimally biased towards the physics processes involved, and are required to have an `L1_MBTS` trigger accept[1] and a primary vertex with at least 3 tracks. These requirements ensure that the events used are from real HI collisions rather than cosmic rays or beam halo muons. Individual trigger towers are then selected by requiring that a positive offline E_T is recorded and that the tower is not marked as "Bad" or "Dead/Disabled" in the offline database. The BCID efficiency binned in offline calorimeter E_T, ϵ_{ET}, is then calculated as the number of tower deposits containing a non-zero E_T and a

---

[1] The Minimum Bias Trigger Scintillator (MBTS) sits in front of each endcap calorimeter and so is used to trigger collision events by detecting the remnants of protons that have been scattered in the forward direction. `L1_MBTS` denotes an Minimum Bias Trigger Scintillator (MBTS) trigger has been fired at Level 1.

BCID flag (a signal saying that the tower has passed BCID), divided by the number containing a non-zero $\mathrm{E_T}$:

$$\epsilon_{ET} = \frac{\text{No.Calo Cell } \mathrm{E_T} \text{ \& BCID} > 0}{\text{No.Calo Cell } \mathrm{E_T}} \tag{6.1}$$

The efficiencies are calculated separately for different sections of the calorimeters: the Barrel region in the range $|\eta| \leq 1.4$ (1.5) for the electromagnetic (hadronic) calorimeter, the Inner Endcap in the range $1.5 < |\eta| \leq 2.5$, the Outer Endcap in the range $2.5 < |\eta| \leq 3.2$ and the Forward Calorimeter in the range $3.2 < |\eta| \leq 4.9$. In the electromagnetic calorimeter the crack region $1.4 < |\eta| \leq 1.5$ has been excluded from results. The crack region is unreliable because a cluster will be partially contained within both the Barrel and Inner Endcap, so careful timing and calibration is required to use the two sets of signals together. In 2010 this had not properly been performed but cabling was added during the Winter 2010-2011 shutdown to improve the situation.

6.2 Results

The BCID efficiency values measured for electromagnetic and hadronic calorimeter trigger towers are summarised in Tables 6.1 and 6.2 for low $\mathrm{E_T}$ only, separated into different partitions.The efficiency as a function of calorimeter $\mathrm{E_T}$ is shown in Figure 6.2 for run 169884 in both the electromagnetic and hadronic calorimeters. Efficiencies are shown as a fraction. All of the errors on efficiency values are below 0.001.

It can be seen that all partitions in both calorimeter layers become more or less fully efficient (plateaued above 98%) by $\mathrm{E_T} = 3$ GeV. All partitions follow a similar turn-on curve shape but the gradient of the curve varies. In the barrel regions maximum efficiency is only achieved at higher $\mathrm{E_T}$ than in the other region because the

E_T Values / GeV	0.5	1.0	1.5	2.0	2.5	3.0
Barrel	0.50	0.71	0.87	0.94	0.98	0.99
Inner EC	0.62	0.85	0.94	0.98	0.99	0.99
Outer EC	0.74	0.93	0.98	0.99	1.00	1.00
FCAL1	0.79	0.93	0.98	0.99	1.00	1.00

Table 6.1: BCID Efficiency for different electromagnetic partitions.

E_T Values / GeV	0.5	1.0	1.5	2.0	2.5	3.0
Barrel	0.45	0.70	0.86	0.93	0.97	0.98
Inner EC	0.58	0.84	0.94	0.97	0.99	0.99
Outer EC	0.73	0.91	0.97	0.99	0.99	1.00
FCAL23	0.64	0.87	0.95	0.98	0.99	0.99

Table 6.2: BCID Efficiency for different hadronic partitions.

effect of noise is greatest here. Noise on the total energy E should be approximately constant in θ but a scaling with $\sin\theta$ is required to translate E to the transverse energy E_T. This scaling reduces the effect of noise on E_T as towers get further from the barrel region.

The BCID efficiency was measured in multiple runs to check for consistency. Figures 6.3 and 6.4 show the comparison between 5 different HI runs, separated into electromagnetic and hadronic partitions. The results from each run are generally consistent, except in the case of the FCal. As previously mentioned, the forward region is most challenging for calorimetry due to large particle fluxes and large energy deposition, so results are likely to be very sensitive to small beam and trigger configuration differences between runs. Runs taken close together show good agreement so this difference is most likely due to changes in the FCal gains that occurred during HI running. A different study of BCID efficiency within the L1Calo system and using proton-proton data has shown long-term stability of the system used for BCID [71].

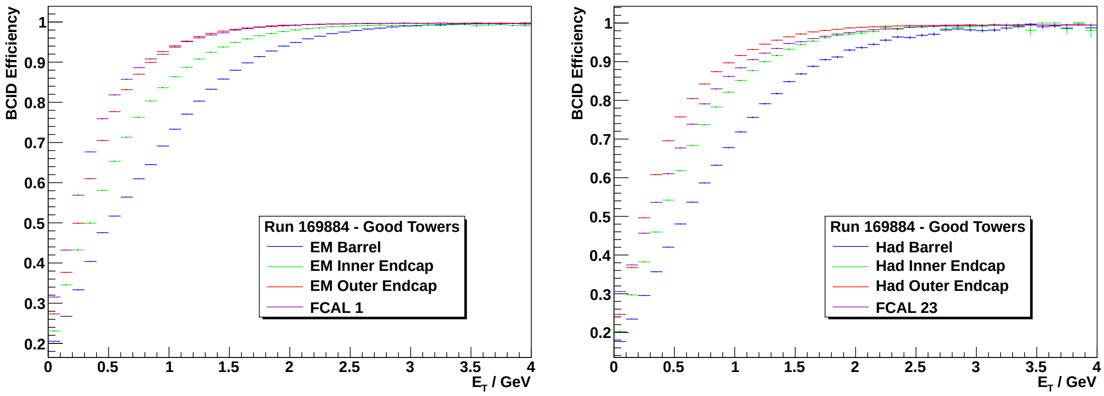

Figure 6.2: BCID efficiency as a function of offline calorimeter E_T for the electromagnetic calorimeter (left) and the hadronic calorimeter (right).

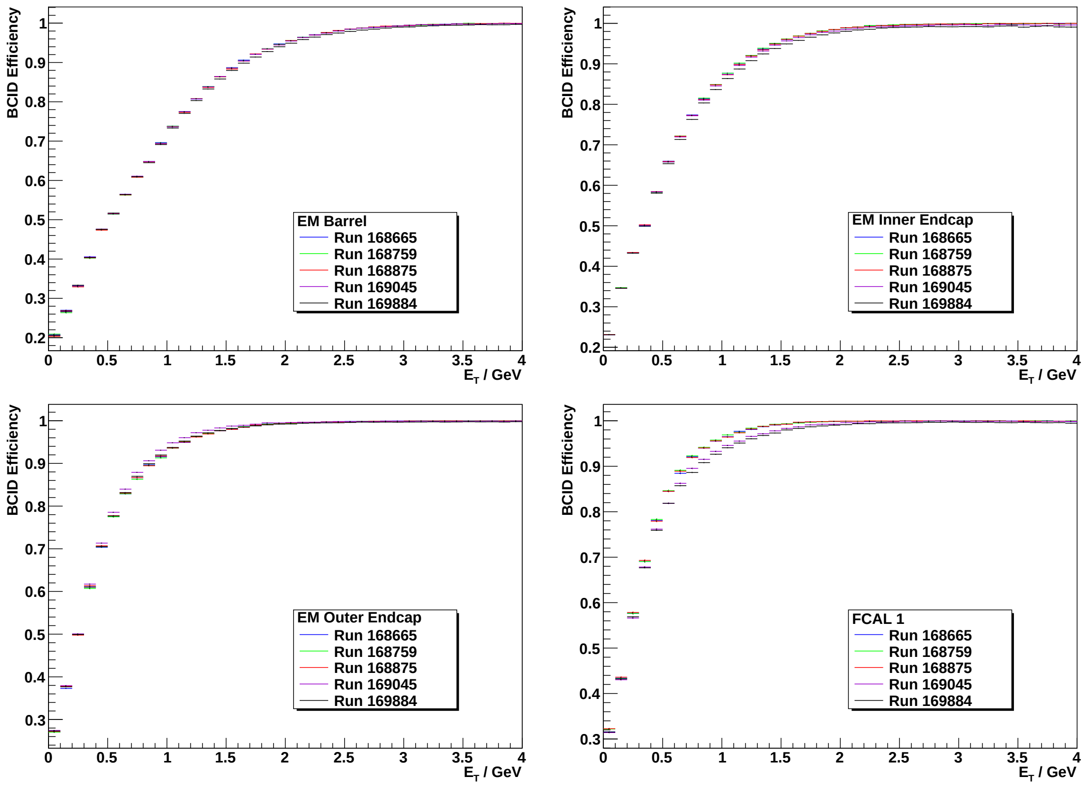

Figure 6.3: BCID Efficiency comparison for electromagnetic calorimeter partitions across different runs as a function of offline calorimeter E_T. Top: Barrel Region (left), Inner Endcap (right). Bottom: Outer Endcap (left), FCal (right).

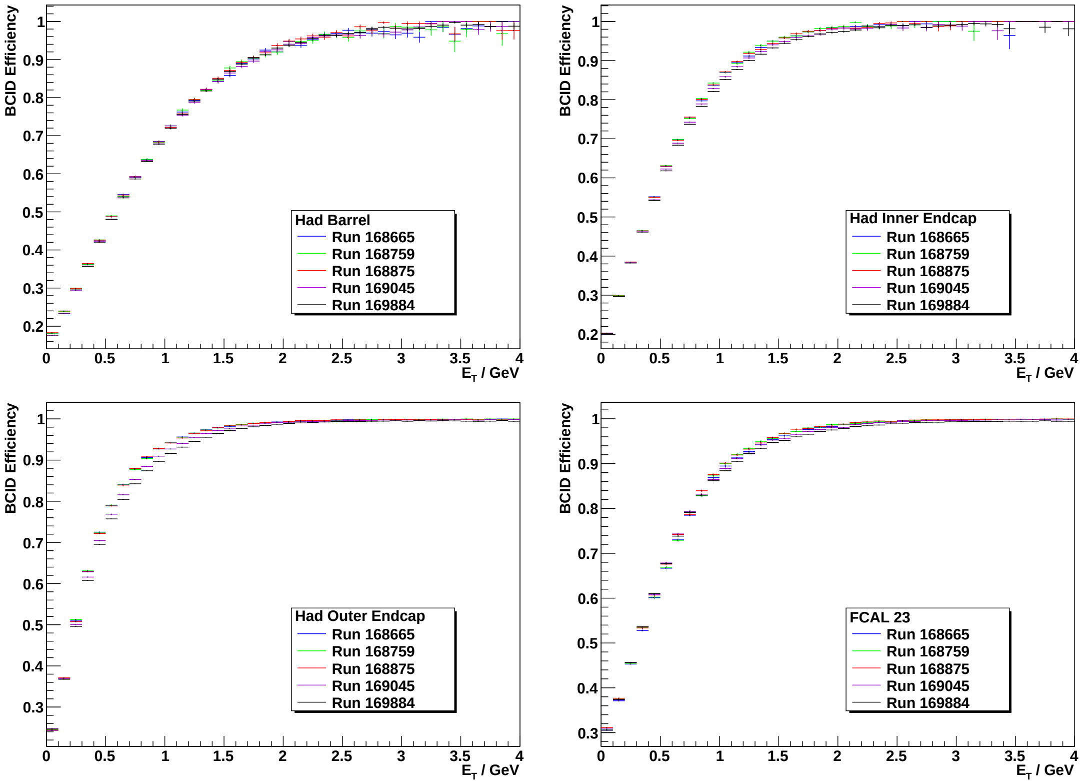

Figure 6.4: BCID Efficiency comparison for electromagnetic calorimeter partitions across different runs as a function of offline calorimeter E_T. Top: Barrel Region (left), Inner Endcap (right). Bottom: Outer Endcap (left), FCal (right).

6.3 BCID On-Off Curves

The reconstructed offline calorimeter E_T values for each tower follow, by definition, a continuous distribution, but the L1Calo E_T values are integer values (i.e. discrete) determined by the output of the Lookup Table as described in Section 5.1. L1Calo will therefore label each trigger tower pulse as having a height of 0 GeV, 1 GeV, 2 GeV etc... It is a useful consistency check to measure the BCID Efficiency as a function of offline calorimeter E_T for each L1Calo pulse height. There is also a difference in the hardware in which the L1Calo and calorimeter values are summed, with a significant noise contribution coming from the electronics of the L1Calo summing chain so not present in the calorimeter value which does not use these electronics. Fluctuations in this noise can cause a noticeable shift between the two values, giving a wide distribution of offline calorimeter E_T for each L1Calo pulse height.

6.3.1 Methodology

The same criteria for selecting trigger towers used previously are also used here, with the additional separation into different L1Calo pulse heights from 0 GeV upwards. The previously shown turn-on curves are therefore split up into on-off curves, one for each pulse height, which shown what contribution to the BCID efficiency comes from each pulse height. The statistics for HI data are too limiting to measure the efficiency beyond an $\mathrm{E_T}$ of 6 GeV. The BCID efficiency for an X GeV pulse height, $\mathrm{Efficiency_X}$ is then defined as:

$$\mathrm{Efficiency_X} = \frac{\mathrm{No.Calo\ Cell\ E_T\ \&\ BCID > 0\ \&\ L1Calo\ E_T = X\ GeV}}{\mathrm{No.Calo\ Cell\ E_T}} \tag{6.2}$$

6.3.2 Results

The relative heights of each curve, where a curve contains signals for only one L1Calo pulse height, shows how much of the efficiency at a given $\mathrm{E_T}$ is due to each L1Calo pulse height. As such, the combination of all on-off curves gives the full efficiency shown in Figure 6.2. Figure 6.5 shows on-off curves for the electromagnetic and hadronic barrel partitions. The curves are very similar for the other partitions though slightly broader in the FCal.

It can be seen that the efficiency which comes from 1 GeV L1Calo pulses is low compared to the others. This is due to the high probability that pulses reconstructed as 1 GeV in the L1Calo hardware will fail the noise cut threshold associated with that tower, based on the FIR filter output of the central time slice. The noise cut is performed by the LUT and is designed to remove towers which are only showing electronic noise. The threshold varies from tower to tower depending on its position in η and ϕ. This causes the pulse height to be set to zero, and is therefore considered as being a 0 GeV L1Calo pulse, despite having an ADC spectrum which allows it to pass BCID. The efficiency associated with 0 GeV L1Calo pulses is therefore

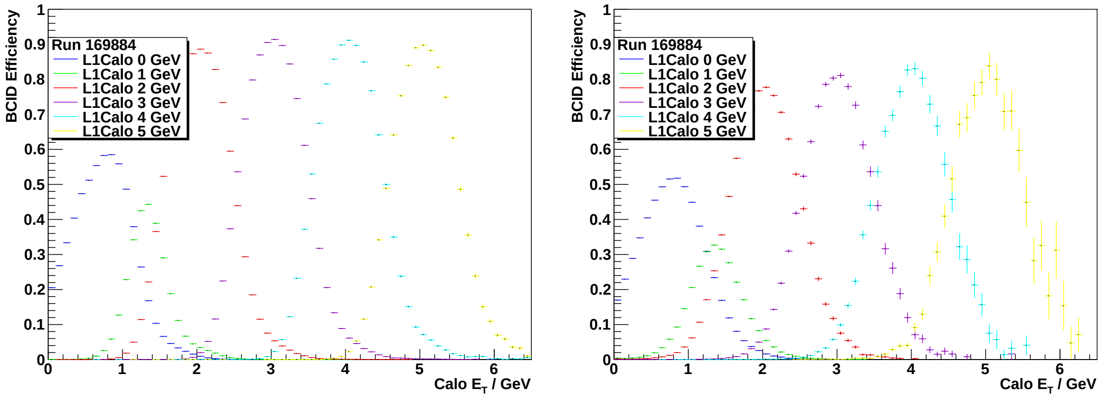

Figure 6.5: On-off curves for Barrel partitions: Efficiency for each individual pulse height. Left: Electromagnetic layer, Right: Hadronic layer.

significant at low calorimeter E_T values but these towers will not then be used to identify physics objects in the CPM and JEM. The peak of each curve is shifted upwards in E_T, away from the point where the L1Calo E_T value is equal to the calorimeter E_T value. This is because of an increased probability to pass noise and BCID requirements at higher E_T but is most pronounced in the earlier curves. This effect also produces asymmetric tails on the distributions but is compensated in the asymmetric shape of the central part of the curves, such that the mean and peak of each curve differ by less than 0.05 GeV (half a bin width). The hadronic layer has lower and wider curves (though of approximately equal area) due to increased noise in the tile calorimeter, which results in a larger range of E_T values being included in each pulse height shape.

6.4 Understanding Badly Performing Towers

The BCID efficiency in the hadronic barrel was seen to be plateauing below the other partitions in Figure 6.2, although it appears to reach almost full efficiency (98%) at higher E_T. To investigate whether this was due to a general problem with this partition or due to individual towers, the efficiencies were calculated for each tower. The tower efficiencies have been split into two ranges: $0.5 \leq E_T < 2.0$ GeV and $E_T \geq 2.0$ GeV. This split has been used to highlight any anomalies but also to exclude the region $E_T < 0.5$ GeV where the results are known to be unreliable due to the ntuple selection bias. The efficiency maps are shown in Figures 6.6 and 6.7 for the electromagnetic and hadronic layers, respectively. As mentioned in Section 5, the towers are of size $\Delta\eta \times \Delta\phi = 0.1 \times 0.1$ in the barrel partition but increase as a function of η so that each block in the efficiency maps represents one tower.

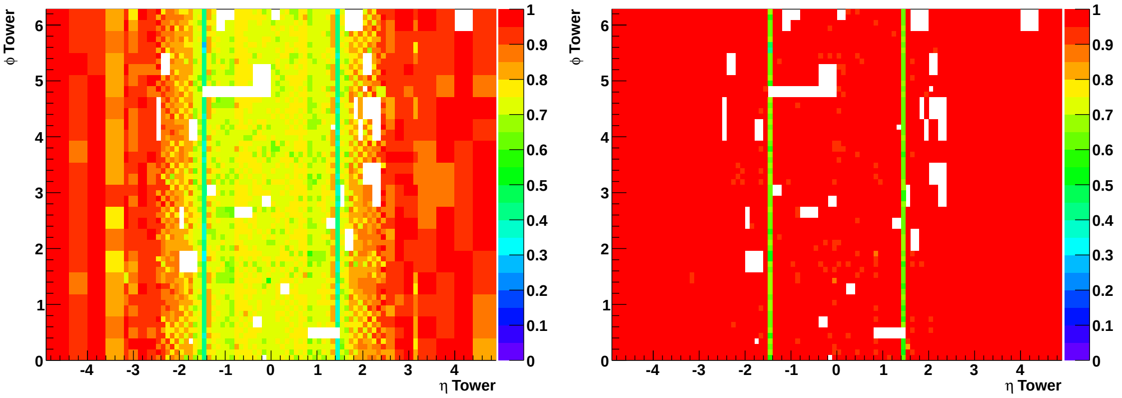

Figure 6.6: Efficiency map for each tower in the electromagnetic layer. Left: for $0.5 \leq E_T < 2.0$ GeV, Right: for $E_T \geq 2.0$ GeV.

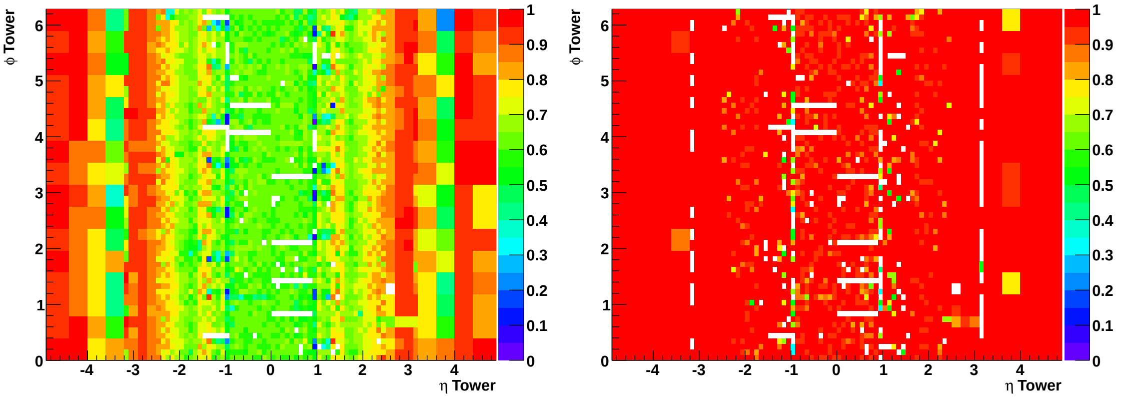

Figure 6.7: Efficiency map for each tower in the hadronic layer. Left: for $0.5 \leq E_T < 2.0$ GeV, Right: for $E_T \geq 2.0$ GeV.

The towers which are shown as white in the maps are those which have been marked as “Bad” or “Dead” in offline databases so have not been included in this study. This is generally due to malfunctioning readout electronics, which make the signals unreliable. In both the electromagnetic and hadronic layers there is a clear checker board pattern visible below E_T of 2.0 GeV, which is an expected effect of the L1Calo design, caused by electronic noise on the PPM electronics. The crack region in the electromagnetic calorimeter, $1.4 < \eta < 1.5$, is clearly visible as having lower efficiency in both E_T ranges. In the hadronic layer there are several towers observed at $\eta = \pm 0.95$ with very low efficiencies (marked as blue in Figure 6.7). These are found in a semi-regular 8 fold pattern on each side which is not quite cyclically symmetric in ϕ or symmetric in $\pm\eta$. These towers explain the lower plateau observed in Figure 6.2. Initially it was not known why these towers should be performing so badly, so further investigation into the behaviour of these towers was performed, including the short study shown in Section 6.4.1.

6.4.1 Differences Between Towers

It is expected and observed that towers at different η values will have different BCID efficiencies, partly due to noise differences but also due to differences in properties such as E_T spectra. To remove any η dependency, the poorly performing towers are only compared to towers at the same η value (± 0.95). The ATLAS calorimeters and trigger are cyclically symmetrical in ϕ so there are not expected to be any differences between towers at fixed η. The E_T spectra for all towers at fixed η have been compared and found to be consistent within statistical fluctuations of each other, as shown in Figure 6.8. This figure shows a comparison between the first poorly performing positive η tower in ϕ and one of its neighbouring towers. Also shown are the ADC spectra across the five time slices used in BCID for these two towers. No pedestal has been subtracted from these values. The ADC counts in each time slice have been summed over all deposits to obtain this plot. Dividing by the number of deposits would give the average shape but this is not necessary as a similar number of deposits should be recorded in each tower.

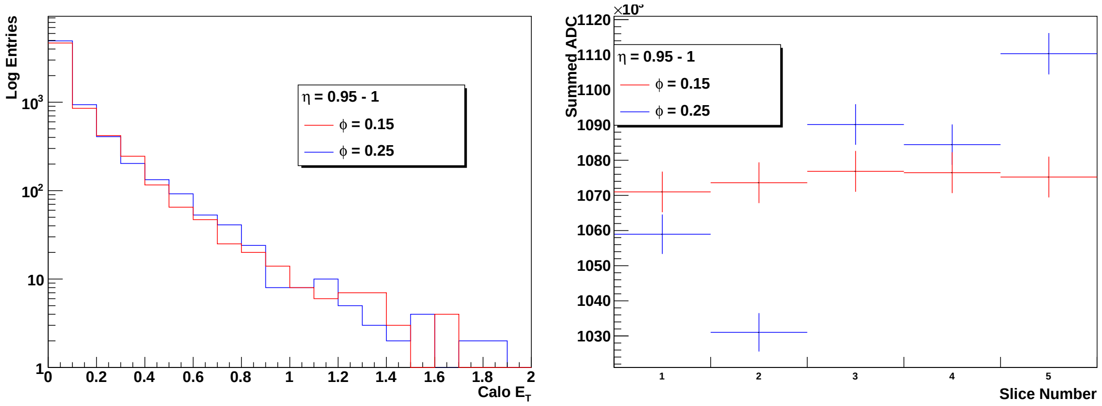

(a) E_T spectra (b) ADC values across 5 time slices

Figure 6.8: Comparison of trigger towers at $\eta = +0.95$. Shown are the first poorly performing tower in ϕ in blue and a tower neighbouring it in ϕ in red. All recorded signals have been summed together.

The average E_T of a deposit in an HI event is very low, as shown in Figure 6.8a, so the ADC values are dominated by the pedestal, which is around 32 counts per deposit. A well behaved tower should therefore have an ADC spectrum that is close to flat but shows a signal-like pulse peaking in the middle slice and a slight asymmetry in the falling edge due to the design of the calorimeter electronics. The well performing tower, in red, behaves as expected for a trigger tower in Heavy Ion collisions. The poorly performing tower, in blue, however, behaves very differently and shows a shape very different from a signal expectation. There appears to be an amplification in the difference between time slices as well as a low second slice and a high fifth slice , at the 1% level, such that the central slice is not the peak. This spectrum does not look like the expected pedestal dominated shape with a small signal enhancement.

Similar distortions are observed in many of the poorly performing towers. To characterise the deviation of the ADC spectrum in each tower, a zero order polynomial is fitted to the ADC spectrum in each tower using a χ^2 minimisation using the assumption that signals are a fluctuation above the pedestal. This is not a statistically accurate χ^2 due to the nature of the test statistic but it is a useful test to characterise the abnormality of a tower. Figure 6.9 shows the ADC spectra and fit to each of the two towers shown previously: the well performing on the left and the poorly performing tower on the right.

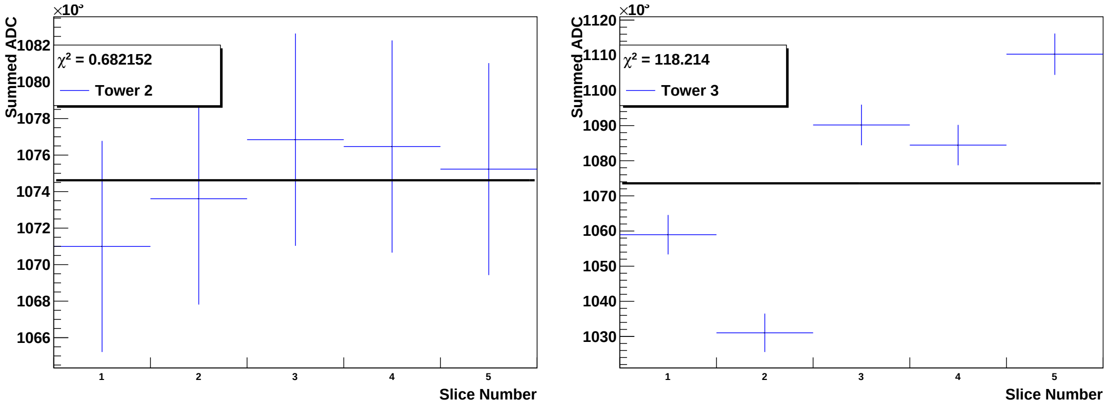

Figure 6.9: Deviation of the two towers shown previously by fitting a 0 order polynomial. Left: well performing tower showing a pedestal dominated signal, Right: poorly performing tower showing a strong distorted signal.

The difference in the χ^2 is very large and this situation is generally replicated across the well performing and poorly performing towers at $\eta = \pm 0.95$. The deviation for each tower has been plotted against the BCID efficiency for deposits with $0.5 \geq E_T < 2$ GeV (as shown in efficiency map in Figure 6.7) to correlate the two quantities. The correlation is shown in Figure 6.10. There is a clear separation of the towers into two populations, one that has low χ^2 values and good efficiency and the other with high χ^2 values and poor efficiency. Only two outliers exist, one from each population, but the populations are otherwise very well separated.

The towers in the bottom right population have all been identified as towers whose readout signals are put through the same tile modules as the MBTS. The MBTS modules use high gains and the MBTS signals can become very large due to the high occupancy of the scintillators during HI. Bunches of cables carry both the MBTS signals and normal hadronic calorimeter trigger tower signals so as the MBTS signals have increased in size the effect of cross talk has also increased on the towers

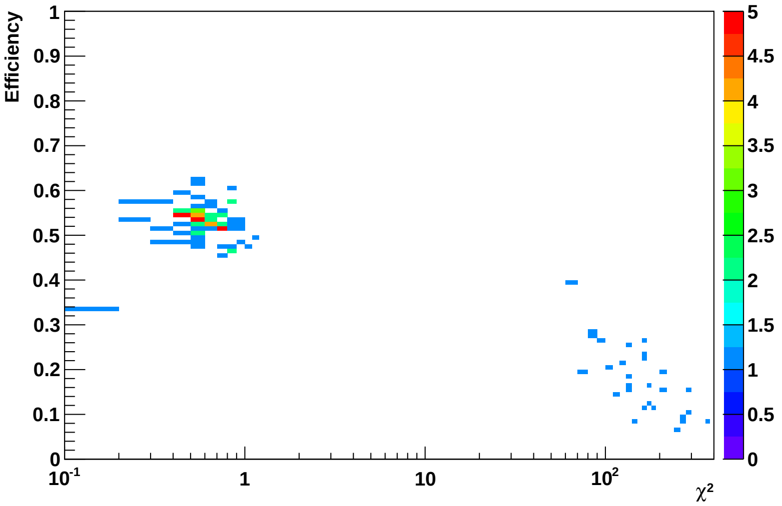

Figure 6.10: BCID efficiency for deposits in the range$0.5 \leq \mathrm{E_T} < 2$ GeV against the χ^2 of the ADC shape deviation for each tower at $\eta = \pm 0.95$.

connected to the same modules at $\eta = \pm 0.95$. This distorts the ADC shape, which causes problems for the BCID system, which, in turn, expects a signal-like shape. As a result of this study and others the MBTS trigger signals were switched off.

6.5 Summary

The BCID efficiency in the L1Calo system has been investigated. The efficiency of all partitions in both calorimeters follows a turn-on curve and becomes almost fully efficient by $\mathrm{E_T} = 3$ GeV. The BCID efficiency is also measured for the different L1Calo pulse heights, which shows the width of the calorimeter $\mathrm{E_T}$ distribution for each pulse height. The hadronic calorimeter is found to have much wider pulse height resolutions than the electromagnetic calorimeter. Several hadronic towers at $\eta = \pm 0.95$ were found to perform significantly worse than other towers in the same region. These towers were found to have heavily distorted pulse shapes compared to well behaving towers. The source of the distortion was identified as cross talk from the MBTS signal, which were later disabled, partly due to this study.

CHAPTER 7

Search For A Higgs Boson Decaying To A b-Quark Pair

7.1 Introduction

Presented here is a search for a standard model Higgs Boson decaying to a b-quark pair in association with a W boson, using the process $WH \rightarrow \ell\nu b\bar{b}$ with the ATLAS detector. The Feynman diagram for Higgs production by WH was previously shown in Figure 2.4d. For much of this chapter, and the following two, the channel will be referred to as "WH". Two analyses, with a large number of similarities, will be described in this chapter: One in which the invariant mass of the reconstructed Higgs system (2 b-jets) is used as the final discriminant and one in which the final discriminant is the output of a Boosted Decision Tree (BDT) trained to extract a signal. The two analyses will be referred to as the "cut-based" and "MVA", respectively. More details of the two analyses are provided in Section 7.4. The general strategy of the cut-based analysis is to apply selection requirements (cuts) optimised to enhance the ratio of signal to background. The MVA analysis takes a different approach, applying only a loose preselection to preserve signal statistics and then allowing the multivariate (MVA) method to separate signal and background.

The analyses presented here use triggers which select events with large transverse missing energy, $E_{\mathrm{T}}^{\mathrm{miss}}$, for which more details will be provided in Section 7.6. The $E_{\mathrm{T}}^{\mathrm{miss}}$ triggers can be useful for selecting WH events in which the W decays to a muon and muon neutrino as the muon leaves almost no deposit in the calorimeters and so both particles contribute to the $E_{\mathrm{T}}^{\mathrm{miss}}$ calculated within the trigger system. This is different to the main WH analyses in which the triggers used are those that select events with single high energy leptons. The analyses presented here will be referred to as the "$E_{\mathrm{T}}^{\mathrm{miss}}$ triggered" while the analyses using the single lepton triggers will be referred to as the "Nominal". The Nominal analyses were produced by another WH analysis group. Differences between the $E_{\mathrm{T}}^{\mathrm{miss}}$ triggered and Nominal analyses will be noted in the text. The $E_{\mathrm{T}}^{\mathrm{miss}}$ triggered analyses will be used on their own to extract results as well as merged with the Nominal to extract results. The merged analyses will be referred to as the "Combined" analyses. The analyses described here, the $E_{\mathrm{T}}^{\mathrm{miss}}$ triggered and Combined, are fitted using the fit model described in Chapter 8 to extract the results presented in Chapter 10.

7.2 Data & Monte Carlo Samples

The dataset used for the WH analyses is the full amount of proton-proton data collected by the ATLAS detector during 2012, at a centre-of-mass energy of 8 TeV. The data recorded must fulfill certain requirements on the normal operation of each sub-detector and, therefore, data quality. The total integrated luminosity passing these requirements is 20.3 fb^{-1}. The data used comes from the `JetTauEtmiss` stream, whereas the Nominal analysis uses the `EGamma` and `Muon` streams. The `JetTauEtmiss` stream will contain events passing $E_{\mathrm{T}}^{\mathrm{miss}}$ triggers with no additional requirements on leptons or jets. As mentioned in Section 4.5, there ise overlap between these three streams.

To understand the distributions expected from background processes and the enhancement in these distributions that would occur in the presence of a signal, Monte Carlo (MC) generators are used to produce simulated data. MC is also required for understanding detector response and correcting for this. The MC samples used in the WH analyses simulate both the signal and backgrounds expected for this search. The samples are generated using a variety of different MC event generators which are optimised for certain type of events. Individual samples may use multiple generators to simulate different portions of the overall process.

The generators simulate the full topology of an event, using current theoretical understanding, and output the 4-momentum vectors of the particles produced. The generator output is known as MC truth as it contains the true information of the particles simulated without any detector effects. The MC truth is passed through a simulation of the ATLAS detector built using GEANT4 [72], which includes the detector geometry and the response of all sub-detectors [73, 74]. The majority of samples use the reduced ATLFastII simulation of the detector rather than the full simulation [75] . This reduces the per event processing time considerably through the use of pre-built calorimeter shower templates (based on particle type, energy and detector position) rather than running the full showering simulation. MC samples are assigned weights based on the number of events in the sample and the cross-section of the process simulated in order to get distributions normalised to the same dataset size of 20 fb^{-1}.

All signal and background events have the output 4-vectors of minimum bias events mixed with them, before the event is passed through the detector simulation, to account for the multiple interactions that occur when the proton beams collide. The distribution of the number of these additional events is set to be the same as is observed in data. A large set of minimum bias events is generated using PYTHIA 8 [76] with an ATLAS tuning of PYTHIA's parameters called AU2 [77] and the MSTW2008LO PDF set [78] for the initial distributions of quark momenta within the beam protons. This set of minimum bias events is resampled for all samples.

The signal process, $WH \to \ell\nu b\bar{b}$ (where $\ell = e, \mu, \tau$), is generated using PYTHIA 8 with the AU2 tuning and the CTEQ6L1 PDF set [79]. The outgoing semi-stable particle 4-vectors are passed through the MC generators PHOTOS [80] and TAUOLA [81] to add final-state radiation and τ decays, respectively. A proportion of the τs produced will decay to e or μ and neutrinos and so would be considered as signal events for this search. The branching ratios used for these decays are 17.82 ± 0.04 % for $\tau \to e\nu_e\nu_\tau$ and 17.39 ± 0.04 % for $\tau \to \mu\nu_\mu\nu_\tau$ [1]. High statistics signal samples are generated for Higgs masses at 5 GeV intervals between 100 and 140 GeV, excluding 105 GeV(for which only a small statistics sample was available. Not only do the properties of the final state particles vary with Higgs mass but so does the expected number of events because, as shown previously in Chapter 2.3, both the Higgs cross section and branching ratios vary with Higgs mass. The NNLO cross section for Higgs production in association with a W boson in proton-proton collisions at a centre-of-mass energy of 8 TeV for the Higgs masses used in the analyses are shown in Table 7.1. The branching ratios of the $H \to b\bar{b}$ decay mode for the same masses are shown in Table 7.2, calculated using HDECAY [82]. $ZH, H \to b\bar{b}$ samples were also generated, using the same setup, as there can be significant contamination between the different $VH, H \to b\bar{b}$ modes.

Background processes must also be simulated to determine the expected yield in data in the absence of a signal. Different MC generators and configurations are used to simulate the different background processes, a summary of which is provided below:

- Samples containing a vector boson and additional jets ($W/Z+$ jets) are gen-

m_H (GeV)	$\sigma(WH)$ (pb)	QCD Scale (%)	PDF+α_s (%)
100	1.447	± 1.0	± 2.3
110	1.071	± 1.0	± 2.4
115	0.9266	± 1.0	± 2.3
120	0.8052	± 1.0	± 2.5
125	0.7046	± 1.0	± 2.3
130	0.6169	± 0.9	± 2.4
135	0.5416	± 1.0	± 2.5
140	0.4768	± 1.0	± 2.4

Table 7.1: Inclusive cross sections and uncertainties for WH production in pp collisions at 8 TeV. The values are produced by the Higgs Cross Section Working Group [83]. The uncertainties included are the QCD scale uncertainty, which covers the uncertainty in determining the renormalisation scale to account for missing higher orders in the calculation, and the combined uncertainty due to initial proton parton densities and running QCD coupling.

m_H (GeV)	Branching ratio	Relative Up Uncertainty	Relative Down Uncertainty
100	0.789	+1.78%	−1.83%
110	0.744	+2.13%	−2.18%
115	0.703	+2.40%	−2.46%
120	0.648	+2.76%	−2.83%
125	0.577	+3.21%	−3.27%
130	0.494	+3.71%	−3.78%
135	0.404	+4.25%	−4.32%
140	0.315	+4.80%	−4.83%

Table 7.2: Branching Ratios for the Standard Model $H \to b\bar{b}$ Decay Mode at different Higgs masses, m_H. The values are produced by the Higgs Cross Section Working Group [83].

erated by SHERPA [84] using the CT10 PDF set [85]. Samples are produced separately for different leptons, $p_{\mathrm{T}}(W/Z)$ ranges, and hadron flavours. The separation of samples and the statistics generated in each is chosen to ensure good modelling in the more sensitive regions (high signal-to-background) of the analyses that have low event rates.

- A very large $t\bar{t}$ sample (approximately 100 million events) is generated using POWHEG [86] with the CT10 PDF set interfaced to PYTHIA, to handle hadronisation and parton showering, using the Perugia2011C tune [87] and CTEQL1 PDF set [79]. $t\bar{t}$ decays are filtered to ensure that all recorded events have at least one lepton in the final state.

- Single top samples for the s-channel and Wt-channel are produced using the same MC generators and settings used for the $t\bar{t}$ samples while the t-channel uses ACERMC [88] interfaced to PYTHIA, both using the Perugia2011C tune and the CTEQL1 PDF set.

- Diboson samples are generated using POWHEG interfaced to PYTHIA, uwith the CT10 PDF set and the AU2 generator tuning. Diboson samples are produced separately for WW, WZ and ZZ.

- Multijet interactions are unfeasible to simulate in high enough statistics to be of any use to the analyses so an estimate of the yields in each analysis region is derived from data and then used as a representation of this background. Multijet has a huge production cross section at the LHC but only a tiny proportion of multijet events contain objects of similar kinematics to the signal process. The yields from this background are taken from the templates and normalisations performed by the $VH, H \to b\bar{b}$ search group within ATLAS. The details of the derivation can be found in [40]. For the $E_{\mathrm{T}}^{\mathrm{miss}}$ triggered analyses the yield is expected, and found, to be completely negligible, as it is much easier for a jet to fake an electron than a muon and the multijet events mostly give a low (fake) reconstructed $p_{\mathrm{T}}(W)$. A number of the analysis selection requirements, particularly for the $E_{\mathrm{T}}^{\mathrm{miss}}$ triggered analyses, are chosen to suppress this hard to model background.

7.3 Object Selection

The objects reconstructed and selected in the $E_{\mathrm{T}}^{\mathrm{miss}}$ triggered WH analyses are muons, electrons, $E_{\mathrm{T}}^{\mathrm{miss}}$ and jets. Additionally, the jets are b-tagged, a procedure which is described in Section 7.5. Two categories of electrons and muon are defined, "veto" and "signal", where veto leptons are a subset of the signal leptons. The lepton and jet categories are required to select signal-like events but also to veto events which contain objects in addition to those required for the signal.

Veto muons [89] are made up of 3 different types: those reconstructed from a combination of an inner detector track matched with a muon spectrometer track within $|\eta| < 2.7$; those with only a muon spectrometer track within $2.5 < |\eta| < 2.7$ and those with an inner detector track matched to a small calorimeter deposit within $|\eta| < 0.1$ where the muon spectrometer chambers are joined and therefore not fully efficient due to coverage. The 3rd category are required to have $p_{\mathrm{T}} > 20$ GeV, while the other two must have $p_{\mathrm{T}} > 7$ GeV, impact parameters of less than 0.1 mm (10 mm) in the transverse (longitudinal) plane and fractional track isolation of less than 0.1. Fractional track isolation is defined as the p_{T} sum of tracks within a cone of radius $\Delta R = 0.2$, centered around the muon, divided by the muon's transverse momentum.

Signal muons must pass all the criteria for loose muons but the type is restricted to those reconstructed from an inner detector track matched with a muon spectrometer track within $|\eta| < 2.5$. The p_{T} cut is raised from 7 GeV to 25 GeV and the fractional track isolation cut tightened to 0.04. An additional requirement is added that the fractional calorimeter isolation must be less than 0.04. Fractional calorimeter isolation is defined as the E_{T} sum of calorimeter deposits within a cone of $\Delta R = 0.3$, centered around the muon, divided by the muon's transverse energy.

Veto electrons must satisfy the ATLAS "very loose" operating point of a likelihood built out of variables from matched inner detector tracks and calorimeter clusters [90]. The electrons are required to be within $|\eta| < 2.47$ and have $p_{\mathrm{T}} > 7$ GeV. The same track isolation requirement for loose muons is applied for loose electrons. For the $E_{\mathrm{T}}^{\mathrm{miss}}$ triggered analyses there is no signal electron category, only veto, but for the Nominal analysis a signal category is defined. Electrons passing the veto criteria, $p_{\mathrm{T}} > 25$ GeV, plus the same track and calorimeter isolation requirements used for signal muons, and the ATLAS "very tight" likelihood categorisation are defined as signal electrons for the Nominal analysis.

Jets are identified with the anti-k_T clustering algorithm [91] using data from the calorimeters with a clustering radius of $R = 0.4$ [92]. Information from both calorimeters is calibrated to the hadronic energy scale based on the candidate jet's properties using a global sequential calibration [93]. Jets must additionally be calibrated based on the amount of additional energy deposits arising from pileup events, additional interactions occuring during the same bunch crossing [94]. Two categories of jets are defined, veto and signal, as was done for the leptons. Veto jets are those with either $p_{\mathrm{T}} > 20$ GeV and $|\eta| < 2.5$ or $p_{\mathrm{T}} > 30$ GeV and $2.5 < |\eta| < 4.5$. Signal jets are those with $p_{\mathrm{T}} > 20$ GeV and $|\eta| < 2.5$. All signal jets must pass a Jet Vertex Fraction (JVF) cut of more than 0.5 designed to reject jets from additional interactions occurring when the beams cross. The JVF is defined as the fraction of the jet's p_{T} which comes from tracks originating from the primary vertex [95]. The forward jet p_{T} cut is higher than for signal jets because low p_{T} forward jets are expected from pileup, and without tracking in this region a JVF cut cannot be made, whereas a high p_{T} jet is not consistent with the signal kinematics.

In the case of the electrons, muons and jets overlapping each other, the following rules are applied to resolve which objects are present. First, jets within $\Delta R < 0.4$ of an electron are removed. Second, jets within $\Delta R < 0.4$ of a muon are removed if the number of tracks within the cone is less than 4, consistent with a muon plus final state radiation, but the muon is removed instead if there are at least 4. Finally muons within $\Delta R < 0.2$ of an electron are removed if they are calorimeter-seeded muons, but the electron is removed if they are not.

The magnitude and direction of $E_{\mathrm{T}}^{\mathrm{miss}}$ is constructed from vector sums of the visible calibrated objects in an event [96]. Calorimeter clusters are recalculated based on the final calibrations of the electrons, taus, photons and jets used in the ATLAS $E_{\mathrm{T}}^{\mathrm{miss}}$ algorithm. All calorimeter clusters within $|\eta| < 4.5$ are used. The momenta of calibrated muons are added in but the soft calorimeter deposits associated with these muons are explicitly removed to avoid double counting. Additional corrections to the magnitude and direction of $E_{\mathrm{T}}^{\mathrm{miss}}$ are made to account for the contributions expected from pileup and underlying event.

7.4 Event Selection

The analyses' event selections are designed to first select a leptonically decaying W boson and then find two associated b-jets to identify processes of the type $WH \to \ell\nu b\bar{b}$. The trigger is an important aspect of these analyses but will be described in 7.6 rather than here. The analysis cuts which vary between the cut-based and MVA analyses and vary between $p_{\mathrm{T}}(W)$, the transverse momentum of the W, regions are summarised in Table 7.3.

A W boson decaying to a muon and a muon neutrino is identified, in the $E_{\mathrm{T}}^{\mathrm{miss}}$ triggered analyses, by selecting events with exactly one signal muon (as described in Section 7.3), no additional veto leptons and $E_{\mathrm{T}}^{\mathrm{miss}}$ as the signature of a neutrino. The value of $E_{\mathrm{T}}^{\mathrm{miss}}$ must be above 20 GeV in both the cut-based and MVA analy-

	Cut-based			MVA
$p_{\mathrm{T}}(W)$	$120 - 160$ GeV	$160 - 200$ GeV	> 200 GeV	> 120 GeV
$m_T(W)$	< 120 GeV	< 120 GeV	< 120 GeV	-
$\Delta R(jj)$	$0.7 - 2.3$	$0.7 - 1.8$	< 1.4	> 0.7 or $p_{\mathrm{T}}(W) > 200$ GeV
$E_{\mathrm{T}}^{\mathrm{miss}}$	> 20 GeV	> 20 GeV	> 50 GeV	> 20 GeV

Table 7.3: Table of $p_{\mathrm{T}}(W)$ dependent kinematic cuts applied to the cut-based and MVA

ses, with the additional requirement of $E_{\mathrm{T}}^{\mathrm{miss}} > 50$ GeV in the cut-based analysis if the reconstructed $p_{\mathrm{T}}(W)$ is calculated to be above 200 GeV. This requirement is included to remove poorly reconstructed events. The value of $p_{\mathrm{T}}(W)$ is determined by combining the muon and $E_{\mathrm{T}}^{\mathrm{miss}}$ vectors. For the $E_{\mathrm{T}}^{\mathrm{miss}}$ triggered analyses there are additional cuts of $p_{\mathrm{T}}(W) > 120$ GeV and that $E_{\mathrm{T}}^{\mathrm{miss}}$(NoMuon), $E_{\mathrm{T}}^{\mathrm{miss}}$ with the muon contributions to the calculation removed, must be above 120 GeV. This is done so that the $E_{\mathrm{T}}^{\mathrm{miss}}$ triggered analyses only use regions where it is believed the $E_{\mathrm{T}}^{\mathrm{miss}}$ triggers are well modelled [40]. Additionally, the multijet background is negligible in the high p_{T}(W) regions. In the Nominal analyses, events are also selected which have exactly one signal electron if the event has a high reconstructed $p_{\mathrm{T}}(W)$, due to problems in the data driven multijet description for low $p_{\mathrm{T}}(W)$. At low $p_{\mathrm{T}}(W)$ in the Nominal analyses, the $E_{\mathrm{T}}^{\mathrm{miss}}$ cut is replaced by a cut on H_T, the magnitude of the sum of the lepton, $E_{\mathrm{T}}^{\mathrm{miss}}$ and 2 leading jets.

The W transverse momentum is also used to split the analyses into separate regions with different signal-to-background ratios and enhance the sensitivity of the analyses. In the cut-based $E_{\mathrm{T}}^{\mathrm{miss}}$ triggered analysis the regions used are 120 GeV $<$ $p_{\mathrm{T}}(W) <$ 160 GeV, 160 GeV $< p_{\mathrm{T}}(W) <$ 200 GeV and $p_{\mathrm{T}}(W) >$ 200 GeV. The MVA $E_{\mathrm{T}}^{\mathrm{miss}}$ triggered analysis consists of only one $p_{\mathrm{T}}(W)$ region, $>$ 120 GeV. The Nominal analyses have the additional regions of $p_{\mathrm{T}}(W) >$ 90 GeV and 90 GeV $<$ $p_{\mathrm{T}}(W) <$ 120 GeV for the cut-based analysis and $p_{\mathrm{T}}(W) <$ 120 GeV for the MVA.

The transverse mass of the reconstructed W, $m_T(W) = \sqrt{2p_T^{\ell}p_T^{\nu}(1 - \cos(\phi^{\ell} - \phi^{\nu}))}$, is reconstructed from the lepton and neutrino vectors to check that the identified lepton and neutrino are consistent with coming from the decay of a W. In the cut-based analysis $m_T(W)$ is required to be less than 120 GeV while in the MVA analysis this variable is not cut on. Instead it is used as a variable to discriminate between signal and background, a procedure that will be described in Section 7.7. Using the transverse mass is a powerful way to remove multijet events but does little to most of the other backgrounds that contain real Ws.

The events must contain exactly 2 or 3 signal jets with no additional veto jets. A cut is applied to the distance between the two jets (or two leading jets in the 3 jet case), using ΔR as was defined in Equation 4.3. This distance, $\Delta R(jj)$, must be greater than 0.7 in the MVA analysis unless the condition of $p_{\mathrm{T}}(W) > 200$ GeV is met, while in the cut-based analysis the cut is optimised in several $p_{\mathrm{T}}(W)$ regions: $0.7 < \Delta R(jj) < 2.3$ for 120 GeV $< p_{\mathrm{T}}(W) <$ 160 GeV, $0.7 < \Delta R(jj) < 1.8$ for 160 GeV $< p_{\mathrm{T}}(W) <$ 200 GeV and $\Delta R(jj) < 1.4$ for $p_{\mathrm{T}}(W) >$ 200 GeV. The Nominal Cut-based analysis has the additional cuts of $0.7 < \Delta R(jj) < 3.4$ for $p_{\mathrm{T}}(W) <$ 90 GeV and $0.7 < \Delta R(jj) < 3.0$ for 90 GeV $< p_{\mathrm{T}}(W) <$ 120 GeV. These jet cuts reduce significantly the $t\bar{t}$ background which contains more jets in the final state and generally has a larger separation between the two jets.

The two leading jets must then be b-tagged using the procedure described in Section 7.5. Applying b-tagging is very important to reduce the backgrounds due to $W/Z+$ light jets, those jets initiated by a strange, up or down quark. The third jet in the 3 jet case must not pass b-tagging. Once the candidate $WH \rightarrow \ell\nu b\bar{b}$ events have been selected, the candidate $H \rightarrow b\bar{b}$ decays are reconstructed from the invariant mass of the di-b-jet system:

$$m_{b\bar{b}} = \sqrt{(E_b + E_{\bar{b}})^2 - (p_b + p_{\bar{b}})^2}, \tag{7.1}$$

where p_b and $p_{\bar{b}}$, the momenta of the b and $\bar{b}$ initiated jets, are summed vectorially. The resolution of the di-b-jet mass is improved by adding in energy from soft secondary muons found within the b-jet and removing the calorimetry deposits associated with these muons [97]. The di-b-jet mass is used as the signal region discriminant in the cut-based analysis and as a discriminating variable in the MVA analysis, which will be described in Section 7.7. The di-b-jet invariant mass distributions, m_{bb}, for the $E_{\mathrm{T}}^{\mathrm{miss}}$ triggered analysis can be found in Section 7.8. It is important that there is good data description by the MC in the Nominal regions before the $E_{\mathrm{T}}^{\mathrm{miss}}$ triggered analysis is merged with it.

7.5 b-jet Tagging

One of the most important tools for extracting a signal from the $WH \rightarrow \ell\nu b\bar{b}$ decay mode is the use of b-tagging. The technique of b-tagging is used to differentiate b quark initiated jets from other jets and exploits the lifetime of the b-hadrons the b-quark will intially form as well as its mass. The lifetime of the b-hadrons allows them to travel some distance from the primary interaction point before decay, so the high granularity tracking of ATLAS can be used to reconstruct the corresponding secondary vertex. The large mass of b hadrons, roughly 5 to 10 GeV, compared to the lighter hadrons they decay into means that there are generally a larger number of decay products than for light hadrons. Jets initiated by b quarks will therefore have a larger number of tracks than light jets and a different shower shape which can be discriminated by the highly performant ATLAS calorimeters.

The algorithm used to tag b-jets in the WH analyses is called $MV1c$ [98, 99], a neural network based discriminator that has been trained primarily to reject charm jets. The rejection of charm jets has been prioritised over the slightly better light jet rejection performance of the previous $MV1$ algorithm, improving by a factor of approximately 2. The algorithms output a b-tagging weight, w, such that a cut can be placed at a specific weight, known as an operating point. The $MV1c$ algorithm has been commissioned to allow multiple exclusive operating points to be used to categorise jets [100]. The loose 80%, medium 70% and tight 50% operating points are used, where the percentage refers to the portion of b-jets which pass that operating point. Using the operating points exclusively means that to be considered as part of the category for a certain operating point, a jet must not pass the tighter operating points, e.g. jets are only counted as loose if they are not also medium. By categorising both leading jets using the exclusive $MV1c$ operating points, the events can be categorised as 0-tag, 1-tag, 2LL-tag, 2MM-tag or 2TT-tag, as shown in Figure 7.1. The splitting of the double b-tagged events enhances the sensitivity of the analyses by separating events into regions with different signal-to-background ratios.

The double b-tagged events are considered in signal regions in the fit to extract results, while the single b-tagged events are considered in control regions and the untagged events are not used. In the single b-tagged events, it is the distributions of $MV1c$ b-tagging operating points which are used in the fit instead of using distributions of either di-b-jet invariant mass or BDT output. Four bins are used for the tagged jet representing the 50%, 60%, 70% and 80% exclusive operating points although the 60% operating point has not been used. The single b-tagged $MV1c$ distributions are very useful in constraining the background normalisations, particularly the different flavour contributions to W/Z+jets, as the shapes of these differ far more in the b-tagging distributions than in either di-b-jet invariant mass or BDT output. The single b-tagged event $MV1c$ distributions for the cut-based and MVA analyses can be found in Section 7.8.

7.6 Triggering Strategy and Impact on Event Yields

The $E_{\mathrm{T}}^{\mathrm{miss}}$ triggered analyses make use of the lowest threshold unprescaled $E_{\mathrm{T}}^{\mathrm{miss}}$ triggers which are built, at trigger level, out of calorimeter based objects with no use of muons. Due to changes in the trigger configuration during the 2012 running,

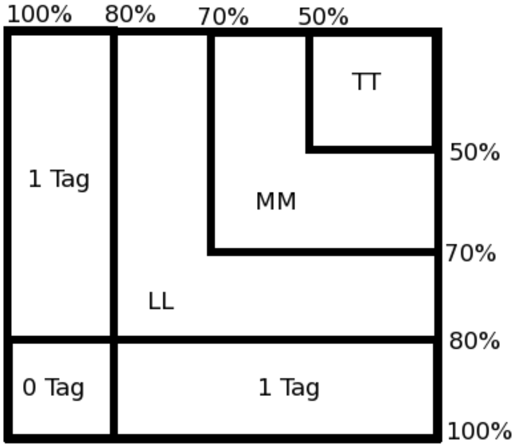

Figure 7.1: Splitting of dijet events into different categories based on the b-tagging efficiency points passed by the 2 leading jets. The event category can be found from the region in which the intersection of jet 1's tag weight (x-axis) and jet 2's tag weight (y-axis) falls.

a combination of slightly different triggers is used during the year but all have a threshold of 80 GeV. The triggers vary slightly in the calibrations performed at trigger level and in the treatment of different bunches within a bunch train, where differences can occur due to the long time period of a calorimeter pulse compared to a bunch crossing. In the Nominal analysis, the lowest threshold unprescaled single lepton triggers are used for both electrons and muons. The $E_{\mathrm{T}}^{\mathrm{miss}}$ triggers are used here because of inefficiencies observed in the single muon triggers due to the lack of complete coverage in the Level 1 muon trigger chambers and problems caused by very high p_{T} muons, which are hard to trigger. The muon triggers plateau at an efficiency of approximately 80% at high p_{T}.

The efficiency of the $E_{\mathrm{T}}^{\mathrm{miss}}$ triggers in $WH \to \mu\nu b\bar{b}$ events is shown in Figure 7.2 as a function of muon p_{T}, $E_{\mathrm{T}}^{\mathrm{miss}}$ and $E_{\mathrm{T}}^{\mathrm{miss}}$ recalculated without any muon contributions (as this is close to the variable which the $E_{\mathrm{T}}^{\mathrm{miss}}$ triggers actually use). The efficiencies are calculated using signal MC at a Higgs mass of 125 GeV. Efficiencies are shown both inclusively and exclusively of events passing the muon triggers used

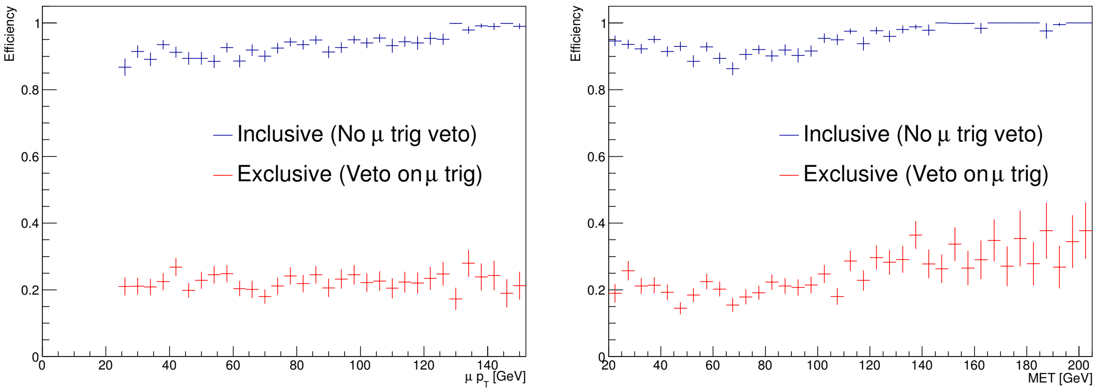

(a) Function of muon p_{T}

(b) Function of $E_{\mathrm{T}}^{\mathrm{miss}}$

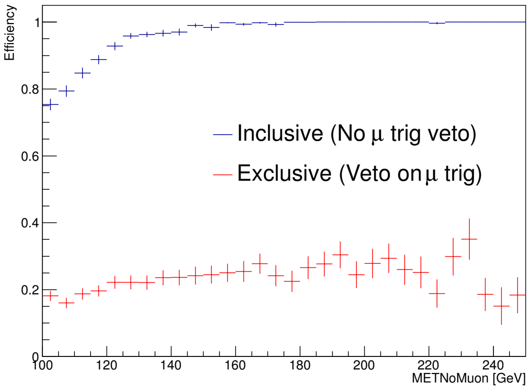

(c) Function of $E_{\mathrm{T}}^{\mathrm{miss}}$ without μ contribution

Figure 7.2: $E_{\mathrm{T}}^{\mathrm{miss}}$ trigger efficiency for the $WH \rightarrow \ell\nu b\bar{b}$ Signal Monte Carlo at a Higgs mass m_H=125 GeV. The efficiency is shown as a function of $p_{\mathrm{T}}(\mu)$, $E_{\mathrm{T}}^{\mathrm{miss}}$ (MET) and $E_{\mathrm{T}}^{\mathrm{miss}}$ without the muon contributions counted (METNoMuon). The efficiency is shown both inclusively and exclusively, with a veto on the muon triggers used in the Nominal analysis. A preselection of exactly one signal muon, 2 loose jets has been applied.

in the Nominal analyses, the exclusive category having additional vetoes on wether the event passes the muon triggers used in the Nominal analyses. A preselection of exactly one signal muon, 2 loose jets and $E_{\mathrm{T}}^{\mathrm{miss}}$(NoMuon), $E_{\mathrm{T}}^{\mathrm{miss}}$ without muon contributions, greater than 100 GeV has been applied. This makes the efficiency appear high as many events that would not pass the $E_{\mathrm{T}}^{\mathrm{miss}}$ trigger also do not pass the $E_{\mathrm{T}}^{\mathrm{miss}}$ requirement. The $E_{\mathrm{T}}^{\mathrm{miss}}$ triggers used have been predicted from signal MC to be, in terms of the full $E_{\mathrm{T}}^{\mathrm{miss}}$ calculation, 80% efficient for $E_{\mathrm{T}}^{\mathrm{miss}} = 100$ GeV, 97% efficient for $E_{\mathrm{T}}^{\mathrm{miss}} = 120$ GeV and fully efficient above $E_{\mathrm{T}}^{\mathrm{miss}} = 160$ GeV [40].

The position of analysis muons within the ATLAS detector is shown in Figure 7.3 for the muon triggered and $E_{\mathrm{T}}^{\mathrm{miss}}$ triggered analyses with an arbitrary normalisation. The positions are obtained using signal MC at a Higgs mass of 125 GeV. The positions shown are offline calibrated muon coordinates rather than trigger RoI as these are not meaningful for the $E_{\mathrm{T}}^{\mathrm{miss}}$ triggered analyses. Figures 7.3a and 7.3b show the positions of muons in the Nominal and $E_{\mathrm{T}}^{\mathrm{miss}}$ triggered analyses, respectively, after applying a preselection and skimming of exactly one signal muon, 2 loose jets and $E_{\mathrm{T}}^{\mathrm{miss}}$ without muon contributions greater than 100 GeV has been applied. Figures 7.3c and 7.3d show the position in the Nominal and $E_{\mathrm{T}}^{\mathrm{miss}}$ triggered analyses after the full cut-based analysis selection has been applied. It can be seen that the muons recovered in the $E_{\mathrm{T}}^{\mathrm{miss}}$ triggered analyses fall generally close to the centre of ATLAS, around $\eta = 0$, as this is where the muon trigger coverage has problems and where very high p_{T} muons are more likely to be found. Particularly evident between Figure 7.3a and Figure 7.3b is the recovery of muons lost due to feet of ATLAS, in the region covered by $|\eta| < 1.1$ and $-2 < \phi < -1$. The large feet of ATLAS increases the material budget in this region and decreases the amount of instrumentation that can be installed there. The μ triggered analyses show a reduced yield of muons in this region while the $E_{\mathrm{T}}^{\mathrm{miss}}$ triggered analyses show an increased yield in this region because the $E_{\mathrm{T}}^{\mathrm{miss}}$ trigger is able to recover these muons.

The $E_{\mathrm{T}}^{\mathrm{miss}}$ trigger has been used in these analyses to try to recover signal statistics lost from the Nominal analyses due to inefficiencies in the muon triggers. The number of events recovered by using the $E_{\mathrm{T}}^{\mathrm{miss}}$ triggers exclusively as a fraction of the number passing the muon triggers is shown in Figure 7.4a for the cut-based analysis and Figure 7.4b for the MVA. The regions considered are signal regions with two b-tags passing the loose tagging requirement. The yields used are prefit expectations from MC, the raw number of events coming from the analysis of the MC with all calibrations applied but none of the normalisations derived from fits to data applied. The ratios are calculated at each of the Higgs masses used (100 GeV and 110-140 GeV) and are inclusive of jet multiplicity, b-tagging category, and $p_{\mathrm{T}}(W)$. The b-tagging regions are merged together as no dependency on the b-tagging category is

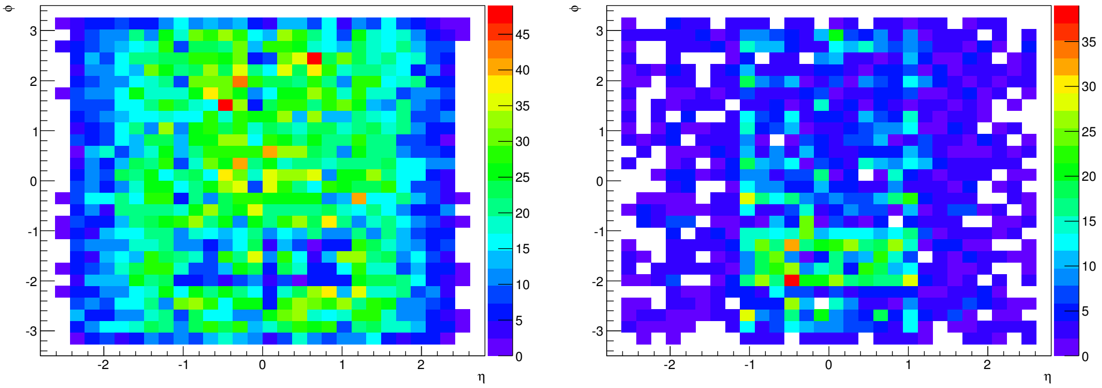

(a) μ Triggered
Signal μ, ≥ 2 Loose Jets

(b) Exclusive $E_{\mathrm{T}}^{\mathrm{miss}}$ Triggered
Signal μ, ≥ 2 Loose Jets

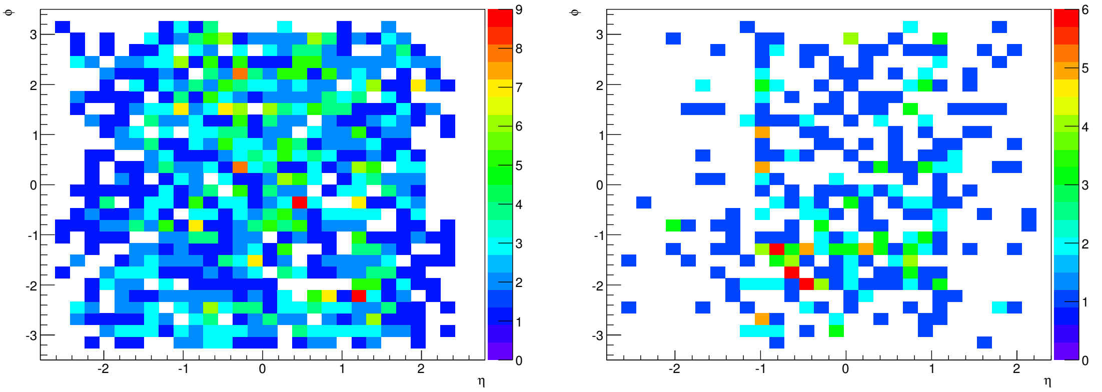

(c) μ Triggered
Full Event Selection

(d) Exclusive $E_{\mathrm{T}}^{\mathrm{miss}}$ Triggered
Full Event Selection

Figure 7.3: Positions of muons within the ATLAS detector from MC that are triggered by the muon triggers (from the Nominal analyses) and exclusively by the $E_{\mathrm{T}}^{\mathrm{miss}}$ triggers (vetoing on the analysis muon triggers). Positions shown are offline muon coordinates and not trigger RoI. The normalisation used is arbitrary. The upper plots have a basic selection applied while the lower plots use the full cut-based event selection.

found in the ratio. The $E_{\mathrm{T}}^{\mathrm{miss}}$ triggered analyses cover $p_{\mathrm{T}}(W) > 120$ GeV whereas the Nominal analyses cover $p_{\mathrm{T}}(W) > 0$ GeV, which gives a fractional recovered yield of about 8% as can be seen in Figure 7.4. In the more sensitive $p_{\mathrm{T}}(W) > 120$ GeV regions, in which the $E_{\mathrm{T}}^{\mathrm{miss}}$ triggered analyses contribute, the increase in recovered signal yield is in the range of 20-35% dependent on region. The yield of electron triggered events is not considered here. Additional plots separated by jet multiplicity and $p_{\mathrm{T}}(W)$ range are shown in Appendix A.

7.7 Multivariate Analysis

The use of the di-b-jet invariant mass distribution as the signal discriminant in the cut-based analysis is not optimal for extracting a signal because the main backgrounds have largely similar values to the signal. Multivariate techniques are therefore used to differentiate the signal from the background. Multivariate techniques use a number of analysis variables, the correlations between which can be exploited to separate the signal and background. A Boosted Decision Tree (BDT) [101] is chosen as the multivariate technique to be used in the WH search. An individual decision tree consists of stages of branches, connected at nodes, which splits events based on a binary cut on an individual variable. This classifies each event based on how many of the cuts are passed or failed. Half of the MC statistics available for signal and background are used to train the decision tree such that weights are assigned to each input variable based on how important it is for separating signal and background. The weights for each variable can be applied and combined to produce a single discriminating value. The other half of the samples is then used to test the training by comparing the final output of the training and test samples.

Individual decision trees are very susceptible to instability caused by artifacts in the information used to determine the split at each level. A BDT improves on this by reweighting the events based on how far they fall from the main population of their

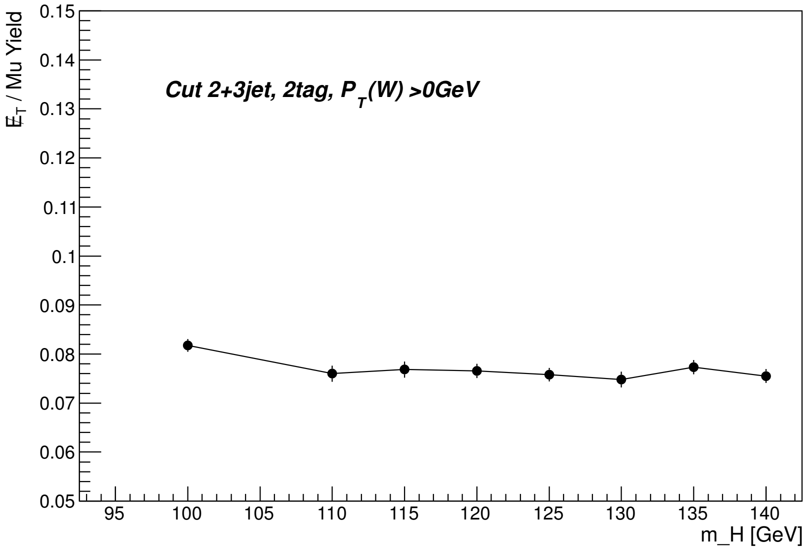

(a) Cut-based 2-jet & 3-jet Inclusive

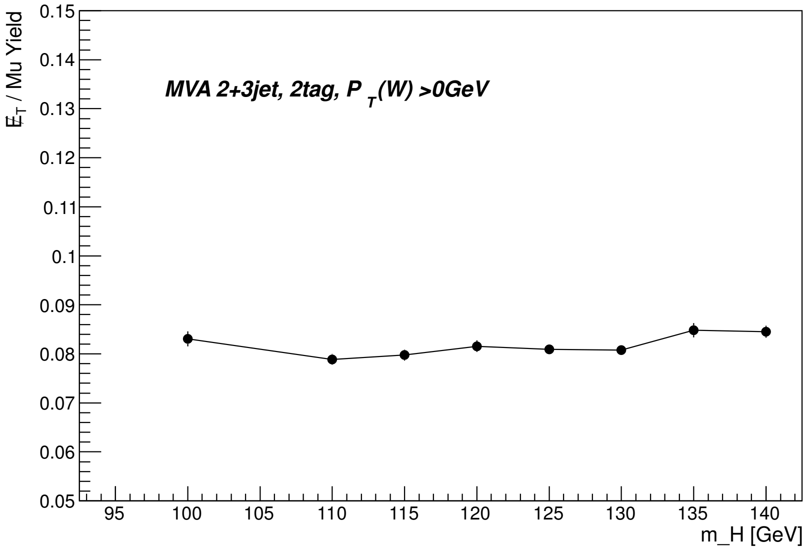

(b) MVA 2-jet & 3-jet Inclusive

Figure 7.4: Ratio of exclusive $E_{\mathrm{T}}^{\mathrm{miss}}$ triggered to μ triggered signal yields in the cut-based and MVA analysis as a function of Higgs mass, m_H. The yields are all prefit Monte Carlo expectations. All b-tagging regions and $p_{\mathrm{T}}(W)$ regions are merged together to obtain the yields ($p_{\mathrm{T}}(W) > 120$ GeV for the $E_{\mathrm{T}}^{\mathrm{miss}}$ triggered and $p_{\mathrm{T}}(W) > 0$ GeV for the μ triggered). The error on each point contains only statistical and trigger uncertainties.

sample type. A new tree is formed from these reweighted events and the process is repeated. The weight for each variable is then taken as the average of the weights determined in each tree. This not only gives a more stable weighting but also provides better signal and background separation.

Training was performed by the ATLAS groups performing the Nominal WH analyses to determine the analysis variable weights to be used in the final discriminant. The variables used in the BDT are the following: Reconstructed W boson p_{T} ($p_{\mathrm{T}}(W)$); Missing transverse energy ($E_{\mathrm{T}}^{\mathrm{miss}}$); Reconstructed W transverse mass ($m_T(W)$); p_{T} of each of the two b-tagged jets ($p_{\mathrm{T}}(b-jet1)$, $p_{\mathrm{T}}(b-jet2)$); Di-b-jet mass (m_{bb}); Separation of the two b-jets ($\Delta R(bb)$); Angle between the reconstructed W and di-b-jet system ($\Delta\phi(W, bb)$); and the miniumum of the angles between the muon and each b-jet ($\min(\Delta\phi(\mu, b - jetx))$). These variables were used because they were found to have the best separation between signal and background or, in combination, to have powerful correlations.

The program TMVA [102] is used to construct a separate BDT for each signal region but with the different b-tagging classifications merged. The BDT ouput distributions for the $E_{\mathrm{T}}^{\mathrm{miss}}$ triggered analysis can be found in Section 7.8. The gain in statistics from the $E_{\mathrm{T}}^{\mathrm{miss}}$ triggered MVA analysis with respect to the Nominal analysis was shown previously in Section 7.6.

7.8 Prefit $E_{\mathrm{T}}^{\mathrm{miss}}$ triggered Regions

The prefit distributions of regions used in the $E_{\mathrm{T}}^{\mathrm{miss}}$ triggered cut-based analysis are shown in Figures 7.5 to 7.11 and for the MVA analysis in Figures 7.12 to 7.14. Each plot shows both the data, as points with error bars, and the prefit Monte Carlo, as stacked histograms. The prefit distributions contain the raw event yields with all calibrations applied but with no normalisations derived from fits applied. The statistical uncertainty on the data is represented by the error bars on the points and the total prefit statistical and systematic uncertainty on the Monte Carlo is represented by the shaded area. The expected Higgs signal is shown both stacked on top of the background histograms at the standard model expected cross section times branching ratio and unstacked as an unfilled red histogram. The unstacked signal is scaled by a factor shown in the legend, chosen separately in each region to ensure it is visible. Each plot contains, below the main axes, the ratio of the data yield to the prefit background plus signal expectation. The binning chosen for the di-b-jet invariant mass and BDT output distributions is explained in Chapter 8. Events falling beyond the upper bound of the final bin in the di-b-jet invariant mass or BDT output distributions are included in the final bin. The choice of analysis regions, in the context of the fit, is described in Section 8.2.

7.9 Summary

The $E_{\mathrm{T}}^{\mathrm{miss}}$ triggers have been used to recover events lost by the Nominal single lepton triggered $WH \to \ell\nu b\bar{b}$ analyses. Events are lost because the muon triggers never reach full efficiency. The recovered signal yield is approximately 8% of the total Nominal muon triggered signal yield (without considering electron triggered yield), but between 20% and 35% in the high $p_{\mathrm{T}}(W)$ regions in which the $E_{\mathrm{T}}^{\mathrm{miss}}$ triggered events are used. The recovered events are used in both a cut-based analysis and an MVA analysis and are split into the same regions as the Nominal analysis. The $E_{\mathrm{T}}^{\mathrm{miss}}$ triggered analyses are restricted to high $p_{\mathrm{T}}(W)$ events where the data can be

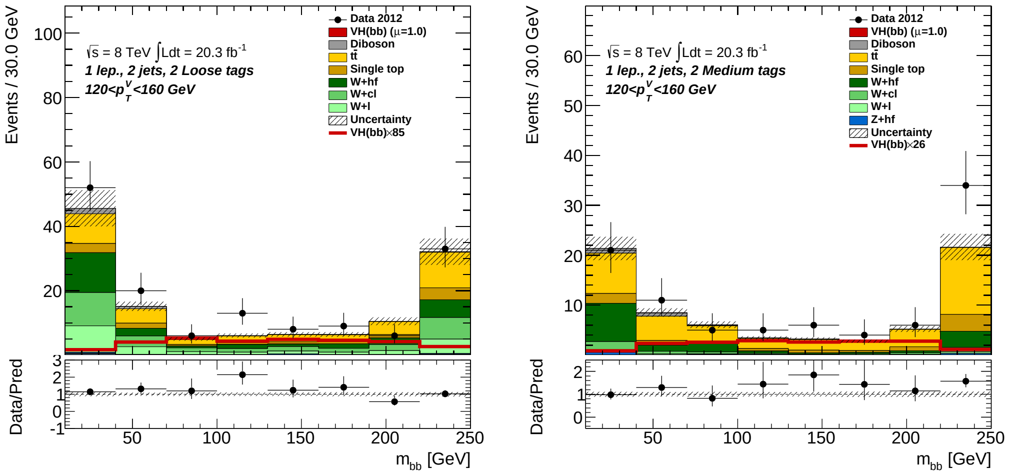

(a) 2 Loose Tags

(b) 2 Medium Tags

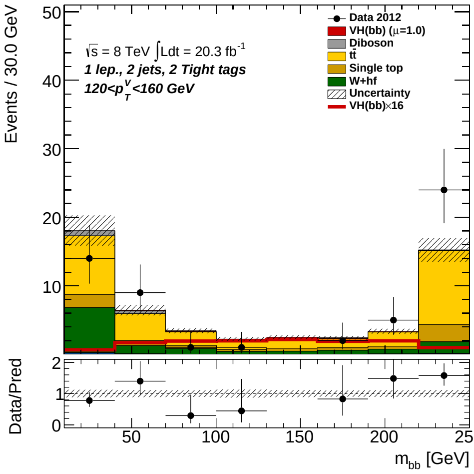

(c) 2 Tight Tags

Figure 7.5: Prefit distributions of the di-b-jet invariant mass, m_{bb}, in the cut-based $E_{\mathrm{T}}^{\mathrm{miss}}$ triggered 2-jet $p_{\mathrm{T}}(W) = 120 - 160$ GeV region, split into b-tagging categories. The data is shown as points with error bars and the prefit Monte Carlo background yield is shown as stacked histograms. The uncertainty on the total background yield is represented as a shaded area. The expected Higgs signal, from a sample at $m_H = 125$ GeV, is shown both stacked on top of the background histograms at the standard model expectation and un-stacked but scaled by the factor stated in the legend. The lower part of each plot shows the ratio of the data yield to the prefit background and signal prediction.

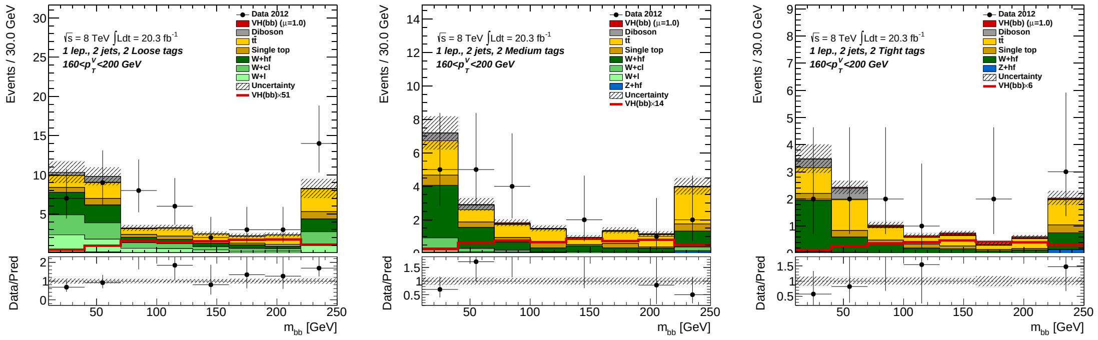

(a) 2 Loose Tags (b) 2 Medium Tags (c) 2 Tight Tags

Figure 7.6: Prefit distributions of di-b-jet invariant mass, m_{bb}, in the cut-based E_T^{miss} triggered 2-jet $p_T(W) = 160 - 200$ GeV region. Format is the same as Figure 7.5.

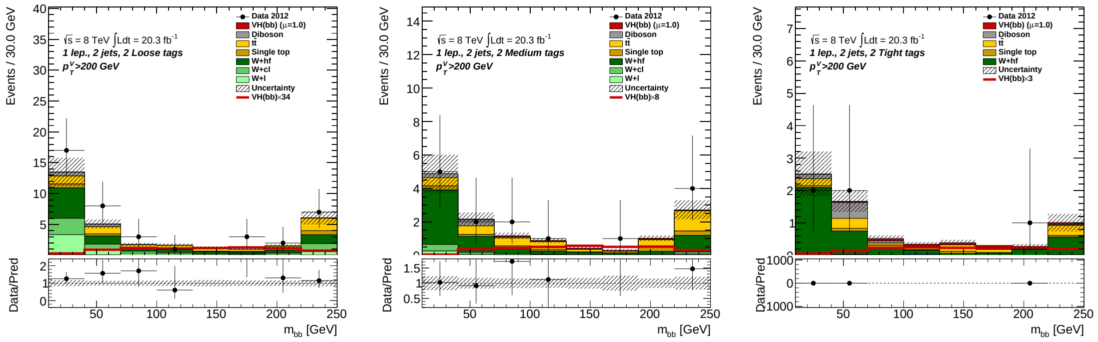

(a) 2 Loose Tags (b) 2 Medium Tags (c) 2 Tight Tags

Figure 7.7: Prefit distributions of di-b-jet invariant mass, m_{bb}, in the cut-based E_T^{miss} triggered 2-jet $p_T(W) > 200$ GeV region. Format is the same as Figure 7.5.

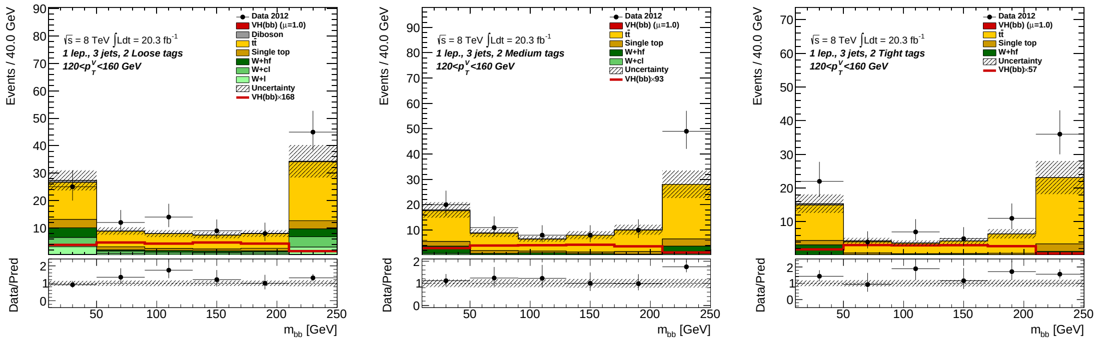

(a) 2 Loose Tags (b) 2 Medium Tags (c) 2 Tight Tags

Figure 7.8: Prefit distributions of di-b-jet invariant mass, m_{bb}, in the cut-based E_T^{miss} triggered 3-jet $p_T(W) = 120 - 160$ GeV region. Format is the same as Figure 7.5.

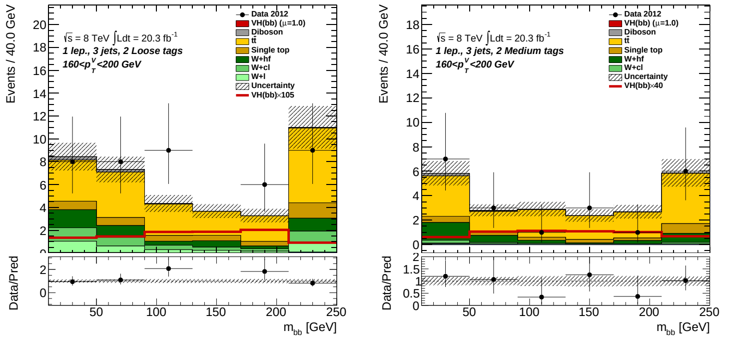

(a) 2 Loose Tags (b) 2 Medium Tags (c) 2 Tight Tags

Figure 7.9: Prefit distributions of dijet invariant mass, m_{bb}, in the cut-based $E_{\mathrm{T}}^{\mathrm{miss}}$ triggered 3-jet $p_{\mathrm{T}}(W) = 160 - 200$ GeV region. Format is the same as Figure 7.5.

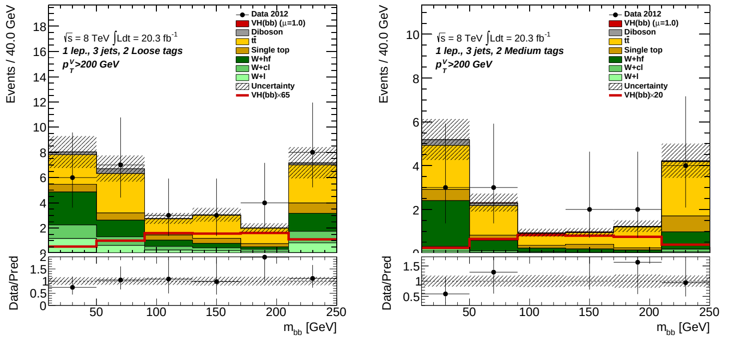

(a) 2 Loose Tags (b) 2 Medium Tags (c) 2 Tight Tags

Figure 7.10: Prefit distributions of dijet invariant mass, m_{bb}, in the cut-based $E_{\mathrm{T}}^{\mathrm{miss}}$ triggered 3-jet $p_{\mathrm{T}}(W) > 200$ GeV region. Format is the same as Figure 7.5.

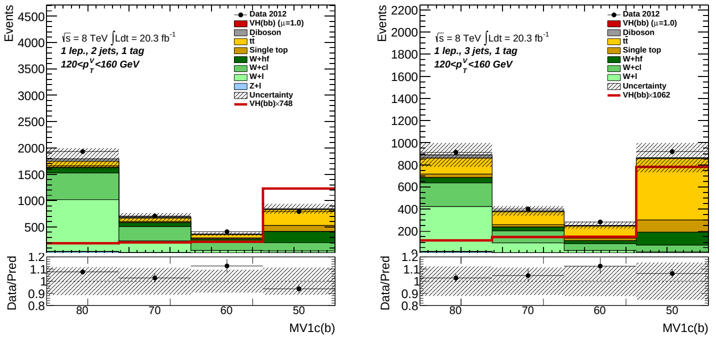

(a) 2 Jet (b) 3 Jet

Figure 7.11: Prefit distributions of the b-tagging weight, $MV1c$, in the cut-based $E_{\mathrm{T}}^{\mathrm{miss}}$ triggered 1-tag 2-jet and 3-jet $p_{\mathrm{T}}(W) > 120$ GeV region. Format is the same as Figure 7.5.

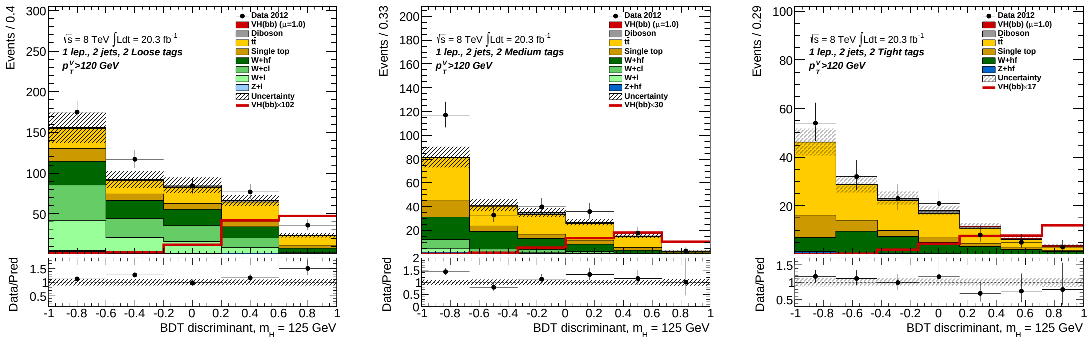

(a) 2 Loose Tags (b) 2 Medium Tags (c) 2 Tight Tags

Figure 7.12: Prefit distributions of BDT output in the MVA $E_{\mathrm{T}}^{\mathrm{miss}}$ triggered 2-jet $p_{\mathrm{T}}(W) > 120$ GeV region. Format is the same as Figure 7.5.

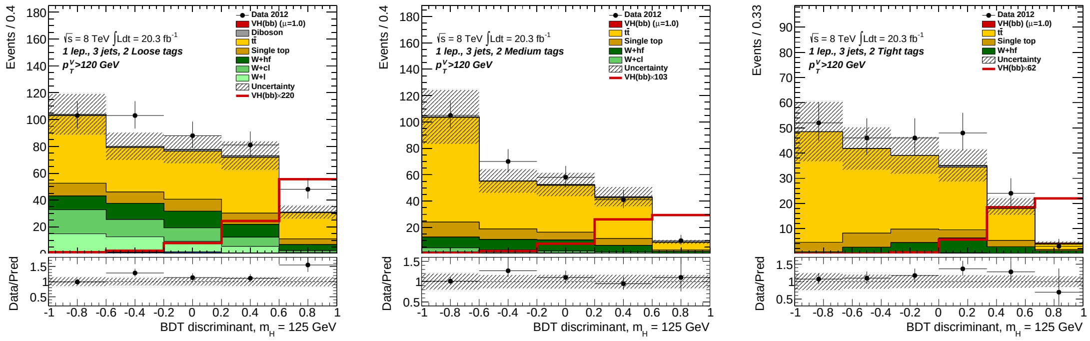

(a) 2 Loose Tags (b) 2 Medium Tags (c) 2 Tight Tags

Figure 7.13: Prefit distributions of BDT output in the MVA $E_{\mathrm{T}}^{\mathrm{miss}}$ triggered 3-jet $p_{\mathrm{T}}(W) > 120$ GeV region. Format is the same as Figure 7.5.

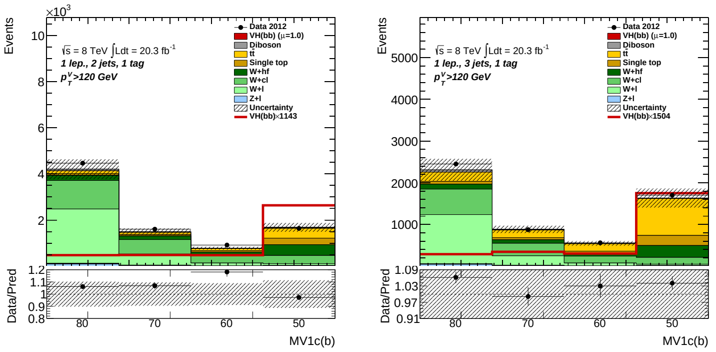

(a) 2 Jet (b) 3 Jet

Figure 7.14: Prefit distributions of the b-tagging weight, $MV1c$, in the MVA $E_{\mathrm{T}}^{\mathrm{miss}}$ triggered 1-tag 2-jet and 3-jet $p_{\mathrm{T}}(W) > 120$ GeV region. Format is the same as Figure 7.5.

modelled well and where the most significant regions are found, the regions with the highest signal-to-background ratio. Distributions of the di-b-jet invariant mass (in the cut-based analysis), BDT output (MVA analysis) and MV1c b-tag operating points have been produced for both the $E_{\mathrm{T}}^{\mathrm{miss}}$ triggered analyses, which can be found in Section 7.8, and merged with the Nominal regions produced by another WH analysis group to produce Combined regions. The fits applied to these analyses will be described in Chapter 8 and the results will be presented in Chapter 10. A study performed on the correlation of the different $VH, H \rightarrow b\bar{b}$ analyses will presented in Chapter 9.

CHAPTER 8

Statistical Fit Model

This chapter describes the fit used to extract the results for the $E_{\mathrm{T}}^{\mathrm{miss}}$ triggered and Combined WH analyses, that were described in Chapter 7. For the convenience of the reader, a glossary of selected terms is included below. These terms are important for the description of the fit model used for the WH analyses and the understanding of the results in Chapters 9 and 10. The regions and systematics used in the fits are covered in sections 8.2 and 8.3.

8.1 Glossary of Terms

- **Prefit**: The expected yield for each MC sample in each analysis bin. Yields are normalised to theoretical cross sections and the integrated luminosity of the dataset, but have not been directly normalised to the data or adjusted in any other way.

- **Postfit**: The expected yield after all normalisations from the fit have been taken into account. MC yields will be changed based on background normalisations and the signal strength, but data will remain the same as Prefit.

- **Nuisance Parameter, θ**: Parameters used in the fit to account for the different systematic uncertainties and normalisations. Each nuisance parameter is allowed to float in the fit, but is constrained by a Gaussian probability density in the case of a systematic uncertainty and by a log-normal probability density in the case of a normalisation.

- **Asimov dataset**: A pseudo-dataset created to be the most representative of all the possible real datasets that could be obtained. A fit to the Asimov dataset will yield the expected values for all parameter estimators. The yields are built from the nominal MC predictions. Fits to the Asimov dataset use values for the nuisance parameters that come from a background-only fit to the data (signal strength fixed at 0). A fit of the nominal MC templates to the Asimov dataset in which the signal strength is allowed to float can then be used to obtain values for the expected performance of the fits.

- **$\mathbf{CL}_S$**: A frequentist method of setting limits based on the ratio of the confidence level for the signal plus background hypothesis to the background-only hypothesis [103]. The CL_S method takes account of background fluctuations better than conventional confidence interval calculations and prevents this causing unphysical limits.

- **Pull**: The postfit central value and uncertainty of a nuisance parameter expressed as a shift from the prefit central value and as a fraction of the prefit uncertainty. A pull will show any shift from the prefit value of the parameter, suggesting a bias, or a changing in size of the error which suggests the uncertainty was over/under estimated. Pulls can come from either fits to the real dataset or to the Asimov dataset.

- **Prior**: A somewhat subjective assessment of the size of an uncertainty that does not have an experimental origin. Uncertainties of experimental origin can be propagated through the MC to obtain systematically shifted templates of the MC, but other uncertainties such as the uncertainty on the ratio between jet multiplicities have a prior placed on them which estimates the uncertainty of the parameter, based on previous studies on the regions and samples involved.

- **Signal Strength**, μ: Multiple of the Standard Model expected value for the cross section times branching ratio of the process being searched for/measured. The best fit value measured for the signal strength is labelled as $\hat{\mu}$. More details can be found in Chapter 2.
- **Parameter of Interest (PoI)**: A parameter of the fit that represents the end measurement and is not constrained or otherwise input to the fit as the nuisance parameters are. The $WH \rightarrow \ell\nu b\bar{b}$ signal strength is the parameter of interest in these fits so is allowed to float completely freely.
- **p-value,** p_0: The probability of a given value to be observed assuming that the null, background-only, hypothesis is true. This is interpreted as the probability for the background to fluctuate to produce the observed result with zero contribution from signal. If the probability is very low then there is good evidence to reject the background-only hypothesis and accept a signal plus background hypothesis.

The WH fit is implemented using the Roostats package [104], which implements the RooFit toolkit [105] for LHC analyses. A binned likelihood is constructed from Poisson probability terms representing each of the bins from the analysis regions, which will be detailed in Section 8.2, and considering all systematic uncertainties and normalisations, which will be described in Section 8.3. Separate likelihoods are constructed for each of the $E_{\mathrm{T}}^{\mathrm{miss}}$ triggered and Nominal analyses. The likelihood, $\mathcal{L}(\mu, \theta)$, is a function of the signal strength value, μ, and the values of the nuisance parameters, θ. The signal strength is allowed to float freely with no penalty on the likelihood, but any shift of the nuisance parameters from their prefit values incurs a penalty that increases the likelihood, $\mathcal{L}(\mu, \theta)$. Statistical uncertainties in each bin can be incorporated in the same way as other nuisance parameters. The likelihood is then used to define the test statistics, q_μ, such that:

$$q_\mu = -2\ln\frac{\mathcal{L}(\mu, \hat{\hat{\theta}}_\mu)}{\mathcal{L}(\hat{\mu}, \hat{\theta})}, \tag{8.1}$$

where $\hat{\hat{\theta}}_\mu$ are the values of θ, the nuisance parameters, that maximise the likelihood for that value of μ, while $\hat{\mu}$ and $\hat{\theta}$ are the best fit parameters that maximise the likelihood. The ability of the nuisance parameters to move in this way broadens the contour of the likelihood as a function of μ, providing less sensitivity to the best fit value of μ. A likelihood for the background-only hypothesis, q_0, can be constructed by fixing $\mu = 0$, which allows the nuisance parameters to find their best values in the absence of a signal. The test statistics corresponding to the signal plus background hypothesis, q_μ, and the background-only hypothesis, q_0, can be used to calculate confidence levels independently, but here they are used as a ratio, $fracq_\mu q_0$, to input to the CL_S calculation [106]. This allows a determination of whether the data observed can be described by the background alone or whether any difference observed is more signal-like. The CL_S method is used to calculate the upper limit, at 95% confidence level, for the signal strength as well as for p_0, described previously, and the observed value of $\hat{\mu}$. The 1σ and 2σ intervals of these results, which are also useful for interpreting the result, are calculated by shifting q_μ (Equation 8.1) by 1 and 2 units respectively, and recalculating $\hat{\mu}$ while keeping all other parameters fixed. A separate signal plus background likelihood, q_μ, must be constructed and the results calculated for each Higgs mass hypothesis in the analysis as the expected signal will be different. For the MVA, this could also mean different background expectations if the BDT trainings at each mass point were used. For the MVA analyses presented here, the $m_H = 125$ GeV training is used for all mass points for simplicity.

The observed results do not give any indication of how sensitive any individual fit is, due to statistical fluctuations that could occur in the data, and many of the observed results are not meaningful without a comparison to the expected results.

The expected results can be obtained by replacing the real dataset with the Asimov dataset, such that all nuisance parameters get their postfit values from a background-only fit to the real dataset, but the pseudo-data events are built from the nominal MC yield. The inclusion of normalisation nuisance parameters means that the Asimov dataset will be built with the background MC scaled by normalisations from real data, which should reflect better the statistics in data. Setting $\mu = 0$ in the Asimov dataset can be used to see how strict the limits on $\hat{\mu}$ can be set, while setting $\mu = 1$ in the Asimov, assuming a signal exists, will show the size of the expected fluctuation (an increased event yield) to the background that would be observed in data from a standard model signal. These are the results that will be presented in Chapter 10 to obtain the expected performance of the analyses and as a source of comparison for the observed results using the real dataset.

8.2 Fit Regions and Binning

The regions used in the WH analyses were briefly outlined in Section 7.5 but are described more completely here.

The $E_{\mathrm{T}}^{\mathrm{miss}}$ triggered analyses use only regions with $p_{\mathrm{T}}(W) > 120$ GeV, but the splitting is different between the cut-based and MVA analyses. The cut-based analysis further splits the $p_{\mathrm{T}}(W)$ range into three: 120 GeV $< p_{\mathrm{T}}(W) <$ 160 GeV, 160 GeV $< p_{\mathrm{T}}(W) <$ 200 GeV and $p_{\mathrm{T}}(W) >$ 200 GeV, while the MVA analysis uses the range inclusively. For events containing two b-tagged jets the cut-based analysis uses the final calibrated di-b-jet invariant mass distribution as input to the fit and the MVA analysis uses the BDT output distribution, as described in Section 7.7. For both analyses the $p_{\mathrm{T}}(W)$ region(s) are separated into 2-jet and 3-jet events and, within each jet multiplicity, into b-tagging categories based on the b-tags of the two jets as shown previously in Figure 7.1 (labelled as LL,MM,TT). This gives a total of 6 regions for each $p_{\mathrm{T}}(W)$ range. Both analyses also use the distribution of exclusive $MV1c$ b-tagging operating points (50,60,70 and 80%) of the tagged jet as an input to the fit. For single tagged events in the cut-based analysis, the 3 separate $p_{\mathrm{T}}(W)$ ranges are merged back into one that matches the categories in the MVA for consistency. In both analyses the $MV1c$ distributions are split into that for 2-jet events and that for 3-jet events. The $E_{\mathrm{T}}^{\mathrm{miss}}$ triggered cut-based fits therefore consist of 20 regions and the MVA fits consist of 8 regions. These regions were all shown in Section 7.8.

For the Combined analyses, the regions for $p_{\mathrm{T}}(W) > 120$ GeV are the same as in the $E_{\mathrm{T}}^{\mathrm{miss}}$ triggered analyses but additional regions are present for $p_{\mathrm{T}}(W) < 120$ GeV. The same jet multiplicity and b-tagging category splitting is used. The cut-based analysis splits the low $p_{\mathrm{T}}(W)$ range into two: 0 GeV $< p_{\mathrm{T}}(W) <$ 90 GeV and 90 GeV $< p_{\mathrm{T}}(W) <$ 120 GeV, in which the di-b-jet invariant mass distributions are fitted. The MVA analysis does not split the low $p_{\mathrm{T}}(W)$ range and uses the BDT output distribution. Both analyses use the $MV1c$ distributions in a single $p_{\mathrm{T}}(W)$ range ($p_{\mathrm{T}}(W) <$ 120 GeV), set up in the same way as for the $E_{\mathrm{T}}^{\mathrm{miss}}$ triggered analyses. The fit regions for the $E_{\mathrm{T}}^{\mathrm{miss}}$ triggered and Combined analyses are summarised in Table 8.1. The $p_{\mathrm{T}}(W)$ regions used are shown and whether the variable used in each region is the di-b-jet invariant mass ($m_{b\bar{b}}$), BDT output or distributions of $MV1c$ b-tagging operating points (50,60,70 and 80%).

	Cut-based					MVA	
$p_{\mathrm{T}}(W)$/ GeV	$0-90$	$90-120$	$120-160$	$160-200$	>200	<120	>120
$E_{\mathrm{T}}^{\mathrm{miss}}$ triggered							
1-tag	-		$MV1c$			-	$MV1c$
2-tag	-		$m_{b\bar{b}}$	$m_{b\bar{b}}$	$m_{b\bar{b}}$	-	BDT
Combined							
1-tag	$MV1c$		$MV1c$			$MV1c$	$MV1c$
2-tag	$m_{b\bar{b}}$	$m_{b\bar{b}}$	$m_{b\bar{b}}$	$m_{b\bar{b}}$	$m_{b\bar{b}}$	BDT	BDT

Table 8.1: Summary of the regions used in the $E_{\mathrm{T}}^{\mathrm{miss}}$ triggered and Combined cut-based and MVA analyses.

The $MV1c$ distributions are used in the fit in their original binning because there are only 4 bins in each of the original distributions and the statistics are high. The di-b-jet invariant mass and BDT output distributions contain a very large number of bins, to give flexibility for the fit, and so must be rebinned for fitting to reduce the bin-to-bin statistical variations and fit complexity. Rebinning is particularly important in the high $p_{\mathrm{T}}(W)$ regions and tight b-tagging categories, where the expected data yields are very low and the MC has statistical limitations. An algorithm is implemented in the fitting procedure that attempts to choose an optimal binning strategy for both sensitivity and fit efficiency, the time that the fits take to run [40].

The cut-based analysis di-b-jet invariant mass distribution is rebinned based on a figure of merit that is proportional to the fraction of total expected signal events and the fraction of total expected background events in a candidate merged bin. The figure of merit for the MVA BDT output distribution bin merging is proportional to the fraction of total expected background events in the candidate merged bin and the statistical significance of the bins that will be merged. For both analyses an additional constraint is imposed that the statistical uncertainty in the background prediction cannot go above 10% in any bin.

The optimisation of the binning by an algorithm in the fit will most likely result in variable bin sizing in the final distributions. Roostats is only able to accommodate fixed bin sizes and so is unable to use the output of the binning optimisation algorithm. The binning chosen by the algorithm is therefore mapped into constant width bins. The BDT output value is not a physical observable so this causes no problems in interpretation but the di-b-jet invariant mass distributions would need to be remapped to physically understand the contents of each bin. The binning structure determined by the algorithm is used in both the prefit plots in Chapter 7 and for the postfit plots in Chapter 10, as well as the appendices described in each.

8.3 Systematics

A large number of systematic uncertainties are considered for the WH analyses, which come from a mixture of theoretical predictions, experimental uncertainties in the ATLAS recommended calibrations for identification and reconstruction; and corrections for different MC samples (to match data distributions) derived by the ATLAS VH search group. The sources of these uncertainties for the $E_{\mathrm{T}}^{\mathrm{miss}}$ triggered analyses are very briefly outlined here and referenced where appropriate but a more complete description can be found in [40]. The names used within the fit for the systematics are in brackets and different type face as follows: (`SystematicName`). The majority of systematics used affect only the normalisation of the distributions used in the fit but some affect the shape of the distributions and these will be noted in the description of those systematics. The following uncertainties are of experimental origin:

- The total integrated luminosity of the dataset used has an uncertainty of ±2.8% (`Lumi`) as described in Section 4.6 [65] and the distribution of the number of additional pileup interactions has an uncertainty of ±3.7% (`MuScale`).
- Corrections applied to the lepton isolation requirements (`LepIso`) as described in Section 7.3.
- The efficiency of muon reconstruction (`MuonEffic`) [89], as well as muon energy calibration components from the Inner Detector (`MuonEResolID`) and Muon Spectrometer (`MuonEResolMS`) [107].
- The efficiency of electron reconstruction (`ElecEffic`), energy resolution (`ElecEResol`) and absolute energy scale (`ElecE`) [90], which affect the number of events vetoed in the $E_{\mathrm{T}}^{\mathrm{miss}}$ triggered analyses.
- Calibrations covering the absolute Jet Energy Scale (JES)(`JetNP1-6`), JES η dependence (`JetEtaModel` and `JetEtaStat`), differences between the full AT-

LAS simulation and the ATLFastII simulation as described in Section 7.2 (`JetNonClos`), JES dependence on the number of additional pileup interactions (`JetMu`) and reconstructed primary vertices (`JetNPV`), the contribution of pileup to a jet's p_{T} (`JetPilePt`) and the average energy density in the event (`JetPileRho`) from these additional interactions. Additional jet flavour based uncertainties are included to cover the differences for JES in b-jet response (`JetFlavB`) and the contribution from soft muons and neutrinos in b-decays (`JetBE`), the unknown mixture of light jets and gluon jets in different sample types (`JetFlavComp_Top`, `JetFlavComp_Wjets`, `JetFlavComp_Zjets` and `JetFlavComp_VHVV`), and differences in light jet and gluon jet JES response (`JetFlavResp_Top`, `JetFlavResp_Wjets`, `JetFlavResp_Zjets` and `JetFlavResp_VHVV`) [108].

- The energy resolution of jets (`JetEResol`) [109], with an additional contribution for the resolution of b-jets (`BJetReso`) [97].
- Efficiency of jets passing the JVF selection (`JetJVF`) as described in Section 7.3 [95].
- Modelling of the b-tagging efficiency (described in Section 7.5 for truth matched b-jets (`BTagB0Effic - BTagB9Effic`), truth matched c-jets (`BTagC0Effic - BTagC14Effic`) and light jets (`BTagL0Effic - BTagL9Effic`). Uncertainties are included to cover the differences observed in b-tagging efficiencies between samples produced with different MC samples (`BTagBSherpa`, `BTagBPythia8`, `BTagCSherpa` & `BTagCPythia8`) and an additional dependence observed for close together truth matched c-jets (`BTagTruthTagDR`) [98, 99].
- Calibration of calorimeter cluster energy summing for $E_{\mathrm{T}}^{\mathrm{miss}}$ absolute scale (`METScaleSoftTerms`) and resolution (`METResoSoftTerms`) [96].
- Modelling of the $E_{\mathrm{T}}^{\mathrm{miss}}$ trigger turn-on based on the choice of MC used (`METTrigZ`) and the statistics in the turn-on region (`METTrigStat`) [40]. These uncertainties only affect the turn-on region (described in Section 7.6) so are

not expected to have a sizeable impact on the WH analyses that use only highly boosted events.

The absolute normalisations of cross sections for the $t\bar{t}$ (`norm_ttbar`), W+2 b-jets (`norm_Wbb`) and W+c-jet+light-jet (`norm_Wcl`) samples are included in the fit as normalisations with log-normal probability densities, rather than being included as uncertainties, to constrain the normalisation to be positive and physical. The normalisation is defined as a multiple of the prefit expectation determined by the fit and therefore represents the scaling between the prefit and postfit yields. Additional normalisation-based uncertainties are included for the $t\bar{t}$ and $W/Z+jets$ samples in the fit but are implemented as normalisation ratios constrained by Gaussian probability densities. Some of these nuisance parameters are decorrelated between the low and high $p_{\mathrm{T}}(W)$ regions, jet multiplicities or jet flavour combinations, which effectively increases the total number of nuisance parameters.

Priors are placed on these additional normalisation ratio uncertainties based on MC expectations and studies of these backgrounds and regions made by the ATLAS VH analysis groups. The set of additional normalisation ratio uncertainties is chosen such that their products and sums constrain all regions in the $t\bar{t}$ and V+jets flavour combinations. For the $t\bar{t}$ background an additional ratio between the normalisation of 2-jet and 3-jet multiplicities is included (`ttbarNorm_J3`). The Combined fits include an additional ratio between the $p_{\mathrm{T}}(W) < 120$ GeV and $p_{\mathrm{T}}(W) > 120$ GeV regions (`ttbarHighPtV`) that is not needed for the $E_{\mathrm{T}}^{\mathrm{miss}}$ triggered fits as only the high $p_{\mathrm{T}}(W)$ regions are included. For the V+jets background (where $V = W$ or Z) additional ratios are included between the the normalisations of the different di-jet flavours: V+2 c-jets and V+2 b-jets (`VccVbbRatio`), V+b-jet+light-jet and V+2 b-jets (`VblVbbRatio`) and V+b-jet+light-jet and V+b-jet+c-jet (`VblVbcRatio`). The normalisation of the yield of V+2 light-jets (`VlNorm`) is included as a standard uncertainty with a prior rather than as a normalisation. Additional uncertainties, with priors, are included for the ratio between the rates of the 2-jet and 3-jet multiplicities in V+2 b-jets (`VbbNorm_J3`), V+c-jet+light-jet (`VclNorm_J3`) and V+2 light-jets (`VlNorm_J3`). These systematic uncertainties must have priors placed on them, rather than having direct template-based variations from MC analysis, because these systematics do not come from calibrations but are, instead, designed to account for differences in the predicted p_{T} spectra and jet flavour distributions. The priors are estimates of the maximum discrepancy expected in the ratio and are based on studies performed within the ATLAS VH group.

Nuisance parameters that only apply to specific MC samples are outlined below. The sources of these are a mixture of theoretical calculations, differences observed between MC predictions and corrections applied due to mis-modelling observed in the comparison of the MC prediction with the data.

- Signal: The calculation of the Higgs cross sections and branching ratios depend on a large number of indirect constraints and theoretical predictions. The $H \rightarrow b\bar{b}$ branching ratio has an m_H-dependent value and uncertainty (`TheoryBRbb`) as shown in Table 7.2 [83]. The production of VH via the processes $qq \rightarrow VH$ and $gg \rightarrow ZH$, which contaminates the WH analyses and is therefore treated as signal, are calculated separately and have separate uncertainties. The visible cross section relies on the QCD renormalisation scale (`TheoryQCDscale_ggZH` and `TheoryQCDscale_qqVH`), which covers the uncertainty in determining the renormalisation scale to account for missing higher orders in the calculation, and its impact on the $p_{\mathrm{T}}(V)$ spectra (`TheoryVPtQCD_ggZH` and `TheoryVPtQCD_qqVH`) which have shape components, the PDF sets (`TheoryPDF_ggZH` and `TheoryPDF_qqVH`) and impact on the acceptance (`TheoryAccPDF_ggZH` and `TheoryAccPDF_qqVH`). There is also an effect from the acceptance across different jet multiplicites (`TheoryAcc_J2_ggZH`, `TheoryAcc_J2_qqVH`, `TheoryAcc_J3_ggZH` and `TheoryAcc_J3_qqVH`), and the NNLO contribution to the $p_{\mathrm{T}}(V)$ spectra (`TheoryVHPt`) which has a shape component [40].

- V+jets where $V = W$ or Z: Reweighting for mis-modelling in the ϕ angle between the two jets (`VDPhi`), the $p_{\mathrm{T}}(V)$ spectra (`VPtV`) and di-jet invariant mass (`VMbb`) that are derived in phase space regions designed to isolate these samples and which have shape components [40].

- $t\bar{t}$: Reweighting of the $p_{\mathrm{T}}(t)$ spectra to match that measured in data by a previous ATLAS analysis (`TopPt`) which has a shape component [110] and MC generator variations in the shapes of the di-b-jet invariant mass (`TtbarMBBCont`) which has only a shape component and $E_{\mathrm{T}}^{\mathrm{miss}}$(`TtbarMetCont`) which has a shape component.

- Single Top: Theoretical predictions for production cross sections (`stopsNorm`, `stoptNorm` & `stopWtNorm`) [111] and normalisation differences observed in different regions, and parton showering of different MC generators (`SChanAcerMC`, `SChanAcerMCPS`, `TChanPtB2`, `WtChanAcerMC` and `WtChanPythiaHerwig`). The last two have a shape component.

- Diboson: Perturbative corrections to the cross section (`VVJetScalePtST1`, `VVJetScalePtST2`) which have a shape component, PDF and α_S variations (`VVJetPDFAlphaPt`) and the di-b-jet invariant mass measured using different MC generators in the three diboson channels (`VVMbb_WW`, `VVMbb_WZ` & `VVMbb_ZZ`) which vary only the shape and have no normalisation component.

- Modelling of the normalisation of the muon multijet estimate (`SysMJMuNorm`) and the affect of track isolation in producing the multijet muon templates (`SysMJMuTrkIso`). Additional multijet systematics are used in the Nominal analysis to account for the modelling of the multijet estimate for electrons (`SysMJElNorm`, `SysMJElTrkIso` and `SysMJElCaloIso`) and the reweighting applied only for multijet electron events (`SysMJDR` and `SysMJPtV`). Of these systematics, all but `SysMJMuNorm` and `SysMJElNorm` have a shape variation component.

As has just been described, there are a huge number of nuisance parameters in each analysis fit. Coupled with the large number of regions, and therefore bins, this leads to very long fit times, as each bin's expectation for each sample must be varied by each nuisance parameter. Additionally, many of the samples contain very low MC statistics in some regions so systematic variations become susceptible to "noise". To improve fit times and reduce artifacts caused by low MC statistics, the systematics are "smoothed" and "pruned" before the fit.

The smoothing is used for systematics that can effect the shape of a sample's distribution rather than just the normalisation, for example, the $E_{\mathrm{T}}^{\mathrm{miss}}$ calibration. In these systematics, small statistics can cause disproportionally large bin-to-bin migrations that bring with them large instabilities in the fit. For these systematics, the systematically shifted templates for each sample are smoothed by merging bins together until all bins in the template have a statistical error of below 5% for the given sample.

Pruning removes from the fit those nuisance parameters that do not significantly contribute to the pulls of the other nuisance parameters or the parameter of interest. Normalisation-based nuisance parameters are pruned if the total difference in the yield between the nominal and shifted expectations of a particular sample type is below 0.5%. For nuisance parameters that vary only the shape and not the normalisation of the distribution, the condition is changed to require that the difference in each bin is below 0.5% for the nuisance parameter to be pruned. If the signal expectation in a particular region is less than 2% of the background expectation, then nuisance parameters are pruned for all samples wthat are also less than 2% of the total background expectation and for which the nuisance parameter changes the total background expectation by less than 0.5%.

8.4 Nuisance Parameter Pulls & Ranking

A good way to understand the behaviour of the nuisance parameters in the likelihood is to compare the pulls in the real dataset and those from the Asimov dataset. There should be a very high degree of similarity because the signal is small compared to the background expectation and so the background should determine the values of the nuisance parameters. As described at the start of this Chapter, the Asimov dataset is constructed from the Nominal background MC yield. The MC can then be fitted to the Asimov dataset with all nuisance parameters initialised to their best fit values from a background-only fit to data. The fit to data may shift some of the pulls of nuisance parameters by a considerable amount, providing evidence that the background was wrongly modelled. Changes in the uncertainty of the parameter from the prefit $\pm 1\sigma$ values suggest that the size of the nuisance parameter was wrongly estimated. The fit to the Asimov dataset can shift the nuisance parameters, but the starting values are the data best fit values so well behaved nuisance parameters should remain unshifted with central values of 1 for normalisations and 0 for other nuisance parameters. The size of the uncertainties should not change relative to the best fit values from data.

Comparisons between the data fit and the Asimov fit are shown in Figure 8.1 for the cut-based $E_{\mathrm{T}}^{\mathrm{miss}}$ triggered analysis and in Figure 8.2 for the MVA $E_{\mathrm{T}}^{\mathrm{miss}}$ triggered analysis. The pulls are grouped based on the source of the uncertainty. The best fit pulls from data are shown as black points and bars while the pulls from the Asimov dataset are shown as red points and bars. In each case the point shows the central value of the nuisance parameter relative to its prefit value and the length of the bar shows the size of the uncertainty compared to the prefit value as indicated by the $\pm 1\sigma$ green band and $\pm 2\sigma$ yellow band. The pull values for the Asimov dataset are relative to the values of the nuisance parameters after the background-only fit to the real dataset, rather than the prefit values, which is why the majority of the Asimov pulls stay at 0 (1 for normalisations). This is a sign of good behaviour of the individual nuisance parameters and stability of the fit.

An additional comparison of the nuisance parameter values from a fit to data between the cut-based and MVA $E_{\mathrm{T}}^{\mathrm{miss}}$ triggered analyses is shown in Figure 8.3. This takes the black points and bars from Figures 8.1 and 8.2, with the MVA data values kept black and the cut-based data values changed to red. For some nuisance parameters only one of the two analyses is present because the other has been completely pruned following the procedure described in Section 8.3. Several theory based nuisance parameters are completely pruned from the cut-based analysis because the lower signal to background ratio in the signal regions prevents any sensitivity to, or constraint of, these nuisance parameters. The nuisance parameters pruned from the MVA fit are mostly those applied to Z+jets. For both analyses all nuisance parameters originating from lepton $E_{\mathrm{T}}^{\mathrm{miss}}$ trigger calibrations are completely pruned as the $E_{\mathrm{T}}^{\mathrm{miss}}$ triggered analyses only use events that are beyond the turn-on of the variables these relate to. The values for the absolute normalisations of the cross sections for $t\bar{t}$, W+2 b-jets and W+c-jet+light-jet samples are shown in Table 8.2 for both the cut-based and the MVA fit.

Normalisation	Cut-based	MVA
$t\bar{t}$	1.27 ± 0.20	1.37 ± 0.30
W+2 b-jets	0.52 ± 0.27	0.73 ± 0.27
W+c-jet+light-jet	1.24 ± 0.22	1.23 ± 0.17

Table 8.2: Absolute normalisations for backgrounds in the $E_{\mathrm{T}}^{\mathrm{miss}}$ triggered fits.

The nuisance parameters wthat were found to have the largest pulls or sizeable differences between the cut-based and MVA fit values were investigated within the ATLAS VH search group to ensure that the reason was understood. No problems, dramatical shifts or bias, were found with any of the nuisance parameters or fit setup.

The size and shift of the nuisance parameters do not show how big the shift in the value of $\hat{\mu}$ observed could be because of one of these parameters. To understand this a different procedure must be used, termed “Nuisance Parameter Ranking”. Here, this test is performed only on data, not using the Asimov dataset. The best

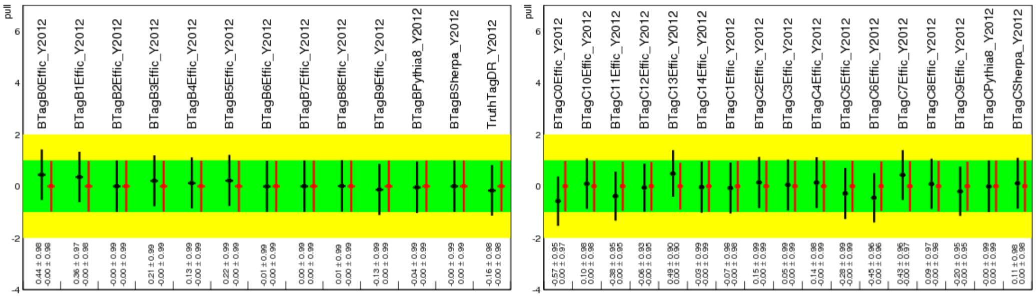

(a) b-tagging b-jets (b) b-tagging c-jets

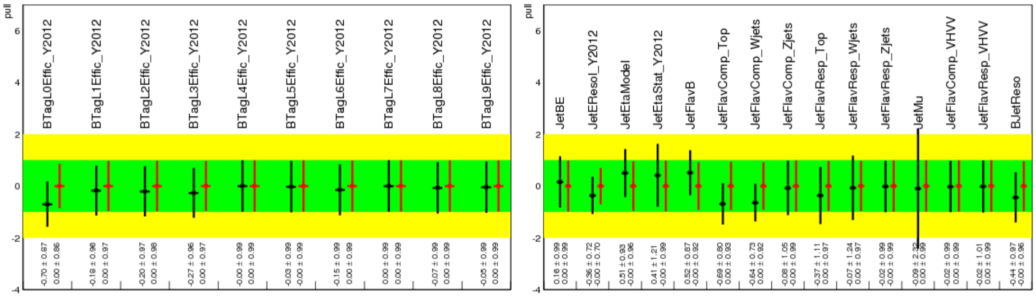

(c) b-tagging light-jets (d) Jet Energy Scale

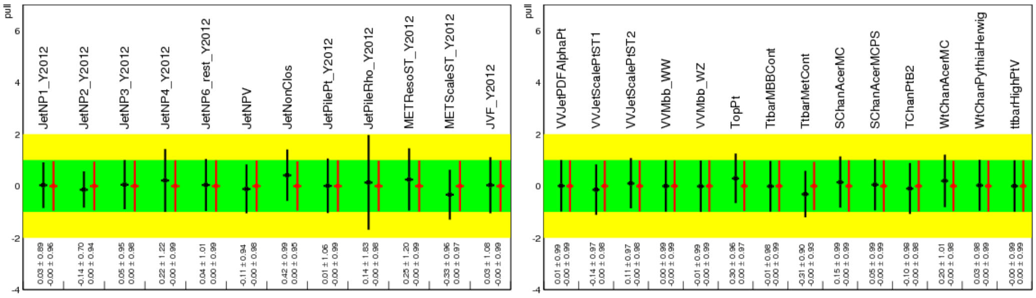

(e) Jet Energy Scale (f) $t\bar{t}$,Single t,VV Modelling

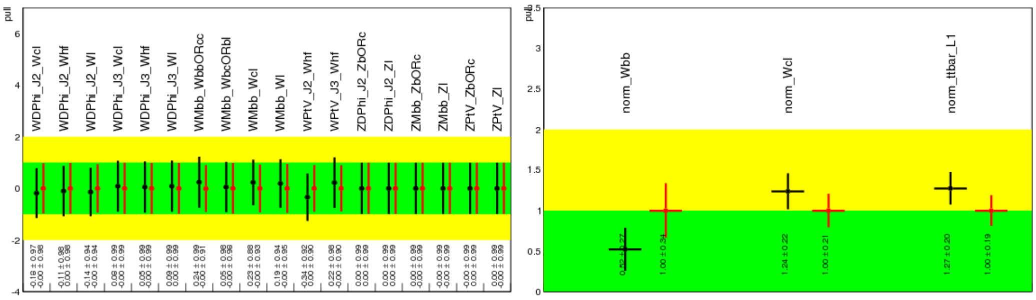

(g) W/Z+jets Modelling (h) W+jets,$t\bar{t}$ Normalisation

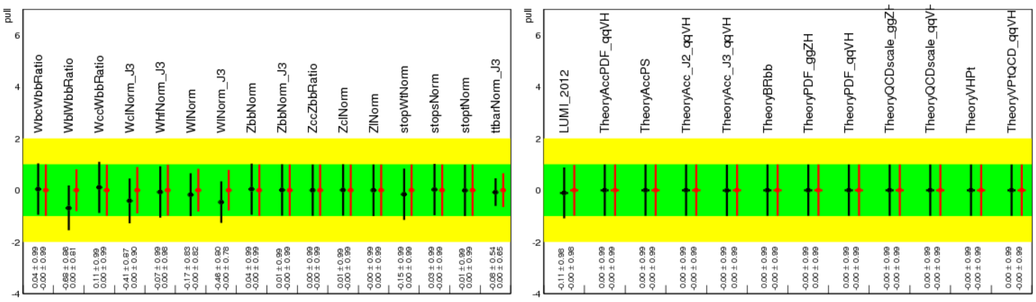

(i) Normalisation Ratios (j) Luminosity and Theory

Figure 8.1: Comparison of nuisance parameters in data (black) and Asimov (red) fits from the cut-based $E_{\mathrm{T}}^{\mathrm{miss}}$ triggered analysis. Each point and line represents the postfit pull central value and uncertainty of a particular nuisance parameter. The green and yellow bands represent the 1σ and 2σ prefit errors on the uncertainty.

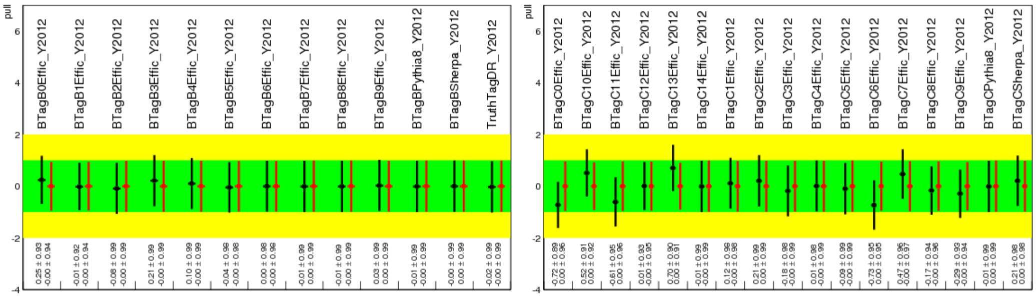

(a) b-tagging b-jets (b) b-tagging c-jets

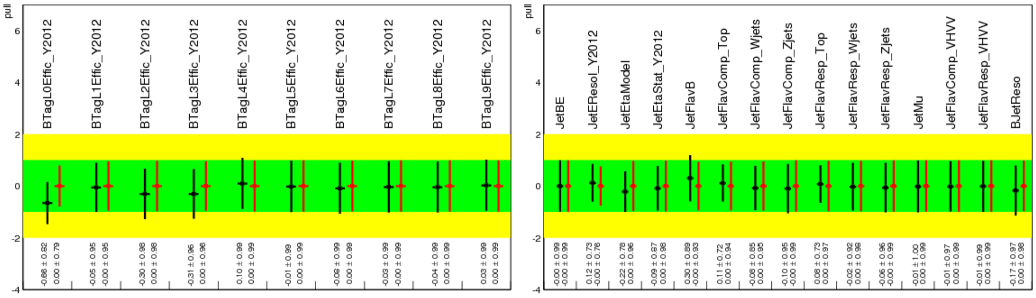

(c) b-tagging light-jets (d) Jet Energy Scale

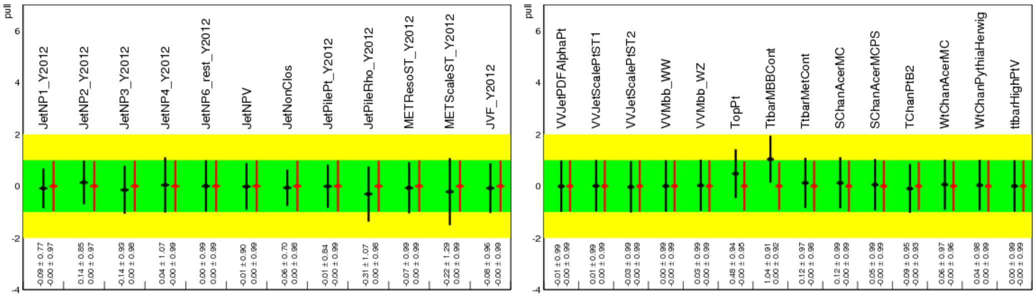

(e) Jet Energy Scale (f) $t\bar{t}$,Single t,VV Modelling

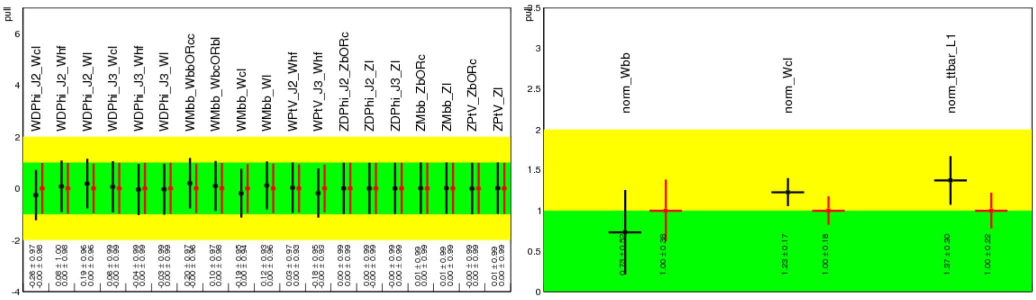

(g) W/Z+jets Modelling (h) W+jets,$t\bar{t}$ Normalisation

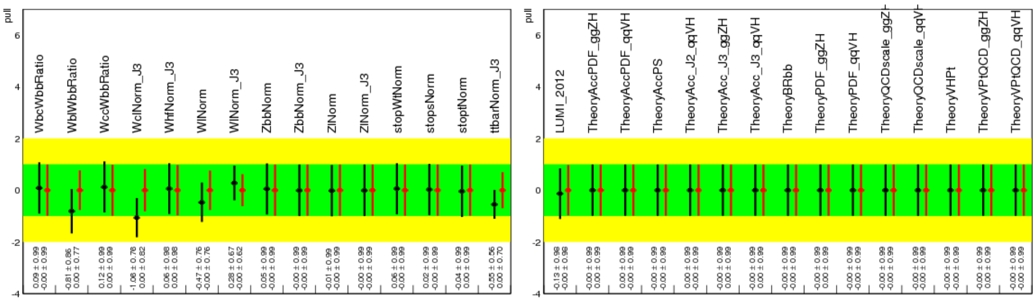

(i) Normalisation Ratios (j) Luminosity and Theory

Figure 8.2: Comparison of nuisance parameters in data (black) and Asimov (red) fits from the MVA $E_{\mathrm{T}}^{\mathrm{miss}}$ triggered analysis. Each point and line represents the postfit pull central value and uncertainty of a particular nuisance parameter. The green and yellow bands represent the 1σ and 2σ prefit errors on the uncertainty.

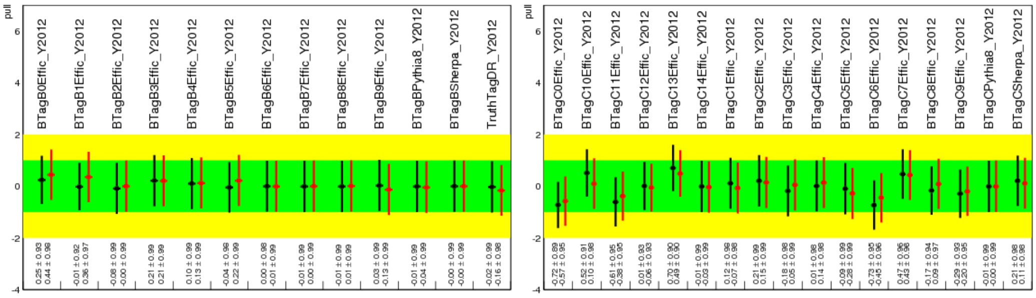

(a) b-tagging b-jets (b) b-tagging c-jets

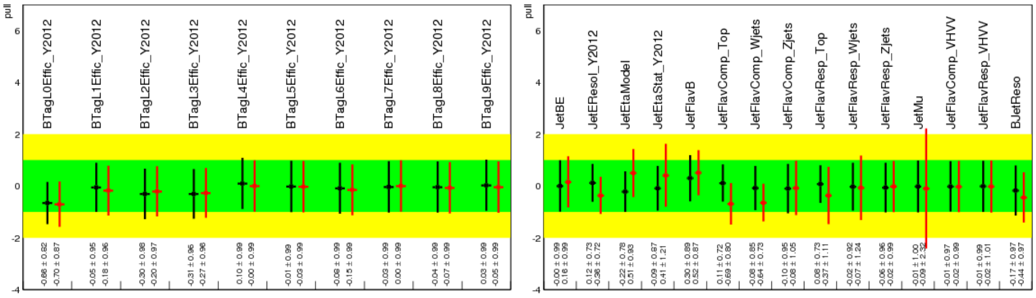

(c) b-tagging light-jets (d) Jet Energy Scale

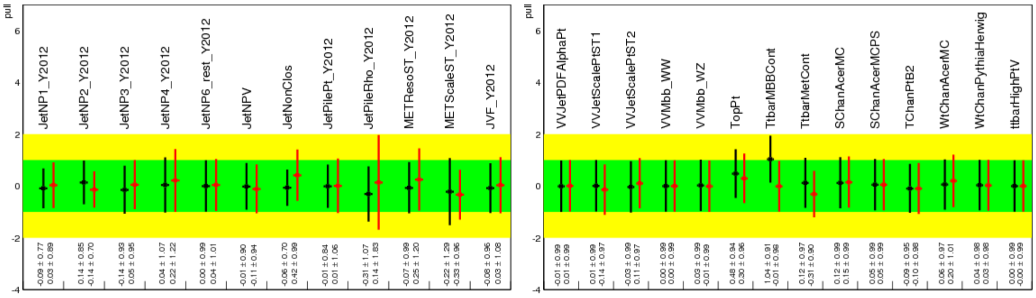

(e) Jet Energy Scale (f) $t\bar{t}$,Single t,VV Modelling

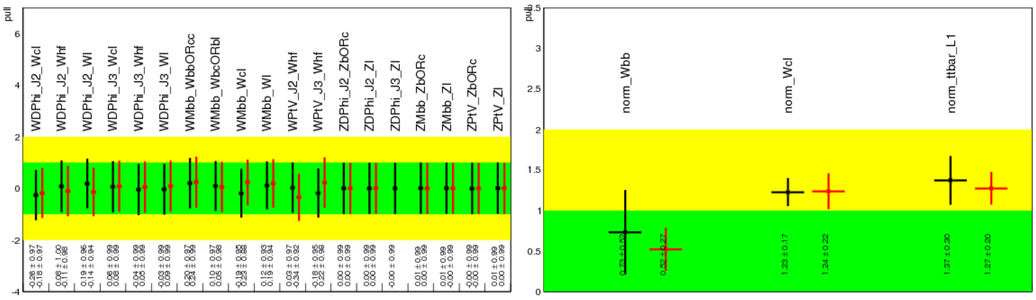

(g) W/Z+jets Modelling (h) W+jets,$t\bar{t}$ Normalisation

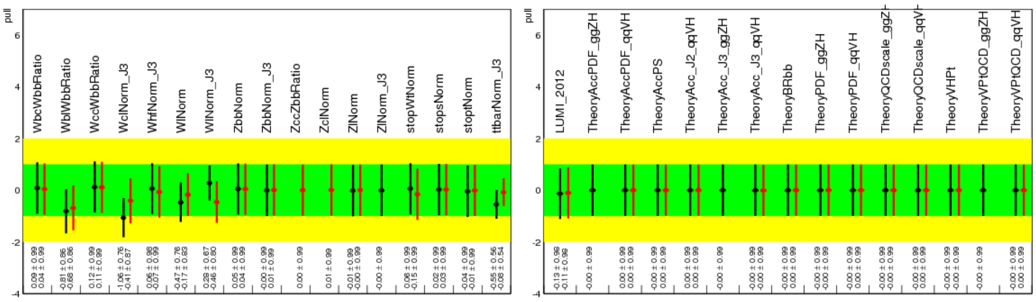

(i) Normalisation Ratios (j) Luminosity and Theory

Figure 8.3: Comparison of nuisance parameters in fits of the cut-based (red points) and MVA (black points) $E_{\mathrm{T}}^{\mathrm{miss}}$ triggered analyses. Each point and line represents the postfit pull central value and uncertainty of a particular nuisance parameter. The green and yellow bands represent the 1σ and 2σ prefit errors on the uncertainty.

fit values of each of the nuisance parameters are first obtained through a fit to data and the value of $\hat{\mu}$ is then found using the CL_S method. Each nuisance parameter is then shifted up and down by its associated error with all other nuisance parameters fixed. From this the likelihood can be maximised and a new value of $\hat{\mu}$ calculated from both the upward and downward shift. The nuisance parameters that show the largest fractional shift in $\hat{\mu}$ are ranked highest.

The ranking for the top 15 nuisance parameters in the $E_{\mathrm{T}}^{\mathrm{miss}}$ triggered analyses can be found in Figure 8.4 and for the Combined analyses in Figure 8.5. The description of the contents of the plots can be found in the captions. The ranking plots for the Nominal analyses can be found in Appendix B. It is predominantly the $W+$ heavy flavour jet normalisations and the nuisance parameters that are normalisation ratios that rank highly in the $E_{\mathrm{T}}^{\mathrm{miss}}$ triggered and Combined analyses. This is to be expected as, along with $t\bar{t}$, this is one of the biggest backgrounds, but in contrast to $t\bar{t}$, it has large uncertainties due to the lack of a clear control region in data. In the $E_{\mathrm{T}}^{\mathrm{miss}}$ triggered cut-based analysis the highest ranked nuisance parameter is the absolute normalisation of the yield of W+2 b-jets (`norm_Wbb`) and in the MVA analysis it is the normalisation ratio of W+b-jet+light-jet to W+2 b-jets (`WblWbbRatio`) that is ranked highest. For the Combined analyses it is the W+2 b-jets/W+2 c-jets di-jet invariant mass shape for $p_{\mathrm{T}}(W) > 120$ GeV (`VMbb`) and the absolute W+2 b-jets normalisation (`norm_Wbb`) wthat are ranked highest for the cut-based and MVA respectively. The ranking for the Combined analyses is similar to the ranking for the Nominal analyses, which can be found in Appendix B. As previously mentioned, some nuisance parameters are decorrelated in different $p_{\mathrm{T}}(W)$ regions and different jet flavours, which is why individual nuisance parameters can appear multiple times in the ranking. For these nuisance parameters, the regions which the ranking comes from is included in the name.

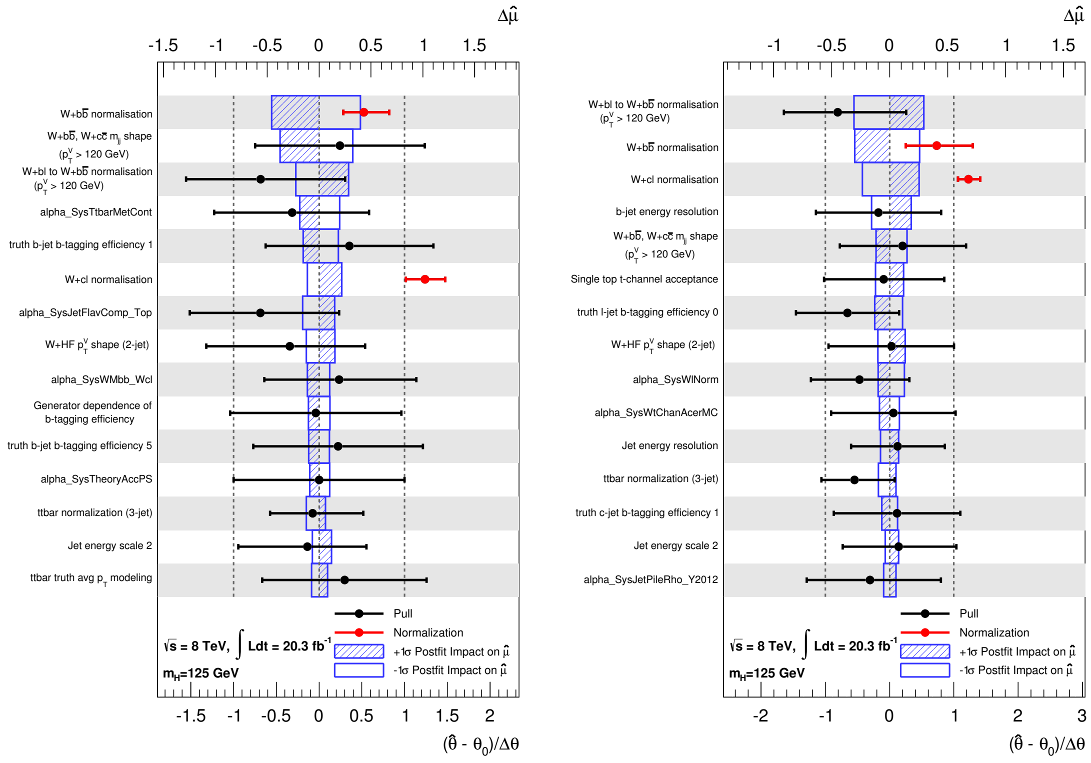

(a) Cut-based

(b) MVA

Figure 8.4: Ranking of systematics and normalisations based upon their impact on the fitted $\hat{\mu}$ value for the $E_{\mathrm{T}}^{\mathrm{miss}}$ triggered cut-based and MVA analyses. The 15 highest ranking nuisance parameters are shown in each case. The bottom x axis and the points show the relative shift of the postfit values of the nuisance parameters, $(\hat{\theta}-\theta_0)/\Delta\theta$, in terms of the postfit value, $\hat{\theta}$, prefit value, θ_0, and the prefit 1σ uncertainty on the nuisance parameter, $\Delta\theta$. The error bars on the points indicate the postfit uncertainty in terms of the relative shift. The top x axis and boxes show the shift in the fitted $\hat{\mu}$ value when the nuisance parameter is fixed to its postfit value shifted up and down by the corresponding uncertainty. The shaded part of the box corresponds to $\hat{\theta} + \Delta\theta$ while the unshaded corresponds to $\hat{\theta} - \Delta\theta$.

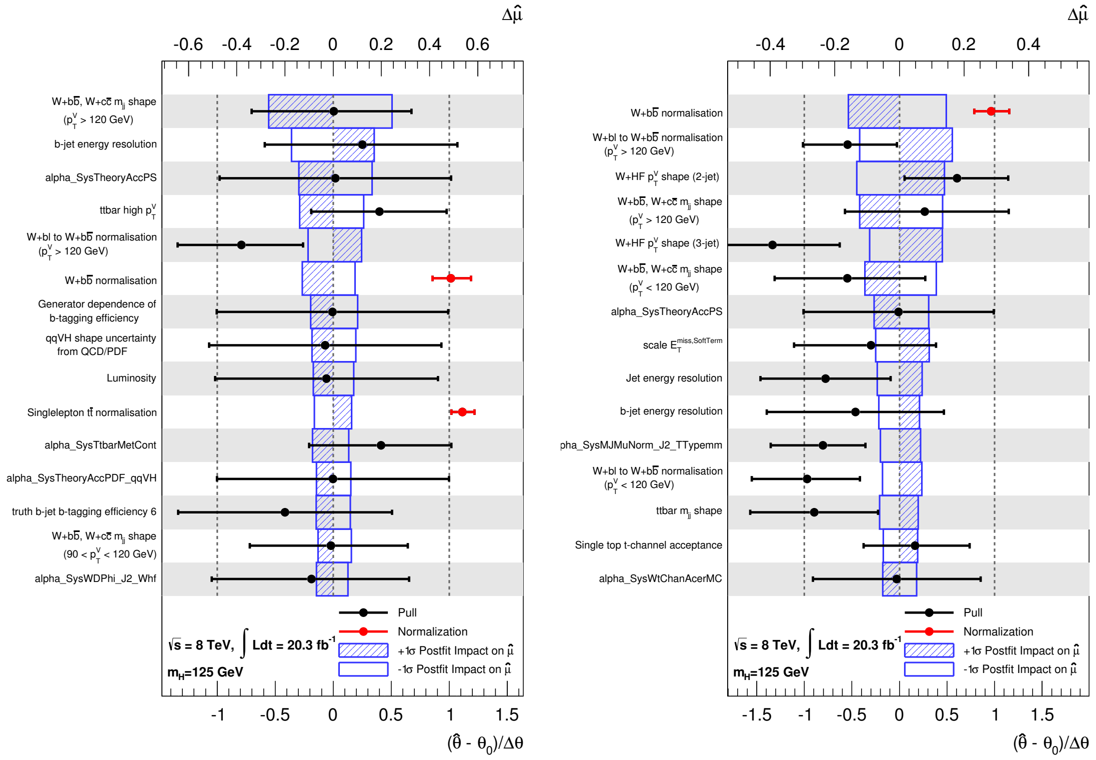

(a) Cut-based

(b) MVA

Figure 8.5: Ranking of systematics and normalisations based upon their impact on the fitted $\hat{\mu}$ value for the Combined cut-based and MVA analyses. The 15 highest ranking nuisance parameters are shown in each case. The bottom x axis and the points show the relative shift of postfit values of the nuisance parameters, $^{(\hat{\theta}-\theta_0)}/_{\Delta\theta}$, in terms of the postfit value, $\hat{\theta}$, prefit value, θ_0, and prefit 1σ uncertainty on the nuisance parameter, $\Delta\theta$. The error bars on the points indicate the postfit uncertainty in terms of the relative shift. The top x axis and the boxes show the shift in the fitted $\hat{\mu}$ value when the nuisance parameter is fixed to its postfit value shifted up and down by the corresponding uncertainty. The shaded part of the box corresponds to $\hat{\theta} + \Delta\theta$ while the unshaded corresponds to $\hat{\theta} - \Delta\theta$.

8.5 Summary

The fits used to extract results for the signal strength, $\hat{\mu}$, from the $WH \to \ell\nu b\bar{b}$ $E_{\mathrm{T}}^{\mathrm{miss}}$ triggered and Combined analyses have been described. The fit regions and binning in the cut-based and MVA analyses have been designed to exploit fully the dataset available while maintaining an efficient and robust fit. A large number of nuisance parameters have been considered, with additional fits run to determine their impact on the fitted value of $\hat{\mu}$ and, using the Asimov dataset, to check their behaviour. The fits can be used to calculate the expected and observed values of the 95% confidence level limits on $\hat{\mu}$, p_0 values, and significance as well as the observed best fit value of $\hat{\mu}$. These fits are applied to the analyses described in Chapter 7 to produce the results presented in Chapter 10. This fit model, with some extensions, is used to estimate the correlations between the $VH, H \to b\bar{b}$ cut-based and MVA analyses in Chapter 9.

CHAPTER 9

Correlation of the $VH, H \to b\bar{b}$ Cut-based and MVA analyses

9.1 Introduction

The complexity of the individual channels within the $VH, H \to b\bar{b}$ cut-based and MVA analyses is extremely high, both in terms of selection and fitting procedure. Object selection is common, though still complex, between the two different analyses, but the event selection and regions used are different. The ATLAS $VH, H \to b\bar{b}$ search is split up into 3 individual channels for the processes $ZH \to \nu\nu b\bar{b}$, $WH \to \ell\nu b\bar{b}$ and $ZH \to \ell\ell b\bar{b}$ which will be referred to as the 0,1 and 2 lepton channels, respectively. The complexity of the combined $VH, H \to b\bar{b}$ analyses is extremely high due to the huge number of regions considered when combining the 3 individual channels as well as the need to account for the constraint on each channel from the others. Aside from the regions used, the fit model is the same for the cut-based and MVA analyses. For this chapter only, "Combined" is used to refer to the combination of the 3 individual channels to form the full $VH, H \to b\bar{b}$ analyses rather than the merging of the $E_{\mathrm{T}}^{\mathrm{miss}}$ triggered and Nominal WH analyses as in Chapters 7, 8 & 10. The $E_{\mathrm{T}}^{\mathrm{miss}}$ triggered analyses are not represented in this chapter, this study only uses the main 3 channels of the $VH, H \to b\bar{b}$ search.

The cut-based and MVA event selections are such that the cut-based events are a subset of those used in the MVA analysis[1]. There should therefore be a high degree of correlation between the cut-based and MVA fit results, but this needs to be confirmed and the level of correlation estimated to ensure that there is the expected level of statistical consistency between the two analyses. The MVA analysis is known to be more sensitive, but by looking at the correlation with the perhaps more robust cut-based analysis it can be ensured that no artifacts are sculpted by the MVA in the output distributions. Toy Monte Carlo methods are often employed to study the response of a fit, but they cannot be used for this task, as they will not reproduce the overlap between the two analyses, so a modified Bootstrap method is used. This is useful for studying the statistical, but not systematic, correlation of the two analyses.

9.2 Bootstrapping

Bootstrapping methods are very useful for studying confidence intervals in situations where there are a large number of complex dependencies on physical and experimental responses. In these cases, an exact analytical form for the parameter of interest is not known. Bootstrapping is based on the plug-in principle and resampling [112]. The plug-in principle concerns replacing an unknown cumulative distribution function with an estimate of that parameter, such as the average of the data points. Resampling is the idea of using the data to approximate the statistical fluctuations in the parameter of interest. The data events are sampled by pick-and-replace such

---

[1] There is one exception to this in the 2 lepton analysis where a different mass window is used for a $t\bar{t}$ control region.

that data points are picked at random and then placed back in the set of events to be picked from. Some data points will therefore appear multiple times in the final sampling whilst some will not be represented [113, 114].

This method as stated is not practical for a study of correlation between the $VH, H \rightarrow b\bar{b}$ cut-based and MVA analyses. There are technical issues related to the resampling and problems in building the cut-based and MVA datasets coherently. As such, a modified bootstrap method is instead employed. The modified bootstrap method builds coherent pairs of cut-based and MVA pseudodatasets through sampling from the full Monte Carlo Asimov dataset, built with $\hat{\mu} = 1$. It is important to preserve the level of statistics that would be available for a real data sample, so the Monte Carlo events selected for the final pseudodatasets must be unweighted, but the Monte Carlo event weights must also be taken into account or the pseudodatasets would become too unrepresentative.

The modified bootstrap is implemented by randomly sampling a Poisson distribution for each analysed Monte Carlo event. The Poisson distribution is built with an expected value, λ, equal to the weight for that specific event. This is statistically equivalent to resampling because each event is allowed to be picked 0,1,2 etc... times but is technically more feasible than looping over the final dataset and actually performing resampling. To build the cut-based and MVA pseudodatasets coherently, the random seed for the Poisson sampling is set to be the Monte Carlo event number such that events will get the same Poisson weight whichever analysis they are part of. Each pseudodataset is therefore a subset of the total available Monte Carlo statistics, with the possibility of double counting. Data driven backgrounds comprised of templates, such as the multijet backgrounds in the $VH, H \rightarrow b\bar{b}$ search, can not be included when producing pairs of bootstrap pseudodatasets in this way.

Consistent sets of nominal Monte Carlo and bootstrapped pseudodatasets were

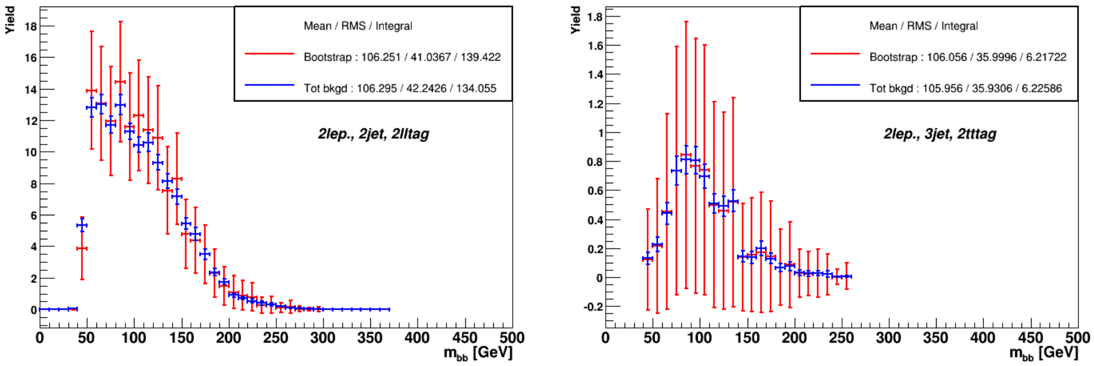

Figure 9.1: Bootstrapping validation plots for regions in the 2-lepton cut-based analysis, showing the nominal Monte Carlo yield compared to the mean yield of the bootstrap pseudodatasets. Left: $p_{\mathrm{T}}(Z) = 120 - 160$ GeV, 2 jets both b-tagged at the loose 80% operating point. Right: $p_{\mathrm{T}}(Z) = 160 - 200$ GeV, 3 jets of which 2 are b-tagged at the tight 50% operating point. The mean, RMS and total yield is shown in the legend for both the nominal Monte Carlo sample and bootstrap pseudodatasets.

produced by the groups contributing the three main analysis channels within the $VH, H \to b\bar{b}$ search [115]. The event selection for the three channels follows the standard $VH, H \to b\bar{b}$ procedure, more details of which can found in [40], with a couple of exceptions[2]. The cut-based fits use dijet invariant mass distributions, while the MVA fits used boosted decision tree outputs. Both use jet b-tagging weight distributions, separated into different regions based on the Vector Boson transverse momentum, $p_{\mathrm{T}}(V)$. The modified bootstrap method is intended to make statistically similar (and overlapping) pseudodatasets varying about the Monte Carlo expectation. The average yield of the bootstrap replica pseudodatasets should therefore be equal to the nominal Monte Carlo yield (within errors) in each fit region. This has been verified for each set of inputs before the fitting procedure is performed. Examples of these validation plots are shown for the 2 Lepton analysis in Figures 9.1 and 9.2.

---

[2] The $E_{\mathrm{T}}^{\mathrm{miss}}$ triggered 1 Lepton events are not included and the lowest $p_{\mathrm{T}}(Z)$ region of the 0 Lepton analysis is omitted.

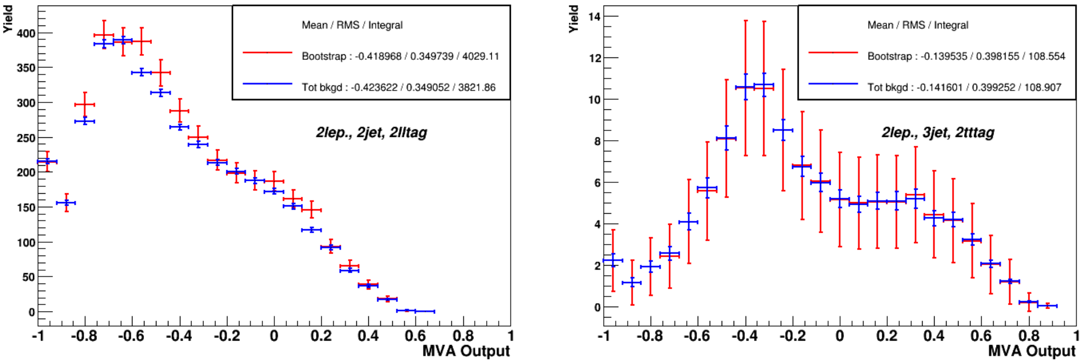

Figure 9.2: Bootstrapping validation plots for regions in the 2-lepton MVA analysis showing the nominal Monte Carlo yield compared to the mean yield of the bootstrap pseudodatasets. Left: $p_{\mathrm{T}}(Z) = 0 - 120$ GeV, 2 jets both b-tagged at the loose 80% operating point. Right: $p_{\mathrm{T}}(Z) > 120$ GeV, 3 jets of which 2 are b-tagged at the tight 50% operating point. The mean, RMS and total yield is shown in the legend for both the nominal Monte Carlo sample and bootstrap pseudodatasets.

9.3 Methodology

To extract the correlation between the cut-based and MVA analyses, each of the bootstrapped pseudo-datasets from both analyses must be fitted. The fit model used is the same as described in Chapter 8, where the 1 lepton specific details are described. The same fit model is used for the 0, 1 and 2 lepton channels as well as the combination, although some additional nuisance parameters, correlations and decorrelations are required for this. The additional details and full statement of the regions used are described in [40]. The channels are fitted both individually and combined for the full $VH, H \rightarrow b\bar{b}$ fit. For each bootstrapped pseudo-dataset, the pseudo-data are fitted with the nominal Monte Carlo (without the data-driven multijet templates) to obtain values for the parameter of interest ($\hat{\mu}$), nuisance parameters and their respective errors. From the values measured in a number of pairs of cut-based and MVA bootstrap pseudodatasets, the correlation for a particular parameter can then be calculated. The distributions of $\hat{\mu}$ for the cut-based and MVA pseudodatasets are shown in Figures 9.3-9.6 for each of the individual channels as well as the combination of all three. 800 pairs of replicas are used for each channel while 700 sets of pairs of replicas for the Combined fits. The width of the

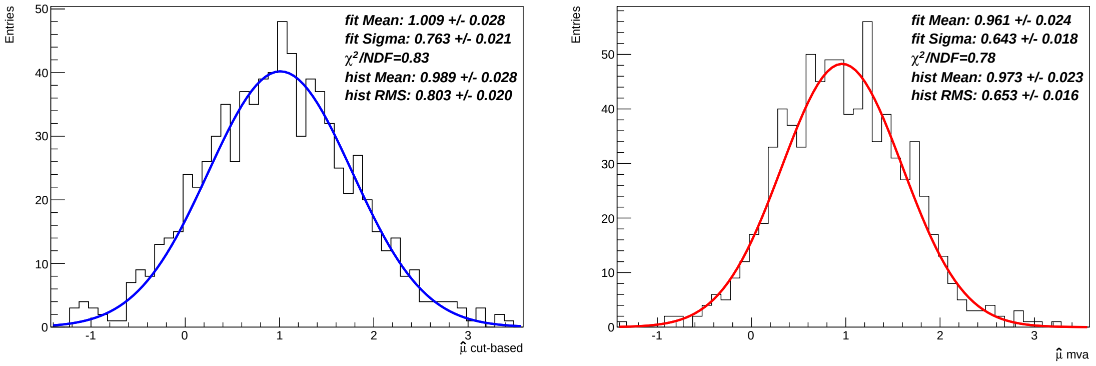

(a) Cut-based (b) MVA

Figure 9.3: Distributions of $\hat{\mu}$ from the bootstrap pseudodataset for the 0 lepton analysis. Shown for 800 replicas in both the cut-based and MVA analyses.

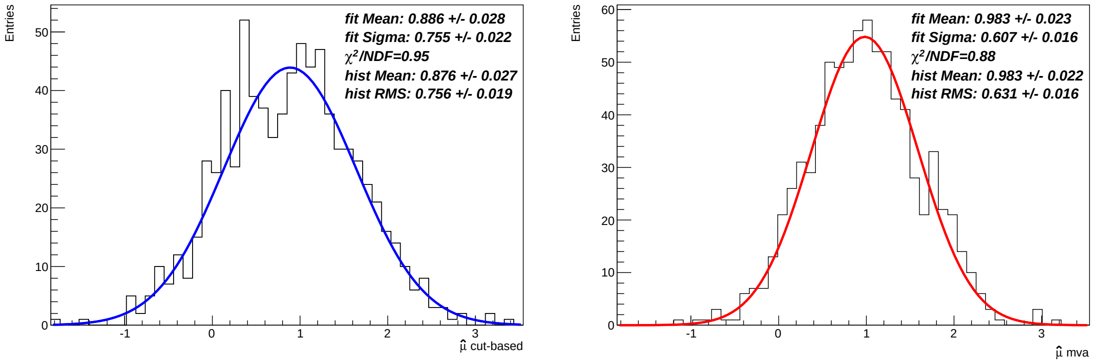

(a) Cut-based (b) MVA

Figure 9.4: Distributions of $\hat{\mu}$ from the bootstrap pseudodataset for the 1 lepton analysis. Shown for 800 replicas in both the cut-based and MVA analyses.

distribution gives some indication as to the statistical resolution of the parameter in a real data fit.

9.4 Results

The pairs of values for parameters are taken from the cut-based and MVA fit results for coherent pairs of inputs. These are then plotted together and a correlation value is calculated. The parameter of interest, $\hat{\mu}$, is the main parameter investigated and

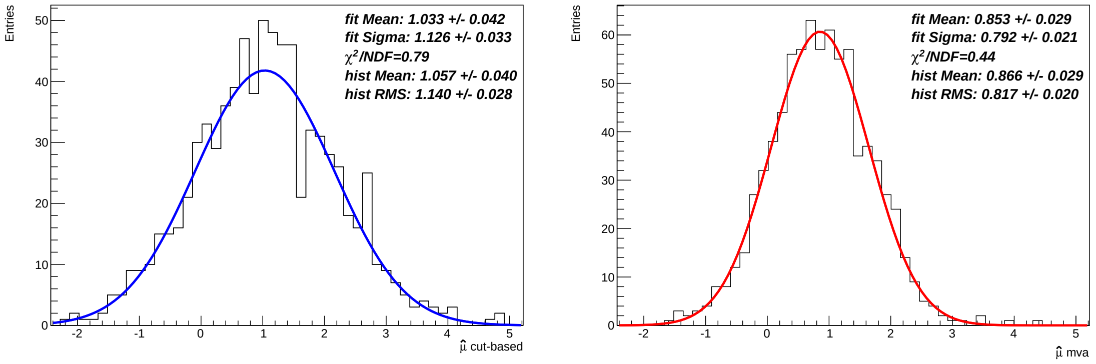

(a) Cut-based

(b) MVA

Figure 9.5: Distributions of $\hat{\mu}$ from the bootstrap pseudodataset for the 2 lepton analysis. Shown for 800 replicas in both the cut-based and MVA analyses.

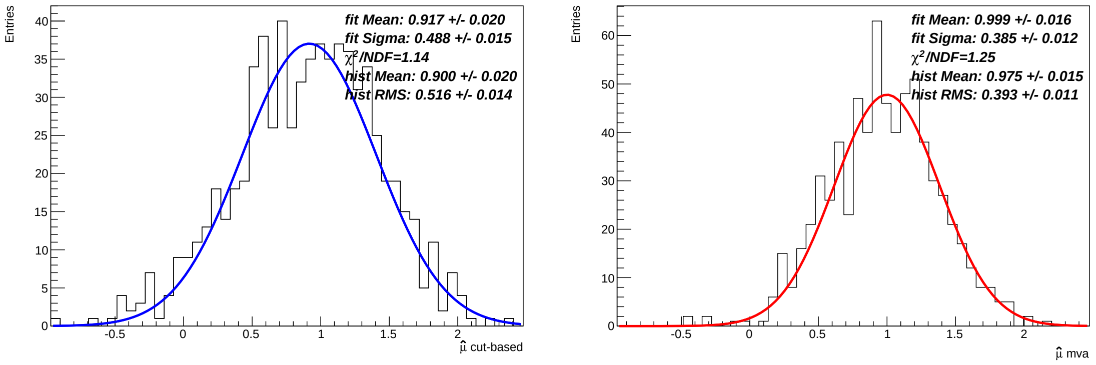

(a) Cut-based

(b) MVA

Figure 9.6: Distributions of $\hat{\mu}$ from the bootstrap pseudodataset for the Combined analysis. Shown for 700 sets of replicas in both the cut-based and MVA analyses.

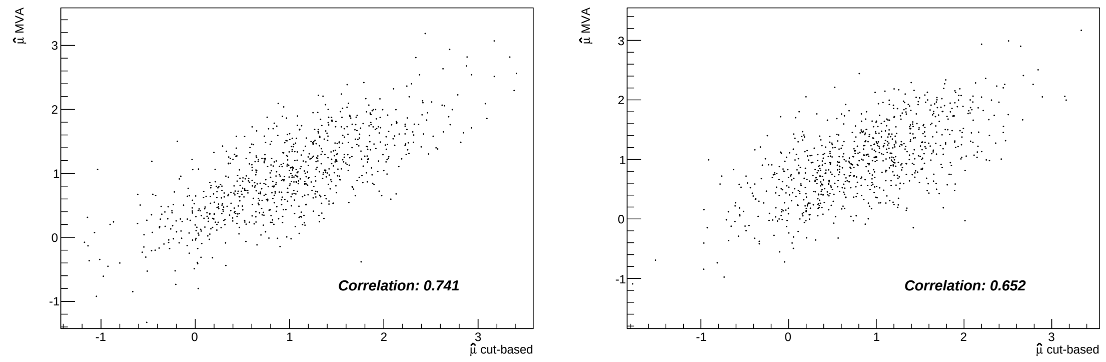

(a) 0 Lepton (b) 1 Lepton

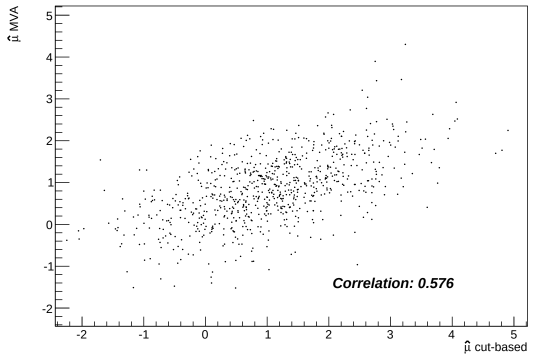

(c) 2 Lepton

Figure 9.7: Correlation of $\hat{\mu}$ from the individual lepton cut-based and MVA bootstrap pseudodatasets. Shown for 800 pairs of replicas in each channel.

the only parameter for which results are presented here. A large number of nuisance parameters and background normalisations were investigated, leading to better understanding of the behaviour of these parameters of the fit. Correlation plots for some of the normalisations and nuisance parameters are shown in Appendix E. The scatter plots of $\hat{\mu}$ for the individual channels are shown in Figure 9.7 and for the Combined fit in Figure 9.8. The correlation values calculated from the scatter plots are shown on the plots and summarised in Table 9.1 for each of the 3 individual lepton channels as well as the combination of all three.

It can be seen from Figures 9.7 and 9.8 and from Table 9.1 that the 0 lepton channel has the highest correlation between the cut-based and MVA analyses, followed by the 1 lepton whilst the 2 lepton channel is least correlated. The Combined corre-

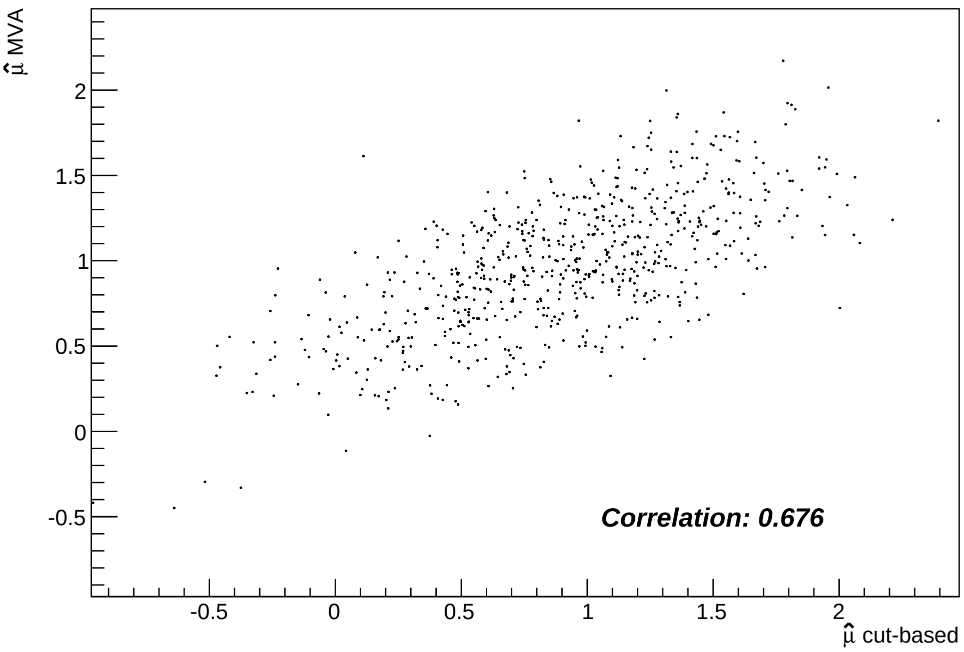

Figure 9.8: Correlation of $\hat{\mu}$ from the Combined cut-based and MVA bootstrap pseudodatasets. Shown for 700 sets of pairs of replicas in each channel.

Lepton Channel	Cut-based MVA Correlation
0	0.741
1	0.652
2	0.576
Combined	0.676

Table 9.1: Correlation of the $VH, H \to b\bar{b}$ bootstrapped cut-based and MVA analyses.

lation is close to the average of the correlation in the three individual channels. It is expected that the 0 lepton channel will have the strongest cut-based MVA correlation as this channel contains the fewest regions, as it does not contain the low $p_{\mathrm{T}}(V)$ regions present in the other channels. This reduces the potential fluctuations and leads to a larger commonality between the cut-based and MVA results. The correlation is believed to be over-estimated here due to the exclusion of the region $p_{\mathrm{T}}(Z) = 90 - 120$ GeV, the inclusion of which would allow for greater fluctuations. The 2 lepton analysis shows the lowest correlation because the cut-based selected events are not entirely a subset of the MVA selected events in one of the $t\bar{t}$ control

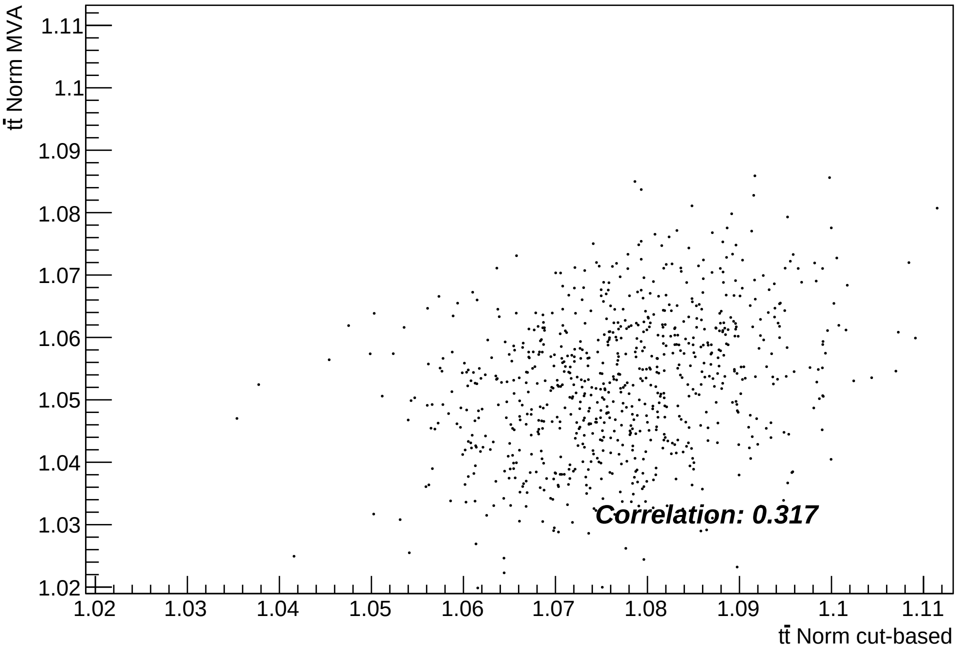

Figure 9.9: Correlation of the $t\bar{t}$ normalisation factor from the 2 lepton cut-based and MVA bootstrap pseudodatasets. Shown for 800 sets of pairs of replicas in each channel.

regions. The regions that strongly constrain $t\bar{t}$ events are different between the two analyses. This is validated by the very low level of correlation observed in the 2 lepton $t\bar{t}$ normalisation as shown in Figure 9.9.

There is some concern that bootstrapping methods contain a bias that reduces the spread of results due to the statistical similarities of the many replica pseudodatasets, being drawn as they are from the same pool of events. This would manifest as a small correlation for a small number of pairs of replicas that grows steadily higher as more pairs of replicas are introduced. An effect would also likely to be visible in the way the mean of the parameter evolves with increased pairs of replicas. For this reason the results were also calculated with a smaller number of replicas. Figure 9.10 shows the measured correlation of $\hat{\mu}$ as a function of the number of replicas used for each channel. Figure 9.11 shows the mean value of $\hat{\mu}$ as a function of the number of replicas used. The individual channel results do not appear to show a bias from the bootstrapping method, the fluctuations in the correlation merely appear to settle down as more replicas are added rather than the correlation increasing. From the Combined correlation as a function of replicas alone, Figure 9.10d, it looks like there is a bias as the correlation seems to drift upwards. This is in fact just due to large early downward fluctuations in the individual channels occurring at different numbers of replicas. Once the individual channels are stable, the Combined also appears stable. In Figure 9.11 the 1 lepton, 2 lepton and Combined channels do not reach a mean $\hat{\mu}$ value of 1.0, which is of some concern as the bootstrap inputs were built with $\hat{\mu} = 1.0$ and the validation plots described and shown in Section 9.2 showed good agreement in all regions, including those with high sensitivity/significance. The explanation for this is not known but is suspected to be due to failed fits (that were excluded), which are more likely to happen at extreme true values of $\hat{\mu}$. It is not understood why either the cut-based or MVA would have a higher value for $\hat{\mu}$. This shift should not affect the validity of the correlation results.

As mentioned previously, the correlation of errors on parameters from the fit can also be calculated. This is useful to understand better the stability of the fits. The correlation of the error on $\hat{\mu}$ in the Combined analysis is calculated to be 0.487 and the corresponding scatter plot is shown in Figure 9.12. The correlation of the error on $\hat{\mu}$ is smaller than for $\hat{\mu}$ in all channels. Another interesting parameter to calculate the correlation of is $\hat{\mu}$ divided by the error on $\hat{\mu}$ which gives a crude version of $\hat{\mu}$ significance. This is not a true value of the significance as it is allowed to be negative, but provides a useful measurement. The correlation of the $\hat{\mu}$ “significance” in the Combined channel is calculated to be 0.692, very similar to that of $\hat{\mu}$ and is shown in Figure 9.13a. Figures 9.13b and 9.14 show the how the correlation and mean “significance” values change as a function of the number of replicas. It can be seen in Figure 9.13a that the spread of “significance” values is smaller in the case of the MVA analysis compared to the cut-based analysis, as well as the MVA analysis having a much higher average “significance” in Figure 9.14. This is a clear indication that the MVA analysis is more sensitive than the cut-based analysis, which tallies

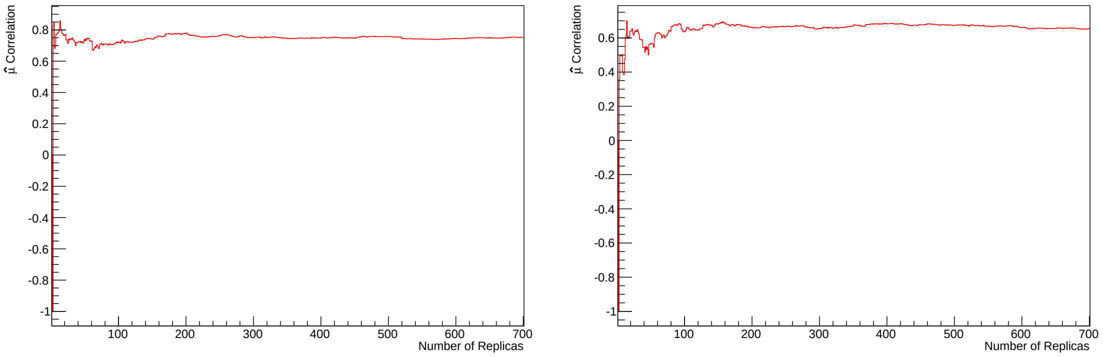

(a) 0 lepton (b) 1 lepton

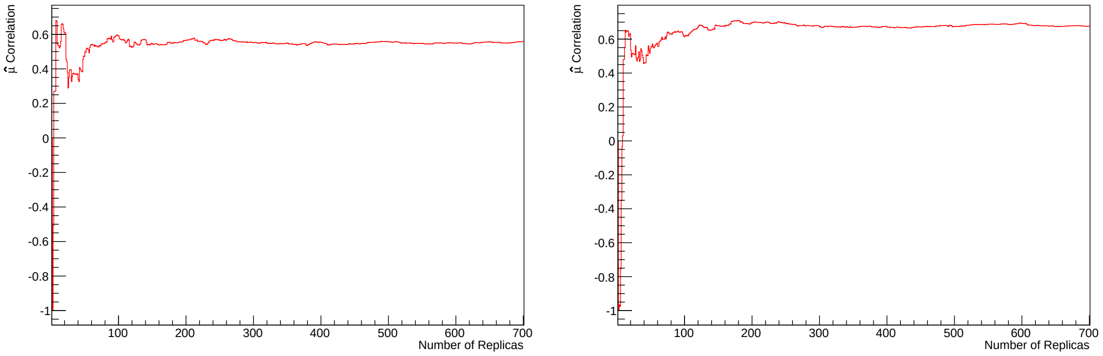

(c) 2 lepton (d) Combined

Figure 9.10: Measured correlation of $\hat{\mu}$ for each channel as a function of the number of sets of pairs of pseudodatasets. Shown for 1 to 700 sets of pseudodatasets for each channel and for the combined.

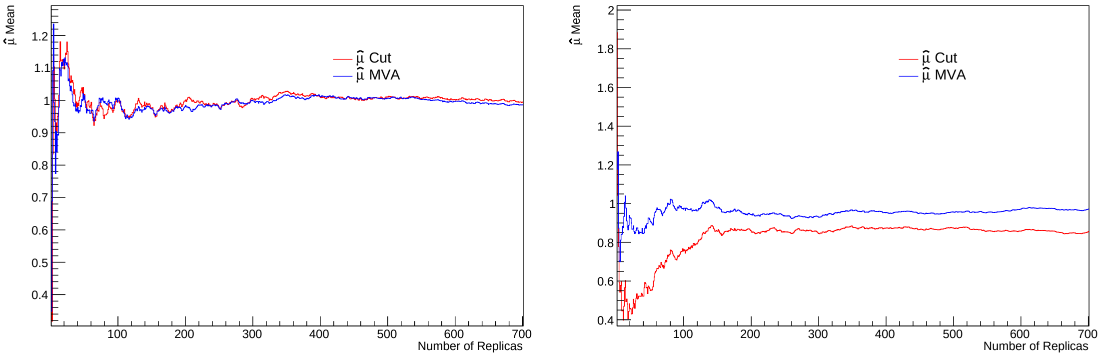

(a) 0 lepton

(b) 1 lepton

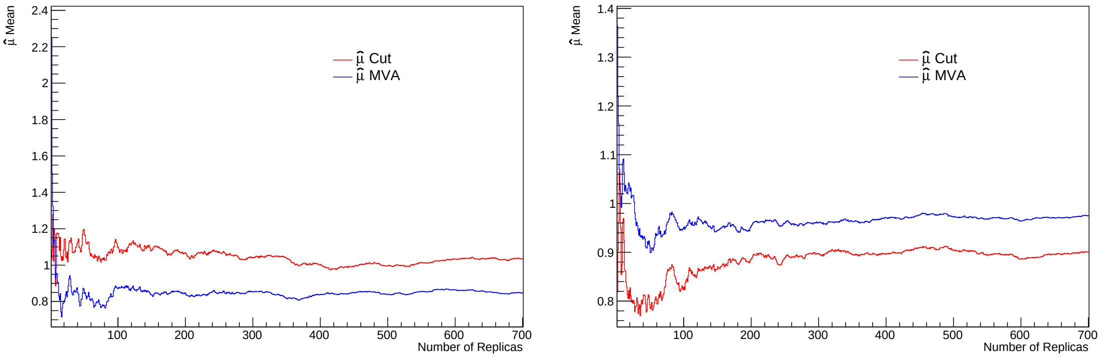

(c) 2 lepton

(d) Combined

Figure 9.11: Measured mean of $\hat{\mu}$ for each channel in the cut-based and MVA analyses as a function of the number of sets of pairs of pseudodatasets. Shown for 1 to 700 sets of pseudodatasets for each channel.

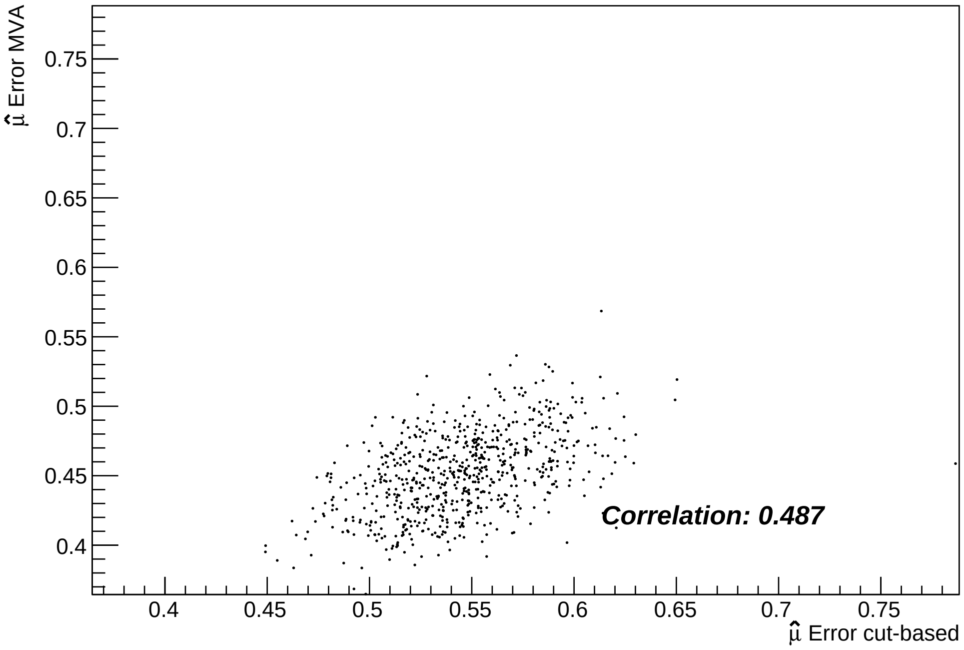

Figure 9.12: Correlation of the error on $\hat{\mu}$ from the Combined cut-based and MVA bootstrap pseudodatasets. Shown for 700 sets of pairs of replicas in each channel.

to a very close degree to results from Asimov fits.

9.5 Consistency of the Cut-based and MVA Results

The correlation study provides information useful for estimating the consistency of the results obtained from the cut-based and MVA fits. The correlation results were in place by the time the $VH, H \to b\bar{b}$ results were unblinded so could be used to assess the consistency of each single lepton channel as well as the Combined results. The unblinded data results in each channel are shown in Figure 9.15 in comparison to the bootstrap replicas results shown previously. The values for $\hat{\mu}$ and the difference between the cut-based and MVA values are summarised in Table 9.2.

The value of the $\hat{\mu}$ correlation and the differences in $\hat{\mu}$ shown in Table 9.2 provide

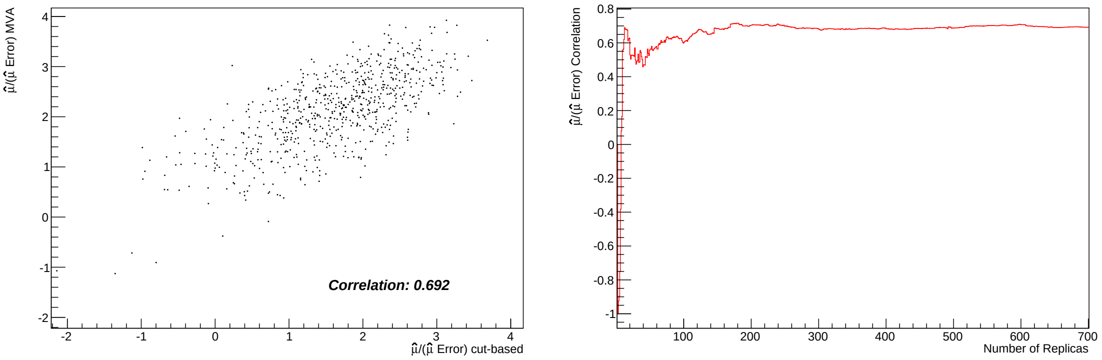

(a) "Significance" Correlation

(b) "Significance" correlation as a function of number of replicas

Figure 9.13: Correlation of "significance": $\hat{\mu}$/error on $\hat{\mu}$ from the Combined cut-based and MVA bootstrap pseudodatasets. Left: For 700 sets of pairs of replicas in each channel. Right: Shown as a function of the number sets of pairs of pseudodatasets from 1 to 700 sets.

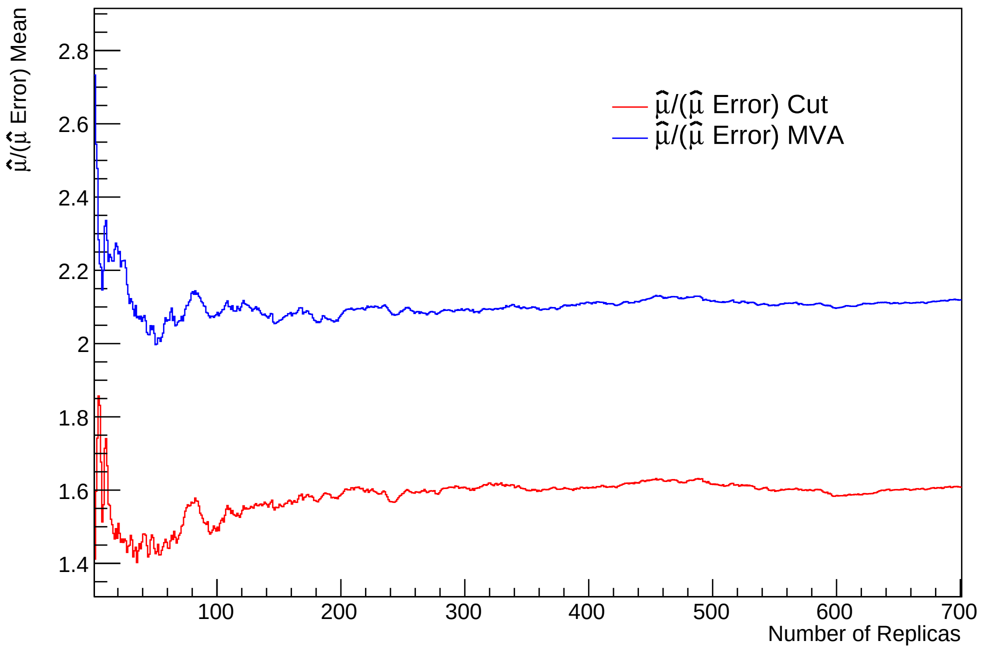

Figure 9.14: Measured mean of $\hat{\mu}$/error on $\hat{\mu}$ for the Combined cut-based and MVA analyses as a function of the number of sets of pairs of pseudodatasets. Shown for 1 to 700 sets of pairs of pseudodatasets.

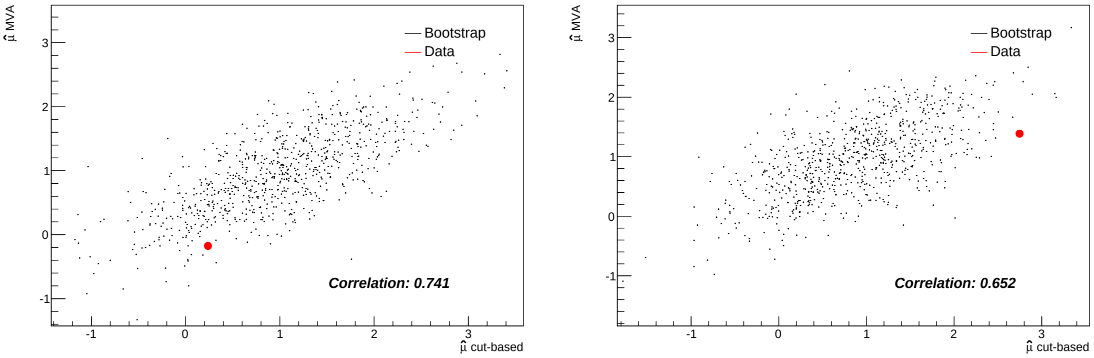

(a) 0 lepton

(b) 1 lepton

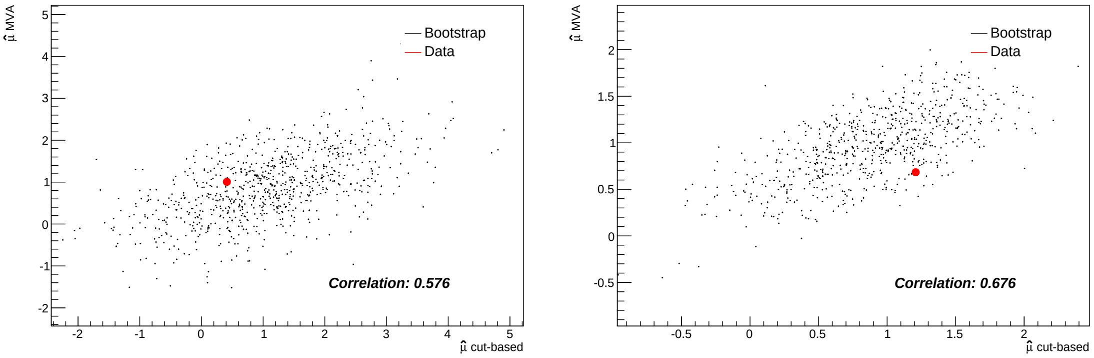

(c) 2 lepton

(d) Combined

Figure 9.15: Distribution of $\hat{\mu}$ pairs from the individual lepton and Combined cut-based and MVA bootstrap pseudodatasets compared to the data result. Shown for 800 pairs of replicas in each individual lepton channel and 700 pairs for the Combined analysis. Bootstrap replicas are shown as black points with the data results marked in red.

Channel	$\hat{\mu}$ Cut	$\hat{\mu}$ MVA	$\hat{\mu}$ Cut - $\hat{\mu}$ MVA
0	0.249	-0.215	0.464
1	2.741	1.361	1.38
2	0.419	0.962	-0.543
Combined	1.230	0.651	0.579

Table 9.2: Values of the observed $\hat{\mu}$ value from data for each of the $VH, H \to b\bar{b}$ channels. Values are shown for the cut-based and MVA analyses, as well as giving the difference between the two.

one way of estimating the consistency, but this is incomplete without an estimate of the difference expected between the the cut-based and MVA $\hat{\mu}$ values. The difference between the bootstrap replica $\hat{\mu}$ values (cut-based - MVA) is shown in Figure 9.16. The difference between the data results can then be compared to the standard deviation of the fits to these distributions. The distribution of $\hat{\mu}$ difference is assumed to be centred about 0 and symmetrical for the purpose of the estimate. From this the number of standard deviations away from 0 that the data results are can be used as the z value in a two-tailed normal distribution to find the probability of getting at least as extreme a value as is observed. A two-tailed calculation is used because it does not matter which value is higher, only the absolute difference. This calculation yields a probability, or consistency estimate, of 36.75% in the 0 lepton channel, 1.51% in the 1 lepton, 55.12% in the 2 lepton and 13.30% for the Combined fit.

The analysis of the bootstrapped pseudodatasets provided a useful way to study the statistical correlation between the cut-based and MVA $VH, H \to b\bar{b}$ analyses. The correlations of the three individual channels as well as in the Combination have been calculated, all of which show a high degree of correlation. By evaluating the expected difference between the cut-based and MVA $\hat{\mu}$ values, the statistical consistency of the values obtained from data has been estimated.

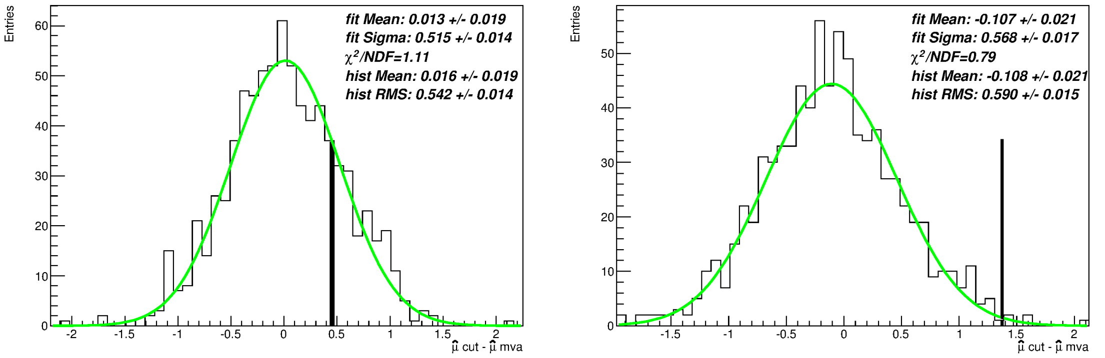

(a) 0 lepton (b) 1 lepton

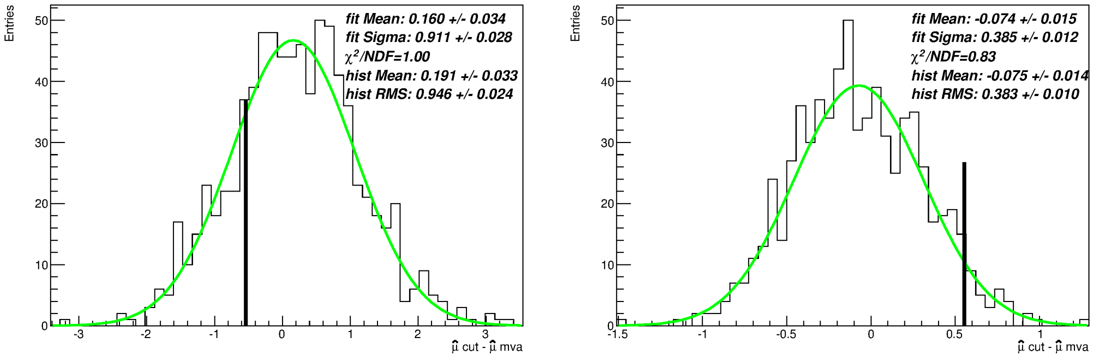

(c) 2 lepton (d) Combined

Figure 9.16: Distributions of the difference between the cut-based and MVA $\hat{\mu}$ values from the pairs of bootstrap pseudodatasets. The black lines show the difference observed in data.

CHAPTER 10

Results For The Search For $WH \to \ell\nu b\bar{b}$

The $E_{\mathrm{T}}^{\mathrm{miss}}$ triggered and Combined $WH \to \ell\nu b\bar{b}$ cut-based and MVA analyses distributions described in Chapter 7 are fitted using the fit model described in Chapter 8 to extract results for the signal strength, the upper limit on the signal strength and the significance of any observed signal. As the background and signal normalisations are allowed to float in the fits, the distributions in each of the fit regions change from prefit to postfit. The postfit distributions for the $E_{\mathrm{T}}^{\mathrm{miss}}$ triggered regions fitted on their own are shown in Section 10.1, while the postfit distributions for the Combined analysis, in which the $E_{\mathrm{T}}^{\mathrm{miss}}$ triggered regions are merged with the Nominal (single lepton triggers) regions are shown in Appendix D. The results obtained from the $E_{\mathrm{T}}^{\mathrm{miss}}$ triggered cut-based and MVA fits are described in Section 10.2 and the results from the Combined fits in Section 10.3. For reference, the results obtained from the Nominal fits, not using the $E_{\mathrm{T}}^{\mathrm{miss}}$ triggered regions, can be found in Appendix C.

10.1 Postfit $E_{\mathrm{T}}^{\mathrm{miss}}$ Triggered $WH \to \ell\nu b\bar{b}$ Regions

The postfit distributions for the regions used in the $E_{\mathrm{T}}^{\mathrm{miss}}$ triggered Cut-based analysis are shown in Figures 10.1 - 10.7 and for the MVA analysis in Figures 10.8 - 10.10. Each plot shows both the data, as points with error bars, and the postfit Monte Carlo, as stacked histograms. The statistical uncertainty on the data is represented by the error bars on the points and the total postfit statistical and systematic uncertainty on the Monte Carlo is represented by the shaded area. The blue dashed line represents the prefit total background yield, as shown in the prefit stacked plots in Chapter 7. The expected Higgs signal is shown both stacked on top of the stacked background histograms normalised to the standard model expected cross section times branching ratio and unstacked as an unfilled red line. The unstacked signal is scaled by a factor shown in the legend, chosen by an algorithm separately in each region to ensure it is visible on the scale of the plot. Each plot contains, below the main axes, the ratio of the data yield to the postfit background plus signal expectation.

The description of the choice of binning can be found in Chapter 8. Some of the bins contain very low statistics so large fluctuations are evident. This is especially true for regions where the expected number of events per bin is below 1. The postfit description of the data by the MC is reasonable when accounting for the systematic and statistical uncertainties. The agreement is better than it was prefit (shown as the blue dashed line in each plot) because the background normalisations are allowed to float in the fit. The total uncertainty on the MC expectation in each bin is reduced from the prefit value. This is due to the fit constraining the uncertainties of some individual nuisance parameters, as was shown in Figures 8.1 and 8.2, which reduces their potential effect. In the cut-based analysis, the higher $p_{\mathrm{T}}(W)$ regions contain slightly less signal than the lower ones but considerably lower background leading to higher sensitivity in these regions. The lower $p_{\mathrm{T}}(W)$ regions contribute more to the background normalisations as discussed previously. For both cut-based and MVA analyses, the signal statistics are higher in the stricter b-tagging categories and the background much lower.

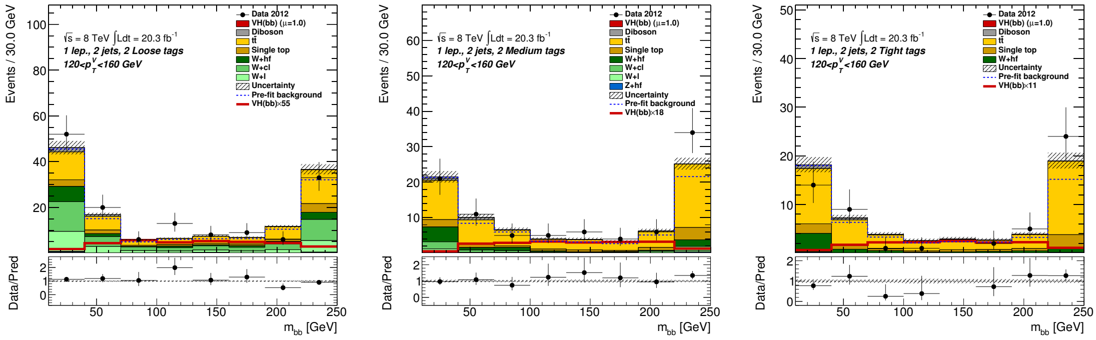

(a) 2 Loose Tags (b) 2 Medium Tags (c) 2 Tight Tags

Figure 10.1: Postfit distributions of the dijet invariant mass, m_{bb}, in the cut-based $E_{\mathrm{T}}^{\mathrm{miss}}$ triggered 2-jet $p_{\mathrm{T}}(W) = 120 - 160$ GeV regions, split into b-tagging categories. The data is shown as points with error bars and the postfit Monte Carlo background yield is shown as a stacked histogram. The uncertainty on the total background yield is represented as a shaded area and the prefit total background yield is shown as a blue dashed line. The expected Higgs signal, from a sample at $m_H = 125$ GeV, is shown both stacked on top of the background histograms at the Standard Model expectation and un-stacked, but scaled, by a factor stated in the legend. The lower part of each plot shows the ratio of the data yield to the postfit background and signal prediction.

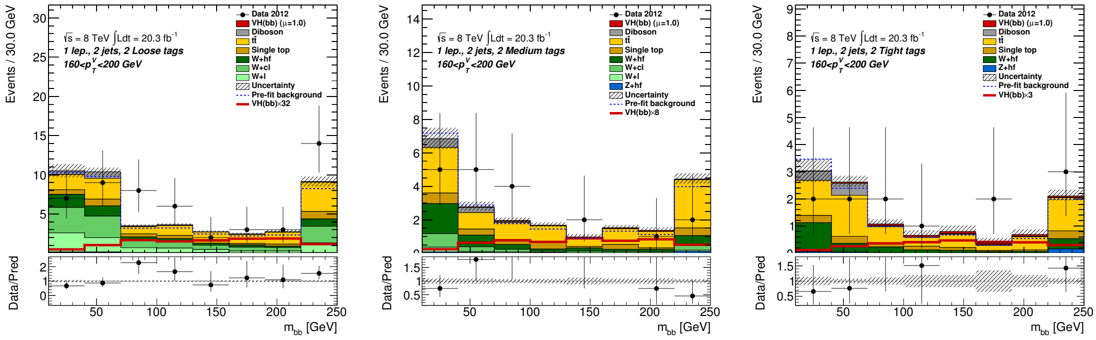

(a) 2 Loose Tags (b) 2 Medium Tags (c) 2 Tight Tags

Figure 10.2: Postfit distributions of dijet invariant mass, m_{bb}, in the cut-based $E_{\mathrm{T}}^{\mathrm{miss}}$ triggered 2-jet $p_{\mathrm{T}}(W) = 160 - 200$ GeV regions. The format is the same as Figure 10.1.

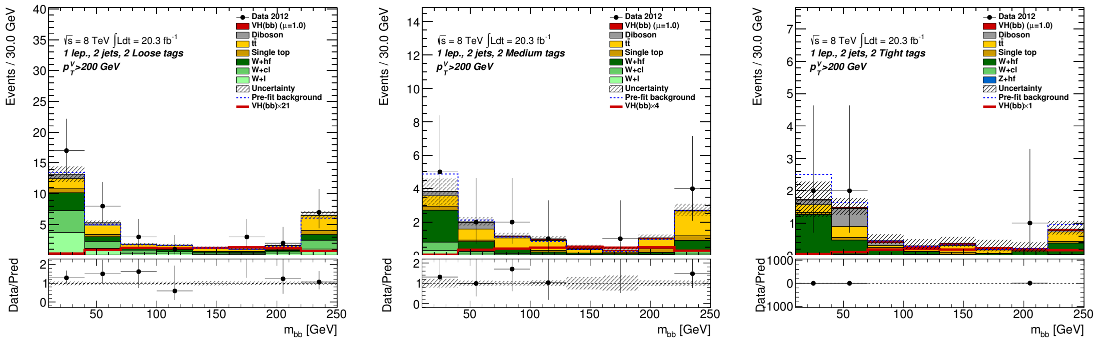

(a) 2 Loose Tags (b) 2 Medium Tags (c) 2 Tight Tags

Figure 10.3: Postfit distributions of dijet invariant mass, m_{bb}, in the cut-based $E_{\mathrm{T}}^{\mathrm{miss}}$ triggered 2-jet $p_{\mathrm{T}}(W) > 200$ GeV regions. The format is the same as Figure 10.1.

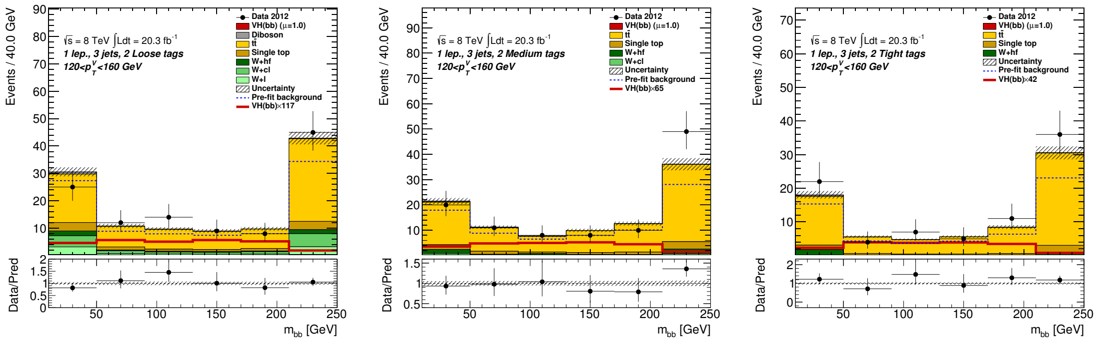

(a) 2 Loose Tags (b) 2 Medium Tags (c) 2 Tight Tags

Figure 10.4: Postfit distributions of dijet invariant mass, m_{bb}, in the cut-based $E_{\mathrm{T}}^{\mathrm{miss}}$ triggered 3-jet $p_{\mathrm{T}}(W) = 120 - 160$ GeV regions. The format is the same as Figure 10.1.

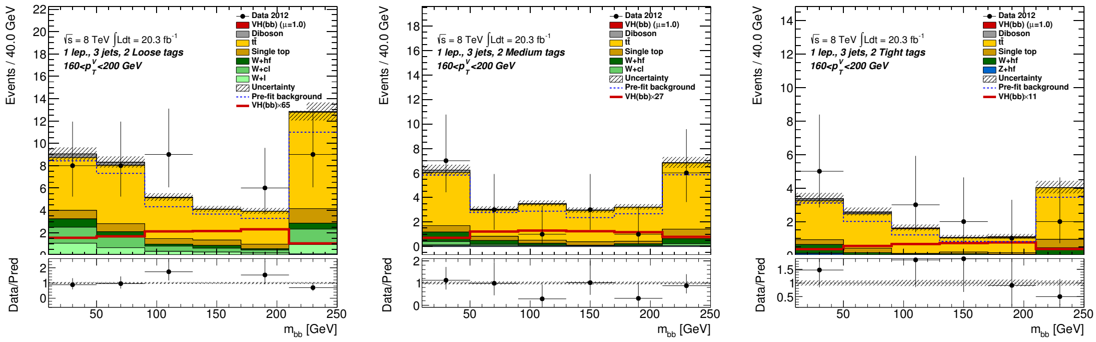

(a) 2 Loose Tags (b) 2 Medium Tags (c) 2 Tight Tags

Figure 10.5: Postfit distributions of dijet invariant mass, m_{bb}, in the cut-based $E_{\mathrm{T}}^{\mathrm{miss}}$ triggered 3-jet $p_{\mathrm{T}}(W) = 160 - 200$ GeV regions. The format is the same as Figure 10.1.

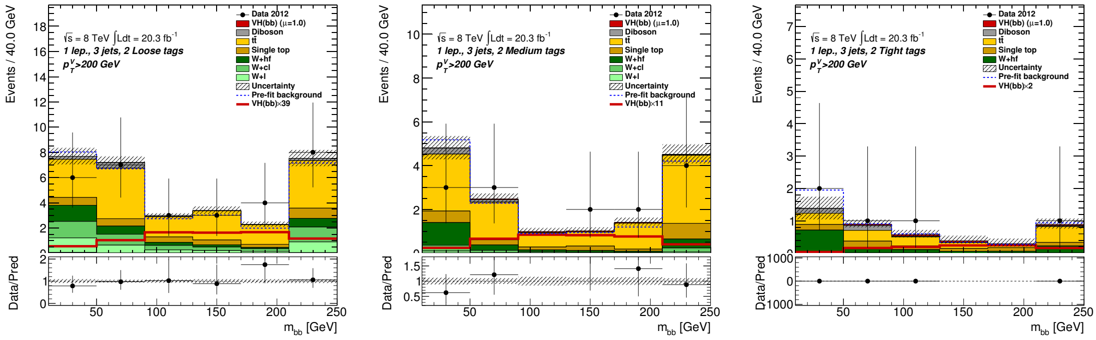

(a) 2 Loose Tags (b) 2 Medium Tags (c) 2 Tight Tags

Figure 10.6: Postfit distributions of dijet invariant mass, m_{bb}, in the cut-based $E_{\mathrm{T}}^{\mathrm{miss}}$ triggered 3-jet $p_{\mathrm{T}}(W) > 200$ GeV regions. The format is the same as Figure 10.1.

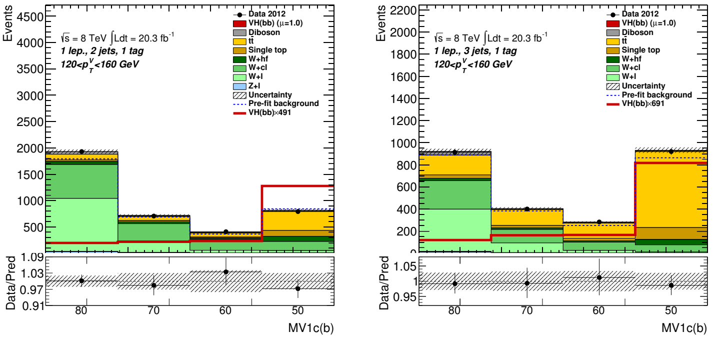

(a) 2 Jet (b) 3 Jet

Figure 10.7: Postfit distributions of the b-tagging weight, $MV1c$, in the cut-based $E_{\mathrm{T}}^{\mathrm{miss}}$ triggered 1-tag 2-jet and 3-jet $p_{\mathrm{T}}(W) > 120$ GeV regions. The format is the same as Figure 10.1.

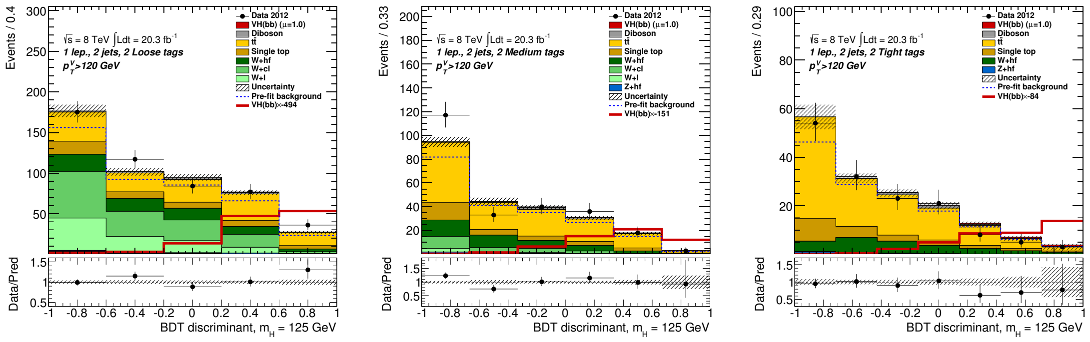

(a) 2 Loose Tags (b) 2 Medium Tags (c) 2 Tight Tags

Figure 10.8: Postfit distributions of the BDT output in the MVA $E_{\mathrm{T}}^{\mathrm{miss}}$ triggered 2-jet $p_{\mathrm{T}}(W) > 120$ GeV regions. The format is the same as Figure 10.1.

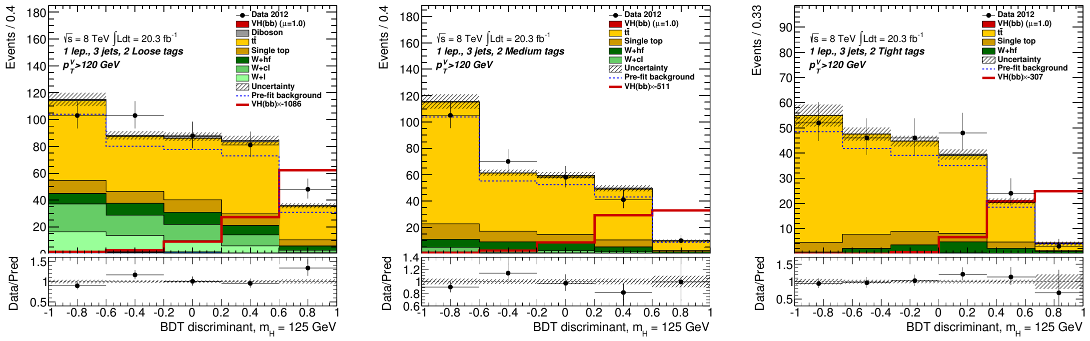

(a) 2 Loose Tags (b) 2 Medium Tags (c) 2 Tight Tags

Figure 10.9: Postfit distributions of the BDT output in the MVA $E_{\mathrm{T}}^{\mathrm{miss}}$ triggered 3-jet $p_{\mathrm{T}}(W) > 120$ GeV regions. The format is the same as Figure 10.1.

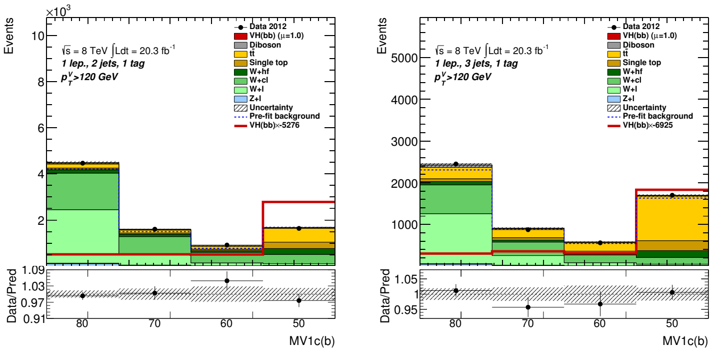

(a) 2 Jet (b) 3 Jet

Figure 10.10: Postfit distributions of the b-tagging weight, $MV1c$, in the MVA $E_{\mathrm{T}}^{\mathrm{miss}}$ triggered 1-tag 2-jet and 3-jet $p_{\mathrm{T}}(W) > 120$ GeV regions. The format is the same as Figure 10.1.

10.2 $E_{\mathrm{T}}^{\mathrm{miss}}$ Triggered $WH \to \ell\nu b\bar{b}$ Results

The $E_{\mathrm{T}}^{\mathrm{miss}}$ triggered dataset is fitted against the background expectation and each signal hypothesis, from $m_H = 100$ GeV to 140 GeV in steps of 5 GeV excluding 105 GeV, to extract results at each mass point. Most results are produced at each mass point but the final quoted results for the signal strength and significance will be for a signal hypothesis at $m_H = 125$ GeV.

The 95% CL upper bounds for the cross section times branching ratio for the $WH \to \ell\nu b\bar{b}$ decay mode are obtained at each mass point and are shown in Table 10.1 and Figure 10.11a for the cut-based analysis and in Table 10.2 and Figure 10.11b for the MVA analysis. The tables include the observed limit from data, the expected limit, which is obtained from a fit to the Asimov dataset, and the $\pm 1, \pm 2\sigma$ shifts from the expected limit, using the Asimov dataset shifted by $\pm 1, \pm 2\sigma$. These are represented in Figure 10.11 by a solid line with points for the observed, a dashed line for the expected, a green band covering the $\pm 1\sigma$ shift from the expected and the yellow band covering the $\pm 2\sigma$ shift. The results produced for the MVA analysis use BDT output weights from the training at $m_H = 125$ GeV at all masses.

To understand how significant any deviation from the background expectation is, the local p_0 is calculated. This is the probability for the background to fluctuate upwards at least as much as is observed in the data. A small expected/observed p_0 means that it would require a large statistical excess of background events to replicate that result. The observed p_0 can be compared to the expected p_0 obtained from a fit to Asimov dataset, including the signal at a signal strength of $\hat{\mu} = 1.0$. Expected and observed p_0 values are listed for each mass point for the cut-based and MVA analyses in Table 10.3 and shown in Figure 10.12. The solid black line represents the observed while the dotted blue line represents the expected. The local p_0 is shown at each mass point with horizontal bands translating this into a significance.

The observed $\hat{\mu}$ value for the cut-based analysis is $\hat{\mu}_{Cut} = 1.617^{+2.051}_{-1.694}(\text{stat.})^{+1.264}_{-0.957}(\text{syst.})$ and for the MVA analysis is $\hat{\mu}_{MVA} = -0.231^{+1.859}_{-1.565}(\text{stat.})^{+0.990}_{-0.872}(\text{syst.})$. The observed (expected) significance in the cut-based analysis is 0.815 (0.504) and in the MVA analysis is -0.111 (0.508).

Due to the large number of signal regions used in the fit, it is hard to visualise any excess or deficit of events in any individual region. For this reason all the fit regions have been combined together in Figure 10.16. To combine together all bins in all fit regions that contain different variables (di-b-jet mass and b-tagging weight), it is not the value of the bin but instead bins are combined based on the metric of $\log_{10}(S/B)$ in each bin where S and B are the signal and background yield in that particular bin. The full yield of signal, background and data from all bins within a range for $\log_{10}(S/B)$ are combined into a single bin in Figure 10.16. All yields used are postfit. The lower portion of the plot shows the ratio of data to the postfit background yield as points with statistical errors and a red line representing the expected ratio in the presence of a standard model Higgs signal at a signal strength of $\hat{\mu} = 1.0$. The red line therefore represents the yields of background plus signal divided by background. By comparing where the data points fall relative to the black dotted line at Data/Pred = 1.0 and the red line, it can seen whether there is an excess or deficit in data and how consistent the observation is with the background only or signal hypotheses. The points showing the largest discrepancy give an indication of the sensitivity of the regions contributing to the excess/deficit.

m_H (GeV)	Exp.	$+2\sigma$	$+1\sigma$	-1σ	-2σ	Obs.
100	2.34	4.36	3.25	1.68	1.25	2.74
110	2.94	5.49	4.09	2.12	1.58	4.13
115	3.34	6.23	4.65	2.41	1.79	3.64
120	4.03	7.51	5.61	2.90	2.16	5.00
125	4.79	8.93	6.66	3.45	2.57	6.28
130	5.88	10.97	8.19	4.24	3.16	6.81
135	7.69	14.35	10.71	5.54	4.13	8.65
140	10.51	19.60	14.62	7.57	5.64	15.10

Table 10.1: Expected and observed limits from the 95% CL upper bound on the cross section times branching ratio as a function of m_H for the $E_{\mathrm{T}}^{\mathrm{miss}}$ triggered cut-based analysis. Values are expressed as a multiple of the standard model expectation. The $\pm1\sigma$ and $\pm2\sigma$ shifts from the expected values are also shown.

m_H (GeV)	Exp.	$+2\sigma$	$+1\sigma$	-1σ	-2σ	Obs.
100	4.15	7.74	5.77	2.99	2.23	4.06
110	3.71	6.92	5.16	2.67	1.99	3.63
115	3.59	6.69	4.99	2.59	1.93	3.76
120	3.83	7.15	5.33	2.76	2.06	3.63
125	4.41	8.23	6.14	3.18	2.37	4.30
130	5.85	10.91	8.14	4.21	3.14	6.78
135	8.59	16.03	11.96	6.19	4.61	9.14
140	14.77	27.56	20.56	10.64	7.93	14.08

Table 10.2: Expected and observed limits from the 95% CL upper bound on the cross section times branching ratio as a function of m_H for the $E_{\mathrm{T}}^{\mathrm{miss}}$ triggered MVA analysis. Values are expressed as a multiple of the standard model expectation. The $\pm1\sigma$ and $\pm2\sigma$ shifts from the expected value are also shown.

m_H (GeV)	Exp p_0	Obs p_0
100	0.16416	0.40774
110	0.20906	0.24992
115	0.23813	0.53022
120	0.2808	0.28994
125	0.30697	0.20762
130	0.33456	0.32048
135	0.37451	0.37073
140	0.40219	0.21048

(a) Cut-based analysis

m_H (GeV)	Exp p_0	Obs p_0
100	0.30826	0.56826
110	0.27624	0.53454
115	0.26666	0.46782
120	0.27956	0.57875
125	0.30374	0.5501
130	0.34956	0.37092
135	0.39624	0.45704
140	0.44161	0.62789

(b) MVA analysis

Table 10.3: Expected and observed local p_0 values as a function of m_H for the $E_{\mathrm{T}}^{\mathrm{miss}}$ triggered cut-based and MVA analyses.

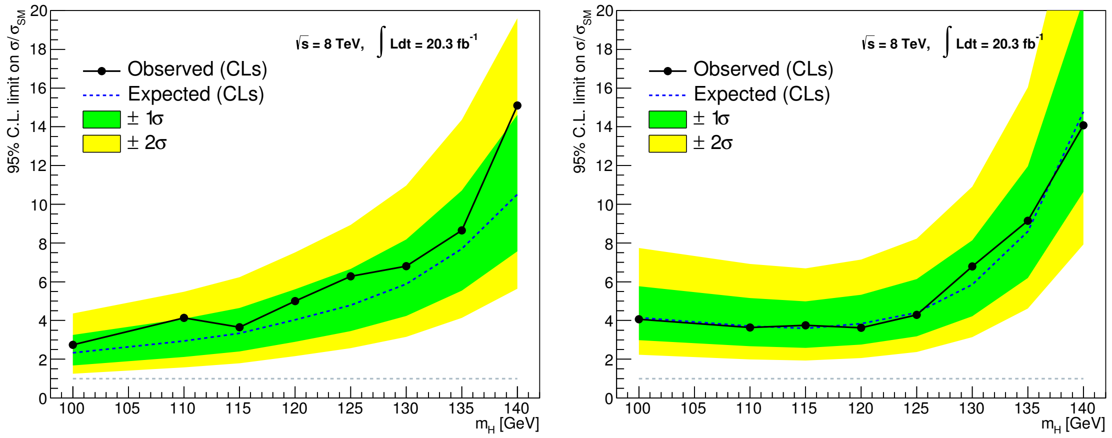

(a) Cut-based analysis

(b) MVA analysis

Figure 10.11: Expected and observed limits from the 95% CL upper bound on the cross section times branching ratio as a function of m_H for the $E_{\mathrm{T}}^{\mathrm{miss}}$ triggered analyses. Values are expressed as a multiple of the standard model expectation. The observed values are shown as a solid line while the expected values, for the background-only case, are shown as a dashed line with the green and yellow shaded areas representing the $\pm 1\sigma$ and $\pm 2\sigma$ shifts from the central expected value. The grey dashed line represents the Standard Model value of $\hat{\mu} = 1.0$.

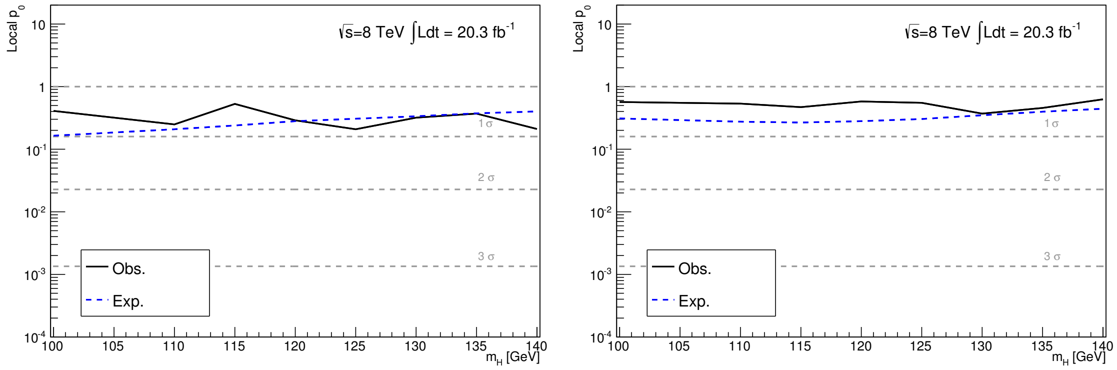

(a) Cut-based analysis

(b) MVA analysis

Figure 10.12: Expected and observed local p_0 values as a function of m_H for the $E_{\mathrm{T}}^{\mathrm{miss}}$ triggered analyses. The observed values are shown as a solid line while the expected values, for a standard model Higgs Boson, are shown as a blue dashed line. Each expected and observed value is calculated using the signal sample at that particular value of m_H. The horizontal dashed lines convert the p_0 values to significance values.

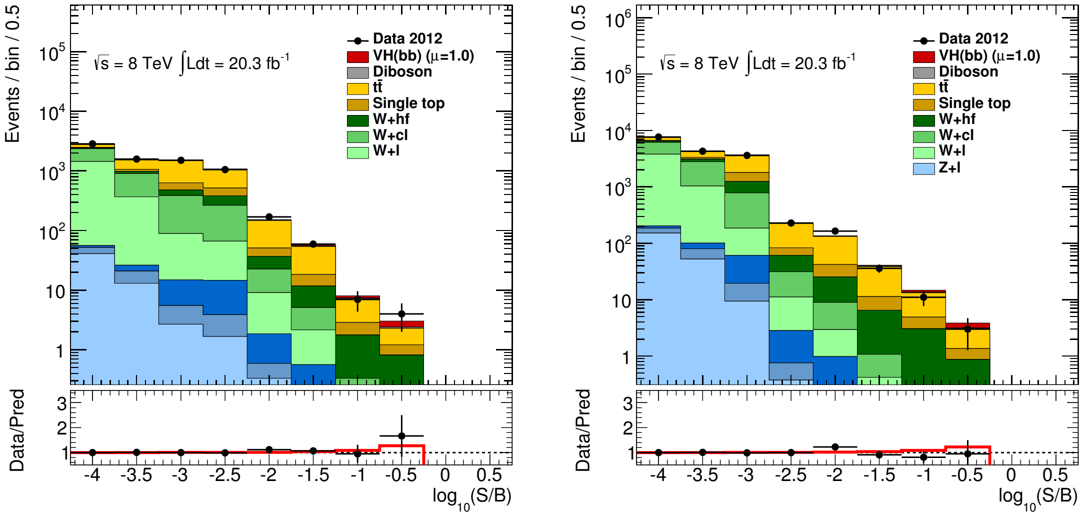

(a) Cut-based (b) MVA

Figure 10.13: Yields ordered by $\log_{10}(S/B)$ for the $E_{\mathrm{T}}^{\mathrm{miss}}$ triggered cut-based and MVA analyses. The bins from all signal regions are combined into bins based on the calculated $\log_{10}(S/B)$ from the postfit background event yields and the expected signal yield. The lower part of each plot shows, through the ratio of data to prediction, the statistical pull of the data as points along with the expected pull from the Standard Model expectation as a red line.

10.3 Combined $WH \rightarrow \ell\nu b\bar{b}$ Results

The Combined dataset, the merging of the $E_{\mathrm{T}}^{\mathrm{miss}}$ triggered and Nominal single lepton triggered datasets, is fitted in the same way as the $E_{\mathrm{T}}^{\mathrm{miss}}$ triggered for the same range of hypothesised Higgs masses as was described in Section 10.2.

The set of results that was produced for the $E_{\mathrm{T}}^{\mathrm{miss}}$ triggered cut-based and MVA analyses is also produced for the Combined cut-based and MVA analyses. The description of the methods used to produce the results, the categories in tables and the contents of figures are the same as in Section 10.2. The limits, as a function of m_H, on the cross section times branching ratio are shown in Table 10.4 and Figure 10.14a for the cut-based analysis and Table 10.5 and Figure 10.14b for the MVA analysis. The local p_0, as a function of m_H, is shown for the cut-based and MVA analyses in Table 10.6 and Figure 10.15. All bins from all fit regions in the cut-based and MVA analyses are combined (separately for the cut-based and MVA analyses) based on the value of $\log_{10}({}^{S}\!/_{B})$ in each bin in Figure 10.16. The observed $\hat{\mu}$ value for the cut-based analysis is $\hat{\mu}_{Cut} = 2.316^{+0.670}_{-0.646}(\text{stat.})^{+0.723}_{-0.608}(\text{syst.})$ and for the MVA analysis is $\hat{\mu}_{MVA} = 1.231^{+0.538}_{-0.511}(\text{stat.})^{+0.499}_{-0.425}(\text{syst.})$. The observed (expected) significance in the cut-based analysis is 2.759 (1.295) and in the MVA analysis is 1.905 (1.534).

m_H (GeV)	Exp.	$+2\sigma$	$+1\sigma$	-1σ	-2σ	Obs.
100	0.81	1.52	1.13	0.59	0.44	1.18
110	0.99	1.85	1.38	0.72	0.53	1.73
115	1.09	2.04	1.52	0.79	0.59	2.01
120	1.28	2.38	1.78	0.92	0.69	2.83
125	1.65	3.08	2.30	1.19	0.89	4.01
130	2.04	3.80	2.83	1.47	1.09	4.24
135	2.64	4.93	3.68	1.91	1.42	4.53
140	3.74	6.99	5.21	2.70	2.01	5.99

Table 10.4: Expected and observed limits from the 95% CL upper bound on the cross section times branching ratio as a function of m_H for the Combined cut-based analysis. Values are expressed as a multiple of the Standard Model expectation. The $\pm 1\sigma$ and $\pm 2\sigma$ shifts from the central expected values are also shown.

m_H (GeV)	Exp.	$+2\sigma$	$+1\sigma$	-1σ	-2σ	Obs.
100	1.54	2.87	2.14	1.11	0.83	2.78
110	1.30	2.43	1.81	0.94	0.70	2.09
115	1.09	2.03	1.51	0.78	0.58	1.91
120	1.15	2.15	1.61	0.83	0.62	2.02
125	1.36	2.54	1.89	0.98	0.73	2.50
130	1.83	3.42	2.55	1.32	0.98	3.06
135	2.81	5.24	3.91	2.02	1.51	5.62
140	5.34	9.96	7.43	3.85	2.86	9.33

Table 10.5: Expected and observed limits from the 95% CL upper bound on the cross section times branching ratio as a function of m_H for the Combined MVA analysis. Values are expressed as a multiple of the Standard Model expectation. The $\pm 1\sigma$ and $\pm 2\sigma$ shifts from the central expected values are also shown.

m_H (GeV)	Exp p_0	Obs p_0
100	0.00751	0.13534
110	0.02021	0.08398
115	0.03104	0.06559
120	0.05237	0.0165
125	0.09766	0.0029
130	0.14747	0.01106
135	0.20927	0.05493
140	0.28367	0.12549

(a) Cut-based analysis

m_H (GeV)	Exp p_0	Obs p_0
100	0.09234	0.0366
110	0.05888	0.07839
115	0.02893	0.04006
120	0.03528	0.0353
125	0.0612	0.02665
130	0.12424	0.05262
135	0.21962	0.01338
140	0.34719	0.0531

(b) MVA analysis

Table 10.6: Expected and observed local p_0 values as a function of m_H for the Combined cut-based and MVA analyses.

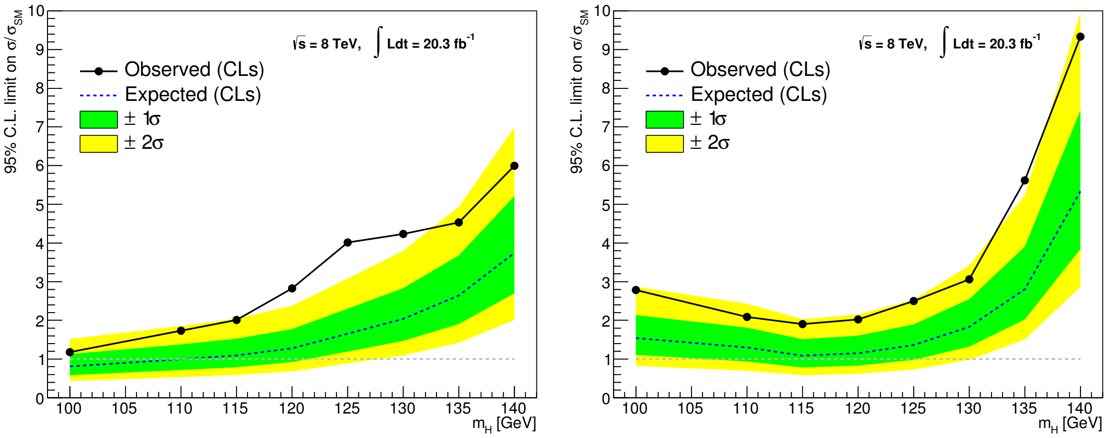

(a) Cut-based analysis

(b) MVA analysis

Figure 10.14: Expected and observed limits from the 95% CL upper bound on the cross section times branching ratio as a function of m_H for the combined analyses. Values are expressed as a multiple of the Standard Model expectation. The observed values are shown as a solid line, while the expected values, for the background only case, are shown as a dashed line with the green and yellow shaded areas representing the $\pm 1\sigma$ and $\pm 2\sigma$ shifts from the central expected values.

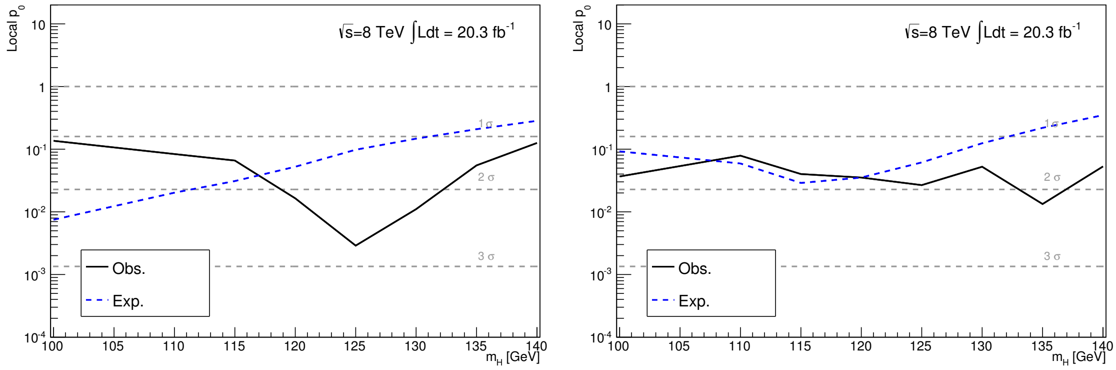

(a) Cut-based

(b) MVA

Figure 10.15: Expected and observed local p_0 values as a function of m_H for the Combined analyses. The observed values are shown as a solid line while the expected values, for a Standard Model Higgs Boson, are shown as a blue dashed line. Each expected and observed value is calculated using the signal sample at that particular value of m_H. The horizontal dashed lines convert the p_0 values to significance values.

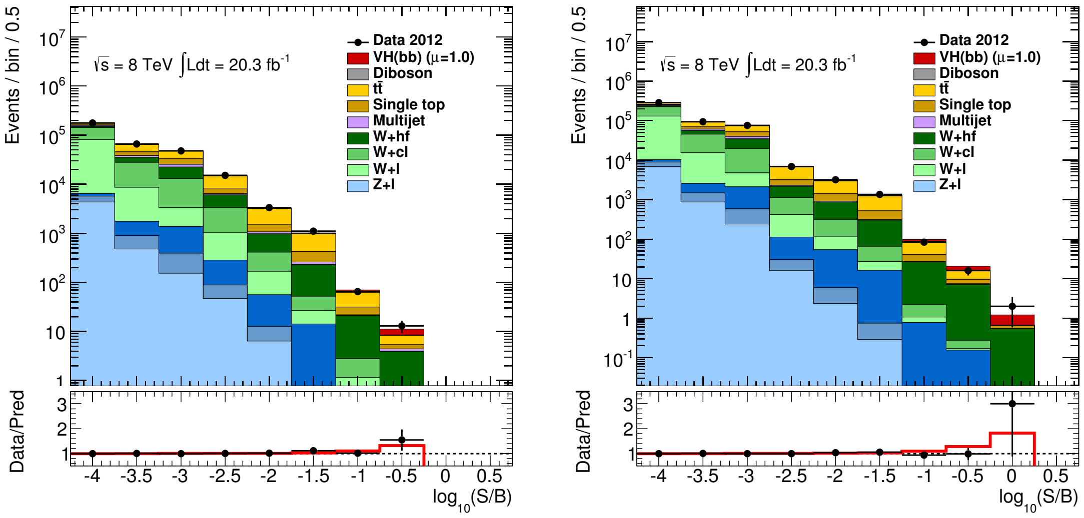

(a) Cut-based

(b) MVA

Figure 10.16: Yields ordered by $\log_{10}(S/B)$ for the Combined cut-based and MVA analyses. The bins from all signal regions are combined into bins based on the calculated $\log_{10}(S/B)$ from the postfit background event yields and the expected signal yield. The lower part of each plot shows, through the ratio of data to prediction, the statistical pull of the data as points along with the expected pull from the Standard Model expectation as a red line.

10.4 Discussion of Results

A summary of the results is provided in Table 10.7 and Table 10.8 for the $E_{\mathrm{T}}^{\mathrm{miss}}$ triggered and Combined analyses, respectively. Results are shown for both the cut-based and MVA analyses at a hypothesised Higgs mass of $m_H = 125$ GeV. The values shown are the 95% CL upper limits on the signal strength, $\hat{\mu}$, where the fit is performed using the Asimov dataset, both excluding and including systematics, and the real datasets as well as the significances obtained from the Asimov and real datasets. The observed central value for the signal strength, $\hat{\mu}$, is also included but with the statistical and systematic errors combined in quadrature to give a single error.

	Cut-based	MVA
Stat-Only Expected Limit	4.168	3.783
Systematics Expected Limit	4.788	4.414
Systematics Observed Limit	6.281	4.303
Expected Significance	0.504	0.508
Observed Significance	0.815	-0.111
$\hat{\mu}$	$1.617^{+2.409}_{-1.946}$	$-0.231^{+2.106}_{-1.792}$

Table 10.7: Summary of the main $E_{\mathrm{T}}^{\mathrm{miss}}$ triggered cut-based and MVA fit results at 95% CL.

	Cut-based	MVA
Stat-Only Expected Limit	1.195	1.022
Systematics Expected Limit	1.654	1.369
Systematics Observed Limit	4.012	2.507
Expected Significance	1.295	1.534
Observed Significance	2.759	1.905
$\hat{\mu}$	$2.316^{+0.986}_{-0.886}$	$1.231^{+0.733}_{-0.665}$

Table 10.8: Summary of the main Combined cut-based and MVA fit results at 95% CL.

10.4.1 Expected Results

The $E_{\mathrm{T}}^{\mathrm{miss}}$ trigger cut-based and MVA analyses provide only weak expected 95% CL upper limits on the cross-section times branching ratio of the $WH, H \rightarrow b\bar{b}$ process, 4.788 and 4.414, respectively. The MVA analysis is more sensitive than the cut-based, giving a gain of 7.3% in the expected limit, so it is the MVA that should be considered as the stronger of the two irrespective of any observed result. The expected values for the MVA are lower, and therefore more sensitive, only for the 120 GeV, 125 GeV, 130 GeV because all masses use the BDT weights trained using the 125 GeV signal sample. Using a training at each mass point to produce results for that mass point should improve the sensitivity of all but the 125 GeV mass point (where this is already true) but requires much larger technical overheads. The expected significance of the MVA is less than a percentage point higher than the cut-based (0.508 compared to 0.504) but neither reach an expected significance above 1σ for any of the mass region, as can be seen from the p_0 plots in Figures 10.12a and 10.12b. The $E_{\mathrm{T}}^{\mathrm{miss}}$ triggered analyses suffer from poor background constraints as can be seen by the high ranking of the nuisance parameters associated with background normalisations in Figure 8.4 from Chapter 8. The other main problem present in the $E_{\mathrm{T}}^{\mathrm{miss}}$ triggered analyses is the lower signal statistics than in the Nominal analyses, causing a large statistical error on final results. Despite the lower sensitivity of the $E_{\mathrm{T}}^{\mathrm{miss}}$ triggered analyses, they still present valuable additional statistics for studying Higgs production and decay in this mode.

The main motivation behind the $E_{\mathrm{T}}^{\mathrm{miss}}$ triggered analyses was not to use them to produce results in isolation from the Nominal analyses, but to instead combine them to increase the sensitivity of the Nominal analysis. This has been done by increasing the signal statistics in the most sensitive regions, at high $p_{\mathrm{T}}(W)$. The Combined analyses have sensitivity close to the Standard Model expected signal, providing expected 95% CL upper limits of 1.654 for the cut-based and 1.369 for the MVA. Both analyses reach closer to 1 at lower Higgs masses. As was the case for the $E_{\mathrm{T}}^{\mathrm{miss}}$

triggered analyses, the sensitivity of the MVA analysis would be improved at masses other than 125 GeV by using the BDT training from each mass. The MVA analysis has a higher sensitivity, giving a 17.2% better expected limit, than the cut-based so should be considered the main result, as in the case of the $E_{\mathrm{T}}^{\mathrm{miss}}$ triggered analyses. The expected significance of the MVA analysis is 18.5% higher than the cut-based at $m_H = 125$ GeV. The MVA analysis has an expected significance between 1σ and 2σ for most of the mass range while the cut-based analysis goes above 2σ for low masses.

The $E_{\mathrm{T}}^{\mathrm{miss}}$ triggered analyses alone are not sensitive enough to distinguish the signal hypothesis from the background-only hypothesis. However, the $E_{\mathrm{T}}^{\mathrm{miss}}$ triggered analyses are very important in improving the sensitivity of the WH search. The Combined cut-based and MVA analyses are more sensitive than the Nominal analyses shown in Appendix C, due to the addition of the $E_{\mathrm{T}}^{\mathrm{miss}}$ triggered events, an increase in sensitivity of 5.1% for the Cut-based analysis and 6.2% for the MVA analysis. This improvement is greater than many of the analysis techniques used in these analyses. The Combined MVA analysis shows the best sensitivity in the search for the $WH \to \ell\nu b\bar{b}$ decay mode so should be considered the strongest WH result. The expected significance of 1.4 in the Nominal analysis (from Appendix C) is improved to 1.5 in the Combined analysis due to the additional yield from the $E_{\mathrm{T}}^{\mathrm{miss}}$ triggered analyses.

10.4.2 Observed Results

The $E_{\mathrm{T}}^{\mathrm{miss}}$ triggered cut-based dataset shows an excess above the background-only expectation, larger than the expected signal from a standard model Higgs boson with a mass of 125 GeV and gives a signal strength $\hat{\mu} = 1.617$ at $m_H = 125$ GeV. The $E_{\mathrm{T}}^{\mathrm{miss}}$ triggered MVA dataset shows a deficit below the background expectation and gives a signal strength $\hat{\mu} = -0.231$ at $m_H = 125$ GeV. The cut-based analysis therefore has a weaker than expected limit on the cross-section times branching of $WH \to \ell\nu b\bar{b}$ across the full mass range and the MVA slightly stronger than expected as shown in Figure 10.11. The excess in the cut-based analysis causes the observed p_0 to be close to the expected for the majority of the mass region, as shown in Figure 10.12a, with the smallest observed p_0 being 0.20762 at $m_H = 125$ GeV compared to an expected value of 0.30697 and giving a significance of 0.815. The deficit in the MVA analysis causes a higher p_0 to be observed than is expected for the entire mass range, as shown in Figure 10.12b, with the smallest observed p_0 being 0.37092 at $m_H = 130$ GeV compared to an expected value of 0.34956. At $m_H = 125$ GeV the observed (expected) p_0 is 0.5501(0.30374). The observed p_0 going above 0.5 means that the data looks like a downward fluctuation of the background, an opposite effect to the signal expectation. A p_0 above 0.5 is interpreted as a negative significance, in this case yielding a significance of -0.111.

The source of the excess and deficit in the $E_{\mathrm{T}}^{\mathrm{miss}}$ triggered analyses can be seen in Figure 10.16. In the cut-based analysis the portion with the highest S/B, the last filled bin, shows an excess above the background larger than the Standard Model signal expectation. The excess can not be seen in individual analysis regions or bins, as the bins that contribute to the highest S/B region have very low (< 1) expected yields. In the MVA analysis the highest S/B bin, the last filled bin, contains 3 data events, which fall almost exactly on the background-only expectation, while the next two, lower S/B, bins have a deficit compared with the background expectation.

The Combined cut-based dataset shows an excess above the background expectation larger than the expected signal from a standard model Higgs boson with a mass of 125 GeV and gives a signal strength $\hat{\mu} = 2.316$ at $m_H = 125$ GeV. The Combined MVA dataset shows an excess above the background expectation similar to the expected signal from a standard model Higgs boson with a mass of 125 GeV and gives a signal strength $\hat{\mu} = 1.231$ at $m_H = 125$ GeV. This causes weaker than expected limits to be set on the cross section times branching ratio of the $WH \to \ell\nu b\bar{b}$ for both analyses as shown in Figure 10.14. The cut-based observed limit is high across most of the mass range due to the wide resolution of the di-b-jet mass and furthest from the expected at $m_H = 125$ GeV where the observed (expected) limit is 4.01 (1.65) times the standard model expectation. The observed MVA limit is close to the $+2\sigma$ error from the expected throughout the full mass range with an observed (expected) limit of 2.50 (1.36) at $m_H = 125$ GeV. The resolution of the different Higgs mass MVA distributions has not been tested so it is not known whether it is expected that a signal at $m_H = 125$ GeV would cause the broad excess observed. There is a large excess in the cut-based analysis, which causes a much smaller than expected p_0 for much of the mass range, as shown in Figure 10.15a, with the smallest being 0.0029 at $m_H = 125$ GeV compared to an expected value of 0.09766, which gives an overall observed significance of 2.759. The broad excess in the MVA analysis leads to low observed p_0 values across the full mass range, much of which is below the expected, as shown in Figure 10.15b. The observed p_0 is 0.01338 at $m_H = 135$ GeV compared to an expected value of 0.21962. The observed (expected) p_0 at $m_H = 125$ GeV is 0.02665 (0.0612), which gives an observed significance of 1.905.

The source of the excess in each of the Combined analyses can be seen in Figure 10.16. In the cut-based analysis the largest difference between data and background expectation occurs in the bin with the highest $^{S}/_{B}$, the last filled bin, where the data falls higher than the background and Standard Model signal expectation with an excess also observed in the third bin from the right. The MVA analysis has an excess in the bin with the highest $^{S}/_{B}$, the last filled bin, although the next two bins are very close to the background expectation. The excess is from analysis bins with a very high $^{S}/_{B}$ where the approximately 1 additional data event is very significant. The main result from the Combined MVA analysisis $\hat{\mu} = 1.231^{+0.733}_{-0.665}$ with an observed significance of 1.905. This result is closer to the Standard Model signal hypothesis than the background-only hypothesis but is still not inconsistent with the background only.

The consistency of the Combined cut-based and MVA analyses can be evaluated using the method described in Chapter 9. Bootstrapped pseudodatasets were not produced for the $E_{\mathrm{T}}^{\mathrm{miss}}$ triggered analyses so for this estimate the value for the

Nominal analysis will be used. It is therefore assumed that the correlation for the Combined is distributed in the same way as for the Nominal. The difference between the values of $\hat{\mu}$ from the cut-based and MVA analyses is 1.085, which is compared to the standard deviation of the difference of the bootstrapped Nominal analyses, calculated previously in Section 9.5 to be 0.568. This gives a 1.91σ difference between the cut-based and MVA analysis, a two tailed consistency of 5.6%.

10.5 Comparison of Results

The main result obtained from the Combined MVA analysis can be compared to existing results in this channel as well as global Higgs searches and measurements. The final Tevatron result was a combination between all $VH, H \to b\bar{b}$ channels from both CDF and D0 and measured a signal strength of $\hat{\mu} = 1.59^{+0.69}_{-0.72}$ with 2.8 σ significance at $m_H = 125$ GeV [23]. This appears to be compatible with the result presented in this chapter but the comparison is not especially helpful because of the very different energy and initial state ($p\bar{p}$ compared to pp). The calculations that go into the Standard Model prediction for the Tevatron case compared to the LHC are somewhat different so cannot be directly compared. A comparison with current results from ATLAS and CMS is more helpful.

The observed signal strength for each of the $VH, H \to b\bar{b}$ channels as well as the combination observed by ATLAS and CMS separately are shown in Figure 10.17. The global picture of Higgs signal strength was shown in Section 2.4: ATLAS has a combined signal strength of $\hat{\mu} = 1.30^{+0.18}_{-0.17}$ and CMS has a corresponding value of $\hat{\mu} = 1.00 \pm 0.13$. The result presented here of $\hat{\mu} = 1.23^{+0.73}_{-0.67}$ is closer to the ATLAS combined result but the error band covers both the ATLAS and CMS combined results.

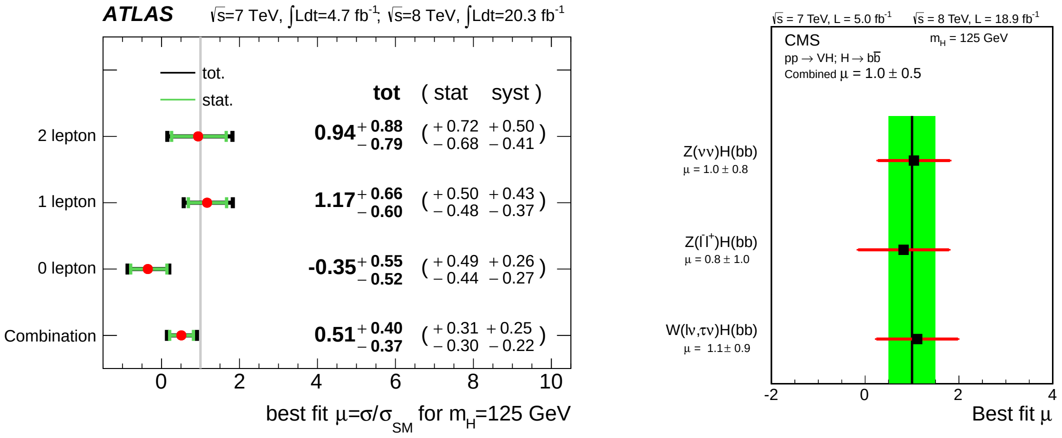

(a) ATLAS (b) CMS

Figure 10.17: Signal strengths observed by ATLAS and CMS for the $VH, H \rightarrow b\bar{b}$ decay modes, expressed as a multiple of the Standard Model expectation [40, 41].

10.5.1 Position within ATLAS VH

ATLAS measures a signal strength $\hat{\mu} = 1.17^{+0.66}_{-0.66}$ for $WH \rightarrow \ell\nu b\bar{b}$ which, when combined with $ZH \rightarrow \nu\nu b\bar{b}$ and $ZH \rightarrow \ell\ell b\bar{b}$, gives a signal strength for $VH, H \rightarrow b\bar{b}$ of $\hat{\mu} = 0.51^{+0.41}_{-0.37}$ [40]. The result presented here is a part of that result so a full comparison is not particularly valid. The ATLAS result contains both 7 TeV and 8 TeV analyses, whereas the result presented here is based only on 8 TeV data. The ATLAS result has some pull from the 7 TeV dataset as well as the pulls from the background normalisations in the $ZH \rightarrow \nu\nu b\bar{b}$ and $ZH \rightarrow \ell\ell b\bar{b}$ channels, but the majority of the events that strongly contribute to the result are the same. The movement of $\hat{\mu}$ due to these pulls is not large so the result presented here is very close to the ATLAS WH cross section times branching ratio within the full VH analysis.

The full $VH, H \rightarrow b\bar{b}$ result of $\hat{\mu} = 0.51^{+0.41}_{-0.37}$ is fairly different to the result presented in this chapter due to the downward pull of the other two $VH, H \rightarrow b\bar{b}$ channels but is consistent within errors. The ATLAS result for the 3 channels combined gives an observed (expected) significance of 1.4 (2.6) while the result presented here has an observed (expected) significance of 1.9 (1.5). The ATLAS analysis is clearly more sensitive due to the addition of both ZH decay modes, but as these pull the WH mode downwards, the observed significance is lower.

10.5.2 Comparison to CMS VH

CMS measures a signal strength of $\hat{\mu} = 1.1 \pm 0.9$ for $WH \to (\ell\nu, \tau\nu)b\bar{b}$ which, when combined with $ZH \to \nu\nu b\bar{b}$ and $ZH \to \ell\ell b\bar{b}$, gives a signal strength for $VH, H \to b\bar{b}$ of $\hat{\mu} = 1.0 \pm 0.5$ [41]. The CMS $WH, H \to b\bar{b}$ and combined $VH, H \to b\bar{b}$ results are very consistent with the result presented here, the $WH, H \to b\bar{b}$ having only a small difference in the observed signal strength and well within errors. The CMS WH result has an observed (expected) significance of 1.4 (1.3). This is slightly worse than the expected limit of 1.4 obtained using the ATLAS Nominal 8 TeV WH analysis only, as shown in Table C.4 in Appendix C. The addition of the $E_{\mathrm{T}}^{\mathrm{miss}}$ triggered regions gains approximately a further 8% in sensitivity, on top of the already better ATLAS sensitivity, which is not a technique used by CMS.

10.6 Conclusion

The $E_{\mathrm{T}}^{\mathrm{miss}}$ triggered analyses have been shown to be useful for recovering events lost in the Nominal WH analyses but do not produce sensitive results on their own. The $E_{\mathrm{T}}^{\mathrm{miss}}$ triggered analyses do, however, provide an important improvement in the sensitivity of the Nominal analyses when merged together to produce the Combined analyses. The Combined MVA analysis is the most sensitive of the different analyses, having an expected limit of 1.369 and an expected significance of 1.534 at $m_H =$ 125 GeV. This analysis measures a signal strength $\hat{\mu} = 1.231^{+0.733}_{-0.665}$ with an observed significance of 1.905. This result is most consistent with the standard model signal hypothesis but does not exclude the background-only hypothesis. The VH analyses are not sensitive enough with the Run I 7 TeV and 8 TeV datasets to make a significant observation of these decay modes. The upcoming Run II data at a higher centre-of-mass energy will therefore be required to make a concrete statement on $VH, H \rightarrow b\bar{b}$ production and will probably need to be combined with the Run I data. All current analysis techniques, including the use of the $E_{\mathrm{T}}^{\mathrm{miss}}$ triggered events, will be required as well as possible improvements. The prospects for VH measurements (using only the $WH \rightarrow \ell\nu b\bar{b}$ and $ZH \rightarrow \ell\ell b\bar{b}$ modes) in Run II are outlined in [116]. The expected significance for a dataset of 300 fb^{-1} is 3.9 σ with an expected error of 25% on the value of $\hat{\mu}$.

CHAPTER 11

Summary and Conclusions

This thesis contains a search for the Standard Model Higgs Boson with the ATLAS experiment at the LHC using the $WH \to \ell\nu b\bar{b}$ production and decay mode.

The studies of the L1Calo bunch crossing identification efficiency, using data recorded during the LHC 2010 Heavy Ion run, were shown in Chapter 6. All partitions of the ATLAS calorimeters were shown to reach near full efficiency (plateaued above 98%) for calorimeter deposits above $\mathrm{E_T} = 3$ GeV. The efficiency was also measured for individual L1Calo pulse heights. Some L1Calo trigger towers were found to have significantly worse performance than others in the same partition. These towers were found to have misformed pulse shapes, the cause of which was determined to be cross talk from the MBTS trigger signal. This study contributed to the decision to disable the MBTS signals.

Chapter 7 described the $E_{\mathrm{T}}^{\mathrm{miss}}$ triggered $WH \to \mu\nu b\bar{b}$ analyses. Two analyses, which share a large degree of similarity, were described: the cut-based analysis and the more complex MVA analysis, which uses a BDT to separate the signal and background. Both analyses use the 2012 LHC data recorded at a centre-of-mass energy of $\sqrt{s} = 8$ TeV. Events selected by the analyses were split into separate regions based on the reconstructed $p_{\mathrm{T}}(W)$ in each event and the b-tagging operating points passed by both jets to produce regions with improved S/B while also maintaining signal efficiency.

The fit model used to extract results from the $E_{\mathrm{T}}^{\mathrm{miss}}$ triggered and Combined cut-based and MVA analyses was described in Chapter 8, including the regions and systematics used in the likelihood-based fit. The pulls of the different contributions to the systematic uncertainty were shown for the $E_{\mathrm{T}}^{\mathrm{miss}}$ triggered analyses and nuisance parameter ranking was shown for the $E_{\mathrm{T}}^{\mathrm{miss}}$ triggered and Combined analyses. The W boson plus heavy flavour jets based nuisance parameters, particularly the normalisations, were generally those ranked as having the largest effect on the fitted value of the $WH \to \ell\nu b\bar{b}$ signal strength, $\hat{\mu}$.

The same fit model was used in Chapter 9 to investigate the correlation between the three VH analysis channels ($ZH \to \nu\nu b\bar{b}$,$WH \to \ell\nu b\bar{b}$ and $ZH \to \ell\ell b\bar{b}$) with some additions to the model for correlations/decorrelations. Pairs of statistically linked pseudo-datasets were created for the different cut-based and MVA analyses by the VH analysis groups using the modified bootstrap method. The correlation was calculated for the signal strength, $\hat{\mu}$, as well as for nuisance parameters of the fit. A high degree of correlation is observed for each of the VH channels, the highest being for $ZH \to \nu\nu b\bar{b}$, as well as in the full VH fits.

The results for the $E_{\mathrm{T}}^{\mathrm{miss}}$ triggered and Combined cut-based and MVA analyses are shown in Chapter 10. Limits on the $WH \to \ell\nu b\bar{b}$ signal strength were calculated as a function of Higgs mass, along with the p_0 value, signal strength ($\hat{\mu}$) and signal significance for all analyses. The $E_{\mathrm{T}}^{\mathrm{miss}}$ triggered analyses had only weak background constraints and a smaller signal expectation than the Nominal analyses. The overall observed (expected) limit is 6.281 (4.788) in the cut-based $E_{\mathrm{T}}^{\mathrm{miss}}$ triggered analysis and 4.303 (4.414) in the MVA analysis.

The main purpose of the $E_{\mathrm{T}}^{\mathrm{miss}}$ triggered analyses was not to extract results exclusively but to improve the signal statistics and sensitivity of the Nominal analyses. The sensitivity of the Combined cut-based analysis is 5.1% higher than the Nominal due to the addition of the $E_{\mathrm{T}}^{\mathrm{miss}}$ triggered events. The increase in sensitivity is 6.2% in the MVA analysis, higher than for the cut-based analysis. The Combined MVA analysis is the most sensitive of the analyses presented, giving a 17.2% better expected limit and an 18.5% higher expected significance than the cut-based analysis. The MVA observed (expected) limit is 2.507 (1.369) and the observed (expected) significance is 1.905 (1.534). The final value of the signal strength for the $WH \to \ell\nu b\bar{b}$ analysis is $\hat{\mu} = 1.231^{+0.733}_{-0.665}$. The consistency with the less sensitive cut-based result of $2.316^{+0.986}_{-0.886}$ is estimated to be 5.6%, assuming that the study of the Nominal $WH \to \ell\nu b\bar{b}$ analysis found in Chapter 9 holds true for the Combined.

The $WH \to \ell\nu b\bar{b}$ analyses do not yet have sensitivity at the Standard Model level, whilst the full $VH, H \to b\bar{b}$ analyses in ATLAS and CMS can currently make no conclusive statement of this mode. The VH channels are a very important test of the Standard Model Higgs Boson, which has been observed in other channels and should therefore by a high priority for the LHC Run II. All VH channels, including the recovery of events using $E_{\mathrm{T}}^{\mathrm{miss}}$ triggers, will be important in studying the $VH, H \to b\bar{b}$ mode [116].

REFERENCES

[1] J. Beringer et al., *The Review of Particle Physics*, Phys. Rev. **D86** (2012) .

[2] A. Martin, W. Stirling, R. Thorne, and G. Watt, *Parton distributions for the LHC*, Eur.Phys.J. **C63** (2009) 189–285.

[3] S. L. Glashow, *Partial Symmetries of Weak Interactions*, Nucl. Phys. **22** (1961) 579–588.

[4] S. Weinberg, *A Model of Leptons*, Phys. Rev. Lett. **19** (1967) 1264–1266.

[5] A. Salam, *in Elementary Particle Theory.* Almqvist and Wiksell, Stockholm, 1968.

[6] P. W. Higgs, *Broken Symmetries and the Masses of Gauge Bosons*, Phys. Rev. Lett. **13** (1964) 508.

[7] F. Englert and R. Brout, *Broken Symmetry and the Mass of Gauge Vector Mesons*, Phys. Rev. Lett. **13** (1964) 321.

[8] G. Guralnik, C. Hagen, and T. Kibble, *Global Conservation Laws and Massless Particles*, Phys. Rev. Lett. **13** (1964) 585.

[9] L. Alvarez-Gaume and J. Ellis, *Eyes on a prize particle*, Nat Phys **7** (2011) 2.

[10] P. W. Higgs, *Broken Symmetries, Massless Particles and Gauge Fields*, Phys. Lett. **12** (1964) 132.

[11] T. Appelquist, J. Terning, and L. Wijewardhana, *Postmodern technicolor*, Phys.Rev.Lett. **79** (1997) 2767–2770.

[12] K. Yamawaki, *Top quark condensate revisited*, Prog.Theor.Phys.Suppl. **123** (1996) 19–36.

[13] B. W. Lee, C. Quigg, and H. B. Thacker, *Weak interactions at very high energies: The role of the Higgs-boson mass*, Phys. Rev. D **16** (1977) .

[14] P. Freund, *Introduction to Supersymmetry.* Cambridge University Press, 1988.

[15] The ATLAS Collaboration, *Expected Performance of the ATLAS Experiment - Detector, Trigger and Physics - Physics*, Tech. Rep. CERN-OPEN-2008-020, CERN, Geneva, 2008.

[16] LHC Higgs Cross Section Working Group, *Handbook of LHC Higgs Cross Sections: 3. Higgs Properties: Report of the LHC Higgs Cross Section Working Group*, Tech. Rep. CERN-2013-004, CERN, Geneva, 2013.

[17] T. Muta, *Foundations of quantum chromodynamics: an introduction to perturbative methods in gauge theories.* World Scientific, 2009.

[18] A. H. M. Yu. L. Dokshitzer, V. A. Khoze and S. I. Troyan, *Basics of Perturbative QCD.* Editions Frontieres, 1991.

[19] B. Andersson, G. Gustafson, G. Ingelman, and T. Sjstrand, *Parton fragmentation and string dynamics*, Physics Reports **97** (1983) .

[20] W.-M. Y. etal, *Review of Particle Physics*, Journal of Physics G: Nuclear and Particle Physics **33** (2006) .

[21] LEP Working Group for Higgs boson searches, ALEPH Collaboration, DELPHI Collaboration, L3 Collaboration, OPAL Collaboration, *Search for the standard model Higgs boson at LEP*, Phys.Lett. **B565** (2003) 61–75 CERN-EP-2003-011.

[22] The ALEPH, DELPHI, L3, OPAL, SLD Collaborations, the LEP Electroweak Working Group, the SLD Electroweak and Heavy Flavour Groups, *Precision Electroweak Measurements on the Z Resonance*, Phys. Rept. **427** (2006) 257.

[23] D. C. CDF Collaboration, *Higgs Boson Studies at the Tevatron*, Phys.Rev. **D88** (2013) 052014.

[24] ATLAS Collaboration, *Observation of an Excess of Events in the Search for the Standard Model Higgs boson with the ATLAS detector at the LHC*, Tech. Rep. ATLAS-CONF-2012-093, CERN, Geneva, Jul, 2012.

[25] CMS Collaboration, *Observation of a new boson with a mass near 125 GeV*, Tech. Rep. CMS-PAS-HIG-12-020, CERN, Geneva, 2012.

[26] G. T. Bodwin, F. Petriello, S. Stoynev, and M. Velasco, *Higgs boson decays to quarkonia and the $H\bar{c}c$ coupling*, Phys.Rev. **D88** (2013) 053003.

[27] ATLAS Collaboration, *Measurement of Higgs boson production in the diphoton decay channel in pp collisions at center-of-mass energies of 7 and 8 TeV with the ATLAS detector*, CERN-PH-EP-2014-198.

[28] ATLAS Collaboration, *Measurement of the Higgs boson mass from the* $H \to \gamma\gamma$ *and* $H \to ZZ^* \to 4\ell$ *channels in pp collisions at center-of-mass energies of 7 and 8 TeV with the ATLAS detector*, Phys. Rev. D **90** (2014) 052004.

[29] CMS Collaboration, *Observation of the diphoton decay of the Higgs boson and measurement of its properties*, The European Physical Journal C **74** (2014) no. 10, .

[30] ATLAS Collaboration, *Measurements of Higgs boson production and couplings in the four-lepton channel in pp collisions at center-of-mass energies of 7 and 8 TeV with the ATLAS detector*, CERN-PH-EP-2014-170.

[31] CMS Collaboration, *Measurement of the properties of a Higgs boson in the four-lepton final state*, Phys. Rev. D **89** (2014) 45.

[32] CMS Collaboration, *Measurement of Higgs boson production and properties in the WW decay channel with leptonic final states*, JHEP **1401** (2014) 096 CMS-HIG-13-023, CERN-PH-EP-2013-221.

[33] ATLAS Collaboration, *Observation and measurement of Higgs boson decays to* WW^* *with the ATLAS detector*, .

[34] ATLAS Collaboration, *Search for Higgs boson decays to a photon and a Z boson in pp collisions at* $\sqrt{s}$*=7 and 8 TeV with the ATLAS detector*, Phys.Lett. **B732** 8–27.

[35] CMS Collaboration, *Search for a Higgs boson decaying into a Z and a photon in pp collisions at* $\sqrt{s} = 7$ *and 8 TeV*, Phys.Lett. **B726** (2013) 587–609.

[36] CMS Collaboration, *Evidence for the 125 GeV Higgs boson decaying to a pair of* τ *leptons*, Journal of High Energy Phys. **05** (2014) 104.

[37] ATLAS Collaboration, *Evidence for Higgs boson Yukawa couplings in the* $H \to \tau\tau$ *decay mode with the ATLAS detector*, .

[38] CMS Collaboration, CMS, *Search for ttH production using the Matrix Element Method*, CMS-PAS-HIG-14-010.

[39] ATLAS Collaboration, *Search for the Standard Model Higgs boson produced in association with top quarks and decaying to* $b\bar{b}$ *in pp collisions at* $\sqrt{s} = 8$ *TeV with the ATLAS detector at the LHC*, .

[40] ATLAS Collaboration, *Search for the* $b\bar{b}$ *decay of the Standard Model Higgs boson in associated* $(W/Z)H$ *production with the ATLAS detector*, ATLAS-HIGG-2013-23, CERN-PH-EP-2014-214.

[41] CMS Collaboration, *Search for the standard model Higgs boson produced in association with a W or a Z boson and decaying to bottom quarks*, Phys.Rev. **D89** (2014) 012003.

[42] ATLAS Collaboration, *A Search for Light CP-Odd Higgs Bosons Decaying to* $\mu^+\mu^-$ *in ATLAS*, Tech. Rep. ATLAS-CONF-2011-020, CERN, Geneva, Mar, 2011.

[43] ATLAS Collaboration, *Search for the Standard Model Higgs boson decay to* $\mu^+\mu^-$ *with the ATLAS detector*, CERN-PH-EP-2014-131.

[44] CMS Collaboration, *Search for a standard model-like Higgs boson in the* $\mu^+\mu^-$ *and* $\mathrm{e}^+\mathrm{e}^-$ *decay channels at the LHC*, .

[45] ATLAS Collaboration, *Updated coupling measurements of the Higgs boson with the ATLAS detector using up to 25* fb^{-1} *of proton-proton collision data*, Tech. Rep. ATLAS-CONF-2014-009, CERN, Geneva, Mar, 2014.

[46] CMS Collaboration, *Combination of standard model Higgs boson searches and measurements of the properties of the new boson with a mass near 125 GeV*, Tech. Rep. CMS-PAS-HIG-13-005, CERN, Geneva, 2013.

[47] CMS Collaboration, *Precise determination of the mass of the Higgs boson and studies of the compatibility of its couplings with the standard model*, Tech. Rep. CMS-PAS-HIG-14-009, CERN, Geneva, 2014.

[48] CMS Collaboration, *Constraints on the Higgs boson width from off-shell production and decay to Z-boson pairs*, Phys.Lett. **B736** (2014) 64.

[49] T. S. Pettersson and P. Lefevre, *The Large Hadron Collider: Conceptual Design*, Tech. Rep. CERN-AC-95-05, CERN, Geneva, 1995.

[50] T. S. Pettersson and P. Lefvre, *The Large Hadron Collider: conceptual design*, Tech. Rep. CERN-AC-95-05 LHC, CERN, Geneva, Oct, 1995.

[51] L. Evans et al., *The LHC Machine*, JINST **3** (2008) S08001.

[52] LHCb Collaboration, *The LHCb Detector at the CERN LHC*, JINST **3** (2008) S08005.

[53] ALICE Collaboration, *The ALICE Experiment at the CERN LHC*, JINST **3** (2008) S08002.

[54] CMS Collaboration, *The CMS Experiment at the CERN LHC*, JINST **3** (2008) S08004.

[55] ATLAS Collaboration, *The ATLAS Experiment at the CERN Large Hadron Collider*, JINST **3** (2008) S08003.

[56] The ATLAS Collaboration, *The ATLAS Detector*, tech. rep., CERN, 2014. `http://www.atlas.ch/photos/index.html`.

[57] M. Capeans, G. Darbo, K. Einsweiller, M. Elsing, T. Flick, M. Garcia-Sciveres, C. Gemme, H. Pernegger, O. Rohne, and R. Vuillermet, *ATLAS Insertable B-Layer Technical Design Report*, Tech. Rep. CERN-LHCC-2010-013. ATLAS-TDR-19, CERN, Geneva, Sep, 2010.

[58] C. Fabjan, *Calorimetry in High-energy Physics, in: Experimental Techniques in Nuclear and Particle Physics.* World Scientific, 1991.

[59] ATLAS Collaboration, *ATLAS calorimeter performance*, Tech. Rep. CERN-LHCC-96-40.

[60] The ATLAS Collaboration, *Liquid Argon Calorimeter - Technical Design Report*, Tech. Rep. CERN-LHCC-1996-41, CERN, Geneva, 1996.

[61] M. Aleksa, F. Bergsma, P. A. Giudici, A. Kehrli, M. Losasso, X. Pons, H. Sandaker, P. S. Miyagawa, S. W. Snow, J. C. Hart, and L. Chevalier, *Measurement of the ATLAS solenoid magnetic field*, JINST **3** (2008) .

[62] The ATLAS Collaboration, *Magnetic Field*, tech. rep., CERN, 2014. `http://atlas.web.cern.ch/Atlas/GROUPS/MUON/magfield/mag_page1.html`.

[63] The ATLAS Collaboration, *First Level Trigger - Technical Design Report*, Tech. Rep. CERN-LHCC-1998-14, CERN, Geneva, 1998.

[64] The ATLAS Collaboration, *Expected Performance of the ATLAS Experiment - Detector, Trigger and Physics - Trigger*, Tech. Rep. CERN-OPEN-2008-020, CERN, Geneva, 2008.

[65] ATLAS Collaboration, *Preliminary Luminosity Determination in pp Collisions at sqrt(s) = 8 TeV using the ATLAS Detector in 2012*, Tech. Rep. ATL-COM-LUM-2012-013, CERN, Geneva, Nov, 2012.

[66] E. F. Eisenhandler, *ATLAS Level-1 Calorimeter Trigger Algorithms*, Tech. Rep. ATL-DAQ-2004-011, CERN, Geneva, Sep, 2004.

[67] D. R. Hadley, *Digital Filtering Performance in the ATLAS Level-1 Calorimeter Trigger*, Tech. Rep. ATL-DAQ-PROC-2010-012, CERN, Geneva, Jun, 2010.

[68] J. Garvey and D. Rees, *Bunch Crossing Identification for the ATLAS Level - 1 Calorimeter Trigger*, Tech. Rep. ATL-DAQ-96-051, CERN, Geneva, May, 1996.

[69] A. Farbin, *ATLAS analysis model*, Journal of Physics: Conference Series **119** (2008) .

[70] *L1Calo Ntuple Example*, `https://twiki.cern.ch/twiki/bin/view/Atlas/LevelOneCaloD3pdExample`.

[71] B. Åsman, R. Achenbach, B. M. M. Allbrooke, G. Anders, V. Andrei, V. Büscher, H. S. Bansil, B. M. Barnett, B. Bauss, K. Bendtz, C. Bohm, J. Bracinik, I. P. Brawn, R. Brock, W. Buttinger, R. Caputo, S. Caughron, L. Cerrito, D. G. Charlton, J. T. Childers, C. J. Curtis, A. C. Daniells, A. O. Davis, Y. Davygora, M. Dorn, S. Eckweiler, D. Edmunds, J. P. Edwards, E. Eisenhandler, K. Ellis, Y. Ermoline, F. Föhlisch, P. J. W. Faulkner, W. Fedorko, J. Fleckner, S. T. French, C. N. P. Gee, A. R. Gillman, C. Goeringer, T. Hülsing, D. R. Hadley, P. Hanke, R. Hauser, S. Heim, S. Hellman, R. S. Hickling, A. Hidvégi, S. J. Hillier, J. I. Hofmann, I. Hristova, W. Ji, M. Johansen, M. Keller, A. Khomich, E. E. Kluge, J. Koll, H. Laier, M. P. J. Landon, V. S. Lang, P. Laurens, F. Lepold, J. N. Lilley, J. T. Linnemann, F. Müller, T. Müller, K. Mahboubi, T. A. Martin, A. Mass, K. Meier, C. Meyer, R. P. Middleton, T. Moa, S. Moritz, J. D. Morris, R. D. Mudd, R. Narayan, M. zur Nedden, A. Neusiedl, P. R. Newman, A. Nikiforov, C. C. Ohm, V. J. O. Perera, U. Pfeiffer, P. Plucinski, S. Poddar, D. P. F. Prieur, W. Qian, P. Rieck, E. Rizvi, D. P. C. Sankey, U. Schäfer, V. Scharf, K. Schmitt, C. Schröder, H. C. Schultz-Coulon, C. Schumacher, R. Schwienhorst, S. B. Silverstein, E. Simioni, G. Snidero, R. J. Staley, R. Stamen, P. Stock, M. C. Stockton, C. L. A. Tan, S. Tapprogge, J. P. Thomas, P. D. Thompson, M. Thomson, P. True, P. M. Watkins, A. T. Watson, M. F. Watson, P. Weber, M. Wessels, C. Wiglesworth, and S. L. Williams, *The ATLAS Level-1 Calorimeter Trigger: PreProcessor implementation and performance*, JINST **7** .

[72] S. Agostinelli et al., *GEANT4: A Simulation toolkit*, Nucl.Instrum.Meth. **A506** (2003) 250–303 SLAC-PUB-9350, FERMILAB-PUB-03-339.

[73] A. Rimoldi and A. Dell'Acqua, *The Full detector simulation for the ATLAS experiment: Status and outlook*, eConf **C0303241** (2003) CHEP-2003-TUMT001.

[74] ATLAS Collaboration, *The ATLAS Simulation Infrastructure*, Eur. Phys. J **C70** (2010) 823.

[75] E. Richter-Was, D. Froidevaux, and L. Poggioli, *ATLFAST 2.0 a fast simulation package for ATLAS*, Tech. Rep. ATL-PHYS-98-131, CERN, Geneva, Nov, 1998.

[76] T. Sjostrand, S. Mrenna, and P. Z. Skands, *A Brief Introduction to PYTHIA 8.1*, Comput.Phys.Commun. **178** (2008) CERN-LCGAPP-2007-04, LU-TP-07-28, FERMILAB-PUB-07-512-CD-T.

[77] *Summary of ATLAS Pythia 8 tunes*, Tech. Rep. ATL-PHYS-PUB-2012-003, CERN, Geneva, Aug, 2012.

[78] A. Sherstnev and R. Thorne, *Parton Distributions for LO Generators*, Eur. Phys. J. **C55** (2008) 553–575.

[79] J. Pumplin, D. Stump, J. Huston, H. Lai, P. M. Nadolsky, et al., *New generation of parton distributions with uncertainties from global QCD analysis*, JHEP **0207** (2002) 012.

[80] P. Golonka and Z. Was, *PHOTOS Monte Carlo: A Precision tool for QED corrections in Z and W decays*, Eur.Phys.J. **C45** (2006) 97–107.

[81] Z. Was, *TAUOLA the library for tau lepton decay*, Nucl.Phys.Proc.Suppl. **98** (2001) 96–102.

[82] A. Djouadi, J. Kalinowski, and M. Spira, *HDECAY: A program for Higgs boson decays in the Standard Model and its supersymmetric extension*, Comput. Phys. Commun. **108** (1998) 56–74, `arXiv:hep-ph/9704448 [hep-ph]`.

[83] LHC Higgs Cross Section Working Group, S. Dittmaier, C. Mariotti, G. Passarino, and R. Tanaka (Eds.), *Handbook of LHC Higgs Cross Sections: 2. Differential Distributions*, CERN-2012-002 (2012) .

[84] T. Gleisberg et al., *Event generation with SHERPA 1.1*, JHEP **02** (2009) 007.

[85] H.-L. Lai, M. Guzzi, J. Huston, Z. Li, P. M. Nadolsky, et al., *New parton distributions for collider physics*, Phys.Rev. **D82** (2010) .

[86] S. Alioli, P. Nason, C. Oleari, and E. Re, *A general framework for implementing NLO calculations in shower Monte Carlo programs: the POWHEG BOX*, JHEP **06** (2010) 043.

[87] ATLAS Collaboration, *New ATLAS event generator tunes to 2010 data*, ATL-PHYS-PUB-2011-008.

[88] B. P. Kersevan and E. Richter-Was, *The Monte Carlo event generator AcerMC version 2.0 with interfaces to PYTHIA 6.2 and HERWIG 6.5*, TPJU-6-2004.

[89] ATLAS Collaboration, *Measurement of the muon reconstruction performance of the ATLAS detector using 2011 and 2012 LHC proton-proton collision data*, CERN-PH-EP-2014-151, `arXiv:1407.3935 [hep-ex]`.

[90] ATLAS Collaboration, *Electron efficiency measurements with the ATLAS detector using the 2012 LHC proton-proton collision data*, ATLAS-CONF-2014-032.

[91] M. Cacciari, G. P. Salam, and G. Soyez, *The anti-k_t jet clustering algorithm*, JHEP **04** (2008) 063.

[92] W. Lampl et al., *Calorimeter clustering algorithms: Description and performance*, ATL-LARG-PUB-2008-002.

[93] ATLAS Collaboration, *A measurement of single hadron response using data at $\sqrt{s} = 8$ TeV with the ATLAS detector*, Tech. Rep. ATL-PHYS-PUB-2014-002, CERN, Geneva, Mar, 2014.

[94] M. Cacciari and G. P. Salam, *Pileup subtraction using jet areas*, Phys. Lett. **B 659** (2008) 119–126.

[95] ATLAS Collaboration, *Tagging and suppression of pileup jets with the ATLAS detector*, Tech. Rep. ATLAS-CONF-2014-018, CERN, Geneva, May, 2014.

[96] ATLAS Collaboration, *Performance of Missing Transverse Momentum Reconstruction in ATLAS studied in Proton-Proton Collisions recorded in 2012 at 8 TeV*, Tech. Rep. ATLAS-CONF-2013-082, CERN, Geneva, Aug, 2013.

[97] A. Buzatu et al., *Invariant Mass Studies for the $H \to b\bar{b}$ Measurements for HCP*, Tech. Rep. ATL-COM-PHYS-2012-1451, CERN, Geneva, 2012.

[98] ATLAS Collaboration, *Calibration of the performance of b-tagging for c and light-flavour jets in the 2012 ATLAS data*, Tech. Rep. ATLAS-CONF-2014-046, CERN, Geneva, Jul, 2014.

[99] ATLAS Collaboration, *Calibration of b-tagging using dileptonic top pair events in a combinatorial likelihood approach with the ATLAS experiment*, Tech. Rep. ATLAS-CONF-2014-004, CERN, Geneva, Feb, 2014.

[100] P. Berta, F. Filthaut, V. Dao, E. Le Menedeu, F. Parodi, G. Piacquadio, T. Scanlon, M. Ughetto, and L. Zhang, *Continuous b-tagging for the ATLAS experiment*, Tech. Rep. ATL-COM-PHYS-2014-035, CERN, Geneva, Jan, 2014.

[101] B. P. Roe, H.-J. Yang, and J. Zhu, *Boosted Decision Trees, A Powerful Event Classifier*, in *Proceedings of PHYSTAT05: Statistical Problems in Particle Physics, Astrophysics and Cosmology.* 2005. `http://www.physics.ox.ac.uk/phystat05/proceedings/files/phystat05-proc.pdf`.

[102] A. Hocker, J. Stelzer, F. Tegenfeldt, H. Voss, K. Voss, et al., *TMVA - Toolkit for Multivariate Data Analysis*, PoS **ACAT** (2007) 040.

[103] A. Read, *Modified frequentist analysis of search results (the CL_S method)*, Tech. Rep. CERN-OPEN-2000-205, 2000.

[104] L. Moneta et al., *The RooStats Project*, in *Proceedings of the 13th International Workshop on Advanced Computing and Analysis Techniques in Physics Research, ACAT2010.*

[105] W. Verkerke and D. Kirkby, *The RooFit toolkit for data modeling*, in *2003 Computing in High Energy and Nuclear Physics, CHEP03.* 2003.

[106] G. Cowan, K. Cranmer, E. Gross, and O. Vitells, *Asymptotic formulae for likelihood-based tests of new physics*, Eur. Phys. J. C **71** (2011) 1554.

[107] ATLAS Collaboration, *Preliminary results on the muon reconstruction efficiency, momentum resolution, and momentum scale in ATLAS 2012 pp collision data*, Tech. Rep. ATLAS-CONF-2013-088, CERN, Geneva, Aug, 2013.

[108] ATLAS Collaboration, *Jet energy measurement with the ATLAS detector in proton-proton collisions at* $\sqrt{s} = 7\ TeV$, Eur.Phys.J. **C73** (2013) 2304 CERN-PH-EP-2011-191.

[109] ATLAS Collaboration, *Jet energy resolution in proton-proton collisions at* $\sqrt{s} = 7\ TeV$ *recorded in 2010 with the ATLAS detector*, Eur. Phys. J. **C 73** (2013) 2306 CERN-PH-EP-2012-191.

[110] ATLAS Collaboration, *Measurements of normalized differential cross-sections for ttbar production in pp collisions at sqrt(s) = 7 TeV using the ATLAS detector*, Phys. Rev. D (2014) .

[111] N. Kidonakis, *Differential and total cross sections for top pair and single top production*, Tech. Rep. DESY-PROC-2012-02/251.

[112] L. Demortier, *Interval Estimation, in: Data Analysis in High Energy Physics.* Wiley-VCH, 2013.

[113] G. Bohm and G. Zech, *Introduction to statistics and data analysis for physicists.* Verl. Dt. Elektronen-Synchrotron, Hamburg, 2010.

[114] B. Efron, *Bootstrap methods: another look at the jacknife*, The Annals of Statistics **2** (1979) 1–26.

[115] ATLAS Higgs Group HSG5. Private communication.

[116] ATLAS Collaboration, *Prospects for the study of the Higgs boson in the VH(bb) channel at HL-LHC*, Tech. Rep. ATL-PHYS-PUB-2014-011, CERN, Geneva, 2014.

Appendices

APPENDIX A

Ratio of $E_{\mathrm{T}}^{\mathrm{miss}}$ Triggered Yields to Muon Triggered Yields

The yield of events recovered by using the $E_{\mathrm{T}}^{\mathrm{miss}}$ triggers exclusively as a fraction of the yield passing the muon triggers is shown in Figure A.1 for the 2-jet cut-based analysis, Figure A.2 for the 3-jet cut-based, Figure A.3 for the 2-jet and 3-jet merged cut-based and Figure A.4 for the MVA analyses. Each of these is separated into different $p_{\mathrm{T}}(W)$ ranges as well as shown inclusively. The plots were produced in the same way as described in Section 7.6.

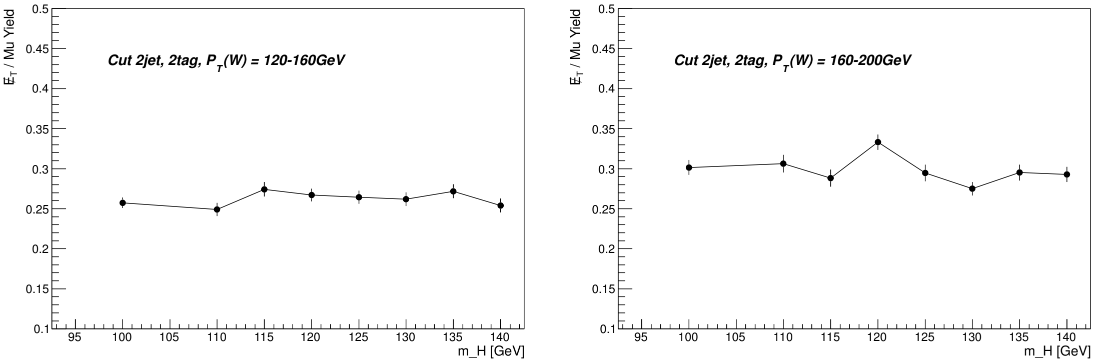

(a) 2-jet $p_{\mathrm{T}}(W) = 120 - 160$ GeV (b) 2-jet $p_{\mathrm{T}}(W) = 160 - 200$ GeV

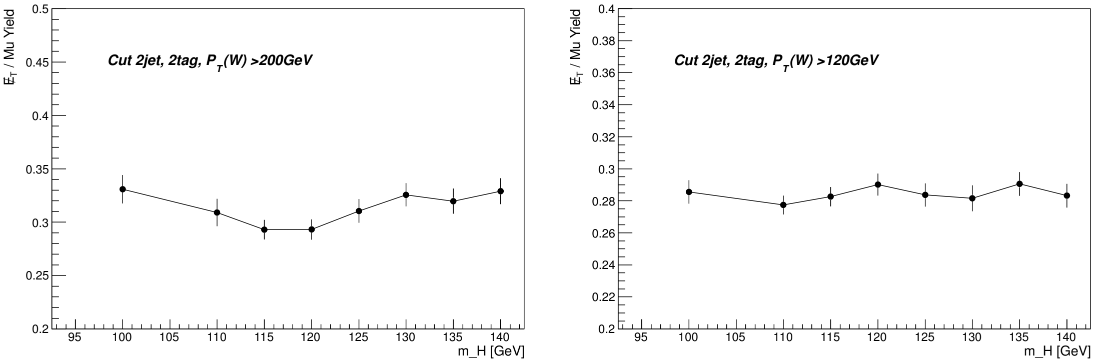

(c) 2-jet $p_{\mathrm{T}}(W) > 200$ GeV (d) 2-jet $p_{\mathrm{T}}(W) > 120$ GeV

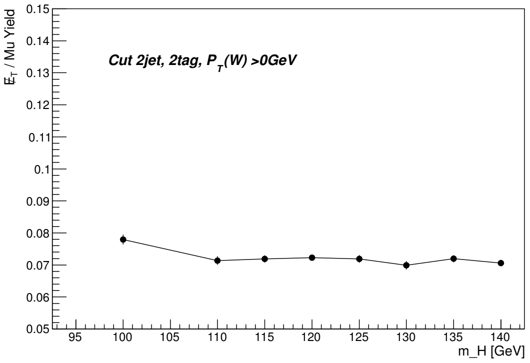

(e) 2-jet Inclusive

Figure A.1: Ratio of exclusive $E_{\mathrm{T}}^{\mathrm{miss}}$ triggered to muon triggered signal yields in the different cut-based 2-jet, 2-tag signal regions as a function of Higgs mass, m_H. The yields are all prefit Monte Carlo expectations. The different b-tagging regions (LL,MM,TT) are merged as no significant difference is observed between these regions. The error on each point contains only statistical and trigger uncertainties.

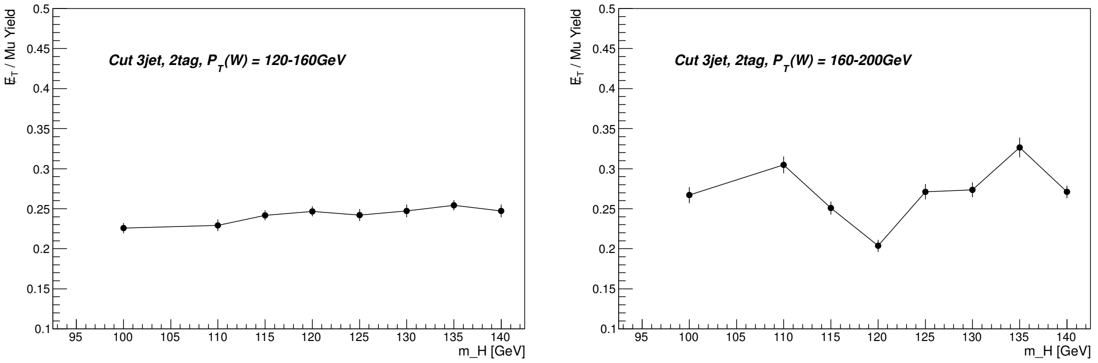

(a) 3-jet $p_{\mathrm{T}}(W) = 120 - 160$ GeV (b) 3-jet $p_{\mathrm{T}}(W) = 160 - 200$ GeV

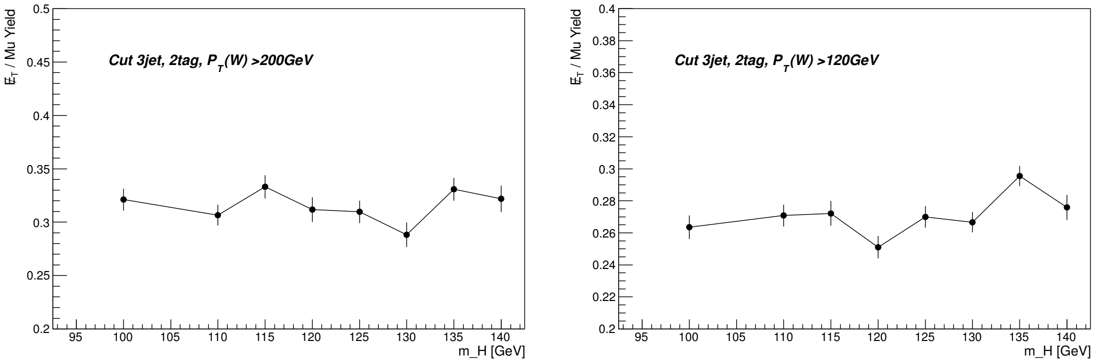

(c) 3-jet $p_{\mathrm{T}}(W) > 200$ GeV (d) 3-jet $p_{\mathrm{T}}(W) > 120$ GeV

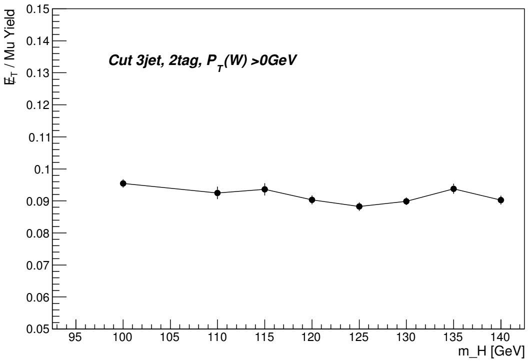

(e) 3-jet Inclusive

Figure A.2: Ratio of exclusive $E_{\mathrm{T}}^{\mathrm{miss}}$ triggered to muon triggered signal yields in the different cut-based 3-jet, 2-tag signal regions as a function of Higgs mass, m_H. The yields are all prefit Monte Carlo expectations. The different b-tagging regions (LL,MM,TT) are merged as no significant difference was observed between these regions. The error on each point contains only statistical and trigger uncertainties.

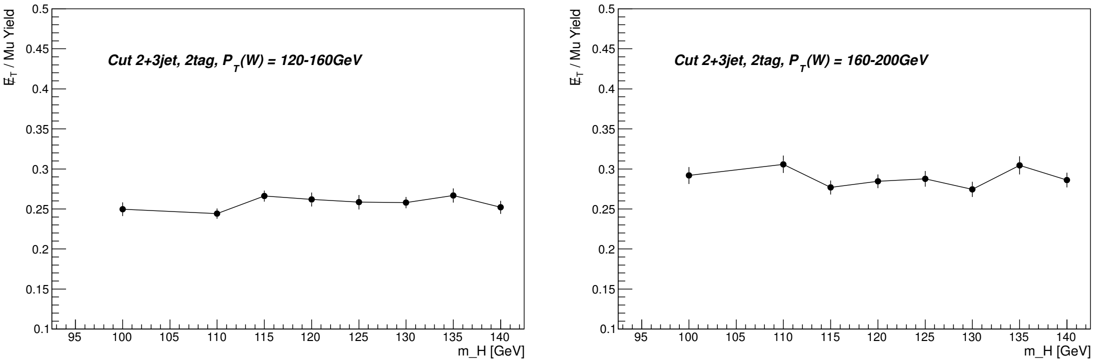

(a) 2-jet & 3-jet $p_{\mathrm{T}}(W) = 120 - 160$ GeV (b) 2-jet & 3-jet $p_{\mathrm{T}}(W) = 160 - 200$ GeV

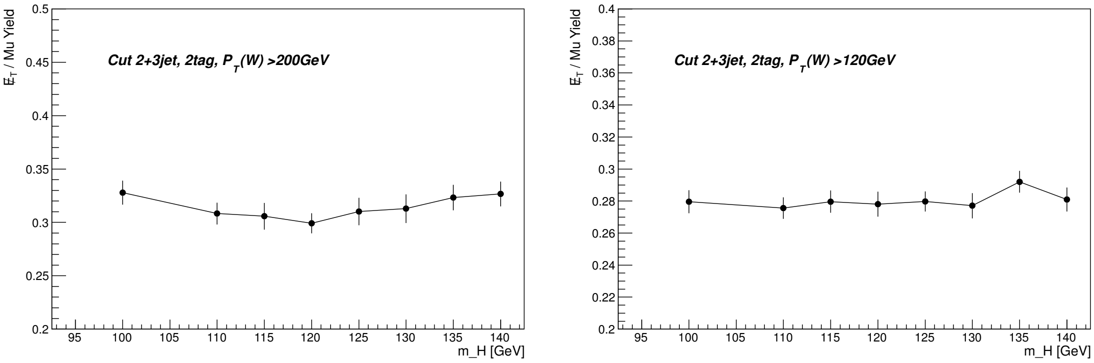

(c) 2-jet & 3-jet $p_{\mathrm{T}}(W) > 200$ GeV (d) 2-jet & 3-jet $p_{\mathrm{T}}(W) > 120$ GeV

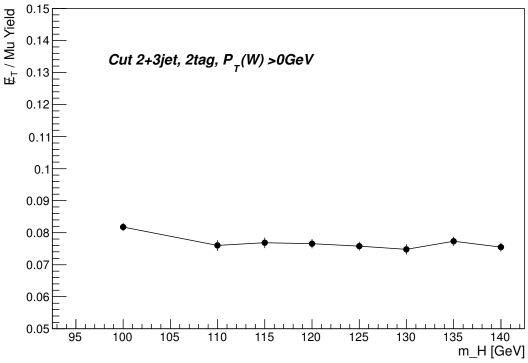

(e) 2-jet & 3-jet Inclusive

Figure A.3: Ratio of exclusive $E_{\mathrm{T}}^{\mathrm{miss}}$ triggered to muon triggered signal yields in the different cut-based 2-jet and 3-jet merged 2-tag signal regions as a function of Higgs mass, m_H. The yields are all prefit Monte Carlo expectations. The different b-tagging regions (LL,MM,TT) are merged as no significant difference is observed between these regions. The error on each point contains only statistical and trigger uncertainties.

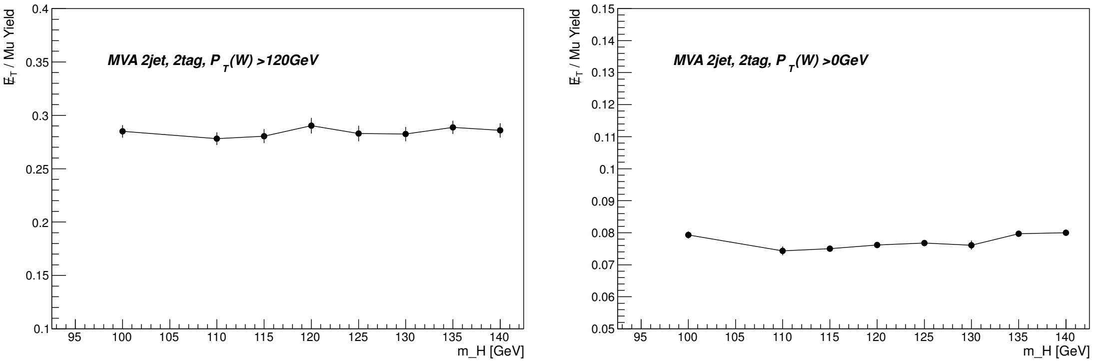

(a) 2-jet $p_{\mathrm{T}}(W) > 120$ GeV (b) 2-jet Inclusive

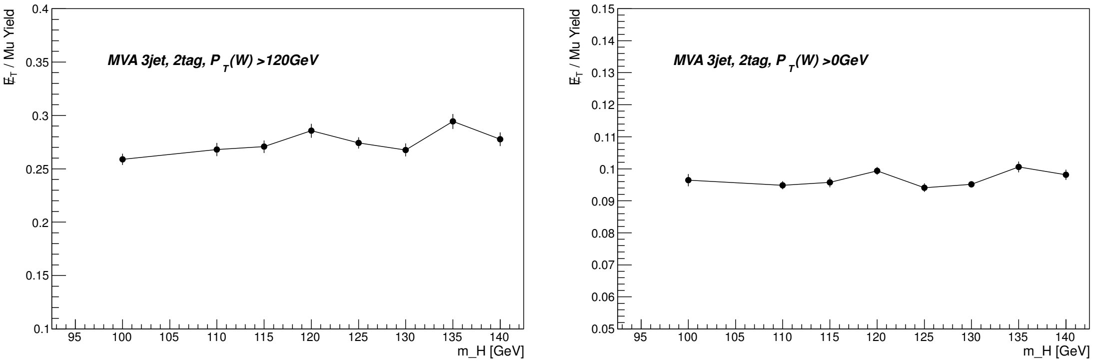

(c) 3-jet $p_{\mathrm{T}}(W) > 120$ GeV (d) 3-jet Inclusive

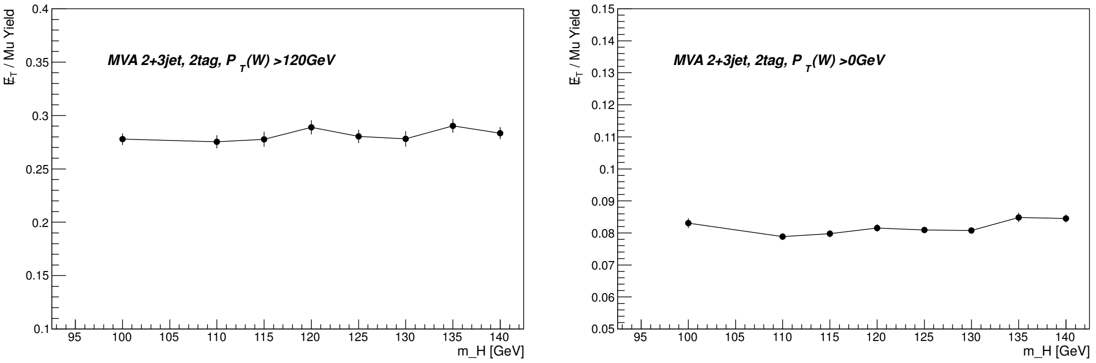

(e) 2-jet & 3-jet $p_{\mathrm{T}}(W) > 120$ GeV (f) 2-jet & 3-jet Inclusive

Figure A.4: Ratio of exclusive $E_{\mathrm{T}}^{\mathrm{miss}}$ triggered to muon triggered signal yields in the different MVA 2-tag signal regions as a function of Higgs mass, m_H. The yields are all prefit Monte Carlo expectations. The different b-tagging regions (LL,MM,TT) are merged as no significant difference is observed between these regions. The error on each point contains only statistical and trigger uncertainties.

APPENDIX B

Nominal $WH \to \ell\nu b\bar{b}$ Nuisance Parameter Ranking

The ranking for the top 15 nuisance parameters in the Nominal analyses can be found in Figure B.1. The method used to obtain the ranking was previously explained in Chapter 8. The highest ranked nuisance parameters for the cut-based analysis is the W+2 b-jets/W+2 c-jets di-jet invariant mass shape for $p_{\mathrm{T}}(W) > 120$ GeV (`VMbb`) and for the MVA analysis it is normalisation ratio of W+b-jet+light-jet and W+2 b-jets (`WblWbbRatio`).

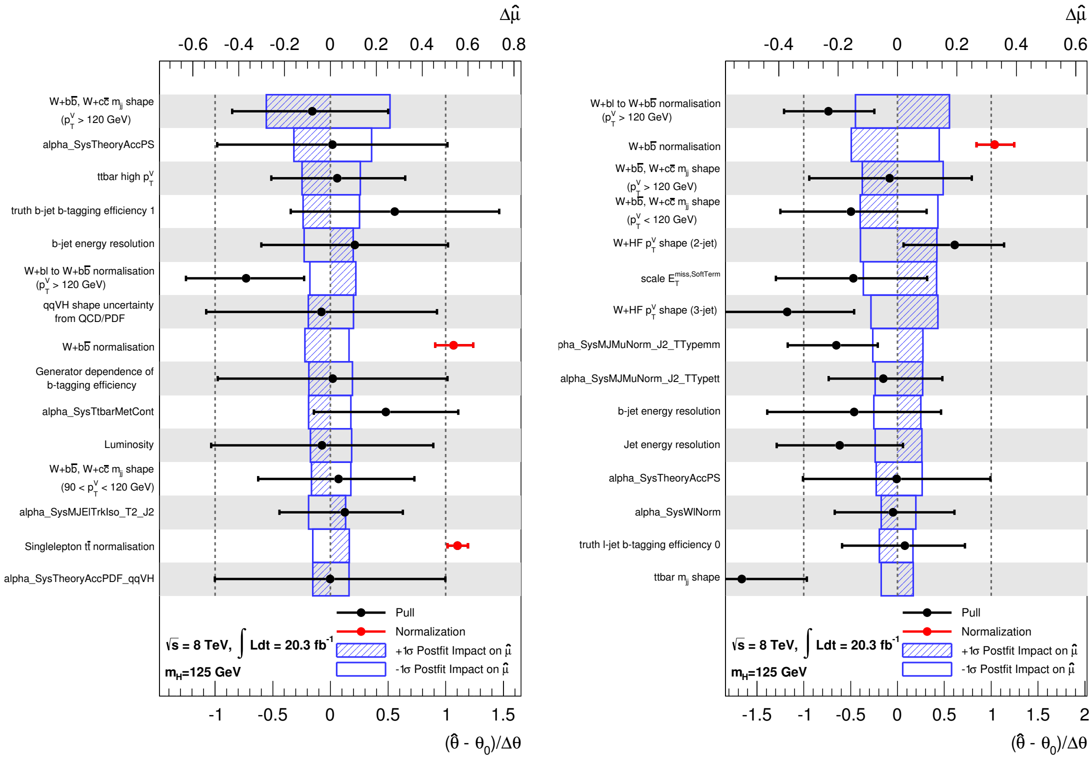

(a) Cut-based (b) MVA

Figure B.1: Ranking of systematics and normalisations based upon their impact on the fitted $\hat{\mu}$ value for the Nominal cut-based and MVA analyses. The 15 highest ranking nuisance parameters are shown in each case. The bottom x axis and points show the relative shift of postfit values of the nuisance parameters, ${}^{(\hat{\theta}-\theta_0)}/_{\Delta\theta}$, in terms of the postfit value, $\hat{\theta}$, prefit value, θ_0, and prefit 1σ uncertainty on the nuisance parameter, $\Delta\theta$. The error bars on the points indicate the postfit uncertainty in terms of the relative shift. The top x axis and boxes show the shift in the fitted $\hat{\mu}$ value when the nuisance parameter is fixed to its postfit value shifted up and down by the corresponding uncertainty. The shaded part of the box corresponds to $\hat{\theta}+\Delta\theta$ while the unshaded corresponds to $\hat{\theta}-\Delta\theta$.

APPENDIX C

$WH \rightarrow \ell\nu b\bar{b}$ Nominal Results

The Nominal dataset, if fitted in the same way as the $E_{\mathrm{T}}^{\mathrm{miss}}$ triggered dataset, for the same range of hypothesised Higgs masses as described in Section 10.2. The set of results shown in Chapter 10 for the $E_{\mathrm{T}}^{\mathrm{miss}}$ triggered and Combined analyses is also produced for the Nominal cut-based and MVA analyses. The description of the methods used to produce the results, the categories in tables and the contents of figures are the same as in Section 10.2. The limits, as a function of m_H, on the cross section times branching ratio are shown in Table C.1 and Figure C.1a for the cut-based analysis and Table C.2 and Figure C.1b for the MVA analysis. The local p_0, as a function of m_H, is shown for the cut-based and MVA analyses in Table C.3 and Figure C.2. All bins from all fit regions in the cut-based and MVA analyses are combined (separately for the cut-based and MVA) based on the value of $\log_{10}({}^{S}\!/_{B})$ in each bin in Figure C.3. Table C.4 contains a summary of the results obtained for the cut-based and MVA analyses at a hypothesised Higgs mass, $m_H = 125$ GeV. The observed $\hat{\mu}$ value for the cut-based analysis is $\hat{\mu}_{Cut} = 2.568^{+0.710}_{-0.686}(\text{stat.})^{+0.758}_{-0.630}(\text{syst.})$ and for the MVA analysis is $\hat{\mu}_{MVA} = 1.125^{+0.578}_{-0.552}(\text{stat.})^{+0.548}_{-0.469}(\text{syst.})$. The observed (expected) significance in the Cut-based analysis is 2.931 (1.237) and in the MVA analysis is 1.584 (1.426).

m_H (GeV)	Exp.	$+2\sigma$	$+1\sigma$	-1σ	-2σ	Obs.
100	0.87	1.63	1.22	0.63	0.47	1.25
110	1.04	1.95	1.45	0.75	0.56	1.93
115	1.14	2.13	1.59	0.82	0.61	2.32
120	1.38	2.57	1.91	0.99	0.74	3.09
125	1.74	3.25	2.43	1.26	0.94	4.35
130	2.14	3.99	2.98	1.54	1.15	5.02
135	2.77	5.16	3.85	1.99	1.48	5.11
140	3.86	7.21	5.38	2.78	2.07	6.74

Table C.1: Expected and observed limits from the 95% CL upper bound on the cross section times branching ratio as a function of m_H for the Nominal Cut-based analysis. Values are expressed as a multiple of the standard model expectation. The $\pm1\sigma$ and $\pm2\sigma$ shifts from the expected are also shown

m_H (GeV)	Exp.	$+2\sigma$	$+1\sigma$	-1σ	-2σ	Obs.
100	1.59	2.96	2.21	1.14	0.85	2.97
110	1.34	2.51	1.87	0.97	0.72	2.05
115	1.11	2.07	1.55	0.80	0.60	2.09
120	1.20	2.23	1.66	0.86	0.64	1.83
125	1.43	2.71	2.02	1.05	0.78	2.52
130	1.93	3.61	2.69	1.39	1.04	3.12
135	2.97	5.55	4.14	2.14	1.60	5.67
140	5.47	10.20	7.61	3.94	2.94	9.88

Table C.2: Expected and observed limits from the 95% CL upper bound on the cross section times branching ratio as a function of m_H for the Nominal MVA analysis. Values are expressed as a multiple of the standard model expectation. The $\pm1\sigma$ and $\pm2\sigma$ shifts from the expected are also shown

m_H (GeV)	Exp p_0	Obs p_0
100	0.01139	0.13452
110	0.02467	0.05695
115	0.03513	0.02922
120	0.06337	0.01273
125	0.10812	0.00169
130	0.15639	0.00275
135	0.21983	0.03346
140	0.28877	0.07505

(a) Cut-based

m_H (GeV)	Exp p_0	Obs p_0
100	0.09914	0.0309
110	0.06618	0.11257
115	0.03086	0.02893
120	0.04258	0.09936
125	0.07549	0.05386
130	0.13731	0.07561
135	0.23431	0.02897
140	0.35017	0.05085

(b) MVA

Table C.3: Expected and observed local p_0 values as a function of m_H for the Nominal Cut-based and MVA analyses.

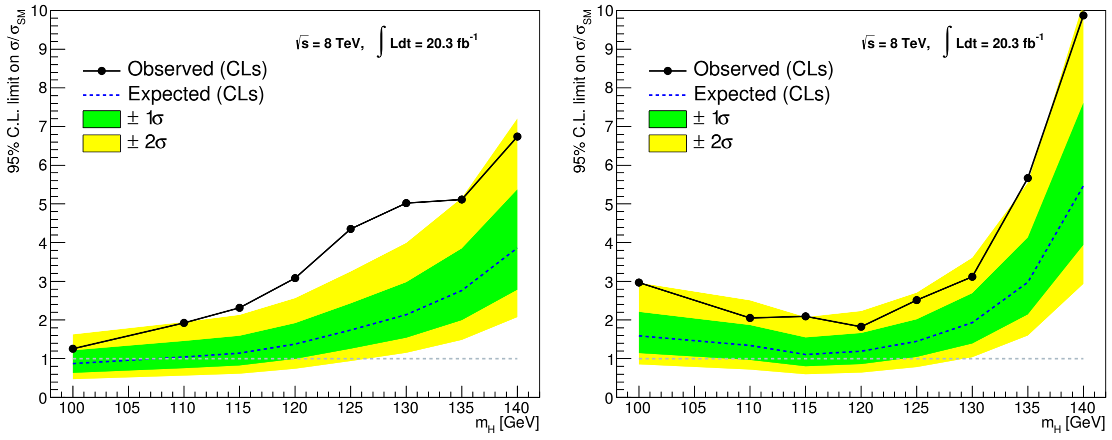

(a) (b)

Figure C.1: Expected and observed limits from the 95% CL upper bound on the cross section times branching ratio as a function of m_H for the nominal analyses. Values are expressed as a multiple of the standard model expectation. The observed is shown as a solid line while the expected, for the background only case, is shown as a dashed line with the green and yellow shaded areas representing the $\pm 1\sigma$ and $\pm 2\sigma$ shifts from the expected.

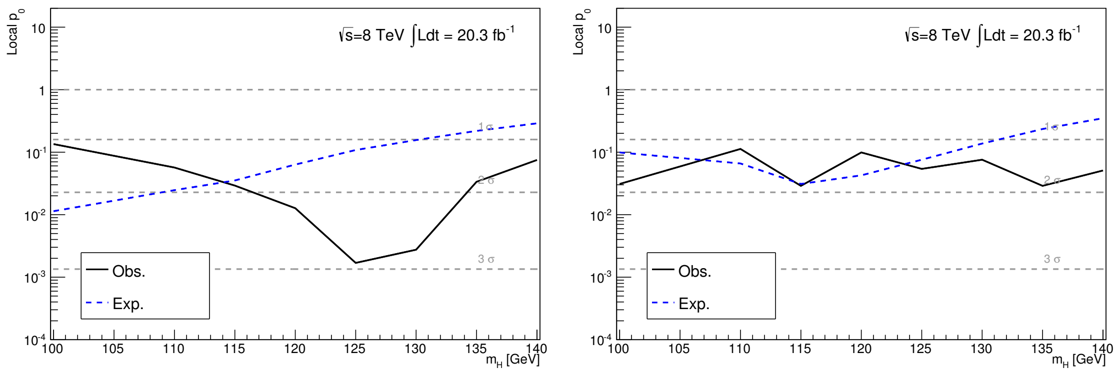

(a) (b)

Figure C.2: Expected and observed local p_0 values as a function of m_H for the nominal analyses. The observed is shown as a solid line while the expected, for a standard model Higgs Boson, is shown as a blue dashed line. The horizontal dashed lines convert the p_0 values to significance values.

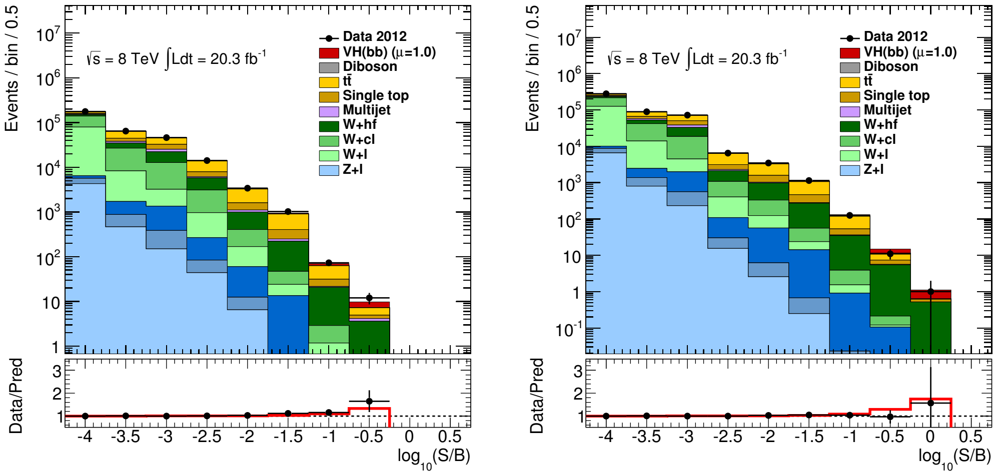

(a) (b)

Figure C.3: Yields ordered by $\log_{10}(S/B)$ for the nominal Cut-based and MVA analyses. Bins from all signal regions are combined into bins based on the calculated $\log_{10}(S/B)$ from the postfit background event yields and the expected signal yield. The lower part of the plots show the statistical pull of the data as points along with the expected pull from the standard model expectation as a red line.

	Cut-based	MVA
Stat-Only Expected Limit	1.258	1.088
Systematics Expected Limit	1.743	1.459
Systematics Observed Limit	4.354	2.521
Expected Significance	1.237	1.426
Observed Significance	2.931	1.584
$\hat{\mu}$	$2.568^{+1.038}_{-0.932}$	$1.125^{+0.797}_{-0.724}$

Table C.4: Summary of the main Nominal Cut-based and MVA fit results

APPENDIX D

Postfit Combined $WH \to \ell\nu b\bar{b}$ Regions

The postfit distributions of regions used in the Combined cut-based analysis are shown in Figures D.1 to D.11 and for the MVA analysis in Figures D.12 to D.16. The plots follow the same structure as described for the $E_{\mathrm{T}}^{\mathrm{miss}}$ triggered analyses in Section 10.1. These plots contain the same events as the Nominal for $p_{\mathrm{T}}(W) <$ 120 GeV while for $p_{\mathrm{T}}(W) >$ 120 GeV the plots contain both the events from the Nominal and the additional $20 - 35\%$ (see Section 7.6) of events from the $E_{\mathrm{T}}^{\mathrm{miss}}$ triggered analyses that were previously shown in Section 10.1. The pull of the events from the $E_{\mathrm{T}}^{\mathrm{miss}}$ triggered and Nominal analyses on each other causes the normalisations in each region to be different from both the individual cases. The data is generally well described by the postfit MC expectations. Good data-MC agreement is found. The agreement is comparable to that of the Nominal analyses (as shown in Appendix C) when considering the smaller statistical fluctuations due to the increase in statistics coming from the additional $E_{\mathrm{T}}^{\mathrm{miss}}$ triggered events.

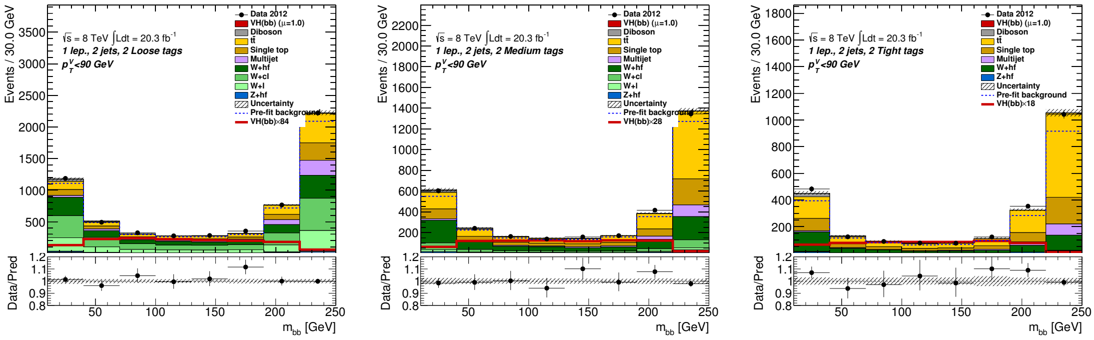

(a) 2 Loose Tags (b) 2 Medium Tags (c) 2 Tight Tags

Figure D.1: Postfit distributions of dijet invariant mass, m_{bb}, in the cut-based combined 2-jet $p_{\mathrm{T}}(W) = 0 - 90$ GeV regions, split into b-tagging categories. The data is shown as points with error bars and the postfit Monte Carlo background yield is shown as stacked histograms. The uncertainty on the total background yield is represented as a shaded area and the prefit total background yield is shown as a blue dashed line. The expected Higgs signal, from a sample at $m_H = 125$ GeV, is shown both stacked on top of the background histograms at the standard model expectation and unstacked but scaled by the factor stated in the legend. The lower part of each plot shows the ratio of the data yield to the postfit background and signal prediction.

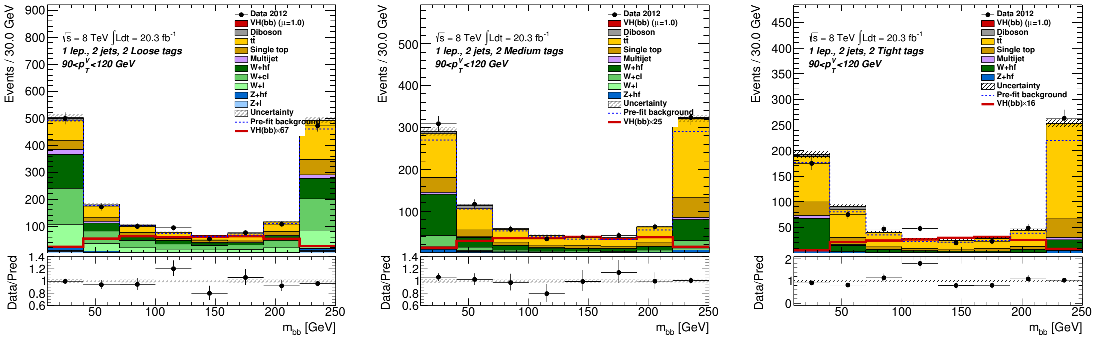

(a) 2 Loose Tags (b) 2 Medium Tags (c) 2 Tight Tags

Figure D.2: Positfit distributions of dijet invariant mass, m_{bb}, in the cut-based combined 2-jet $p_{\mathrm{T}}(W) = 90 - 120$ GeV regions. The format is the same as Figure D.1.

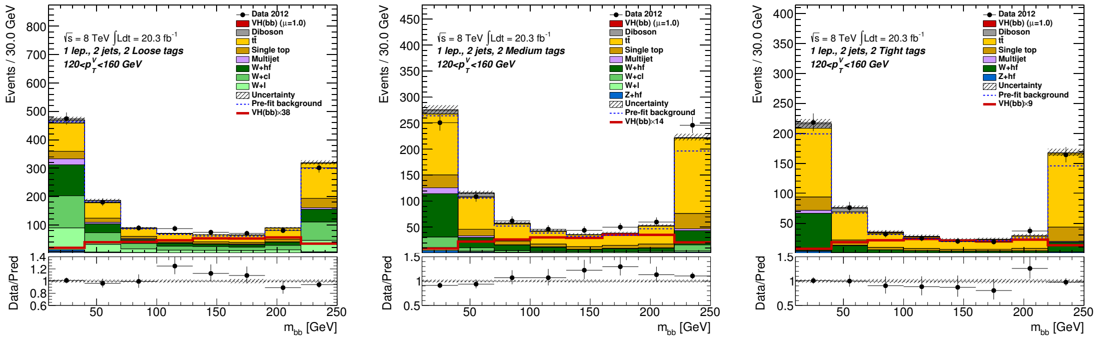

(a) 2 Loose Tags (b) 2 Medium Tags (c) 2 Tight Tags

Figure D.3: Positfit distributions of dijet invariant mass, m_{bb}, in the cut-based combined 2-jet $p_{\mathrm{T}}(W) = 120 - 160$ GeV regions. The format is the same as Figure D.1.

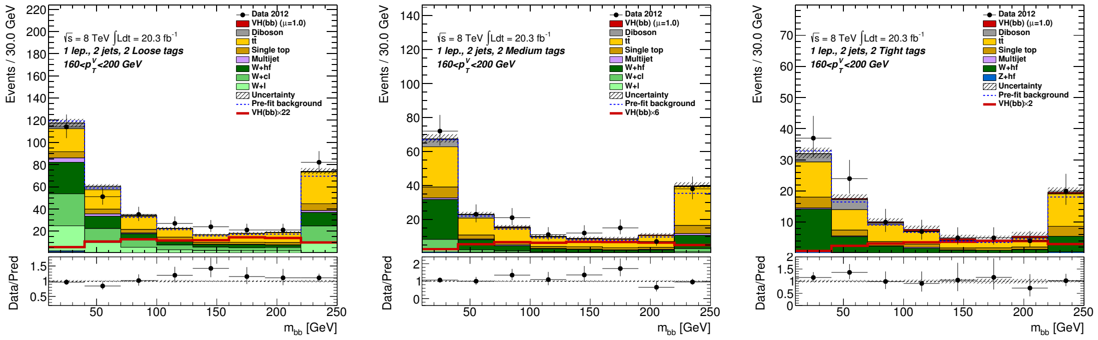

(a) 2 Loose Tags (b) 2 Medium Tags (c) 2 Tight Tags

Figure D.4: Positfit distributions of dijet invariant mass, m_{bb}, in the cut-based combined 2-jet $p_{\mathrm{T}}(W) = 160 - 200$ GeV regions. The format is the same as Figure D.1.

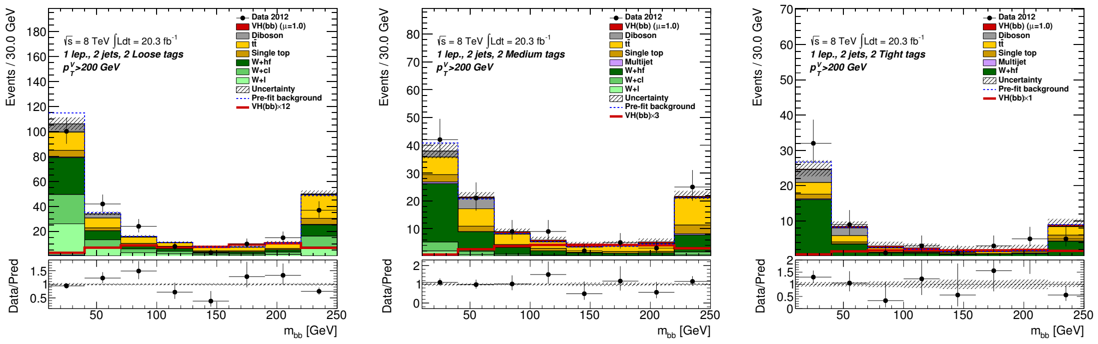

(a) 2 Loose Tags (b) 2 Medium Tags (c) 2 Tight Tags

Figure D.5: Positfit distributions of dijet invariant mass, m_{bb}, in the cut-based combined 2-jet $p_{\mathrm{T}}(W) > 200$ GeV regions. The format is the same as Figure D.1.

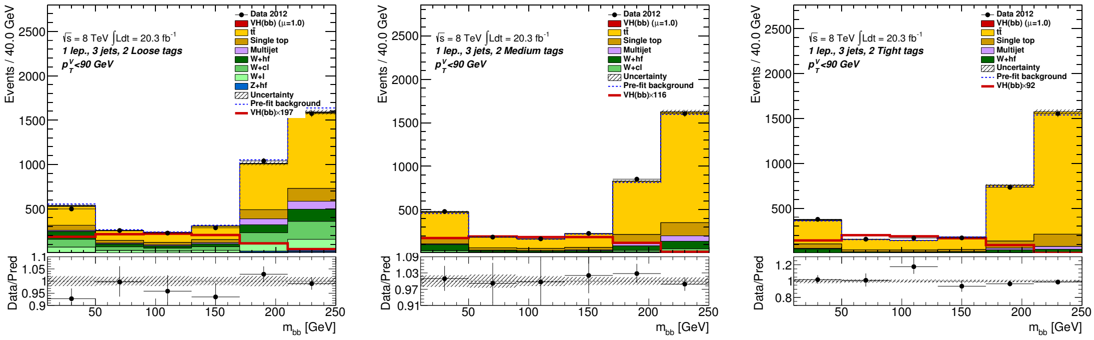

(a) 2 Loose Tags (b) 2 Medium Tags (c) 2 Tight Tags

Figure D.6: Positfit distributions of dijet invariant mass, m_{bb}, in the cut-based combined 3-jet $p_{\mathrm{T}}(W) = 0 - 90$ GeV regions. The format is the same as Figure D.1.

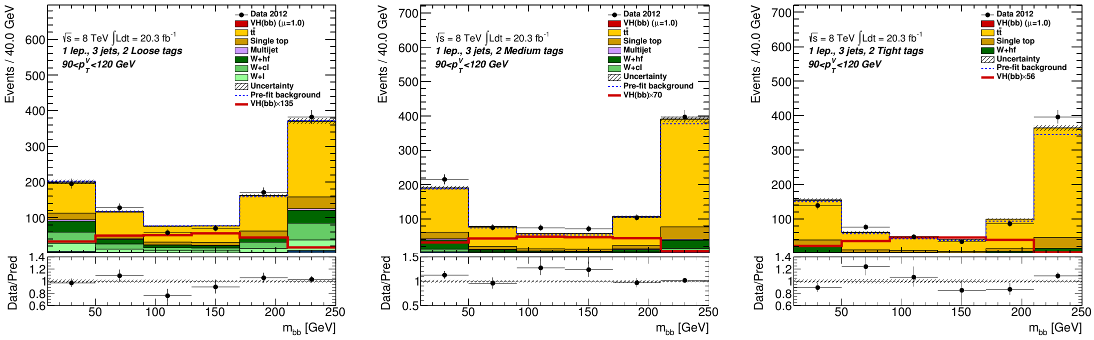

(a) 2 Loose Tags (b) 2 Medium Tags (c) 2 Tight Tags

Figure D.7: Positfit distributions of dijet invariant mass, m_{bb}, in the cut-based combined 3-jet $p_{\mathrm{T}}(W) = 90 - 120$ GeV regions. The format is the same as Figure D.1.

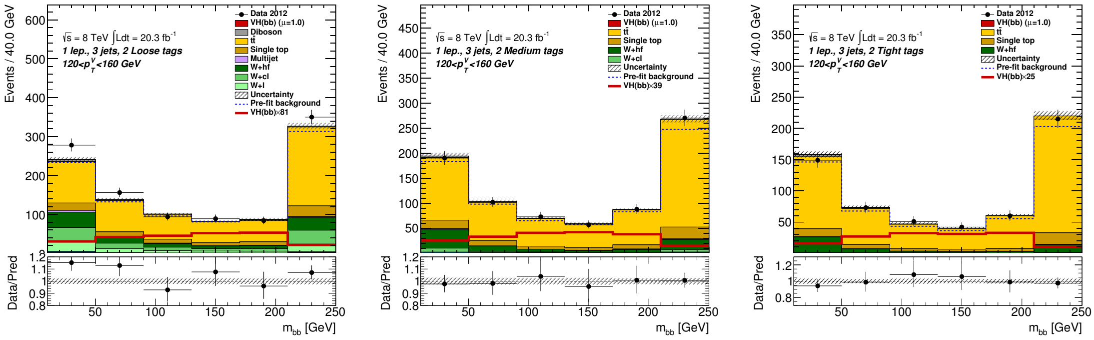

(a) 2 Loose Tags (b) 2 Medium Tags (c) 2 Tight Tags

Figure D.8: Positfit distributions of dijet invariant mass, m_{bb}, in the cut-based combined 3-jet $p_{\mathrm{T}}(W) = 120 - 160$ GeV regions. The format is the same as Figure D.1.

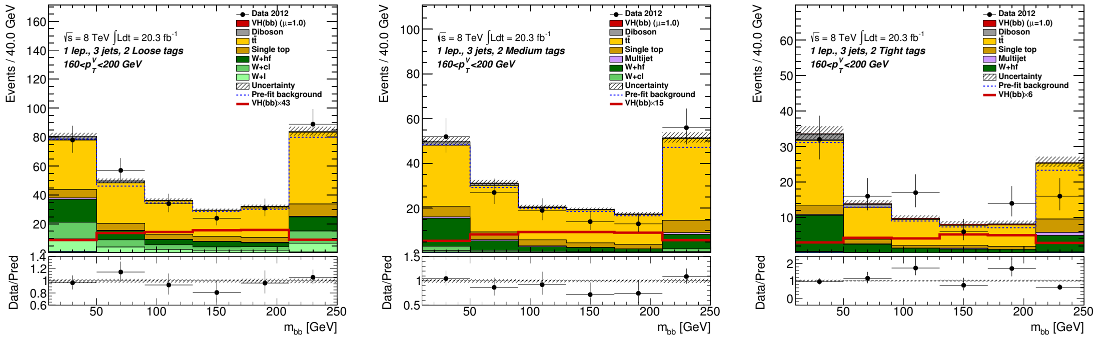

(a) 2 Loose Tags (b) 2 Medium Tags (c) 2 Tight Tags

Figure D.9: Positfit distributions of dijet invariant mass, m_{bb}, in the cut-based combined 3-jet $p_{\mathrm{T}}(W) = 160 - 200$ GeV regions. The format is the same as Figure D.1.

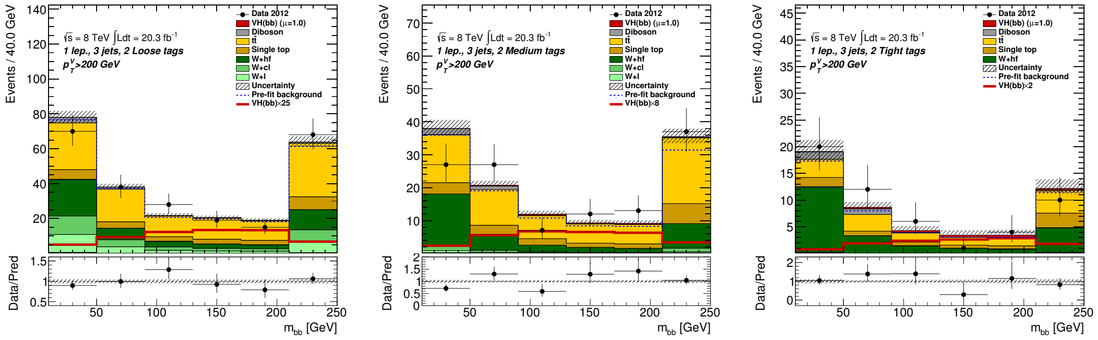

(a) 2 Loose Tags (b) 2 Medium Tags (c) 2 Tight Tags

Figure D.10: Positfit distributions of dijet invariant mass, m_{bb}, in the cut-based combined 3-jet $p_{\mathrm{T}}(W) > 200$ GeV regions, split into b-tagging categories. The format is the same as Figure D.1.

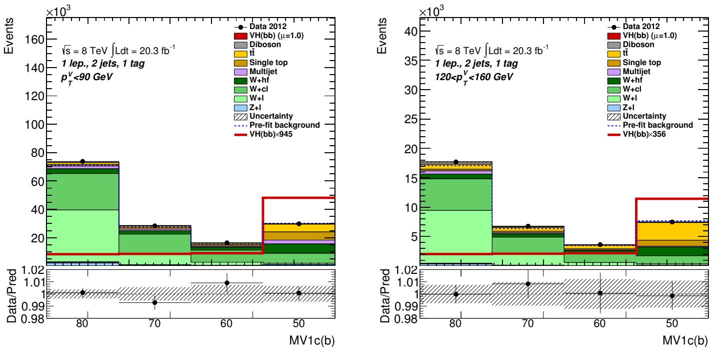

(a) 2 Jet
$p_{\mathrm{T}}(W) < 120$ GeV

(b) 2 Jet
$p_{\mathrm{T}}(W) > 120$ GeV

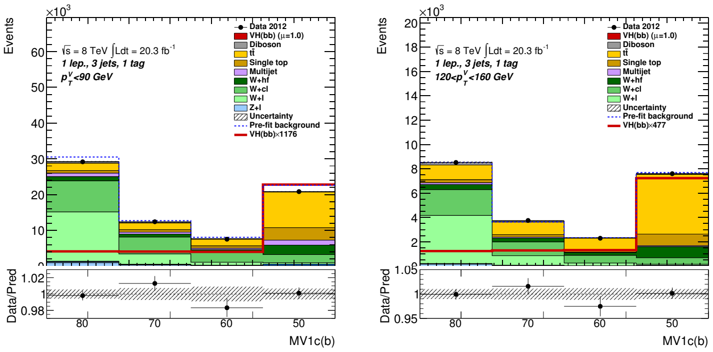

(c) 3 Jet
$p_{\mathrm{T}}(W) < 120$ GeV

(d) 3 Jet
$p_{\mathrm{T}}(W) > 120$ GeV

Figure D.11: Postfit distributions of the b-tagging weight, $MV1c$, in the cut-based combined 1-tag 2-jet and 3-jet $p_{\mathrm{T}}(W) < 120$ GeV and $p_{\mathrm{T}}(W) > 120$ GeV regions. The format is the same as Figure D.1.

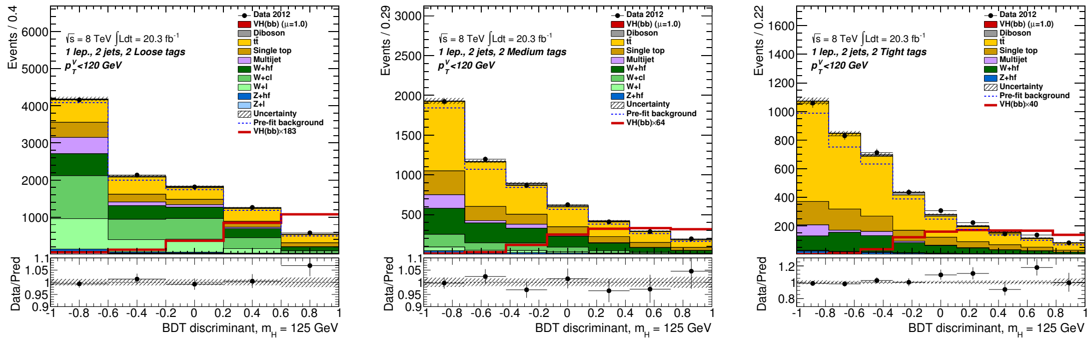

(a) 2 Loose Tags

(b) 2 Medium Tags

(c) 2 Tight Tags

Figure D.12: Postfit distributions of the BDT output in the MVA combined 2-jet $p_{\mathrm{T}}(W) < 120$ GeV regions. The format is the same as Figure D.1.

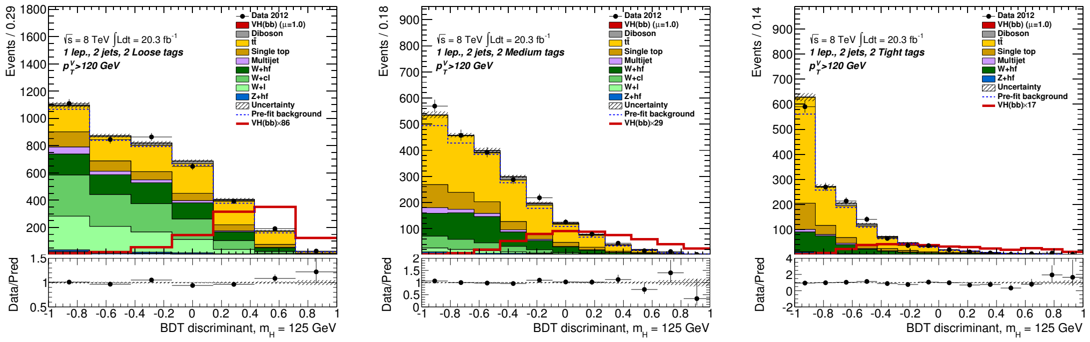

(a) 2 Loose Tags (b) 2 Medium Tags (c) 2 Tight Tags

Figure D.13: Postfit distributions of the BDT output in the MVA combined 2-jet $p_{\mathrm{T}}(W) > 120$ GeV regions. The format is the same as Figure D.1.

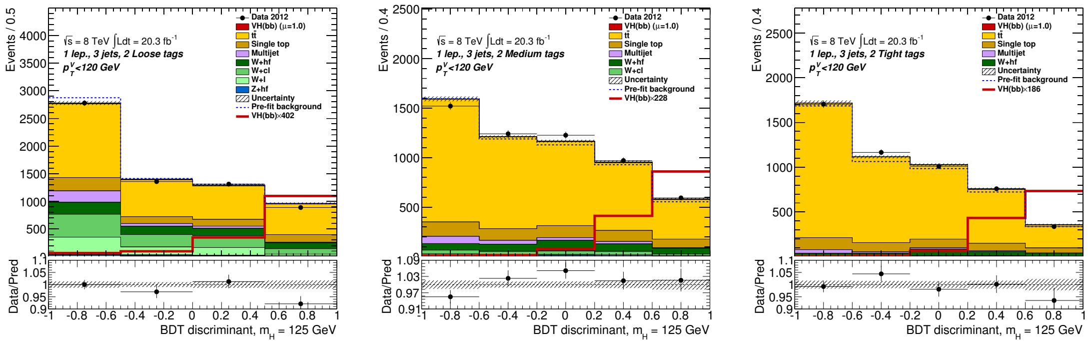

(a) 2 Loose Tags (b) 2 Medium Tags (c) 2 Tight Tags

Figure D.14: Postfit distributions of the BDT output in the MVA combined 3-jet $p_{\mathrm{T}}(W) < 120$ GeV regions. The format is the same as Figure D.1.

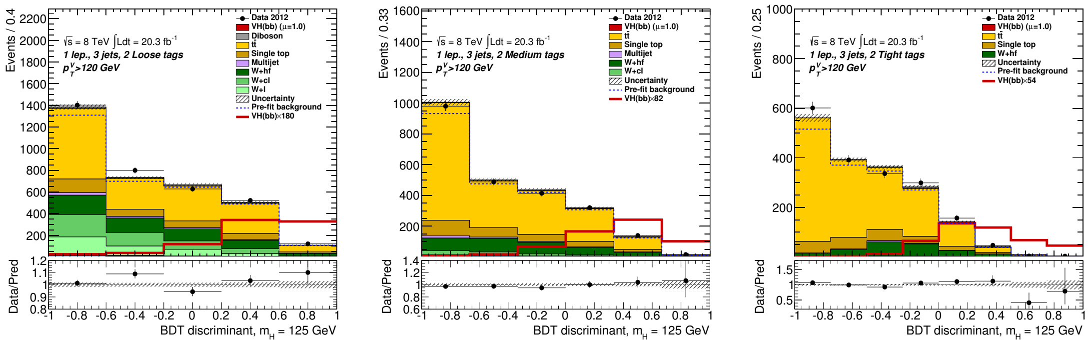

(a) 2 Loose Tags (b) 2 Medium Tags (c) 2 Tight Tags

Figure D.15: Postfit distributions of the BDT output in the MVA combined 3-jet $p_{\mathrm{T}}(W) > 120$ GeV regions. The format is the same as Figure D.1.

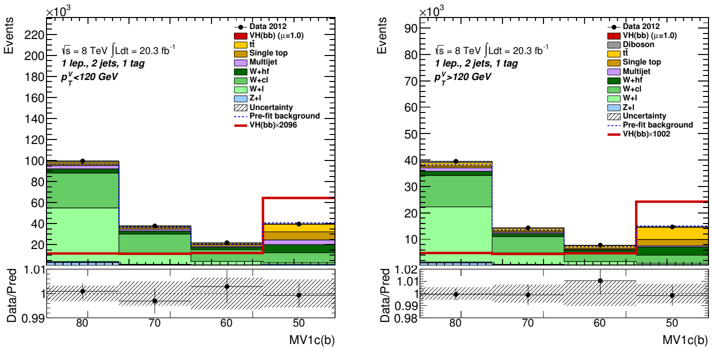

(a) 2 Jet
$p_{\mathrm{T}}(W) < 120$ GeV

(b) 2 Jet
$p_{\mathrm{T}}(W) > 120$ GeV

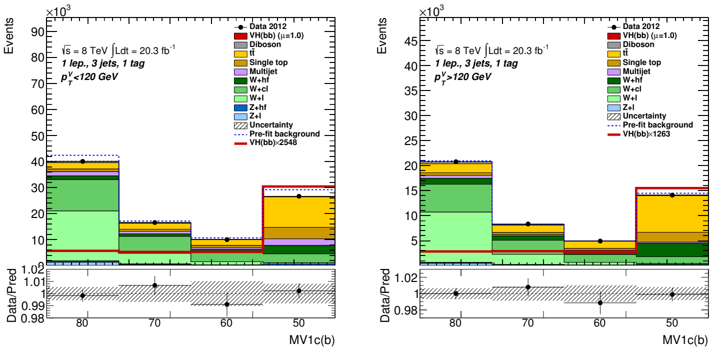

(c) 3 Jet
$p_{\mathrm{T}}(W) < 120$ GeV

(d) 3 Jet
$p_{\mathrm{T}}(W) > 120$ GeV

Figure D.16: Postfit distributions of the b-tagging weight, $MV1c$, in the MVA combined 1-tag 2-jet and 3-jet $p_{\mathrm{T}}(W) < 120$ GeV and $p_{\mathrm{T}}(W) > 120$ GeV regions. The format is the same as Figure D.1.

APPENDIX E

Correlation of Additional Nuisance Parameters

Additional correlation plots are shown here for nuisance parameters in the individual lepton and combined fits. The plots are produced in the same way as the correlation plots shown in Chapter 9. Shown here are the correlations of the individual channel $t\bar{t}$ normalisation in Figure E.1, combined fit $t\bar{t}$ normalisation in Figure E.2, $Wb\bar{b}$ normalisation in Figure E.3, $Zb\bar{b}$ normalisation in Figure E.4, scaling of soft terms in the $E_{\mathrm{T}}^{\mathrm{miss}}$ calculation in Figure E.5 (this was found to be a troublesome parameter in the normal analysis fits due to the nature of the ATLAS $E_{\mathrm{T}}^{\mathrm{miss}}$ calibration), and the 2 leading jet energy scale nuisance parameters in Figures E.6 and E.7.

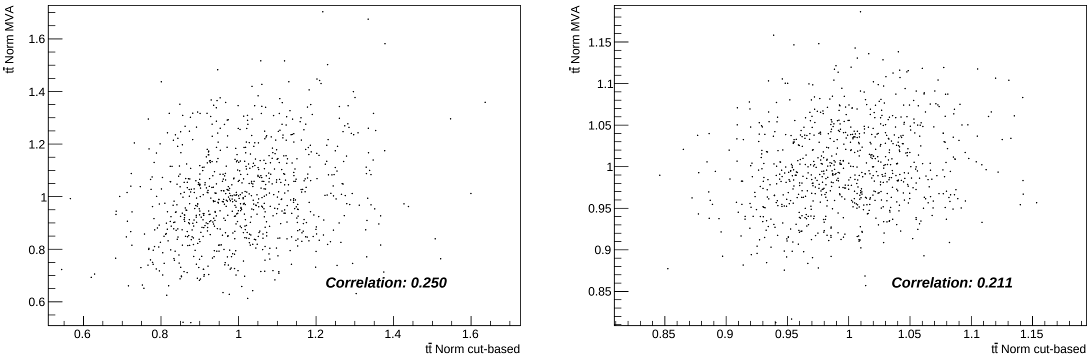

(a) 0 lepton (b) 1 lepton

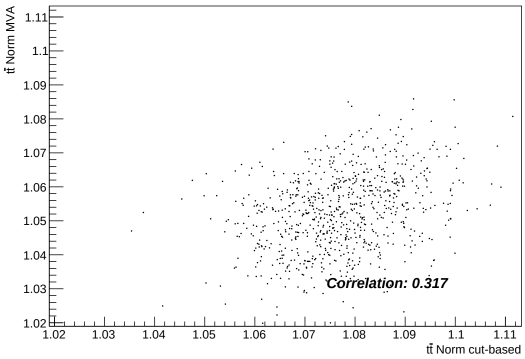

(c) 2 lepton

Figure E.1: Correlation of $t\bar{t}$ normalisation from the individual lepton cut-based and MVA bootstrap pseudo-datasets. Shown for 800 pairs of replicas in each channel.

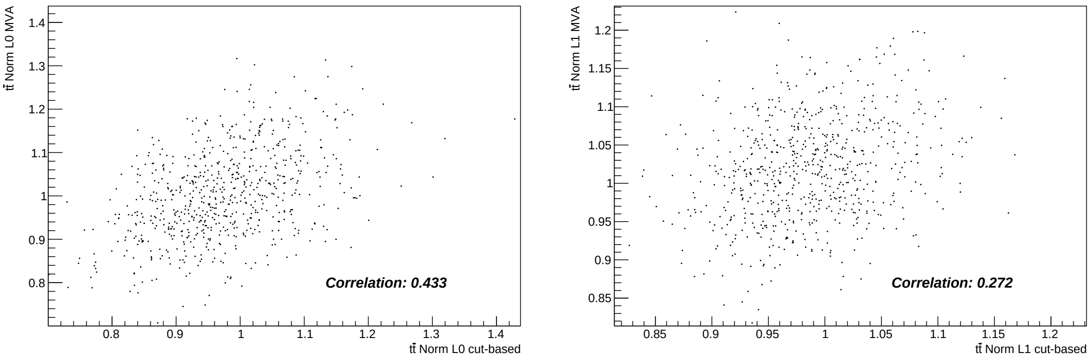

(a) 0 lepton (b) 1 lepton

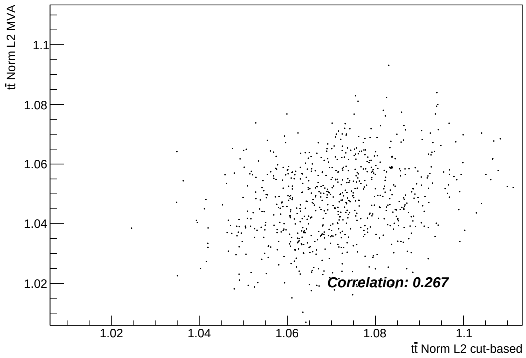

(c) 2 lepton

Figure E.2: Correlation of $t\bar{t}$ normalisation in individual lepton channels in the Combined cut-based and MVA bootstrap pseudo-datasets. Shown for 700 sets of pairs of replicas.

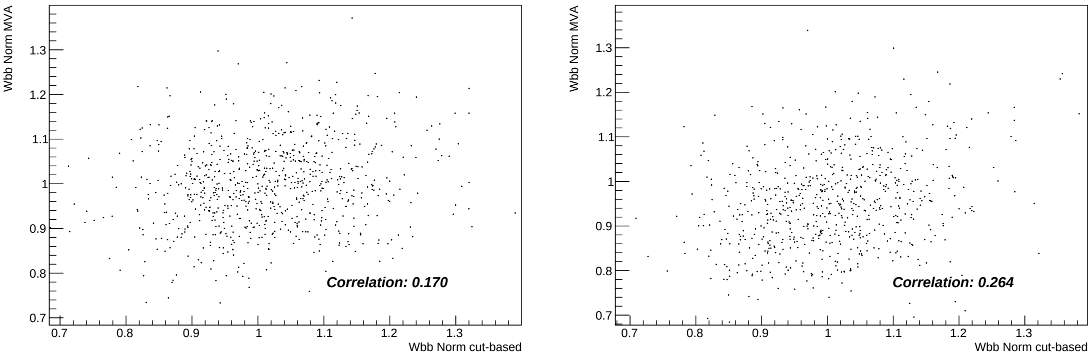

(a) 1 lepton (b) Combined

Figure E.3: Correlation of $Wb\bar{b}$ normalisation from the 1 Lepton and Combined cut-based and MVA bootstrap pseudo-datasets. Shown for 800 pairs of replicas in the 1 lepton channel and 700 sets of pairs of replicas in the Combined.

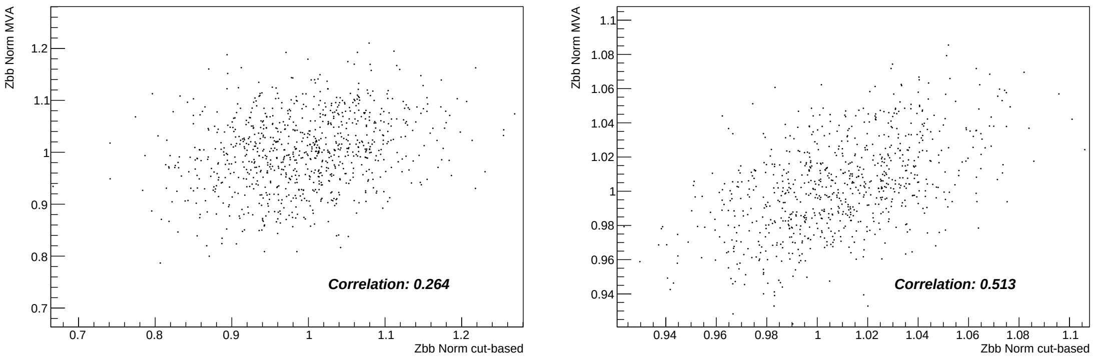

(a) 0 lepton

(b) 2 lepton

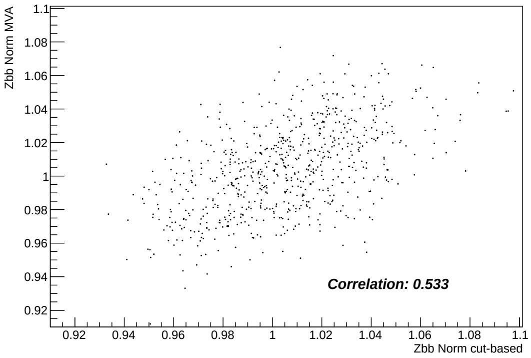

(c) Combined

Figure E.4: Correlation of $Wb\bar{b}$ normalisation from the 0 & 2 lepton and Combined cut-based and MVA bootstrap pseudo-datasets. Shown for 800 pairs of replicas in the 0 & 2 lepton channel and 700 sets of pairs of replicas in the Combined.

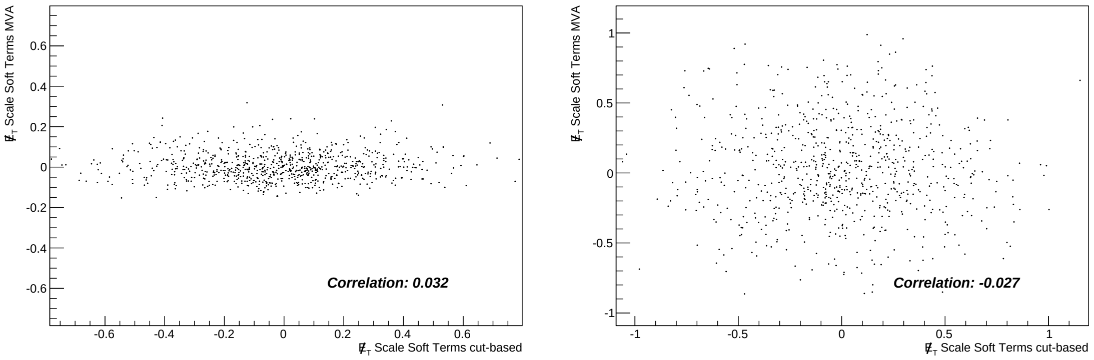

(a) 0 lepton (b) 1 lepton

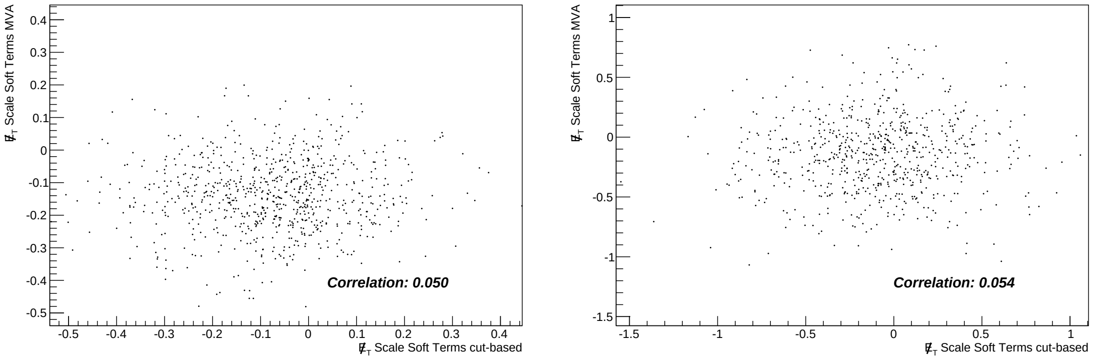

(c) 2 lepton (d) Combined

Figure E.5: Correlation of the scaling of soft terms in the $E_{\mathrm{T}}^{\mathrm{miss}}$ calulation from the individual lepton and Combined cut-based and MVA bootstrap pseudo-datasets. Shown for 800 pairs of replicas in each individual lepton channel and 700 pairs for the Combined analysis.

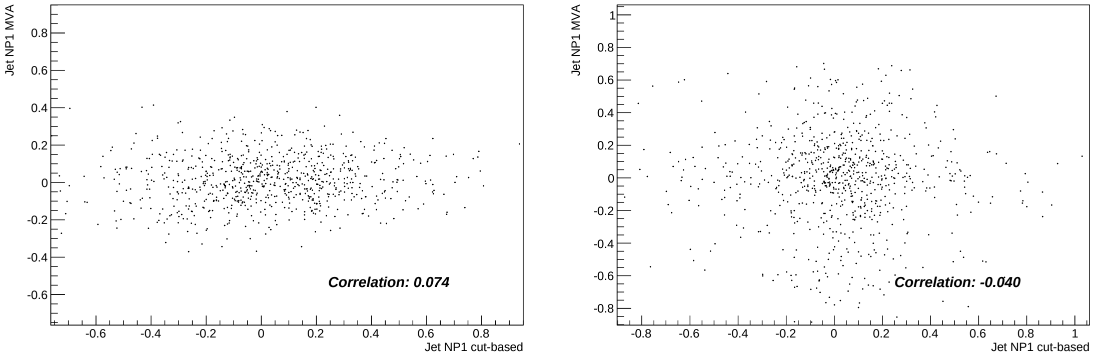

(a) 0 lepton (b) 1 lepton

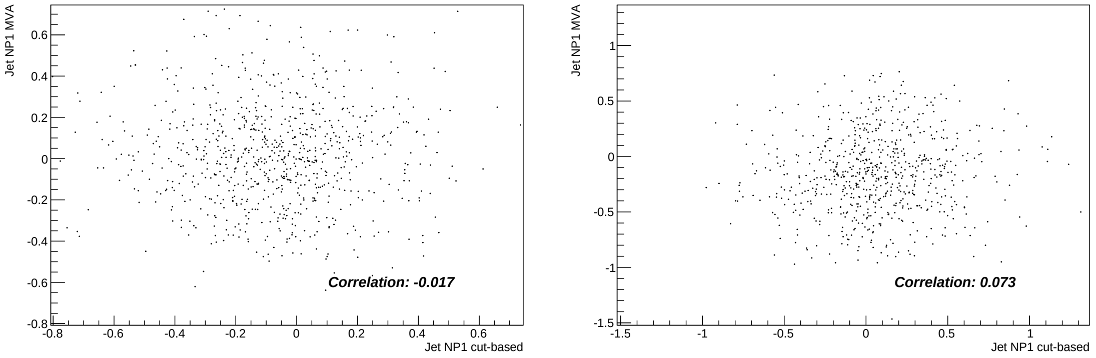

(c) 2 lepton (d) Combined

Figure E.6: Correlation of the leading jet energy scale nuisance parameter from the individual lepton and Combined cut-based and MVA bootstrap pseudo-datasets. Shown for 800 pairs of replicas in each individual lepton channel and 700 pairs for the Combined analysis.

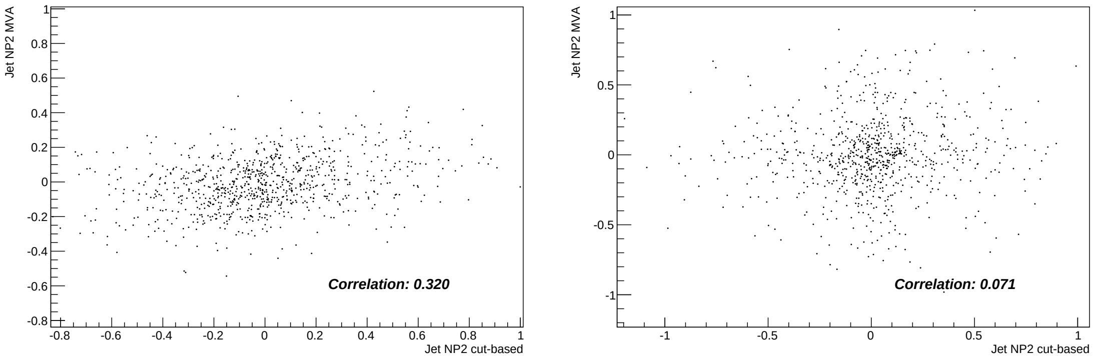

(a) 0 lepton

(b) 1 lepton

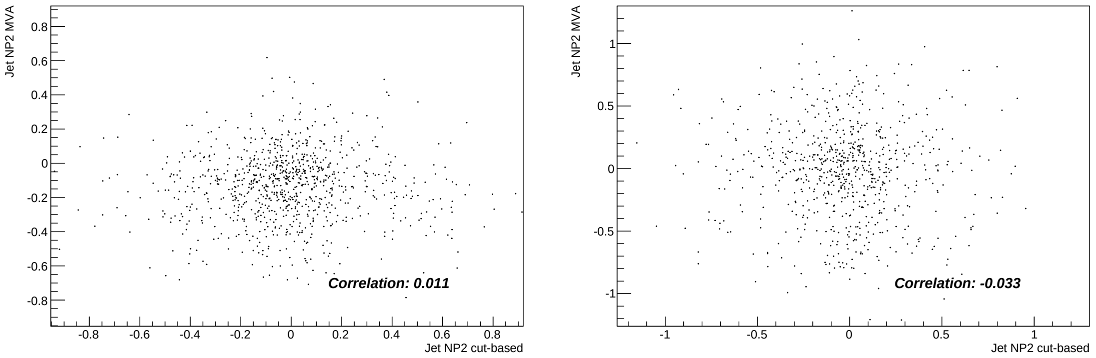

(c) 2 lepton

(d) Combined

Figure E.7: Correlation of the 2nd leading jet energy scale nuisance parameter from the individual lepton and Combined cut-based and MVA bootstrap pseudo-datasets. Shown for 800 pairs of replicas in each individual Lepton channel and 700 pairs for the Combined analysis.